



**HAL**  
open science

# Ion dynamics in the magnetic nozzle of an Electron Cyclotron Resonance Thruster

Romain Pioch

► **To cite this version:**

Romain Pioch. Ion dynamics in the magnetic nozzle of an Electron Cyclotron Resonance Thruster. Physics [physics]. Institut Polytechnique de Paris, 2024. English. NNT : 2024IPPAX064 . tel-04861648

**HAL Id: tel-04861648**

**<https://theses.hal.science/tel-04861648v1>**

Submitted on 2 Jan 2025

**HAL** is a multi-disciplinary open access archive for the deposit and dissemination of scientific research documents, whether they are published or not. The documents may come from teaching and research institutions in France or abroad, or from public or private research centers.

L'archive ouverte pluridisciplinaire **HAL**, est destinée au dépôt et à la diffusion de documents scientifiques de niveau recherche, publiés ou non, émanant des établissements d'enseignement et de recherche français ou étrangers, des laboratoires publics ou privés.



INSTITUT  
POLYTECHNIQUE  
DE PARIS

NNT : 2024IPPAX064

Thèse de doctorat



# Ion dynamics in the magnetic nozzle of an Electron Cyclotron Resonance thruster

Thèse de doctorat de l'Institut Polytechnique de Paris  
préparée à l'École polytechnique

École doctorale n°626 Ecole Doctorale de l'Institut Polytechnique de Paris (EDIPP)  
Spécialité de doctorat : Optique, Laser et Plasma

Thèse présentée et soutenue à Palaiseau, le 26 Novembre 2024, par

**ROMAIN PIOCH**

Composition du Jury :

Anne Bourdon Directrice de recherche, LPP - Ecole Polytechnique	Présidente
Stéphane Mazouffre Directeur de recherche, ICARE - Université d'Orléans	Rapporteur
Renaud Guerout Chargé de recherche, LAPLACE - Université Paul Sabatier	Rapporteur
Laure Vermare Chargée de recherche, LPP - Ecole Polytechnique	Examinatrice
Freddy Gaboriau Maître de conférence, LAPLACE - Université Paul Sabatier	Examineur
Pascal Chabert Directeur de recherche, LPP - Ecole Polytechnique	Directeur de thèse
Victor Désangles Ingénieur de recherche, ONERA	Encadrant de thèse
Matthieu Garcia Ingénieur, CNES	Invité
Ulysse Weller Ingénieur, CNES	Invité

# **Ion dynamics in the magnetic nozzle of an Electron Cyclotron Resonance thruster**

Romain PIOCH

# Résumé

Au cours des dernières décennies, les moyens de propulsion des satellites ont évolué et la propulsion électrique s'est imposée face à la propulsion chimique classiquement utilisée. Les propulseurs électriques produisent, accélèrent et éjectent un gaz ionisé, appelé plasma, pour générer une force de poussée. Le propulseur ECRA est un concept de propulseur électrique développé à l'ONERA qui bénéficie d'un design simple et innovant. Le plasma est accéléré dans un champ magnétique divergent appelé tuyère magnétique. L'objectif de cette thèse est de comprendre les phénomènes régissant l'accélération et l'éjection du plasma dans la tuyère magnétique du propulseur ECRA. Dans un premier temps, l'amélioration du diagnostic de Fluorescence Induite par Laser (LIF) a permis la mesure des deux composantes du champ de vitesse des ions dans la source du propulseur et dans les 20 premiers centimètres de la tuyère magnétique du propulseur. La solution analytique d'un modèle fluide et isotherme décrivant l'expansion d'un plasma dans une tuyère magnétique a été dérivée et comparée aux données expérimentales, et un bon accord a été trouvé entre les mesures et la théorie. Dans un second temps, pour pallier au manque de signal de LIF dans la plume du propulseur à des distances supérieures à 20cm, un diagnostic électrostatique a été développé : la coupe de Faraday directionnelle. Grâce à un design innovant, ce diagnostic permet une sélection angulaire du flux d'ion collecté. Cette propriété directionnelle a été validée grâce à des mesures de flux en face d'une source à ions calibrée puis des mesures de flux d'ions dans la plume du propulseur ECRA. De plus, l'utilisation de ce diagnostic pour estimer la poussée du propulseur donne une erreur de 5% par rapport à la mesure directe de poussée effectuée grâce à une balance. Ce résultat est à comparer à une erreur de plus de 20% obtenue quand une sonde de Faraday plate est utilisée, ce qui valide le niveau de courant mesuré par la coupe de Faraday directionnelle. Ce diagnostic de coupe de Faraday directionnelle a été monté sur un moteur pas à pas, permettant une rotation de la sonde autour d'un axe coupant son orifice d'entrée. Grâce à ce montage, la distribution angulaire de densité de courant des ions a pu être mesurée localement dans la plume du propulseur ECRA. Cette propriété a permis d'évaluer la direction locale du flux d'ions dans une zone s'étendant de 20 à 60 cm de la source du propulseur pour différents débits de gaz, puissances du propulseur, conditions de vide dans l'enceinte de test et topologies de tuyère magnétiques. La comparaison de la direction du flux d'ions avec la direction des lignes de champs magnétique dans la tuyère a permis de mettre en évidence plusieurs résultats. Premièrement, les ions ont une trajectoire colinéaire aux lignes de champ magnétique dans la partie centrale de la plume. Deuxièmement, les ions sont détachés des lignes de champs de la tuyère dans la partie latérale de la plume. La position de ce détachement ne dépend ni des conditions d'opérations du propulseur, ni du niveau de vide dans l'enceinte. En revanche, ces conditions ont une influence sur la trajectoire des ions détachés des lignes de champ magnétique. En effet, il est montré que les ions détachés suivent des trajectoires rectilignes. Par conséquent, les conditions d'opération du propulseur ont une influence sur l'angle que font les ions avec les lignes de champ magnétique à la position du détachement. Pour toutes les conditions testées, ce détachement est plus divergent que le champ magnétique. Enfin, il apparaît que la tuyère magnétique gouvernant la dynamique des ions résulte de la somme du champ magnétique produit par l'aimant permanent du propulseur et de la moyenne azimutale de l'influence du champ magnétique terrestre. Ce résultat inattendu pourrait être expliqué par une dynamique de rotation globale du plasma dans la tuyère magnétique du propulseur ECR.

# Abstract

Over the last decades, the spacecrafts propulsion systems have evolved, and the electric propulsion has been favoured over the traditionally used chemical propulsion. An electric propulsion device produces, accelerates and ejects an ionised gas, called plasma, to generate a thrust force. The ECRA thruster is an electric propulsion concept developed at ONERA which benefits from a simple and innovative design. The plasma is accelerated in a diverging magnetic field, called magnetic nozzle, which simplifies the architecture of the thruster. The objective of this work is to understand the physical phenomena governing the acceleration and the ejection of the plasma in the magnetic nozzle of an ECRA thruster. First, the improvement of the Laser Induced Fluorescence (LIF) diagnostic has allowed for the measurement of the two components of the ion velocity field in the thruster source and within the first 20 centimetres of the magnetic nozzle of the thruster. The analytical solution of a fluid and isothermal model describing the expansion of a plasma in a magnetic nozzle was derived and compared to the experimental data, and a good agreement was found between the measurements and the theory. Secondly, to overcome the lack of LIF signal at distances greater than 20cm in the plume of the ECRA thruster, an electrostatic diagnostic was developed: the directional Faraday cup. Thanks to an innovative design, this diagnostic allows for the angular selection of the collected ion flux. This directional property was validated through ion flux measurements in front of a calibrated ion source and then through ion flux measurements in the plume of the ECRA thruster. Moreover, using this diagnostic to estimate the thrust of the ECR thruster results in an error of 5% compared to the direct thrust measurement performed using a balance. This result is to be compared with an error of more than 20% obtained when a flat Faraday probe is used, which validates the level of current measured by the directional Faraday cup. This cup has been mounted on a stepper motor to measure the angular distribution of ion current density locally in the plume of the ECRA thruster. It has allowed for the measurement of the local direction of ion flux in an area extending from 20 to 60 cm from the thruster source for different gas flow rates, thruster powers, vacuum conditions in the test chamber, and magnetic nozzle topologies. The comparison of the ion flux direction with the direction of the magnetic field lines of the nozzle has highlighted several results. First, the ions have a trajectory collinear to the magnetic field lines in the centre of the plume. Second, they are detached from the magnetic field lines in the lateral part of the plume. The detachment position does not depend on the operating conditions of the thruster or the vacuum level in the vacuum facility. However, these conditions influence the trajectory of the ions already detached. In fact, it has been shown that the detached ions follow straight-line trajectories. Consequently, the thruster operating conditions influence the angle that the ions make with the magnetic field lines at the detachment location. For all tested conditions, this detachment is more divergent than the magnetic field. Finally, it appears that the magnetic nozzle governing the ion dynamics results from the sum of the magnetic field produced by the thruster permanent magnet and the azimuthal average of the influence of the Earth magnetic field. This unexpected result could be explained by a global rotation dynamic of the plasma in the magnetic nozzle of the ECRA thruster.

# Acknowledgements

J'aimerais tout d'abord remercier les deux rapporteurs de ce manuscrit, Renaud Gueroult et Stéphane Mazouffre, pour le temps qu'ils ont pris à relire et examiner ce manuscrit. Je remercie également les autres membres de mon jury, Anne Bourdon, Freddy Gaboriau et Laure Vermare, pour avoir assisté à ma soutenance et pour avoir proposé une séance de questions très intéressante et pertinente.

Je remercie chaleureusement mon encadrant de thèse Victor Désangles, mon directeur de thèse Pascal Chabert, et les membres du CNES qui ont soutenu ce projet, Alberto Rossi dans un premier temps puis Matthieu Garcia et Ulysse Weller. Victor, merci pour tous tes conseils et tes relectures, mais aussi pour les nombreuses discussions éclairantes que nous avons eues. Je reconnais ta large contribution à la réussite de mon doctorat, tu as su me guider tout en me laissant trouver mon autonomie dans mes recherches. J'aimerais aussi souligner tes qualités humaines et ton humilité, tu m'as beaucoup appris et ça a été un réel plaisir de travailler au quotidien avec toi. Pascal, merci pour ton soutien et pour les discussions toujours extrêmement enrichissantes que nous avons eues. Tu m'as grandement aidé à prendre le recul nécessaire pour voir mes résultats sous un angle différent.

Je remercie également Federico Boni qui a terminé sa thèse sur le propulseur ECR quand j'ai commencé la mienne. Federico, tu as été pour moi un mentor et tu m'as appris toutes les techniques du labo. Ton aide m'a été très précieuse lors de mes premières utilisations du B09 et du propulseur. Je retiendrai les (très longs) mois de l'hiver 2021/2022 passés devant la LIF ainsi que mes youhyouh de l'IEPC. Pour tout ça, merci. Je m'excuse cependant de ne pas avoir "résolu le propulseur ECR". Je remercie plus largement tous les permanents de l'équipe FPA de l'ONERA. Toutes et tous, vous avez contribué à la très bonne ambiance qui m'a permis de mener ma thèse dans des conditions optimales. Venir à l'Onera a toujours été un plaisir pour moi. Je remercie particulièrement les doctorants du groupe propulsion avec qui on s'est bien marré, Federico et Séverin qui ont terminé avant moi et Etienne et Giada qui assurent la relève ! À toutes et tous, à très bientôt au Shamrock !

Aux copains de soupe, et j'élargis ce groupe aux ENSTAs qui ont recroisé mon chemin ces trois dernières années, merci. Savoir décompresser fait partie d'un travail de qualité, les séances d'escalade et les bons moments qu'on a partagés ont réellement contribué au bon déroulement de ma thèse.

A ma famille, merci pour tout. A Pap's et Mam's, Aline et Kamel, et bien entendu Danil qui nous a rejoints en cours de route, merci. Je n'en serais très certainement pas là sans votre soutien qui remonte à bien plus loin que ces trois dernières années. Cette thèse est l'accomplissement de tout ce que vous m'avez apporté. Je remercie également toute la famille de Julie pour leur soutien, leur écoute et leur bienveillance.

Enfin, Julie, par ton écoute, ta patience et ton soutien indéfectible, tu as pleinement pris part à cette aventure. À nous d'écrire la suite ensemble. Ta sincérité pure et ta profonde bonté m'ont toujours dépassé, merci pour tout ce que tu fais pour moi !



# Table of Contents

<b>Résumé</b>	<b>i</b>
<b>Abstract</b>	<b>ii</b>
<b>Acknowledgements</b>	<b>iii</b>
<b>List of Figures</b>	<b>viii</b>
<b>List of Tables</b>	<b>xiv</b>
<b>1 Introduction</b>	<b>1</b>
1.1 Basics of plasma physics and electric propulsion . . . . .	1
1.1.1 Kinetic description of a plasma . . . . .	2
1.1.2 Fluid description of a plasma . . . . .	3
1.1.3 Plasma sheath . . . . .	3
1.1.4 Magnetised plasmas . . . . .	6
1.1.5 Basics of Electric Propulsion . . . . .	8
1.1.6 Plasma diagnostics . . . . .	10
1.2 The ECR thruster . . . . .	13
1.2.1 History of the device . . . . .	13
1.2.2 The ECR thruster at the beginning of the study . . . . .	13
1.3 Plasma dynamics in a diverging magnetic nozzle . . . . .	15
1.3.1 Plasma acceleration . . . . .	15
1.3.2 Plasma detachment . . . . .	17
1.4 Objectives of the study and outline of the manuscript . . . . .	19
<b>2 Experimental apparatus</b>	<b>21</b>
2.1 The ECR thruster . . . . .	22
2.1.1 Description of the device . . . . .	22
2.1.2 Magnetic field topology . . . . .	23
2.2 Vacuum Facility and diagnostics . . . . .	24
2.2.1 B09 vacuum chamber . . . . .	24
2.2.2 Ion energy analyser . . . . .	25
2.2.3 Faraday probes . . . . .	25
2.2.4 Thrust balance . . . . .	27
2.3 Measurement of the ion velocity by Laser Induced Fluorescence . . . . .	28
2.3.1 Description of the diagnostic . . . . .	28
2.3.2 LIF Data analysis . . . . .	30
2.4 Generation of an unidirectional and mono-energetic ion beam with an ion source . . . . .	33
2.4.1 Description of the ion source . . . . .	33

2.4.2	Characterisation of the ion beam . . . . .	34
<b>3</b>	<b>Description of the plasma acceleration in the magnetic nozzle of the ECR thruster</b>	<b>37</b>
3.1	Measurements of the ion velocity field in the source and the plume of an ECR thruster	39
3.1.1	Ion velocity field in the source region . . . . .	40
3.1.2	Ion velocity field in the plume region . . . . .	43
3.2	Theoretical model of isothermal expansion of a plasma in a diverging magnetic field .	45
3.2.1	Description of the model . . . . .	45
3.2.2	Verification of the assumptions of the model . . . . .	47
3.2.3	Analytical solution . . . . .	50
3.3	Comparison of the model with experimental data . . . . .	52
3.3.1	Expansion along the axis of the thruster . . . . .	52
3.3.2	Expansion in the whole plume of the thruster . . . . .	54
3.4	Discussion of the results . . . . .	55
3.4.1	Polytropic assumption . . . . .	55
3.4.2	Limits of the assumptions . . . . .	57
<b>4</b>	<b>Development of a Faraday cup for the directional measurement of the ion current density</b>	<b>61</b>
4.1	Design of the directional Faraday cup . . . . .	63
4.2	Angular selectivity of the directional Faraday cup under ballistic ion trajectories . . .	64
4.2.1	Definition and computation of the Acceptance and Opening functions . . . .	64
4.2.2	Validation of the cup directionality in ideal regime . . . . .	67
4.3	Angular distribution of ion current density measured in plasma regime . . . . .	70
4.3.1	Recommended practices for the directional Faraday cup collectors biasing . .	70
4.3.2	Modification of the Acceptance and Opening functions in plasma regime . .	73
<b>5</b>	<b>Experimental characterisation of the ion detachment from the magnetic nozzle of the ECR thruster</b>	<b>81</b>
5.1	Measurement of the plasma detachment location . . . . .	83
5.1.1	Description of the experiment . . . . .	83
5.1.2	Assessment of the local ion trajectory . . . . .	84
5.1.3	Measurement of the local magnetic field direction . . . . .	86
5.1.4	Methodology for assessing the ion detachment location . . . . .	90
5.2	Influence of the thruster operating conditions . . . . .	92
5.2.1	Variation of the microwave power . . . . .	92
5.2.2	Variation of the mass flow rate . . . . .	93
5.2.3	Variation of the vacuum conditions . . . . .	93
5.2.4	Variation of the magnetic topology . . . . .	94
5.3	Discussion of the results . . . . .	95
5.3.1	Location of ion detachment . . . . .	96
5.3.2	Trajectories of the detached ions . . . . .	97
5.3.3	Analysis of the asymmetry of the ion flux distribution . . . . .	100
5.3.4	Plasma mitigation of the magnetic nozzle deformation by the Earth magnetic field . . . . .	105
<b>6</b>	<b>Accuracy of the indirect thrust measurement of an ECR thruster</b>	<b>109</b>
6.1	Comparison between direct and indirect thrust measurements . . . . .	111
6.1.1	Methodology of the indirect thrust measurement . . . . .	111
6.1.2	Results of the comparison for two types of Faraday probes . . . . .	114

6.2	Analysis of the origin of the error when using a Faraday probe with guard ring . . . .	116
6.2.1	Comparison of the ion flux measurements performed with a Faraday probe with guard ring and a directional Faraday cup . . . . .	116
6.2.2	Electrostatic simulation of a Faraday probe with guard ring with the software SIMION . . . . .	118
6.2.3	Estimation of the sheath thickness and its relation to the probe design . . . .	120
6.3	Accuracy of the hypothesis made in the indirect estimation of the thrust . . . . .	123
6.3.1	Local ion trajectories . . . . .	123
6.3.2	Secondary electron emission . . . . .	125
6.3.3	Multiply charged ions . . . . .	125
6.3.4	Charge exchange collisions . . . . .	127
	<b>Conclusion</b>	<b>132</b>
	<b>A Intensities of the Zeeman transitions</b>	<b>137</b>
	<b>B Numerical values of ion saturation bias voltage of the directional Faraday cup</b>	<b>139</b>
	<b>C Direction of a particle following a linear trajectory</b>	<b>141</b>
	<b>D Efficiency of the ECR thruster</b>	<b>143</b>



# List of Figures

1.1	Potential drop in the sheath region according to three different models (inspired from [1]). . . . .	5
1.2	Example of an $I$ - $V$ curve measured with a Langmuir probe (reproduced from [2]). . . . .	11
1.3	Photographs of (a) a Langmuir probe, (b) a Faraday probe with guard ring (left) and a Faraday cup (right) and (c) a Curling probe. . . . .	11
1.4	Schematic of the ECR thruster. . . . .	13
2.1	(a) Schematic and (b) photograph of the ECR thruster. . . . .	22
2.2	(a) Magnetic field lines and (b) magnetic field magnitude along the axis of the ECR thruster for (solid) $M_1$ and (dashed) $M_2$ . . . . .	23
2.3	Schematic of the B09 Vacuum facility. . . . .	24
2.4	Pressure inside the B09 vacuum facility versus xenon mass flow rate with the cryopump switched off and on. . . . .	25
2.5	(a) Faraday probe with guard ring and (b) directional Faraday cup. . . . .	26
2.6	Schematic of the Faraday probe biasing and acquisition circuit. . . . .	26
2.7	Schematic of the thrust stand (reproduced from [3]). . . . .	27
2.8	(a) Signal acquired during the thrust stand calibration and (b) calibration factor associated to the deposition and the retrieval of the calibration weights. . . . .	28
2.9	Laser Induced Fluorescence scheme. . . . .	29
2.10	Laser Induced Fluorescence optical bench. . . . .	29
2.11	(a) Side view and (b) top view of the Laser Induced Fluorescence experimental setup. . . . .	30
2.12	(a) (bottom) Fabry-Perot interferometer signal and (top) conversion from temporal to frequency frame and (b) example of LIF profile. . . . .	31
2.13	LIF profiles with the Zeeman effect correction. . . . .	32
2.14	(a) Schematic and (b) photograph of the ion source. . . . .	33
2.15	(a) Beam current versus discharge current for different values of argon mass flow rate and (b) beam current versus argon mass flow rate for different values of discharge current. . . . .	34
2.16	(a) Current measured during the displacement of a Faraday probe in front of the ion source at a distance of $Z = 7$ cm and (b) beam radius versus the distance from the source. . . . .	35
2.17	Ion source beam radius versus discharge current. . . . .	35
2.18	(a) IV curve measured with a Faraday probe in front of the ion source and (b) ion energy versus floating potential of the ions source. . . . .	36
3.1	Schematic of the source and the plume region. . . . .	39
3.2	Example of the LIF profiles with the Zeeman effect correction. The location in the source is $R = 7$ mm and $Z = 10$ mm. . . . .	40

3.3	(a) $u_{iz}$ and (b) $u_{i\sigma_z}$ in the source of the ECR thruster with the magnetic topology $M_1$ . The dashed black lines represent the physical inner and outer conductor of the ECR thruster source. The thruster is firing at 1 sccm and 32 W. . . . .	41
3.4	(a) $u_{iz}$ and (b) $u_{i\sigma_z}$ in the source of the ECR thruster at the radial coordinate $R = 5$ mm with the magnetic topology $M_1$ . . . . .	42
3.5	(a) Longitudinal and (b) transversal components of the ion velocity in the plume of the ECR thruster with the magnetic topology $M_1$ . The thruster is firing at 1 sccm and 32 W. . . . .	43
3.6	Acceleration of the ions in the axis of the magnetic nozzle of the ECR thruster. The thruster is firing at 1 sccm and 32 W with the magnetic topology $M_1$ . . . . .	44
3.7	2D map of the ion velocity in the plume of the ECR thruster. The thruster is firing at 1 sccm and 32 W with the magnetic topology $M_1$ . . . . .	45
3.8	Two-dimensional map of the local angle between the ion velocity field and the magnetic field for the $M_1$ magnetic configuration. The ion velocity field is represented with red arrows. . . . .	47
3.9	Two-dimensional map of the local angle between the ion velocity field and the magnetic field for the $M_2$ magnetic configuration. The ion velocity field is represented with red arrows. . . . .	48
3.10	Verification of the isothermal approximation for the (a) $M_1$ and (b) $M_2$ magnetic configurations. . . . .	48
3.11	Evolution of the electron temperature $T_e$ for the two magnetic topologies $M_1$ and $M_2$ with (a) the thruster mass flow rate at a power of 32 W and (b) the thruster power at a mass flow rate of 1 sccm. . . . .	49
3.12	Verification of the conservation of the ion flux by comparing $B/\hat{B}$ (black solid line) and $nu/\hat{n}\hat{u}$ (scattered symbols) for the magnetic topologies (a) $M_1$ and (b) $M_2$ . . . . .	50
3.13	Comparison between the measured ion velocity (scattered symbols) and the analytical solution of the isothermal model (solid line) for several thruster operating conditions with the magnetic topologies (a) $M_1$ and (b) $M_2$ along the axis of the thruster. . . . .	52
3.14	Evolution of the subsonic to supersonic transition location for the two magnetic topologies $M_1$ and $M_2$ with (a) the thruster mass flow rate at a power of 32 W and (b) the thruster power at a mass flow rate of 1 sccm. . . . .	53
3.15	Comparison between the measured ion velocity (scattered symbols) and the analytical solution of the isothermal model (solid line) for the different magnetic field lines (a) MFL 1, (b) MFL 2 and (c) MFL OFF of the magnetic topology $M_1$ . . . . .	54
3.16	Comparison of the acceleration of the ions in the axis of the ECR thruster with an isothermal, polytropic and adiabatic expansion model. The thruster is firing at 1 sccm and 32 W with the magnetic topology $M_1$ . . . . .	56
4.1	(a) Schematic and (b) photograph of the directional Faraday cup. . . . .	63
4.2	Schematic of the ellipses resulting from the rotation of the directional Faraday cup in front of an observer. . . . .	64
4.3	Illustration of the recovering area of the ellipses formed by the plate and the opening of the directional Faraday cup for the case where (a) the opening ellipse is inside the plate ellipse, (b) the two ellipses are disjointed and (c) the ellipses partially overlap. . . . .	65
4.4	Schematic of the opening ring thickness $\ell'$ . . . . .	67
4.5	Mesh of the directional Faraday cup in the software SIMION. The ion beam makes an angle of 6 deg with the cup axis. . . . .	68
4.6	Experimental setup to measure the Acceptance and the Opening functions of the directional Faraday cup in ideal regime with the ion source. . . . .	69

4.7	Comparison between the theoretical, simulated and measured (a) Acceptance and (b) Opening function in ideal regime. . . . .	70
4.8	I-V curve with the directional Faraday cup in front of the ECR thruster firing at 1 sccm and 30 W. . . . .	71
4.9	(a) Evolution of $V_b^{IS}$ with the thruster power for several mass flow rates and (b) error on the measurement of the ion current density if the probe collectors are biased at $V_b = -350$ V if $P \leq 35$ W or $V_b = -500$ V if $P \geq 35$ W compared to a bias voltage of $V_b^{IS}$ . . . . .	72
4.10	Schematic of the directional Faraday cup in front of the ECR thruster. . . . .	73
4.11	Simulation of the directional Faraday cup with a different bias voltages of the collectors. The plate is biased at $V_b^{plate} = -300$ V, the cylinder is biased at $V_b^{cyl} = 0$ V and the opening ring is biased at $V_b^{ring} = 0$ V. . . . .	74
4.12	Simulation of the directional Faraday cup with the plate, the cylinder and the ring biased at $V_b = -300$ V. No sheath is simulated. . . . .	75
4.13	Simulation of the Acceptance function for several values of $V_b^{ring}$ with $V_b^{plate} = V_b^{cyl} = -300$ V. No sheath is simulated. . . . .	75
4.14	Simulation of the directional Faraday cup with the plate and the cylinder biased $V_b^{plate} = V_b^{cyl} = -300$ V and the ring is biased at (a) $V_b^{ring} = -300$ V and (b) $V_b^{ring} = 0$ V. . . . .	76
4.15	Simulation of (a) the Acceptance function and (b) the Opening function for several values of $V_b^{ring}$ with $V_b^{plate} = V_b^{cyl} = -300$ V. . . . .	77
4.16	$\alpha$ -scans performed with the directional Faraday cup for several values of $V_b^{ring}$ with $V_b^{plate} = V_b^{cyl} = -350$ V in front of the ECR thruster. The grey solid line is the current collected by a Faraday probe with guard ring facing the thruster. . . . .	78
5.1	Experimental setup used to characterise the ion detachment. . . . .	83
5.2	$\alpha$ -scan with (a) the continuous measurements method at the position ( $\theta = 9$ deg, $\rho = 31.5$ cm) and (b) the discrete measurements method at the position ( $\theta = 2.5$ deg, $\rho = 44$ cm). . . . .	85
5.3	$\alpha$ -scan with the Hall Sensor at the position ( $\theta = 0$ deg, $\rho = 21.5$ cm). The raw data is fitted with a cosine function. . . . .	86
5.4	$(\alpha\theta)$ -maps of the local magnetic field direction at distances $\rho = 21.5$ cm, $\rho = 31.5$ cm and $\rho = 41.5$ cm for the magnetic topologies $M_1$ ((a), (b) and (c)) and $M_2$ ((d), (e) and (f)). . . . .	87
5.5	Schematic of the cartesian and cylindrical coordinate system. . . . .	88
5.6	Magnetic field lines of the ECR thruster magnetic nozzle with and without the consideration of the Earth magnetic field for (a) the magnetic topology $M_1$ and (b) for the magnetic topology $M_2$ . . . . .	90
5.7	$(\alpha\theta)$ -map of the ion flux direction at the distance $\rho = 35.5$ cm from the thruster. The magnetic topology is $M_1$ . . . . .	91
5.8	$(\alpha\theta)$ -maps for different thruster powers at (a) $\rho = 31.5$ cm and (b) $\rho = 41.5$ cm. The mass flow rate of the thruster is 1 sccm. . . . .	92
5.9	$(\alpha\theta)$ -maps for different thruster mass flow rate at $\rho = 31.5$ cm. The power of the thruster is 30 W. . . . .	93
5.10	$(\alpha\theta)$ -maps for different vacuum conditions at (a) $\rho = 21.5$ cm, (b) $\rho = 31.5$ cm and (c) $\rho = 41.5$ cm. The thruster is firing at 1 sccm and 30 W. . . . .	94
5.11	$(\alpha\theta)$ -maps with the magnetic topology $M_2$ at (a) $\rho = 21.5$ cm, (b) $\rho = 31.5$ cm and (c) $\rho = 41.5$ cm. The thruster is firing at 1 sccm and 30 W. . . . .	95
5.12	Detachment angular location $\theta_{det}$ in (a) the $(\rho, \theta)$ frame and (b) the magnetic frame $(B/B_0, \psi/\psi_p)$ . . . . .	96

5.13	Detachment angular location $\theta_{det}$ in the $(R, Z)$ frame. . . . .	97
5.14	Schematic of a particle following a straight line trajectory after being detached from the magnetic nozzle. . . . .	97
5.15	$(\alpha\theta)$ -map at $\rho = 41.5$ cm (label $\alpha_i$ ) with the direction of the ions already detached at $\rho = 21.5$ cm if they follow a straight line trajectory (label $\alpha_{i,\rho=21.5cm} + \text{linear}$ ). The thruster is firing at 1 sccm and 30 W. . . . .	98
5.16	$(\alpha\theta)$ -map at $\rho = 41.5$ cm (black scattered symbols) with the direction of ions detached closer than $\rho = 41.5$ cm if they would have a straight line trajectory tangent to the magnetic field at the location of the detachment. The thruster is firing at 1 sccm and 30 W. . . . .	99
5.17	Skewness of the $\alpha$ -scans for different vacuum conditions at (a) $\rho = 21.5$ cm, (b) $\rho = 31.5$ cm and (c) $\rho = 41.5$ cm with the thruster is firing at 1 sccm and 30 W and skewness of the $\alpha$ -scans for different thruster power at (d) $\rho = 31.5$ cm and (e) $\rho = 41.5$ cm and (f) for different thruster mass flow rate at $\rho = 31.5$ cm. . . . .	101
5.18	$\alpha$ -scan at the position (a) ( $\theta = 26$ deg, $\rho = 31.5$ cm) fitted by a the sum of two Gaussian functions. The thruster is firing at 1 sccm and 30 W. . . . .	102
5.19	Evolution of the fitting parameters $a_2/a_1$ , $\sigma_1$ and $\sigma_2$ and $\mu_2$ with $\theta$ at distances $\rho = 21.5$ cm (resp. (a), (d), (g), (j)), $\rho = 31.5$ cm (resp. (b), (e), (h), (k)) and $\rho = 41.5$ cm (resp. (c), (f), (i), (l)) for two vacuum conditions $V_1$ and $V_2$ . The black dashed lines correspond to the detachment location $\theta_{det}$ . . . . .	103
5.20	Evolution of the fitting parameters $\sigma_1$ and $\mu_2$ with $\theta$ for different thruster microwave power at distance $\rho = 31.5$ cm (resp. (a) and (d)) and $\rho = 41.5$ cm (resp. (b) and (e)) and for different thruster Xenon mass flow rate at distance $\rho = 31.5$ cm (resp. (c) and (f)). The black dashed lines correspond to the detachment location $\theta_{det}$ . . . . .	104
5.21	$\beta$ parameter of the plasma along the axis of the ECR thruster the magnetic topologies $M_1$ and $M_2$ . The thruster is firing at 1 sccm and 30 W. . . . .	106
6.1	Ion energy scan performed with the ion energy analyser fitted with a Gaussian function. The ECR thruster is firing at 1 sccm and 30 W. . . . .	112
6.2	Angular scan of ion current density measured with the Faraday probe with guard ring (FPGR) and with the directional Faraday cup (FCDi) at $\rho = 29$ cm. The ECR thruster is firing at 1 sccm and 20 W. . . . .	113
6.3	Comparison between the direct measurement of the thrust and its indirect estimation from the ion current density measured with either the Faraday probe with guard ring (FPGR) and the directional Faraday cup (FCDi) for (a) several thruster mass flow rates at 30 W of microwave power and (b) several thruster powers at 1 sccm of xenon mass flow rate. . . . .	115
6.4	Comparison between the integrand of equation 6.2 with the ion current density $j_i$ measured with the Faraday probe with guard ring (FPGR) and the directional Faraday cup (FCDi). The ECR thruster is firing at 1 sccm and 20 W. . . . .	117
6.5	Evolution of the mass efficiency $\eta_m$ with the distance from the thruster backplate $\rho$ . The thruster is firing at 1 sccm and 30 W. . . . .	118
6.6	Illustration of the ion collection area in front of a Faraday probe with guard ring for (a) a flat sheath and (b) a non-flat sheath. . . . .	119
6.7	Mesh of the Faraday probe with guard ring in the software SIMION. . . . .	119
6.8	Theoretical Acceptance function (black solid line) of the Faraday probe with guard ring and Acceptance simulated with SIMION at several $\varnothing_{FPGR}/s_{sheath}$ ratios. . . . .	120
6.9	Child-Langmuir sheath thickness for a wall at potential $V_0 = -350$ V. . . . .	121

6.10	FPGR guard ring diameter to fifty Debye length ratio (Brown's criterion [4]) and Child-Langmuir sheath thickness to FPGR guard ring diameter ratio for several electron temperatures and probe bias voltages. . . . .	122
6.11	Examples of three angular scans of ion current measured on the plate of the directional Faraday cup at the angular positions $\theta = -20$ deg, $\theta = 0$ deg and $\theta = 10$ deg. The ECR thruster is firing at 1 sccm and 20 W. . . . .	123
6.12	Comparison between the direct measurement of the thrust and its indirect estimation from the ion current density measured with the directional Faraday cup according to equations 6.8 and 6.9 for (a) several thruster mass flow rates at 30 W of microwave power and (b) several thruster powers at 1 sccm of xenon mass flow rate. . . . .	124
6.13	Ion mass scan measured with the ion analyser at 1 sccm and 30 W. . . . .	126
6.14	Evolution of $\epsilon_{multi}$ with $\eta$ . . . . .	127
6.15	Evolution of the ion energy with the mass flow rate of the ECR thruster. . . . .	128
6.16	Ion energy distribution function measured with the ion energy analyser at (a) 0.6 sccm and (b) 2.5 sccm. . . . .	129
6.17	Evolution of (a) $\kappa$ and $\tau$ and (b) $\epsilon_{cex}$ with the thruster mass flow rate. . . . .	130
C.1	Schematic of a particle following a linear trajectory after being detached from the magnetic nozzle. . . . .	141
D.1	Efficiencies of the ECR thruster used in this manuscript at (a) constant mass flow rate 1 sccm and (b) constant power of 30 W. . . . .	143



# List of Tables

1.1	Orders of magnitude of the plasma parameters in the source and the plume of the ECR thruster (reproduced from Ref. [5]). . . . .	14
2.1	Quantum numbers of the initial and final state of the LIF transition used in this work (Extracted from [6]). . . . .	32
3.1	Value of the sonic speed (in $\text{km.s}^{-1}$ ) for several thruster operating conditions for the two magnetic topologies $M_1$ and $M_2$ . . . . .	53
6.1	Different hypothesis made in the indirect estimation of the thrust of the ECR thruster with the justification associated. . . . .	114
6.2	Averaged absolute values of the relatives errors (in %) made on the indirect thrust estimated from the ion current density measured with the Faraday probe with guard ring (FPGR) and the directional Faraday cup (FCDi). . . . .	116
6.3	Averaged absolute values of the relatives errors (in %) made on the thrust for the different indirect thrust estimation methods of equations 6.8 and 6.9. . . . .	125
A.1	Intensities of the Zeeman transitions with respect to the quantum numbers J and M of the initial and final states (reproduced from [7]). . . . .	137
B.1	Numerical values of $V_b^{IS}$ (in V) measured for the different thruster operating conditions of mass flow rate and power. . . . .	139



# 1 | Introduction

## The plasma state in a nutshell

If a sufficient amount of energy is supplied to a gas, the bond which links the electrons to the atoms or molecules can be broken, leading to the formation of a plasma constituted of negative and positive charges and of remaining neutral particles. There is no phase transition between a gas and a plasma, the transformation being characterised by the degree of ionisation which is the proportion of charged particles among all the particles, including the neutrals, constituting the plasma. Nevertheless, contrary to a gas, the free movement of the charges in a plasma gives it certain properties: a plasma reacts to externally applied electric and magnetic fields, and the collective behaviour of the charged particles creates internal currents. Plasmas are generally classified according to their degree of ionisation: the denomination “hot plasmas” stands for highly ionised plasmas while “cold plasmas” refers to partially ionised plasmas.

The plasma state is the most common state of matter found in the Universe. It constitutes the stars and the major part of the interstellar medium. Auroras, lightnings, solar wind, the trail of shooting stars or the core of flames are all examples of natural plasmas. Besides, plasmas are also used in a wide range of industrial applications. Processes such as plasma etching are widely used for the fabrication of integrated circuits, plasma propulsion is one way to control the motion of spacecrafts, and nuclear fusion is an application for the production of energy.

## 1.1 Basics of plasma physics and electric propulsion

The different sections following this brief introduction to the plasma state are not intended to be a substitute for a complete plasma physics course. Indeed, several books of reference provide a in-depth understanding of the plasma physics and its applications [8–10]. The objective here is to introduce the concepts required for a good comprehension of the work developed throughout the manuscript. In a first part, two descriptions of a plasma, i.e. the kinetic and the fluid descriptions, are presented with the equations associated. From this mathematical framework, some elements of the physics of plasma sheaths and magnetised plasmas are given. The elements constituting the first section are largely inspired from Chabert’s plasma physics course [1]. This part is followed by a focus on the application of plasma physics for the electric propulsion of spacecrafts. Different types of efficiencies, which are computed to compare electric propulsion devices between each other, are introduced. Then, several diagnostics used to measure the plasma parameters are reviewed. Finally, after this introduction to the basics of the plasma physics and the electric propulsion, a review of the state of the art concerning the Electron Cyclotron Resonance thruster, as well as a review of the theoretical models, numerical simulations and experimental results associated to the plasma dynamics in a diverging magnetic nozzle allow to motivate this study.

The objectives of this work and an outline of the manuscript conclude this introduction.

### 1.1.1 Kinetic description of a plasma

The kinetic description of a plasma is a theoretical approach which relies on the equations of statistical physics. In this formalism, each charged particle, ion or electron, is described by a velocity distribution function, denoted by  $f(\mathbf{r}, \mathbf{v}, t)$ , which is the probability to find a particle in the position-velocity phase space  $(\mathbf{r}, \mathbf{v})$  at a given time  $t$ . Therefore, the number of particle  $dN$  which have a position comprised between  $\mathbf{r}$  and  $\mathbf{r} + d\mathbf{r}$  and a velocity comprised between  $\mathbf{v}$  and  $\mathbf{v} + d\mathbf{v}$  at the time  $t$  is given by the following relation:

$$dN = f(\mathbf{r}, \mathbf{v}, t) d\mathbf{r} d\mathbf{v} \quad (1.1)$$

From this definition of the velocity distribution function, the particle density, denoted by  $n(\mathbf{r}, t)$ , which is the number of particle at the position  $\mathbf{r}$  and the time  $t$ , is defined as:

$$n(\mathbf{r}, t) = \int f(\mathbf{r}, \mathbf{v}, t) d\mathbf{v} \quad (1.2)$$

In the remaining of the manuscript, otherwise mentioned, the indexes  $e$  and  $i$  are used to describe a plasma parameter related to the electrons and the ions respectively. Hence,  $n_e$  is the electron density and  $n_i$  is the ion density.

Within the framework of statistical mechanics, it comes that the average velocity of the particle at the position  $\mathbf{r}$  and the time  $t$ , denoted by  $\langle \mathbf{v}(\mathbf{r}, t) \rangle$ , is:

$$\langle \mathbf{v}(\mathbf{r}, t) \rangle = \frac{\int \mathbf{v} f(\mathbf{r}, \mathbf{v}, t) d\mathbf{v}}{\int f(\mathbf{r}, \mathbf{v}, t) d\mathbf{v}} \quad (1.3)$$

and the particle flux, denoted by  $\Gamma(\mathbf{r}, t)$ , is:

$$\Gamma(\mathbf{r}, t) = n(\mathbf{r}, t) \langle \mathbf{v}(\mathbf{r}, t) \rangle = \int \mathbf{v} f(\mathbf{r}, \mathbf{v}, t) d\mathbf{v} \quad (1.4)$$

The conservation equation for the velocity distribution function of a particle is obtained with a balance between the particle flux entering and leaving the phase space and with the consideration of the creation and loss of particles. This equation, which describes the evolution of the distribution function of the particles in a plasma, is called Boltzmann's equation and reads:

$$\frac{\partial f}{\partial t} + \mathbf{v} \cdot \nabla_{\mathbf{r}} f + \frac{\mathbf{F}}{m} \cdot \nabla_{\mathbf{v}} f = \left. \frac{\partial f}{\partial t} \right|_c \quad (1.5)$$

where  $m$  is the mass of the particle,  $\mathbf{F}$  represents the forces acting on the particle. In presence of external electric and magnetic fields, denoted by  $\mathbf{E}$  and  $\mathbf{B}$  respectively, this term is called the Lorentz's force and reads  $\mathbf{F} = q(\mathbf{E} + \mathbf{v} \times \mathbf{B})$ . The right hand term of equation 1.5 includes all of the mechanisms related to collisions, creations and losses of particles in the phase space. When this term is neglected, equation 1.5 is called Vlasov's equation.

The particles of a plasma are often considered to be at thermal equilibrium. In this case, their velocity distribution function follows a Maxwellian distribution which reads:

$$f(\mathbf{v}) = n \left( \frac{m}{2\pi k_b T} \right)^{3/2} e^{-\frac{m(v_x^2 + v_y^2 + v_z^2)}{2k_b T}} \quad (1.6)$$

where  $k_b$  is the Boltzmann's constant and  $T$  is a temperature. Note that in this expression, the space and temporal dimensions  $\mathbf{r}$  and  $t$  are not written explicitly for the sake of clarity. To obtain the velocity distribution function in one dimension, equation 1.6 is integrated over the two other components of the velocity space. Therefore, the distribution function of the component  $v_x$  for example is:

$$f(v_x) = n \sqrt{\frac{m}{2\pi k_b T}} e^{-\frac{mv_x^2}{2k_b T}} \quad (1.7)$$

### 1.1.2 Fluid description of a plasma

It is possible to construct a fluid description of a plasma from the velocity moments of Boltzmann's equation. Contrary to the kinetic description, which describes the behaviour of each particle, the fluid equations give a macroscopic point of view of the evolution of the plasma quantity at a given position in space and time. The conservation equation is obtained from the integration of equation 1.5 in the velocity space. It reads:

$$\frac{\partial n}{\partial t} + \nabla \cdot (n\mathbf{u}) = S - L \quad (1.8)$$

where  $\mathbf{u}$  is the fluid velocity of the particles, and  $S$  and  $L$  represent the volume source and loss terms respectively.

The second fluid equation, corresponding to the momentum conservation of the particles, is obtained from the first momentum of Boltzmann's equation and is written as follows:

$$mn \left[ \frac{\partial \mathbf{u}}{\partial t} + (\mathbf{u} \cdot \nabla) \mathbf{u} \right] = qn (\mathbf{E} + \mathbf{u} \times \mathbf{B}) - \nabla p - m\mathbf{u} [n\nu_m + S - L] \quad (1.9)$$

where  $\mathbf{E}$  and  $\mathbf{B}$  are respectively the electric and magnetic fields external to the plasma,  $q$  is the charge of the particles,  $p$  is called the scalar pressure term and  $\nu_m$  is the frequency of elastic collisions.

The two fluid equations 1.8 and 1.9 do not constitute a closed set of equations. In fact, a closing relation between the fluid variables must be defined to complete this fluid description of a plasma. The polytropic relation is often considered. It links the scalar pressure term with the particle density through a polytropic coefficient, denoted by  $\gamma$ , as follows:

$$\frac{\nabla p}{p} = \gamma \frac{\nabla n}{n} \quad (1.10)$$

The limit  $\gamma \rightarrow 1$  is called the isothermal approximation. In this case, the temperature is constant and the gradient of pressure is associated to a gradient of density by the relation  $\nabla p = k_b T_e \nabla n$ . The case where  $\gamma = 5/3$  is called the adiabatic approximation.

The fluid formalism described above is used in chapter 3 of the manuscript, in which a fluid model is derived to describe the expansion of a plasma in a diverging magnetic nozzle. It also gives the elements to understand the notion of plasma sheath, which is introduced in the following section.

### 1.1.3 Plasma sheath

Because of the great difference in mass between the ions and the electrons, the electron flux is significantly greater than the ion flux. This difference of mobility creates a space charge which generates an electric field  $\mathbf{E}$ , called ambipolar electric field, whose evolution is governed by the Maxwell Gauss equation:

$$\nabla \mathbf{E} = \frac{e(n_i - n_e)}{\epsilon_0} \quad (1.11)$$

where  $\epsilon_0$  is the vacuum permittivity. The generation of this electric field ensures the quasi neutrality in the bulk plasma and balances the fluxes of the different charged particles. The transport of particles, of flux denoted by  $\Gamma$ , is purely diffusive and governed by the equation [1]:

$$\Gamma = \frac{\mu_e D_i + \mu_i D_e}{\mu_i + \mu_e} \nabla n = D_a \nabla n \quad (1.12)$$

where  $\mu_e$  and  $\mu_i$  are the mobility of the electrons and the ions respectively,  $D_e$  and  $D_i$  are the diffusion coefficient of the electrons and the ions respectively, and  $D_a$  is called ambipolar diffusion coefficient. The expressions of  $\mu_e$ ,  $\mu_i$ ,  $D_e$  and  $D_i$  are obtained from equation 1.9 and are function of the elastic collisions coefficients [8]. From equation 1.12, it comes that  $D_i < D_a < D_e$ . This relation shows that the ambipolar electric field accelerates the ions while it confines the electrons to ensure the quasi neutrality in the plasma.

However, if an electrically floating object, a probe or the wall of the experiment for example, is immersed in the plasma, it will collect the charged species until it reaches a steady state potential. Because of the greater mobility of the electrons compared to that of the ions, there is a steady state for which the potential of the object, called the floating potential, is sufficiently low to balance the electron and ion fluxes at the plasma-wall interface. The region close to the object, in which the potential falls and where the quasi-neutrality of the plasma is no longer verified, is called the plasma sheath.

The dimension of the sheath depends on the characteristics of the wall and of the plasma, it can be derived from the fluid equations developed in the previous section. The three main sheath models and their approximations are described below. To derive these expressions, the electric field  $\mathbf{E}$  is expressed as the gradient of a potential  $\phi$ :

$$\mathbf{E} = -\nabla\phi \quad (1.13)$$

In the three sheath models derived below, the collisions are neglected.

### Boltzmann equilibrium model

In the first model, electrons are supposed to be isothermal and their inertia is neglected, meaning that the electrons respond instantaneously and their temperature is constant. The terms of the fluid equation 1.9 (for the electrons) which are not neglected are the pressure gradient term balanced by the electric field term. It reads:

$$\begin{aligned} k_b T_e \nabla n_e &= -n_e e \mathbf{E} = n_e e \nabla \phi \\ \Leftrightarrow n_e &= n_0 e^{e\phi/k_b T_e} \end{aligned} \quad (1.14)$$

where  $n_0$  is the density of the bulk plasma. The ion density is supposed to be constant in the sheath, it is therefore equal to  $n_0$ . The space charge is then written as follows:

$$e(n_i - n_e) = en_0 \left[ 1 - e^{e\phi/k_b T_e} \right] \approx -\frac{e^2 n_0 \phi}{k_b T_e} \quad (1.15)$$

where the approximation of small potential perturbations, i.e.  $|e\phi| \ll k_b T_e$ , allows the series expansion. Thus, from equations 1.11, 1.13 and 1.15, the potential drop in the sheath is expressed (in 1 dimension) as follows:

$$\phi(x) = \phi_0 e^{-\frac{x}{\lambda_D}} \quad (1.16)$$

where the characteristic dimension  $\lambda_D$  is called the Debye length and reads:

$$\lambda_D = \sqrt{\frac{\epsilon_0 k_b T_e}{n_e e^2}} \quad (1.17)$$

The Debye length of a plasma represents the characteristic length at which the electric potentials are screened by the plasma. In this first model, it is the characteristic thickness of the plasma sheath (figure 1.1).

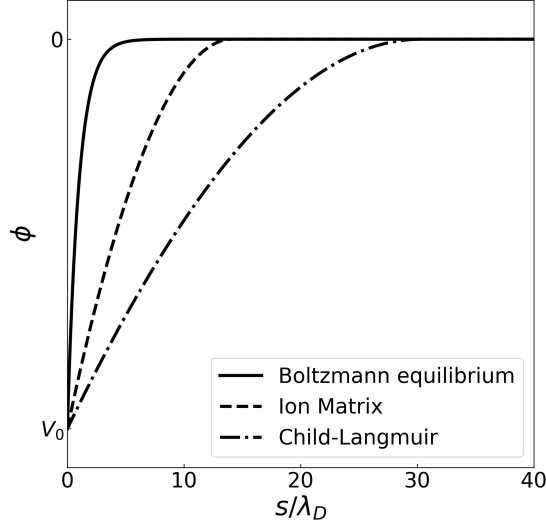


Figure 1.1: Potential drop in the sheath region according to three different models (inspired from [1]).

### Ion matrix model

The second sheath model is called the ion matrix model. The hypothesis of small potential perturbation is no longer assumed but the ion density is still considered to be constant and equal to  $n_0$  in the sheath region. This model is generally used to describe the plasma at the vicinity of an electrode biased negatively. In this case, the electrons are repelled by the wall, so the electron density is null at the plasma-wall boundary. From equations 1.11 and 1.13, it comes:

$$\nabla^2 \phi = -\frac{en_0}{\epsilon_0} \quad (1.18)$$

Since the right hand term of equation 1.18 is constant, the equation can be integrated twice. The potential fall in the plasma sheath (in 1 dimension) thus reads:

$$\phi(x) = -\frac{en_0}{2\epsilon_0} (x - s)^2 \quad (1.19)$$

where  $s$  is the sheath thickness. If the potential of the wall is fixed at  $\phi(0) = V_0$ , then  $s$  reads:

$$s = \lambda_D \sqrt{\frac{2eV_0}{k_b T_e}} \quad (1.20)$$

This expression shows that when the wall is biased at a potential  $V_0$ , the sheath thickness can be several Debye lengths, as illustrated in figure 1.1. However, this model has some limitations: the electrons are not considered in Maxwell Gauss equation 1.11 and the ions do not have any mobility in the sheath. Therefore, the Child-Langmuir model, which is derived below, is more appropriate to get the sheath thickness at the vicinity of a wall biased at a high potential  $V_0$ .

### Child-Langmuir model

The third sheath model is called the Child-Langmuir law. It relies on the same approximations than the ion matrix model but in this case the ion flux is taken into account. In the fluid equation 1.9 for the ions, the pressure term is neglected so this equation reads:

$$\begin{aligned} m_i n_i (\mathbf{u} \cdot \nabla) \mathbf{u} &= -e n_i \nabla \phi \\ \Leftrightarrow \nabla \left( \frac{1}{2} m_i u_i^2 + e \phi \right) &= 0 \end{aligned} \quad (1.21)$$

The equation which governs the evolution of the potential in the sheath (in 1 dimension) in this model is obtained from equations 1.11, 1.13 and 1.21, and reads:

$$\frac{d^2 \phi}{dx^2} = -\frac{j_i}{\epsilon_0} \left( -\frac{2e\phi(x)}{m_i} \right)^{-\frac{1}{2}} \quad (1.22)$$

where  $j_i = en_i u_i$  is the ion current density. If the potential of the wall is  $\phi(0) = V_0$ , the sheath thickness  $s$  is:

$$s = \frac{2}{3} \sqrt{\frac{\epsilon_0}{j_i}} \left( \frac{2e}{m_i} \right)^{1/4} V_0^{3/4} \quad (1.23)$$

The three plasma sheath models derived above show that the evolution of the potential in the sheath region is correlated to the plasma properties, and the characteristic thickness of the plasma sheath ranges from one to several tens of Debye lengths (figure 1.1). Note that the plasma is supposed to be collisionless here. Hence, the description can be refined if the collisions between the charged species are taken into account [1, 8–10].

## 1.1.4 Magnetised plasmas

### Cyclotron motion

As stated above, plasma dynamics is influenced by the presence of external electric and magnetic fields. Although this influence results from a collective behaviour of the charges in the plasma, it is first necessary to recall the equations which govern the movement of a single charged particle in a constant magnetic field. No external electric field is considered here, and the constant magnetic field  $\mathbf{B}$  is oriented along one direction of the cartesian referential such that  $\mathbf{B} = B\mathbf{e}_z$ . The only force that acts on the particle is  $\mathbf{F} = q\mathbf{v} \times \mathbf{B}$ , the equation of motion of the particle is therefore:

$$m \frac{d\mathbf{v}}{dt} = q\mathbf{v} \times \mathbf{B} \quad (1.24)$$

The solution of this equation describes an helicoidal trajectory along the direction of the magnetic field, with a rotation around the magnetic field lines (in the plane  $(\mathbf{e}_x, \mathbf{e}_y)$ ). The angular frequency of the rotation of the particle is called the cyclotron pulsation, denoted by  $\omega_c$ , and reads:

$$\omega_c = \frac{|q|B}{m} \quad (1.25)$$

The velocity of the particle is decomposed into the parallel velocity, denoted by  $v_{\parallel}$ , along the magnetic field direction, and the perpendicular velocity, denoted by  $v_{\perp}$ , in the plane normal to the direction of the magnetic field. The radius of the circular motion of the particle is called the Larmor radius, denoted by  $\rho_L$ , and is:

$$\rho_L = \frac{mv_{\perp}}{|q|B} \quad (1.26)$$

## Drifts

The approximation above describes the behaviour of a particle in a constant magnetic field. In the presence of a constant electric field, the force that acts on the particle is  $\mathbf{F} = q(\mathbf{E} + \mathbf{v} \times \mathbf{B})$  so the equation of motion in this case is:

$$m \frac{d\mathbf{v}}{dt} = q(\mathbf{E} + \mathbf{v} \times \mathbf{B}) \quad (1.27)$$

The solution of this equation is the same helicoidal motion described above, except that a drift of the guiding centre of the particle with a velocity  $v_{DE}$  is associated. This drift is called the  $\mathbf{E} \times \mathbf{B}$  drift and the velocity is:

$$v_{DE} = \frac{\mathbf{E} \times \mathbf{B}}{B^2} \quad (1.28)$$

This expression shows that the  $\mathbf{E} \times \mathbf{B}$  drift does not depend on the mass or the charge of the particles. Therefore, all of the particles of the plasma drift with the same velocity without any generation of current.

In the presence of a gradient of magnetic field in the direction perpendicular to the field, i.e. expressed in the  $(\mathbf{e}_x, \mathbf{e}_y)$  plane, the particles undergo a drift in the direction perpendicular to the gradient. In fact, due to the magnetic field gradient, the Larmor radius of the particle changes along its trajectory, which induces the drift. This drift is called the grad-B drift, and the velocity associated, denoted by  $v_{D\nabla}$  is:

$$v_{D\nabla} = \frac{\mu \mathbf{B} \times \nabla B}{q B^2} \quad (1.29)$$

where  $\mu$ , called the magnetic moment, is the ratio of the perpendicular kinetic energy of the particle to the magnitude of the magnetic field and reads:

$$\mu = \frac{mv_{\perp}^2}{2B} \quad (1.30)$$

It can be shown that  $\mu$  is an adiabatic invariant [8].

In some situations, the magnetic field lines might have a curvature. In this case, an other drift, associated to the centrifugal force, is to be considered. It is called the curvature drift, with the velocity, denoted by  $v_{DR}$  which reads:

$$v_{DR} = -\frac{mv_{\parallel}^2}{R_c} \frac{\mathbf{B} \times \mathbf{n}}{qB^2} \quad (1.31)$$

where  $R_c$  is the curvature radius of the magnetic field and  $\mathbf{n}$  is the centrifugal unit vector.

The last drift presented in this section is derived from the fluid description of the plasma. In fact it applies only to the fluid element (not the particles). In the case of a collisionless plasma, with variations slower than the period of cyclotron gyration and with a negligible convection, Boltzmann's equation 1.9 can be approximated as follows:

$$0 = qn(\mathbf{E} + \mathbf{u} \times \mathbf{B}) - \nabla p \quad (1.32)$$

The cross product of this equation with  $\mathbf{B}$  leads to:

$$\frac{\mathbf{E} \times \mathbf{B}}{B^2} - \frac{\nabla p \times \mathbf{B}}{qnB^2} = \mathbf{u} - \frac{(\mathbf{u} \cdot \mathbf{B}) \mathbf{B}}{B^2} \quad (1.33)$$

This equation shows that, in the direction perpendicular to the magnetic field, a drift, called the diamagnetic drift, is added to the  $\mathbf{E} \times \mathbf{B}$  drift. The velocity associated, different for the electrons and the ions and denoted by  $v_{De}$  and  $v_{Di}$  respectively, reads:

$$\begin{aligned} v_{De} &= \frac{\nabla p_e \times \mathbf{B}}{en_e B^2} \\ v_{Di} &= -\frac{\nabla p_i \times \mathbf{B}}{en_i B^2} \end{aligned} \quad (1.34)$$

This expression shows that a gradient of pressure makes the electrons and the ions drift in opposite directions.

### Axial acceleration

In the particular case of magnetic nozzles, the magnetic field gradient is directed along the magnetic field lines. In this case, the particle accelerate in the magnetic nozzle, as illustrated by the conservation of the magnetic moment:

$$\begin{aligned} \mu &= \frac{mv_{\perp}^2}{2B} = const \\ v_{\perp}^2 + v_{\parallel}^2 &= const \end{aligned} \quad (1.35)$$

From equation 1.35, it comes that the decrease of magnetic field  $B$  in the diverging magnetic nozzle converts the perpendicular motion of the particles into parallel energy.

The theoretical elements given above constitute the basic mathematical framework on which the work presented throughout the manuscript is based. In fact, the manipulation of the fluid equations is used in chapter 3, plasma sheath analysis are used in chapters 4 and 6, and the equations governing the physics of magnetised plasma are to be kept in mind, especially in chapter 5. Moreover, these elements show how plasmas can be manipulated and accelerated by means of external electric and magnetic fields, which justifies their use for the propulsion of spacecrafts. This point is detailed in the following section.

### 1.1.5 Basics of Electric Propulsion

The context of the New Space industry, which disrupted the space market since the early 2000s, has allowed a reduction of the cost and a greater availability of the usage of space technologies, accompanied by the diminution of the size of the spacecrafts. Thus, small spacecrafts, of several tens of centimetres in size, require means of propulsion different from that generally used for larger satellites, and the electric propulsion has become the norm over the traditionally used chemical propulsion. Among the many existing electric propulsion concepts, different technologies are commonly used in space, such as the Hall effect thruster (HET), the gridded ion thruster (GIT) or the field emission electric propulsion device (FEED) [11]. The Electron Cyclotron Resonance thruster (ECR), which is the electric propulsion device studied in this work, has never been launched into space.

Contrary to the traditional chemical propulsion systems, for which the propulsive energy originates from a chemical reaction of an ergol ejected in a physical nozzle, electric propulsion systems are based on the creation of a plasma with electrical power and its ejection at high velocity by means of electric and magnetic fields. Several figures of merit can be computed to compare two different propulsion devices between each other. First, the thrust, denoted by  $T$  and expressed in newton [N], or in the Standard Unit system in  $[\text{kg.m.s}^{-2}]$ , is the force resulting

from the ejection of matter. It is related to the mass flow rate  $\dot{m}$  and the ejection velocity  $v_{ex}$  of the propellant by the following relation:

$$T = \dot{m}v_{ex} \quad (1.36)$$

A great thrust allows for a spacecraft to change its orbit in a restricted amount of time. However, this figure of merit does not take into account how efficient the ejection of propellant is. To this end, one generally uses the specific impulse, denoted by  $I_{sp}$  and expressed in seconds [s], which reads:

$$I_{sp} = \frac{v_{ex}}{g} = \frac{T}{\dot{m}g} \quad (1.37)$$

where  $g$  is the gravitational acceleration on Earth.

The thrust produced by chemical propulsion devices ranges from  $10^3$  to  $10^7$  N, and is associated to specific impulses of a few hundreds of seconds. These high values of thrust are necessary to place the spacecrafts onto orbit, or to change orbits within a few days. On the other hand, electric propulsion devices reach thrusts of the order of  $10^{-5}$  to 1 N, which is not sufficient to place a spacecraft onto orbit but does allow the control and the rising of the orbit. However, they can reach extremely high specific impulses, up to several tens of thousands of seconds, due to the high exhaust velocity achieved by the acceleration of a plasma with an electric field. It makes them very efficient devices in terms of propellant consumption, with a reduced mass of propellant necessary for a given mission.

While the  $I_{sp}$  shows how a given mass of propellant is efficiently used to produce a thrust force, there exist other types of efficiencies to assess the performance of an electric propulsion device [10]. They are computed under the assumption that the ejection of the ions constituting the plasma is axi-symmetrical and directed downstream the source. The contribution of the electrons to the thrust is neglected due to their weak mass compared to that of the ions. First, the ion beam reads:

$$I_b = \pi\rho^2 \int_{-\pi/2}^{\pi/2} j_i(\theta)|\sin(\theta)|d\theta \quad (1.38)$$

where  $j_i$  is the ion current density, and  $\rho$  and  $\theta$  are the distance to the thruster and the angular coordinate respectively.

The mass utilisation efficiency  $\eta_m$  is the proportion of propellant which is ionised and therefore accelerated by the thruster. It is expressed as the ratio between the ion mass flow rate  $\dot{m}_i$  and the gas mass flow rate supplied to the thruster  $\dot{m}$ . It reads:

$$\eta_m = \frac{\dot{m}_i}{\dot{m}} = \frac{m_i I_b}{e\dot{m}} \quad (1.39)$$

The electrical efficiency  $\eta_e$  quantifies the proportion of electrical power which is effectively used to accelerate the plasma. It is the ratio between the beam power  $P_b$  and the total power supplied to the thruster  $P_T$ . It reads:

$$\eta_e = \frac{P_b}{P_T} = \frac{E_i I_b}{P_T} \quad (1.40)$$

An other figure of merit, often used to compare two electric propulsion devices which use different ways to accelerate the plasma, is called the thrust to power ratio and reads:

$$TTPR = \frac{T}{P_T} \quad (1.41)$$

The divergence efficiency  $\eta_d$  quantifies the ability of the ejected matter to effectively contribute to the thrust. It is defined as the ratio between the thrust of the device and an ideal thrust obtained if all of the ions were ejected along the thrust axis. It reads:

$$\eta_d = \frac{T}{\dot{m}_i u_i} = \sqrt{\frac{m_i}{2eE_i}} \frac{T}{\dot{m}_i} \quad (1.42)$$

where  $E_i$  is the ion kinetic energy.

Finally, the total efficiency  $\eta_T$  takes into account all of the efficiencies mentioned above. It reads:

$$\eta_T = \eta_m \eta_e \eta_d^2 = \frac{T^2}{2\dot{m} P_T} \quad (1.43)$$

According to the requirements of the mission of the spacecraft, electric propulsion system manufacturers might want to maximise one type of efficiency over an other. Moreover, knowing the plasma parameters in the plume of electric propulsion devices is insightful on the properties of the plasma acceleration, which can be optimised with regard to these efficiencies. Therefore, there is a need for precise and standardised measurements of the plasma parameters in the plasma plume of electric propulsion devices to access for example the emitted ion flux or the ion energy. A review of some of the plasma diagnostics commonly used is proposed in the following section.

### 1.1.6 Plasma diagnostics

The plasma parameters defined above can be experimentally measured in laboratory plasma using various instruments called plasma diagnostics. This section provides a review of the diagnostics which are relevant for the comprehension of this study. A set of recommended practices, written in the view of a standardisation of the plasma measurements in electric propulsion testings, can be found in Refs [4, 12–17]. Two categories of plasma diagnostics can be distinguished: electrostatic and optical diagnostics. The first category includes a variety of probes used to measure *in situ* the plasma properties. Such diagnostics are said to be perturbative because they are based on the measurement, with an electrode, of the plasma response to a local perturbation. The second category is based on the observation of the plasma, with a camera or after the excitation of the charged species with a laser for example.

#### Langmuir probe

The Langmuir probe [18] is one of the most widely used electrostatic diagnostics. It consists in a metallic electrode placed inside a plasma (figure 1.3a). The current drawn by the plasma is measured for various probe bias voltages, and the analysis of the current-voltage curve (also called *I-V* curve) allows to determine several plasma parameters such as the electron temperature, the electron and ion densities, the plasma potential, the floating potential and the electron energy distribution function [12, 19–21]. Several regions can be distinguished on an I-V curve (figure 1.2). First, when the bias voltage of the probe is low and negative (left part of the curve), all of the electrons of the plasma are repelled and the probe collects mostly ions, leading to a negative current. This region is called the ion saturation region, and the current collected is called the ion saturation current. When the ion flux balances the electron flux, the net current collected on the probe is 0. This condition is reached for a given value of bias voltage called the floating potential, denoted by  $V_f$ . This is the potential reached by a conductive object left floating in a plasma. For bias voltages greater than  $V_f$ , when the bias voltage of the probe increases, it starts to collect more electrons than ions, resulting in a net positive current measured. Above

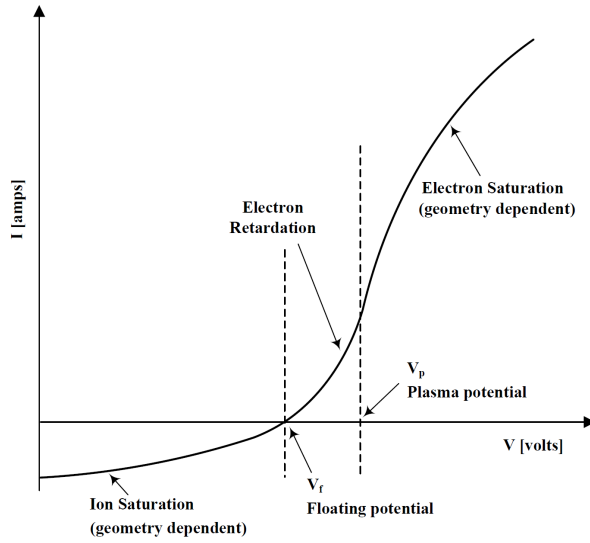


Figure 1.2: Example of an  $I$ - $V$  curve measured with a Langmuir probe (reproduced from [2]).

a certain potential, which is the plasma potential denoted by  $V_p$ , the ions are repelled by the probe which collects mostly electrons. This region is called the electron saturation region. The shape of an  $I$ - $V$  curve, and therefore the theory invoked to retrieve the plasma parameters, depends on the geometry of the Langmuir probe. In fact, the plasma sheath that forms in front of the collectors of the diagnostic must be taken into account in the post processing of the data in order to avoid a wrong estimation of the plasma parameters. If the Langmuir probe electrode is a wire, the sheath thickness will be larger than the probe dimension, and the Orbital Motion Limited (OML) theory might be suited to interpret the  $I$ - $V$  curve [22]. An other model is the Druyvesteyn method, based on the analysis of the second derivative of the  $I$ - $V$  curve [23]. Besides, several levels of complexity can be brought to the design of a Langmuir probe. For example, in the case of a double Langmuir probe, the bias voltage is applied between the tip of two identical electrodes. With such design, there is no need for a stable ground reference. Langmuir probes can also be RF-compensated for the study of radio frequency plasma discharges [24].

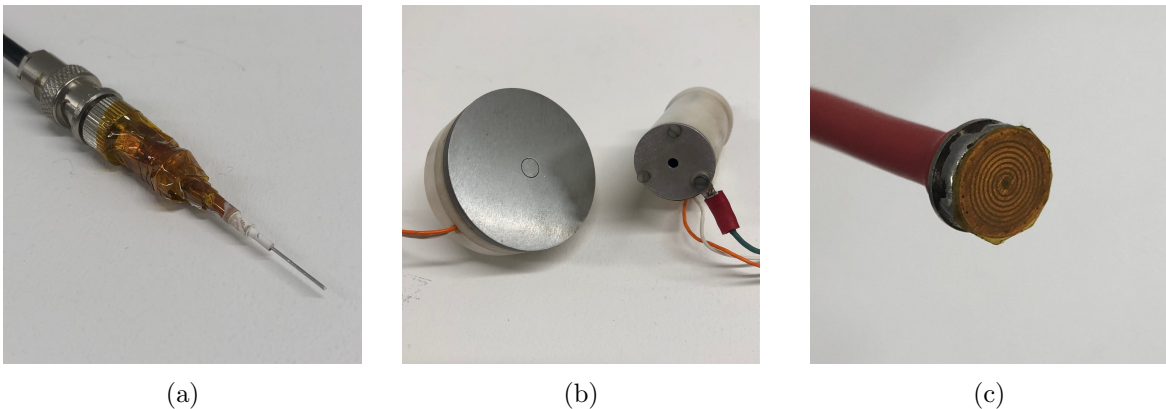


Figure 1.3: Photographs of (a) a Langmuir probe, (b) a Faraday probe with guard ring (left) and a Faraday cup (right) and (c) a Curling probe.

### **Faraday probe**

The Faraday probe is a plasma diagnostic suited to the measurement of the ion current density (figure 1.3b). As shown above in the previous section, an accurate estimation of this plasma parameter is crucial to assess the performances of an electric propulsion device. A Faraday probe has the same working principle than the Langmuir probe, except that the current is measured in the ion saturation region. If the geometry of a Langmuir probe is planar, it is recommended to surround it with a guard ring, biased at the same voltage than the collector, to control the sheath expansion in front of the diagnostic. Brown suggests to take a guard ring diameter greater than 50 times the Debye length of the plasma [4]. This criterion might be too restrictive in some situations. In fact, for small plasma densities, the size of the Faraday probe can become significant and perturb locally the plasma. Moreover, the small gap between the collector and the guard ring, which is exposed to the plasma, is often a source of error in the estimation of the ion current. In addition to these issues, the material of the collector should be chosen considering its secondary electron emission rate. To overcome these sources of uncertainty, Faraday probes are often designed with a cup shape. In Ref. [25], Hugonnaud showed that a Faraday cup is more suited to the measurement of the ion current density in the plume of electric propulsion devices than a planar Faraday probe. He proposed elements for a standardisation of the design and utilisation of Faraday cups, in terms of shape, length and material. In the present work, chapter 4 is dedicated to the design of a particular Faraday cup, called the directional Faraday cup, and the results associated to the utilisation of this diagnostic in the plume of an ECR thruster are presented in chapters 5 and 6.

### **Curling probe**

The curling probe is an electromagnetic diagnostic designed to measure the electron density in the plume of electric propulsion devices (figure 1.3c). Its working principle is very different from that of the two diagnostics presented above. In fact, the curling probe is a small resonator which excites the plasma with a microwave frequency. It creates a wave in the plasma volume probed near the probe surface. The resonance frequency of the probe, measured with a Vector Network analyser (VNA) is proportional to the electron density of the plasma. Boni proposed a way to calibrate the diagnostic for an absolute measurement of the electron density in the plasma plume of an ECR thruster [5, 26].

### **Laser Induced Fluorescence**

In the category of optical diagnostics, the Laser Induced Fluorescence (LIF) is commonly used to measure the ion velocity distribution function. The ions of a plasma are excited with a laser, and their spontaneous desexcitation, associated to the emission of a photon and called fluorescence, is observed with optical spectroscopic techniques. Due to the Doppler effect, the frequency of excitation of a particle is related to its velocity. Therefore, it is possible to retrieve the ion velocity distribution function with a tunable laser diode. The LIF diagnostic offers an excellent spatial resolution and allows to perform measurements with a good temporal resolution. Moreover, the use of three excitation lasers in the three spaces dimensions allows to retrieve the complete ion velocity distribution function. Such experimental setup is called LIF tomography, as presented in Ref. [27].

## 1.2 The ECR thruster

### 1.2.1 History of the device

The utilisation of an Electron Cyclotron Resonance (ECR) source to build an electric propulsion device dates back from the 1960s [28]. However, at this time, poor efficiencies are obtained, and the concept is set aside. In the 1990s, advances in the field of microwave engineering as well as better vacuum performances in the testing facilities renewed the research on the ECR thruster. Sercel led a pioneering experimental and theoretical study of the device [29]. He measured experimentally a total efficiency of around 2% but concluded that, in theory, the device could achieve more than 60% of total efficiency. More recently, since the 2010s, the research around the ECR thruster intensified at ONERA after a patent registered by Larigaldie in 2015 [30] and several doctoral works aimed at better understanding and increasing the technological readiness level and the performances of the device. These studies have been done in the framework of the Horizon 2020 MINOTOR European project. Cannat carried out an experimental characterisation of the first iteration of the thruster design as it is studied today, and obtained thruster efficiencies of the order of 16%, from the thrust estimated with Faraday probe measurements [31]. Vialis adapted several plasma diagnostics for the experimental study of the ECR thruster, including a thrust stand for precise measurements of the thrust of the device [32]. Petterschmitt significantly improved the control of the thruster set point by proposing an improved design of the device. In addition to a great reliability, the design proposed in this work showed promising performances [33]. Porto exclusively focused his work on the numerical simulations of the plasma of the ECR thruster with the development of a full 2D3V Particle In Cell (PIC) code [34]. Finally, Boni proposed a way to measure the electron density in the plume of the ECR thruster with a curling probe. He also continued the experimental characterisation of the device: he measured separately the magnetic and thermal components of the thrust and performed time resolved measurements of the electron density [5]. The ECR thruster is also being studied in other research groups, such as the University Carlos III of Madrid [35, 36] or the University of Michigan [37].

### 1.2.2 The ECR thruster at the beginning of the study

#### Introduction to the device

The ECR thruster, as it is studied nowadays, is constituted of a source which comprises metallic inner and outer conductors (figure 1.4). The coaxial line thus formed is used to deposit electrical power through an electromagnetic microwave at the frequency 2.45 GHz. Inside the source,

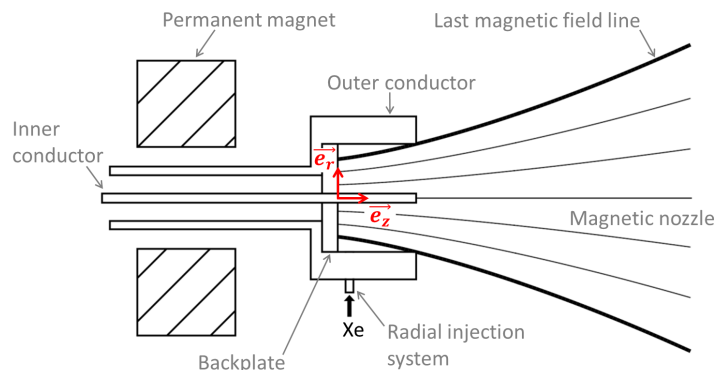


Figure 1.4: Schematic of the ECR thruster.

Parameter	Expression	Source	Plume
Electron density	$n_e$	$10^{11} \text{ cm}^{-3}$	$10^9 \text{ cm}^{-3}$
Neutral density	$n_g$	$10^{13} \text{ cm}^{-3}$	$10^{11} \text{ cm}^{-3}$
Electron temperature	$T_e$	10 eV to 40 eV	10 eV to 40 eV
Ion temperature	$T_i$	0.02 eV	0.02 eV
Electron Larmor radius	$\rho_{L,e}$	0.2 mm	1 mm
Ion Larmor radius	$\rho_{L,i}$	3 mm	15 mm
Debye length	$\lambda_D$	0.1 mm	1 mm

Table 1.1: Orders of magnitude of the plasma parameters in the source and the plume of the ECR thruster (reproduced from Ref. [5]).

an annular shaped permanent magnet produces a magnetic field of strength  $B = 875 \text{ G}$ . With this value of magnetic field, the microwave frequency precisely matches the electron cyclotron frequency (equation 1.25), which allows a very efficient microwave absorption by the electron population. The source is filled with a gas, usually xenon, which is ionised by the collisions with the electrons. The annular shaped permanent magnet also creates a diverging magnetic field downstream the source, called magnetic nozzle. Due to their weak mass, the electrons of the plasma thus created accelerate in the magnetic nozzle by conversion of their perpendicular motion into parallel kinetic energy (see equation 1.35). The charges separation yields an ambipolar electric field which attracts and accelerates the ions in the magnetic nozzle. In a second part of this acceleration, the ions and the electrons of the plasma detach from the magnetic field lines of the magnetic nozzle. The physical processes at stake in this phenomenon remain an opened question, and the different scenarios of plasma detachment which have been formulated are presented in the next section. Eventually, the same amount of ions and electrons are ejected from the ECR thruster. Therefore, there is no need for a neutralising cathode, which simplifies greatly the design of the device. Two prototypes versions arose from the research around the ECR thruster at ONERA, designed to work with powers of 30 W and 200 W respectively and showing great performances with total efficiencies above 50% [38]. The work presented in the present study has been carried out only with the 30 W version of the thruster, and an order of magnitude of the main plasma parameters, measured or estimated, in the source region and the plume region of this device are recalled in table 1.1 (reproduced from Ref. [5]). More details about the technical utilisation of the device are found in the experimental apparatus in chapter 2.

### Estimation of the thrust using Faraday probes

The different studies around the ECR thruster raised a great number of opened questions. Vialis measured the thrust of an ECR thruster with a thrust stand and compared the results with an estimation of the thrust computed from the ion current density measured with a flat Faraday probe with guard ring [3]. He found a discrepancy between these two estimations of the thrust, and since the thrust balance is a calibrated measurement, he concluded that the thrust estimated from the ion flux measurements could be misestimated due to the presence of the plasma sheath that forms in front of the Faraday probe. Peterschmitt also performed this comparison

and systematically found a discrepancy between the thrust measured with the thrust stand and the thrust estimated from ion flux measurements, performed with the same Faraday probe. He suggested that this discrepancy could come from the fact that the bent trajectories of the ions in the magnetic nozzle are not taken into account in the calculation of the thrust. To challenge this approximation, he designed and built a “directional” Faraday cup without performing any measurements with it. The second motivation for the use of a Faraday cup instead of a planar Faraday probe comes from the work of Hugonnaud et al., which retrieved the thrust of a FEED thruster from ion current density measurements and showed the good performances of this diagnostic for the study of the plume of a Hall effect thruster [39, 40]. A significant part of the present study concerns the comprehension and the utilisation of the directional Faraday cup in the plasma plume of the ECR thruster.

### Facility effects

The study of the facility effects on the performance of the ECR thruster in an other active field of research. Wachs et al. studied the background pressure effects on ion dynamics in the magnetic nozzle of an ECR thruster [41]. Thanks to Laser Induced Fluorescence measurements, the authors measured a decrease of the ion velocity at the exit of the acceleration region when the background pressure inside the vacuum facility increased. They attributed this observation to an increase of the electron-neutral collisions at higher background pressures, which reduces the ion acceleration. Baldinucci et al. [42] studied the influence of the electrical condition of the wall around and facing an ECR thruster source. They showed that the performances of the device, such as its thrust, is very little influenced by the presence of a biased grid facing the thruster, no matter the value of the bias voltage of the grid. However, this perturbation has an influence on the thruster floating potential, the plasma plume adapting to the potential condition imposed by the grid. Following this investigation, Boni et al. [43] observed a reduction of the ECR thruster thrust when reducing the distance of the source to the walls of the facility. However, consistently with Baldinucci’s work, the authors found a threshold below which the presence of the wall no longer affects the thruster performances. They also observed that covering the electrical walls of the vacuum facility with a dielectric film, i.e. changing the electrical boundary condition close to the thruster, leads to an increase of the thrust of the device.

## 1.3 Plasma dynamics in a diverging magnetic nozzle

The ECR thruster is not the only device which accelerates a plasma in a divergent magnetic nozzle to produce a thrust force. In fact, it shares this feature with several electric propulsion devices such as the Variable Specific Impulse Magnetoplasma Rocket, or VASIMR thruster [44], the Helicon plasma thruster (HPT) [45] or the Applied Field MagnetoPlasma Dynamic Thruster (AFMPDT) [46] for example. This section reviews the state of the art concerning the studies of the plasma dynamics in a magnetic nozzle.

### 1.3.1 Plasma acceleration

As stated above, it comes from equation 1.35 that the decrease of magnetic field in a diverging magnetic nozzle converts the perpendicular motion of the particles into parallel energy. In an electric propulsion device, this effect accelerates the electrons, which are magnetised. This expansion of the electrons is at the origin of an ambipolar electric field which accelerates the ions. Theoretical studies concerning this plasma acceleration in a diverging magnetic field are based on the kinetic and the fluid formalisms introduced at the beginning of this chapter. Since the dynamics of the electrons drives the acceleration of the ions, the cooling of the electrons is com-

monly investigated to study the acceleration of the whole plasma. It is commonly represented by a polytropic law (equation 1.10). Two approaches are thus considered. On the one hand, the electron cooling can be investigated directly with the measurement of the properties of the electrons. On the other hand, it can be investigated indirectly with the study of the effect of the ambipolar field on the acceleration of the ions.

In Ref. [47], Little and Choueiri derived a fluid model of plasma acceleration in a diverging magnetic nozzle to show how the thermal expansion of the electrons drives the acceleration of the ions. They separated the acceleration of the plasma into two fluid models, one for the isothermal electrons and one for the cold ions. From this model, the authors derived some performances indicator such as the thrust coefficient and the divergence efficiency. The assumptions of this model are equivalent to that used by Smolyakov et al. in Ref. [48]. In this reference, the authors found an analytical solution of the model along the central magnetic field line.

In Ref. [49], Merino et al. explored the influence of the electron cooling rate on the expansion of the ions and the electrons in a diverging magnetic nozzle with fluid simulations. They carried out simulations with the polytropic cooling rates  $\gamma = 1.3$  and  $\gamma = 1$  and highlighted the role of the electron cooling in the loss of thrust production.

However, the closure relation of the fluid models remains an open question. Even if the polytropic law is often considered, some results indicate that an isothermal description of the electrons can be well suited to describe their expansion in a magnetic nozzle. In fact, several studies aim at measuring experimentally the polytropic coefficient  $\gamma$  of a polytropic law describing the electron cooling in a magnetic nozzle. Collard and Jorns performed a two dimensional mapping of the plasma parameters in the magnetic nozzle of a RF plasma source with a Langmuir probe, a Faraday probe, an emissive probe and with Laser Induced Fluorescence [50]. Their experimental setup allowed them to change the amplitude of the peak magnetic field of the magnetic nozzle. They observed a polytropic electron cooling with a coefficient  $\gamma$  comprised between 1 and 1.1 (close to isothermal) independent from the magnetic field strength tested.

A similar behaviour was observed in Ref. [51], in which the authors measured the plasma density and the electron temperature with a RF-compensated Langmuir probe in the magnetic nozzle accelerating a radio-frequency produced plasma. They compared the experimental data to a polytropic model of expansion and found a polytropic coefficient of  $\gamma = 1.15$ .

In Ref. [52], the authors performed measurements in the plume of an ECR thruster. They found a relation between the polytropic cooling rate of the electrons, the electron temperature in the plasma source and the energy of the ions measured at the far end of the vacuum facility in which they performed the testing. They found polytropic indexes ranging from  $\gamma = 1.2$  and  $\gamma = 1.5$ .

Coreyero et al. [53] performed Langmuir probe measurements and LIF measurements in the axis of an ECR thruster. The author evaluated the polytropic law describing the electron cooling along the expansion and found a value of polytropic coefficient which depends on the distance to the thruster, with values of  $\gamma$  ranging from  $\gamma = 1$  close to the source of the thruster to  $\gamma = 1.6$  in the plume.

Finally, in Ref. [54], Vinci et al. measured directly the electron temperature and density in the magnetic nozzle of a Helicon plasma device with a RF-compensated Langmuir probe in a

two dimensional domain. The authors computed the polytropic cooling rate of the electrons and found values ranging from  $\gamma = 1.4$  and  $\gamma = 1.8$ , depending on the magnetic field line considered.

The different studies mentioned above, which aim at describing the acceleration of a plasma in the magnetic nozzle, show that the physics is well established. However, there is no consensus on which approach best describes the experimental measurements. In particular, the description of the measured plasma parameters with a polytropic cooling law for the electrons led in the different experimental campaigns resulted in different values of  $\gamma$ . Moreover, there is a lack of experimental data outside of the central magnetic field line and far from the source of the thruster. Besides, the references presented do not consider the phenomenon of detachment of the plasma from the magnetic field lines, a point which is discussed in the next section.

### 1.3.2 Plasma detachment

Since magnetic nozzle thrusters produce a thrust force which is not 0, the plasma necessarily detaches from the magnetic field lines. Several scenarios are proposed to describe the phenomenon of plasma detachment. This section proposes a review of the different theories, with the existing simulation and experimental results.

Some mechanisms attribute the plasma detachment to collisional processes. First, Moses et al. suggested that the plasma could detach from the magnetic nozzle through resistive diffusion across the magnetic field lines [55]. The authors showed that an adiabatic cooling of the electron would sufficiently increase the collision frequency for an effective detachment of the plasma from the magnetic nozzle. The second collisional theory of detachment involves the recombination of the charged particles into neutrals. This process requires a high electron-ion recombination frequency. The research around both theories have been set aside since it was shown experimentally that the requirements could not be met in real magnetic nozzles [11].

Other theories of plasma detachment exist, which do not involve the collisions between the particles. The first collisionless detachment scenario is called loss of adiabaticity. Particles are said to be detached when their Larmor radius becomes significantly greater than the characteristic length scale of variation of the magnetic field. Hence, during one rotation around a magnetic field line, a particle will encounter a field line sufficiently different to modify its orbit. The parameter which drives the detachment reads:

$$\frac{\rho_L}{L_B} = \frac{mv_{\perp}}{|q|B} \left| \frac{\nabla B}{B} \right| \gg 1 \quad (1.44)$$

This scenario concerns both the electrons and the ions and the detachment of the plasma occurs when both species are demagnetised. It has been described by Hooper et al. in Ref. [56]. The authors found the characteristic detachment parameter to be the square of the plasma radius to the Larmor radius of a hybrid particle of mass  $\sqrt{m_e m_i}$ , denoted by  $G$ , which reads:

$$G \approx \frac{eB_z}{m_e} \frac{eB_z}{m_i} \frac{L^2}{U^2} \quad (1.45)$$

where  $L$  and  $U$  are the characteristic length and velocity of the flow. In a more recent study by Little and Choueiri [57], the authors showed that the condition required for the inertial detachment is:

$$G^{-\frac{1}{2}} \left| \frac{\nabla B}{B} \right| = 0.5 \quad (1.46)$$

However, Ahedo and Merino, in Ref. [58], criticised Hooper’s formulation, which imposes the current ambipolarity everywhere in the plasma flow. To overcome this assumption, the authors proposed the scenario of detachment of the magnetised electrons due to their inertia (also named the Finite Electron Larmor Radius effect).

A different scenario of plasma detachment, called induced field detachment or MHD detachment, has been formulated by Breizman et al. in Ref. [59]. The authors consider that the plasma detachment condition is met when the velocity of the flow exceeds the Alfvén velocity, denoted by  $v_A$ . The parameter which governs this detachment scenario is denoted by  $\beta_f$  and the condition of detachment reads:

$$\beta_f = \left( \frac{v}{v_A} \right)^2 = \frac{\rho u^2 / 2}{B^2 / 2\mu_0} \quad (1.47)$$

where  $\rho$  is the mass density of the plasma  $\mu_0$  is the magnetic permeability of vacuum. In fact, when the fluid is super-Alfvénic, it moves too fast to be affected by a change in the magnetic field. In the magnetohydrodynamic (MHD) framework, when  $\beta_f > 1$ , the “frozen flow” condition induces that the flow drives the magnetic field such that the magnetic field lines are distorted by the movement of the plasma, resulting in a stretched magnetic nozzle. The detachment is therefore considered when the magnitude of the induced magnetic field is greater than the initial magnetic nozzle.

In ref [60], Ahedo and Merino analysed the three main detachment theories, i.e. resistivity, electron inertia and induced magnetic field, with a model assuming cold and partially ionised ions and hot and fully magnetised electrons. They found that, for the three theories, the plasma detaches outwards with respect to the magnetic field due to the creation of diamagnetic electric currents in the plasma.

On the experimental side, Olsen et al. investigated the detachment of the plasma from the magnetic nozzle of the VX-200 Magnetoplasma thruster (VASIMR) [61]. They performed ion flux measurements at several distances in front of the plume of the thruster with several diagnostics (a retarding potential analyser, a HF electric field probe, a plasma momentum flux sensor, a 3-axis magnetometer, a guard ring Langmuir probe, an azimuthal flux probe and two ion flux probe arrays) mounted on a stage translating along the transversal direction. They evaluated the ion streamlines from the transversal integration of the ion flux measurements and compared it to the magnetic field lines of the magnetic nozzle to assess the ion detachment. They did observe a deviation of the ion streamlines from the magnetic field lines and observed that such ion detachment was outward. This result was confirmed by other measurements performed with different diagnostics. Moreover, they distinguished different regions: a magnetised region, a detached but expanding region, a transition region and a ballistic region. However, their experimental setup did not allow them to perform measurements of the true ion flux trajectories. They also pointed out the role of plasma fluctuations in the detachment process.

In Ref. [62], Deline et al. conducted an experiment to observe the detachment of a plasma produced by a pulsed plasma washer gun from a magnetic nozzle produced by five separate magnet coils, allowing to test several magnetic configurations. The authors measured radial profiles of ion flux and electron density thanks to a ring guarded Faraday probe and a triple Langmuir probe respectively. First, they measured a constant electron temperature along the whole acceleration of the plasma, which is consistent with an isothermal electron expansion theory. Second, they found that the ion current density in the axis of the thruster follows the

evolution of the magnetic field in the region close to the thruster, where the parameter  $\beta_f$  is greater than 1. They observed a disagreement for values of  $\beta_f$  lower than 1. This result supports the scenario of MHD detachment. However, these experimental results are not confronted to other detachment theories. In fact, the position at which the ion Larmor radius becomes greater than the magnetic field scale lengths coincides with the position at which the condition  $\beta_f = 1$  is met. This observation does not allow to conclude which detachment theory best describes the experimental observations.

In Ref. [63], the authors performed RF-compensated Langmuir probe, emissive probe and Faraday probe measurements in a magnetic nozzle attached to a radio-frequency plasma source. They measured an increase of the plasma potential at the plume boundary, indicating the presence of an ion confining potential which requires the electrons to be magnetised. Therefore, the location where this potential disappears is associated to the demagnetisation of the electrons. The author found this location to be in agreement with the predictions of the FELR theory stated by Ahedo and Merino in Ref. [58].

To summarise, this review of the main contributions to the characterisation of the plasma expansion in diverging magnetic nozzles and its detachment from the magnetic field lines shows that, on the one hand, several scenarios are plausible to explain the detachment but there is no consensus on the physical mechanisms leading to this phenomenon, and, on the other hand, there is a lack of experimental data to confront the theoretical models and the numerical simulations. These observations constitute the starting point of the present study and motivate this work.

## 1.4 Objectives of the study and outline of the manuscript

The elements given in this introduction motivate the main objective of this thesis: to produce the experimental data necessary to confront theoretical models and simulations which describe the dynamics of a plasma in expansion in a diverging magnetic nozzle. To this end, several plasma diagnostics are used to perform measurements in the plasma ejected in the magnetic nozzle of an ECR thruster. In addition to the existing diagnostics such as the Laser Induced Fluorescence or the ion analyser, an innovative Faraday cup is developed and used to characterise experimentally the detachment of the ions in the magnetic nozzle of the thruster. The manuscript is organised as follows:

In chapter 2, the experimental apparatus in which this work has been carried out is presented. The chapter includes the description of the ECR thruster, the B09 vacuum facility and the plasma diagnostics used throughout the thesis. Then, the Laser induced Fluorescence experimental setup used to measure the two components of the ion velocity field in the plume of the ECR thruster is described. Finally, the experimental characterisation of an ion source used to produce a unidirectional and mono-energetic ion beam is presented.

Chapter 3 focuses on the description of the ion expansion in the source of the ECR thruster and in the 20 first centimetres of the ejection region. First, the measurements of the two components of the ion velocity field performed with Laser Induced Fluorescence are presented. Then, a fluid model of plasma expansion in a diverging magnetic nozzle is developed and an analytical solution is derived and compared to the experimental data.

In chapter 4, the directional Faraday cup is introduced. This diagnostic has been developed

to perform local measurements of the angular distribution of ion current density in the plume of the ECR thruster. After a description of the design of this diagnostic, the Acceptance and Opening functions of the cup are defined, computed, and validated by simulations and experiments in an ideal regime. Then, the behaviour of the directional Faraday probe is investigated when immersed in the plasma plume of the ECR thruster. Simulation results are compared with experimental measurements of the ion current density.

Chapter 5 focuses on the analysis of the ion dynamics at distances greater than 20 cm away from the ECR thruster source. The directional Faraday cup is used to characterise experimentally the detachment of the ions from the magnetic nozzle. First, the experimental setup used to measure the local direction of the ion flux is presented. Then, experimental results obtained for several thruster mass flow rate, thruster power and vacuum condition in the facility are presented in order to investigate the influence of these thruster operating conditions on the ion detachment.

In chapter 6, the accuracy of the indirect estimation of the thrust of the ECR thruster is investigated. First, an introduction of how the thrust is estimated from ion flux measurements in the plume of the thruster and compared to direct thrust measurements performed with a thrust stand is proposed. Results show a discrepancy when a flat Faraday probe with guard ring is used to measure the ion current density instead of the directional Faraday cup, and the origin of this error is analysed. Finally, the hypothesis made to estimate the thrust of the ECR thruster are challenged in order to improve the accuracy of the estimation of the thrust of the ECR thruster.

A conclusion is found at the end of the manuscript to summarise the main findings of this work and present perspectives for future studies.

## 2 | Experimental apparatus

**Motivation and objectives:** A significant part of the work presented in this thesis relies on experimental results. This chapter covers the experimental apparatus and the different diagnostics used throughout the manuscript. To begin with, the ECR thruster is introduced in the first section. The different magnetic topologies used, as well as the magnetic coordinate system, are presented here. The second section is a review of the B09 vacuum chamber in which the testings are performed and the different diagnostics used to characterise the plasma of the ECR thruster. It comprises a description of the Faraday probes and the thrust balance. The third section presents a way to perform non perturbative measurements of the ion velocity by Laser Induced Fluorescence (LIF). After the description of this diagnostic, details are given on how the signals are post-processed to get the two components of the ion velocity field in the plume of the ECR thruster. Finally, the last section introduces the ion source used to study the directional Faraday cup in chapter 4. The ion beam produced by the source is characterised in order to verify that it meets the requirements necessary to this study.

**Main results:** In addition to the presentation of the different diagnostics and the accuracy of the measurements conducted throughout the thesis, two main results are presented in this chapter. On the one hand, a modification of the existing LIF setup allows the measurement of the two components of the ion velocity field. The detailed results of these measurements are the object of chapter 3. On the other other hand, the characterisation of the ion beam produced by the ion source shows that it is sufficiently unidirectional and mono-energetic. These properties justify the utilisation of the ion source for the characterisation of a directional Faraday cup in chapter 4.

## 2.1 The ECR thruster

### 2.1.1 Description of the device

The Electron Cyclotron Resonance (ECR) thruster (figure 2.1) is an electric propulsion device for satellites developed at ONERA. It is constituted of an external conductor that forms a cylindrical cavity of 27 mm in diameter and 20 mm in length called the source, closed at one end by a dielectric piece called the backplate. Inside the source, an inner conductor of 2 mm in diameter has the role of an antenna and forms a coaxial line with the source. Microwaves are fed through the coaxial chamber which is evenly filled with gas, and, at the back of the source, an annular permanent magnet generates a strong diverging magnetic field called the magnetic nozzle. The value of the magnetic field inside the source is chosen so that the cyclotron frequency of the electrons near the backplate matches the microwave frequency, resulting in the generation of a plasma by ECR heating. Electrons and ions expand and accelerate in the magnetic nozzle before detaching from the magnetic field lines, and the ejection of this plasma at high velocity is at the origin of a thrust force. Since 2010, the ECR thruster has been the object of many research at ONERA, in particular through PhD thesis [5, 31–33], yielding an innovative design with high performances. In fact, it gained in maturity on several points : stability of operation, robustness of the design and improvement of the performances.

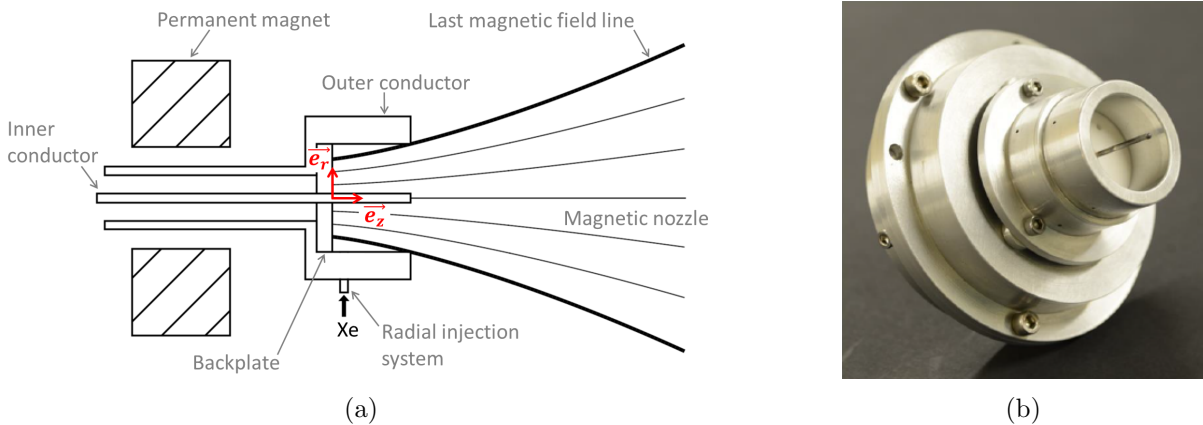


Figure 2.1: (a) Schematic and (b) photograph of the ECR thruster.

Otherwise specified, the gas used in this work is xenon. In fact, this noble gas has a simple chemistry, a low energy of ionisation for a rare gas and a high ion mass, making it one of the best propellant for electric propulsion in terms of performances. However, the ECR thruster can be ignited with different propellants such as argon, iodine or air. The gas is fed to the thruster through a radial injection system, and the mass flow rate is controlled by a Bronkhorst mass flow meter with a 4 sccm range. The precision of the mass flow meter given by the manufacturer is 0.2% of the read value.

The microwave, of frequency 2.45 GHz, is fed to the coaxial chamber of the ECR thruster through a microwave feeding line constituted of a VAUNIX LMS-402D microwave signal generator, a Microwave Amps Ltd power amplifier, a circulator and two directional couplers. The microwave power forwarded to and reflected from the thruster are measured by two LadyBug LB478A diodes. A complete description of the microwave feeding line can be found in Ref. [33]. Power losses due to the absorption, the attenuation and the connections between the element constituting the line are calibrated with a Vectorial Network Analyser (VNA) before each measurement campaign, and the uncertainty of the power deposited to the plasma is estimated to

10% [3]. The version of the thruster has been designed to best work with a microwave power comprised between 15 W and 60 W. However, since it is not the objective of this study to show the best performances of the ECR thruster, the device used in this work is a study model different from the optimised version of Ref. [38]. Inside the vacuum chamber, the microwave power is transmitted to the ECR thruster with two facing coaxial to waveguide transitions so that the thruster is both electrically and mechanically isolated from the vacuum facility. This setup allows precise measurements of the thrust with the thrust balance presented in section 2.2.4.

### 2.1.2 Magnetic field topology

Two magnetic topologies, referred to as  $M_1$  and  $M_2$ , are used throughout this work. They are both diverging magnetic fields produced by two different ring-shaped permanent magnets. In the literature, these magnets are called “Small Magnet” for  $M_1$  and “Big Magnet” for  $M_2$ . The magnetic fields produced by both magnets are simulated with the software Comsol Multiphysics<sup>®</sup> and the associated magnetic field lines are plotted in figure 2.2a. To better report the different divergences of  $M_1$  and  $M_2$ , each line plotted in this figure starts from identical positions for both topologies, evenly spaced between 0 and the radius of the ECR thruster source. This figure shows that  $M_2$  is significantly more diverging than  $M_1$ . Due to the conservation of the magnetic flux, a greater divergence comes with a magnetic field magnitude that decreases sharper with the distance. This is shown in figure 2.2b, where the magnetic field magnitude in the axis of the thruster is plotted for both topologies. Nevertheless, the magnets have been designed so that the ECR heating condition of magnetic field magnitude  $B = 875$  G happens at the same location in the thruster source whether  $M_1$  or  $M_2$  is used.

Because of the annular geometry of the magnets, the magnetic field  $\vec{B}$  is axisymmetrical. It is then suited to use the cylindrical coordinate system  $(\vec{e}_r, \vec{e}_z, \vec{e}_\theta)$  represented in figure 2.1a. In

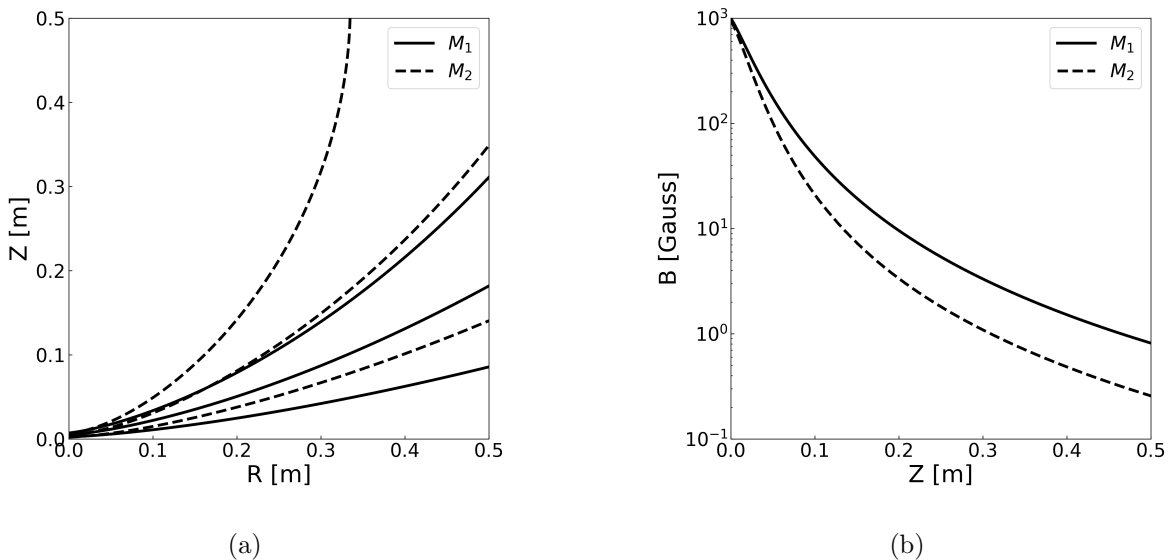


Figure 2.2: (a) Magnetic field lines and (b) magnetic field magnitude along the axis of the ECR thruster for (solid)  $M_1$  and (dashed)  $M_2$ .

this frame,  $\vec{B}$  is expressed as follows :

$$\vec{B} = B_r \vec{e}_r + B_z \vec{e}_z = -\frac{1}{r} \left( \vec{e}_\theta \wedge \vec{\nabla} \psi \right) \quad (2.1)$$

Where the field  $\psi$  is constant along any magnetic field line and is found to be the azimuthal component of the magnetic potential vector, which is defined as the field  $\vec{A}$  such that:

$$\vec{B} = \vec{\nabla} \wedge \vec{A} \quad (2.2)$$

In particular,  $\psi = \psi_p$  along the last magnetic field line. This particular magnetic field line, also labelled LMFL in the remaining of the manuscript, is the most diverging magnetic field line which does not intersect physically the source of the ECR thruster (figure 2.1a). From this description of the magnetic field, the magnetic reference frame  $(B/B_0, \psi/\psi_p)$  is introduced, where  $B_0$  is the magnetic field at the location  $(R = 0, Z = 0)$  of the cylindrical frame. The magnetic frame is “magnetic topology-dependant” and is therefore different for  $M_1$  and  $M_2$ . This frame allows to better compare the measurements performed in  $M_1$  and  $M_2$  between each other and is used specifically in chapter 5.

## 2.2 Vacuum Facility and diagnostics

### 2.2.1 B09 vacuum chamber

The experiments are conducted in the B09 vacuum facility (figure 2.3) in the plasma propulsion lab at ONERA Palaiseau. This vacuum tank is a 2 m in length and 0.8 m in diameter stainless steel cylinder. A set of several pumping systems allows to obtain a background pressure of a few  $10^{-7}$  mbar inside the facility, which enables the testing of the ECR thruster under realistic space conditions. First, a rough pump brings the pressure down to a few  $10^{-2}$  mbar. Then, a series of three Pfeiffer Hi-Pace 2300 turbo-molecular pumps allows for the High Vacuum (HV) condition of a few  $10^{-6}$  mbar. Finally, a cryogenic pump is constituted of a cryo panel placed inside the vacuum chamber chilled by a Sumitomo CH-110 cryo-cooler. It captures by solidification the last molecules remaining inside the chamber and reduces the pressure of one order of magnitude.

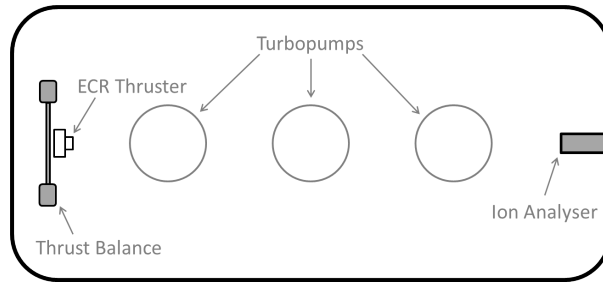


Figure 2.3: Schematic of the B09 Vacuum facility.

The level of vacuum inside the chamber is monitored by a Leybold hot cathode vacuum gauge. It displays an equivalent nitrogen pressure  $p_{N_2}$  linked to the xenon pressure  $p_{Xe}$  by the relation  $p_{Xe} \approx p_{N_2}/2,87$ . This correction factor is gas-dependant and given by the manufacturer of the vacuum gauge. The vacuum pumping speed for xenon  $V_{pump}$  (in  $L.s^{-1}$ ) is calculated as follows:

$$V_{pump} = \frac{\dot{m}}{60 (p_{Xe}(\dot{m}) - p_{Xe}(0))} \quad (2.3)$$

where  $\dot{m}$  is the xenon mass flow rate (in SCCM-Xe) injected inside the vacuum facility and  $p_{Xe}(\dot{m})$  is the xenon pressure inside the tank. The evolution of  $p_{Xe}$  with the mass flow rate  $\dot{m}$  is measured for two different vacuum conditions, referred to as  $V_1$  and  $V_2$  (figure 2.4) For these two conditions, the cryopump is switched on for  $V_1$  and off for  $V_2$  with, for both cases, the rough pump and the turbopumps running.  $V_{pump}$  is calculated from the slope of a linear fit of the data. The values of the pumping speeds are  $V_{pump}^1 = 15380 \text{ L.s}^{-1}$  and  $V_{pump}^2 = 2696 \text{ L.s}^{-1}$ . These measurements show that, in addition to the reduction of the background pressure inside the facility, the cryogenic pump significantly increases the vacuum pumping speed.

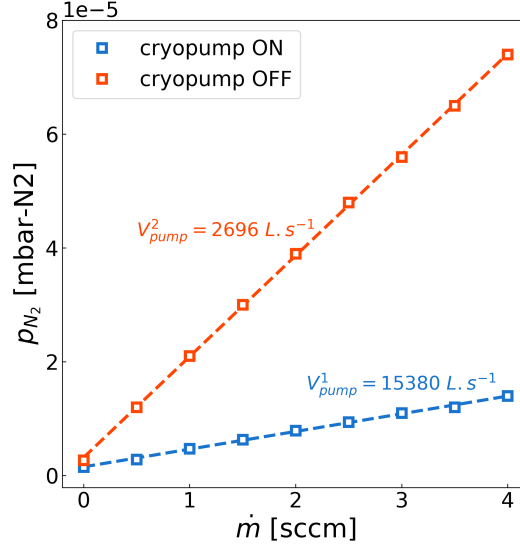


Figure 2.4: Pressure inside the B09 vacuum facility versus xenon mass flow rate with the cryopump switched off and on.

### 2.2.2 Ion energy analyser

A Hiden Analytical PSM003 ion analyser is mounted at the back of the B09 vacuum facility at a distance of 1.7m away from the ECR thruster source (figure 2.3). It comprises a mass spectrometer, to scan the plasma plume over a range of  $m_i/Z$  at a given ion energy and a ion energy analyser, to scan the ion energy at a given  $m_i/Z$  ratio,  $m_i$  and  $Z$  being respectively the mass and the atomic number of the ion considered.

### 2.2.3 Faraday probes

A Faraday probe is an electrostatic diagnostic commonly used to measure *in situ* the ion current density in the plasma plume of an electric propulsion device. It is composed of a metallic surface placed inside the plasma and biased at a voltage  $V_b$  so that it collects or repels the particles of the plasma. If  $V_b > V_p$ , where  $V_p$  is the plasma potential, the ions constituting the plasma with an ion energy  $E_i < V_b - V_p$  are repelled. On the other hand, if  $V_b < V_p$ , the probe repels the electrons. Therefore, for a biasing voltage sufficiently high, all of the ions are repelled and the current drawn by the probe in this case is called electron saturation current. Conversely, if the biasing voltage is sufficiently low and negative, electrons are repelled and the surface collects only ions. In this case, the current drawn is called the ion saturation current. The ion current density  $j_i$  of the plasma is defined as the ion saturation current measured by the probe divided

by the collection area. Due to the energy of the electrons which compose the plasma plume of the ECR thruster, a value of the biasing voltage between -300 V and -500 V, depending on the thruster operating conditions, is necessary to obtain the ion saturation. Guidelines to chose the value of the bias voltage are given in section 4.3.1. With such low negative voltage, the presence of a non-flat plasma sheath in front of the probe collector may induce a distorted collection area and therefore a wrong estimation of the ion current density. This point is addressed in section 6.2.

Two types of Faraday probes are used in this work. First, the Faraday probe with guard ring (figure 2.5a), denoted FPGR in the remaining of the manuscript, is composed of a collector of diameter  $d_{coll} = 5.9$  mm and a guard ring of diameter  $d_{GR} = 5$  cm, both made in molybdenum, with a gap of  $100 \mu\text{m}$  between each other. The guard ring dimension is chosen according to the recommended practices of Ref. [4] and aims to flatten the sheath that forms in front of the probe. Second, a directional Faraday cup (figure 2.5b), denoted FCDi in the remaining of the manuscript, has the same working principle with a different design. It is composed of a collector of  $d_{coll} = 5.9$  mm in diameter surrounded by a hollow conducting cylinder, these parts being made of graphite. A metallic ring with an opening hole of diameter  $d_{ring} = 3$  mm closes the cup. Thanks to its design, the directional Faraday cup captures the local direction of the ion flux collected. Its development is dealt with in detail in chapter 4.

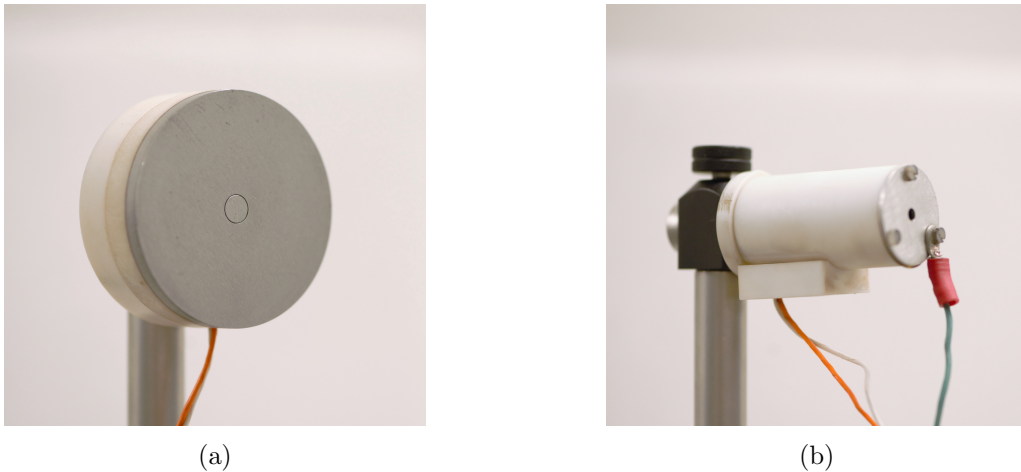


Figure 2.5: (a) Faraday probe with guard ring and (b) directional Faraday cup.

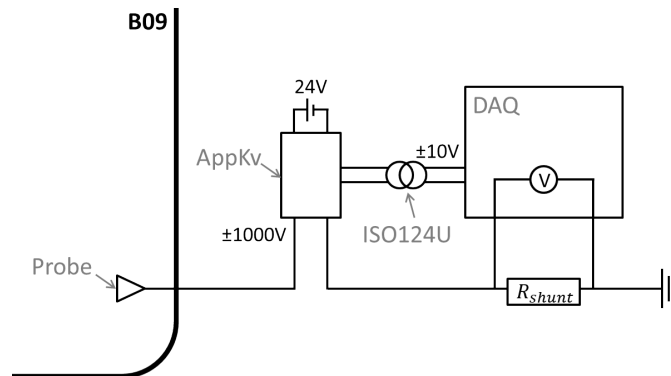


Figure 2.6: Schematic of the Faraday probe biasing and acquisition circuit.

The electrical circuit used for the biasing of the Faraday probe and the acquisition of the current (figure 2.6) is constituted of a National Instrument PCIe 6323 acquisition card (DAQ) which plays two roles. On the one hand, it measures the current drawn by the collector of the probe through a shunt resistor whose value is a few tens of kilo Ohms. This value needs to be adjusted with respect to the current measured in order to protect the DAQ. On the other hand, it generates a setpoint voltage between -10 V and 10 V and feeds it to an ISO124U isolating transformer. This signal is fed to an Applied Kilovolts HP001Z high voltage power supply (AppKv) that generates a voltage worth 10 times the setpoint to bias the probe collector. This circuit is duplicated for every part of a probe that needs to be biased separately. Therefore, thanks to the multiple output and input of the DAQ, the two separate collectors of the same probe can be biased at different voltages if needed.

## 2.2.4 Thrust balance

One direct way to measure the thrust of the ECR thruster is to use a thrust balance, also called thrust stand. The model used in this work (figure 2.7) is a simple pendulum balance hung by 8 thin strips which ensure a perfect pivot and a single degree of freedom. The arm of the balance, where the ECR thruster is mounted, is 332 mm long and kept in position thanks to a magnet and a coil whose voltage is regulated by a Proportional–Integral–Derivative (PID) controller in closed loop. When the thruster generates an horizontal thrust force  $T$ , the voltage applied to the coil necessary to keep the arm steady increases. Therefore, a PID voltage drop  $V_{PID}$  is observed when the thruster is shut off.

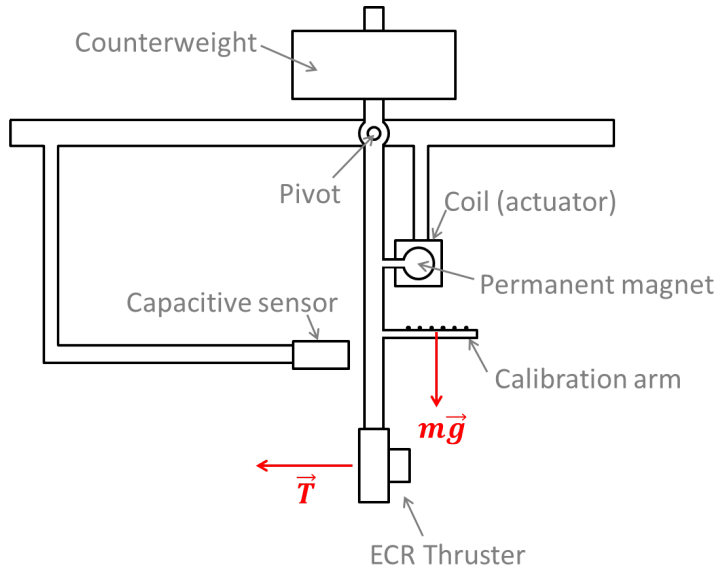


Figure 2.7: Schematic of the thrust stand (reproduced from [3]).

$V_{PID}$  is related to  $T$  by the linear relation  $T = \gamma^{TS} V_{PID}$  where  $\gamma^{TS}$  is a calibration factor obtained by the deposition and the retrieval of five well known weights on the arm of the balance at precise locations. As the mass and position of each weight are known, the force imparted on the arm after the deposition and retrieval of the weights is also known and linked to the PID voltage drop associated to get  $\gamma^{TS}$ . An example of the signal acquired during the calibration phase is plotted in figure 2.8a, with the calibration factors associated represented in figure 2.8b. This calibration phase takes place before each batch of thrust measurements to ensure a calibrated measurement of the thrust of the ECR thruster.

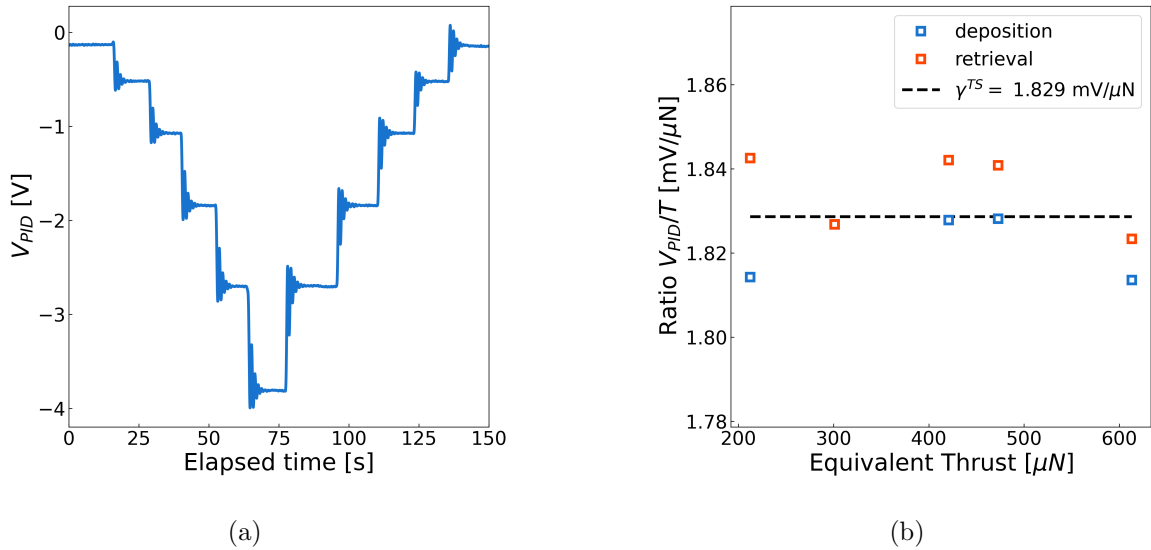


Figure 2.8: (a) Signal acquired during the thrust stand calibration and (b) calibration factor associated to the deposition and the retrieval of the calibration weights.

In this example,  $\gamma^{TS} = 1.829 \pm 0.03 \mu\text{N}/\text{mV}$ , with a relative error  $\Delta\gamma^{TS}$  estimated as three times the standard deviation of the data around the mean value. An estimation of the relative error of the direct thrust measurement with the thrust stand is:

$$\frac{\Delta T}{T} = \sqrt{\left(\frac{\Delta V_{PID}}{V_{PID}}\right)^2 + \left(\frac{\Delta\gamma^{TS}}{\gamma^{TS}}\right)^2} \quad (2.4)$$

where the uncertainty on the PID drop is  $\Delta V_{PID} = 20 \text{ mV}$ . This value is due to the environmental noise that comes from the high sensitivity of the balance. Thus, the relative error for the direct thrust measurements is 5%. This balance has been proven reliable in several studies and is therefore considered to give a reference of the thrust of the ECR thruster. More details on the thrust balance setup and operation can be found in [3]. This diagnostic is specifically used in chapter 6.

## 2.3 Measurement of the ion velocity by Laser Induced Fluorescence

### 2.3.1 Description of the diagnostic

The Laser Induced Fluorescence (LIF in the remaining of the manuscript) is an optical diagnostic used to perform non perturbative measurements of the ion velocity distribution function (IVDF) in a plasma. The ions are excited with a laser and the spontaneous emission of photons (or fluorescence) is observed. The wavelength of the laser is swept around the excitation wavelength  $\lambda_0$ . Due to the Doppler effect and the velocity distribution, the fluorescence signal observed during the wavelength scan is related to the IVDF. The electronic states of excitation and fluorescence constitute the LIF scheme (figure 2.9). In the present work, the metastable state  $5d^2F_{7/2}$  of the xenon ions at 12.59 eV is excited at  $\lambda_0 = 834.955 \text{ nm}$  to the state  $6p^2D_{5/2}$  at 14.07 eV. The fluorescence to the state  $6s^2P_{3/2}$  at 11.79 eV is fast and accompanied by the emission of a photon at the fluorescence wavelength  $\lambda_{flu} = 541.915 \text{ nm}$ .

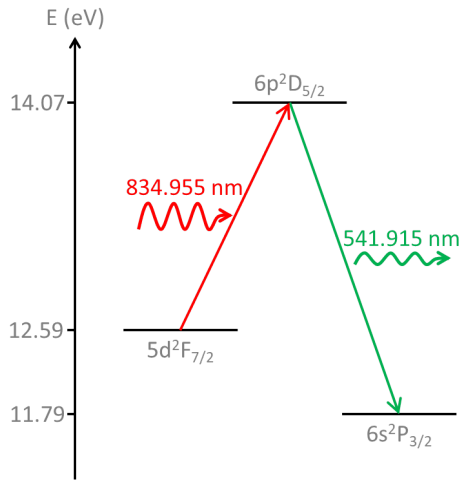


Figure 2.9: Laser Induced Fluorescence scheme.

The optical bench used in this study to perform LIF measurements (figure 2.10) is composed of a SDL Inc. TC10-137 tunable laser diode with a wavelength modulated by a triangular-shaped signal. The period of the modulation signal is comprised between 100 s and 200 s and needs to be adapted to the LIF signal collected, the greater the period, the greater the signal to noise ratio. The laser beam is amplified by a Toptica BoosTA pro laser amplifier. A fraction of the signal is sent to a LM007  $\lambda$ -meter to monitor the laser wavelength in real time and make coarse adjustments of the laser wavelength. To monitor precisely the wavelength of the laser along the wavelength sweep, a part of the signal is sent to a Fabry-Perot interferometer, which is a confocal cavity of length  $L_{FP} = 23$  cm. The remaining of the beam is split by an Acousto-Optic Modulator (AOM) and sent alternatively towards a reference plasma in the reference cell and the ECR thruster plasma in the B09 vacuum chamber by using optical fibres. For both plasmas, the fluorescence signal is collected through an interferometric filter centred around  $\lambda_{flu}$  to suppress the parasite light emitted by the plasma. The signal is collected with a photo multipliers (PM) and amplified with a Stanford Research System SR830 lock in amplifier.

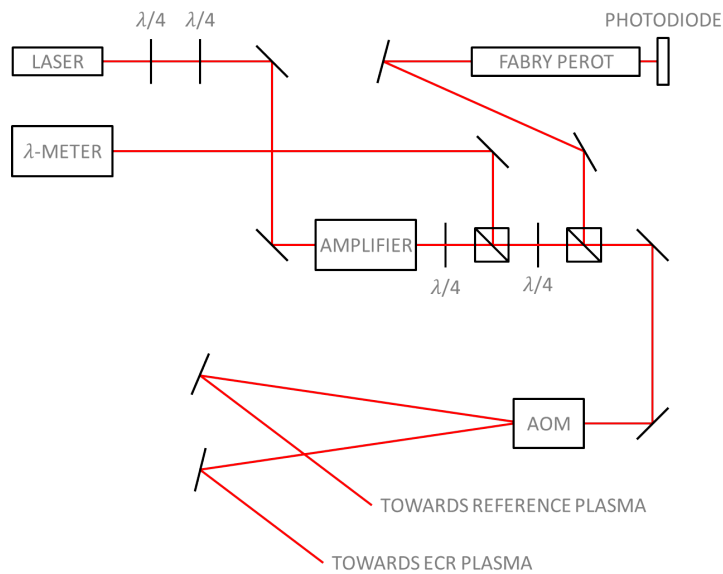


Figure 2.10: Laser Induced Fluorescence optical bench.

The Reference cell is a T-shaped pyrex cavity in which a xenon plasma at steady state is generated with a surfatron fed with microwave with a power of 100 W. The pressure inside the cavity is approximately 1 mTorr. The plasma in this reference cell is supposed to have a null mean velocity [64].

The LIF optical bench and reference cell has been presented in the literature [27]. However, a modification of the laser injection system allows the excitation of the ions in the ECR plasma along two directions through the longitudinal or the transversal injection lenses, as represented in the top view schematic of the experimental setup (figure 2.11a). The longitudinal injection lens faces the ECR thruster source and the transversal injection lens makes an angle of  $90^\circ$  with the longitudinal injection. The detection lens is represented in the side view schematic of the experimental setup (figure 2.11b), it makes an angle of  $28^\circ$  with the axis of the thruster. Therefore, the intersection between the detection axis and the injection axis that forms the measurement volume is estimated to be of the order of  $1 \text{ mm}^3$ , which gives a spatial resolution of 1 mm for this diagnostic. The whole setup is placed on a two-axis translation stage that enables the displacement of the measurement volume location in a two-dimensional plan in front of the ECR thruster source.

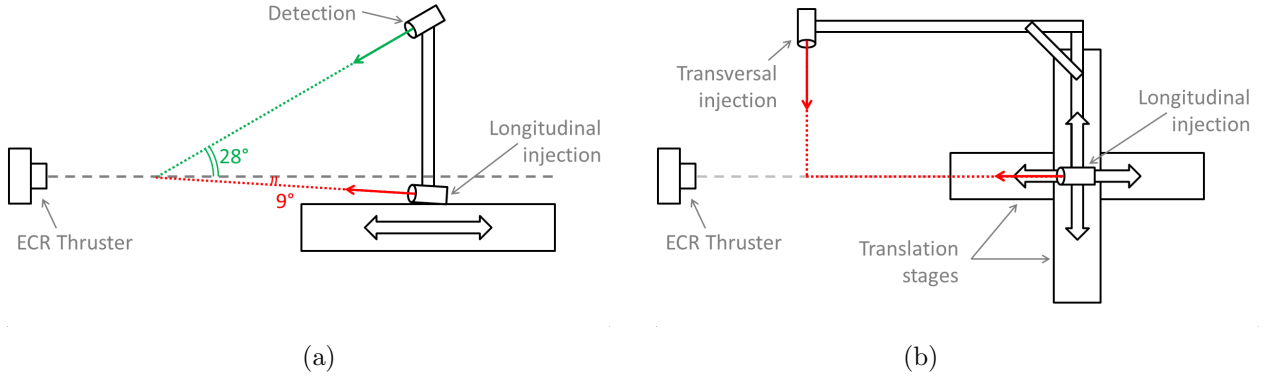


Figure 2.11: (a) Side view and (b) top view of the Laser Induced Fluorescence experimental setup.

If ions have velocity  $v$  projected onto the axis of the excitation laser which is not zero, the wavelength of the laser  $\lambda$  at which they are excited is shifted by Doppler effect and is therefore:

$$\lambda = \lambda_0 \left(1 - \frac{v}{c}\right) \quad (2.5)$$

where  $c$  is the speed of light. Hence, the comparison of the fluorescence signals in the reference cell and in the ECR plasma allows to measure the local velocity of the ions in the ejection region of the ECR plasma plume projected along the axis of the excitation laser. The two components (transversal and longitudinal) of the ion velocity are mapped in an area of  $18 \times 8 \text{ cm}$  in front of the ECR thruster for the two magnetic topologies, and in the axis of the thruster for several operating conditions in microwave power and xenon mass flow rate. Results are presented in chapter 3.

### 2.3.2 LIF Data analysis

A homemade algorithm prepare and analyse the LIF data in an automatised way. In a first part, the data is sliced according to half a period of the triangular shaped signal which modulates the laser wavelength so that the post processing is done during one span of laser wavelength. The

Fabry-Perot interferometer signal is measured with a photo diode (figure 2.12a). It presents interference fringes which are distant from one another of one free spectral range  $\Delta\nu_{FSR}$ , whose expression is:

$$\Delta\nu_{FSR} = \frac{c}{n^{FP}L^{FP}} \quad (2.6)$$

where  $L^{FP}$  and  $n^{FP}$  are respectively the length and the refractive index which constitute the interferometer cavity. Therefore, the free spectral range of the Fabry-Perot interferometer used in this work is  $\Delta\nu_{FSR} = 638$  MHz. An algorithm localises the temporal position of each peak in the Fabry-Perot signal and converts the temporal reference into a wavelength reference (figure 2.12a). In a second part, the position of the peak of fluorescence in the reference plasma allows to determine the wavelength  $\lambda_0$ . Equation 2.5 is then used to convert the wavelength frame into an ion velocity frame. The fluorescence signal of the ECR plasma is fitted with a skewed Gaussian function to simplify the analysis of the ion velocity (figure 2.12b).

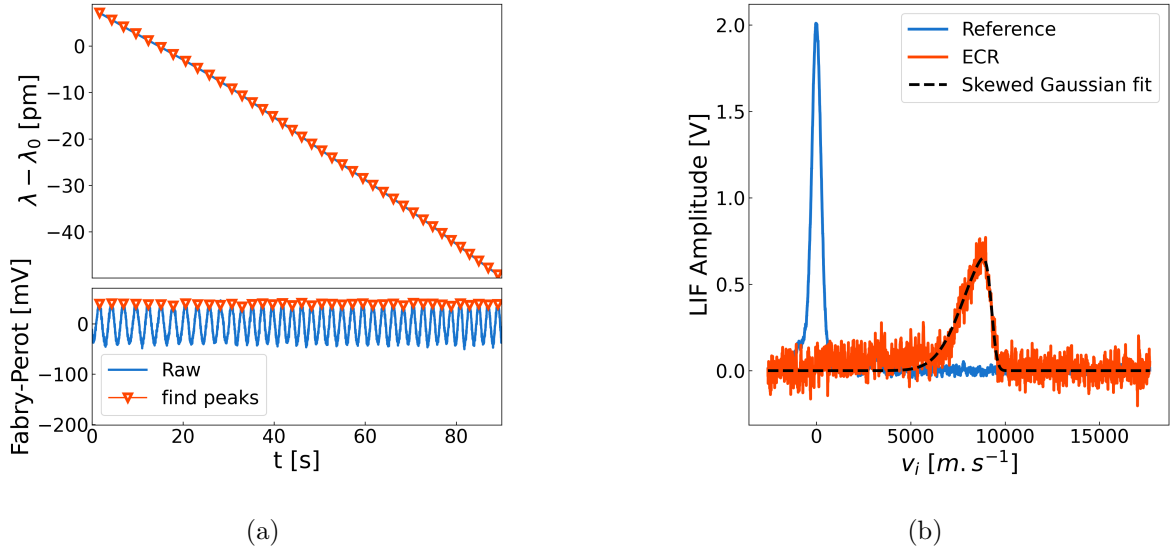


Figure 2.12: (a) (bottom) Fabry-Perot interferometer signal and (top) conversion from temporal to frequency frame and (b) example of LIF profile.

For measurements of ion velocity performed near the thruster source, where the magnetic field is stronger, the fluorescence signals are distorted by the Zeeman effect which is the separation of the electronics levels into sub-levels due to the presence of a strong magnetic field. This effect is visible for measurements of the ion velocity performed in the source of the thruster, where the magnetic field intensity is greater than 400 G. In this case, a correction taking into account this effect must be applied to the signal. The energy  $E$  of a sub-level is given by the law:

$$E = E_0 + \frac{eh}{4\pi m_e} gMB \quad (2.7)$$

where  $E_0$  is the initial energy of the level,  $h$  is the Planck constant,  $m_e$  is the electron mass,  $g$  is the Landé factor,  $M$  is the projection of the quantum angular momentum and  $B$  is the magnetic field magnitude.  $M \in [-J, -J + 1, \dots, J - 1, J]$ ,  $J$  being the total quantum angular momentum. The Landé factor reads:

$$g = 1 + \frac{J(J+1) + S(S+1) - L(L+1)}{2J(J+1)} \quad (2.8)$$

where  $S$  is the quantum spin number and  $L$  is the quantum orbital angular momentum. Therefore, in the transition from an initial state (subscript  $i$ ) to a final state (subscript  $f$ ), the energy difference  $\Delta E$  is:

$$\Delta E = \frac{eh}{4\pi m_e} (g_f M_f - g_i M_i) B \quad (2.9)$$

Not all transitions between two sub-levels are accessible. On the one hand, if the polarisation of the laser is parallel to  $B$  ( $\pi$ -polarisation), the transitions accessible are the ones for which  $\Delta M = 0$ . On the other hand, if the polarisation of the laser is perpendicular to  $B$  ( $\sigma$ -polarisation), only the transitions where  $\Delta M = \pm 1$  are accessible. Given the quantum numbers of the initial and final states of the excitation used in this work (table 2.1), equations 2.9, and the relative intensities of the Zeeman transitions with respect to the quantum numbers  $J$  and  $M$  (Appendix A, table A.1), it is possible to compute the distortion of an IVDF due to the Zeeman effect.

State	L	J	S	g
$5d^2F_{7/2}$	3	7/2	0	1.119
$6p^2D_{5/2}$	2	5/2	0	1.157

Table 2.1: Quantum numbers of the initial and final state of the LIF transition used in this work (Extracted from [6]).

For the measurements of the ion velocity in the source of the ECR thruster, due to the external conductor walls, it is only possible to use the longitudinal laser injection. An optimisation algorithm finds the original ion velocity distribution function from the distorted fluorescence signal observed in the ECR plasma under the assumption that the ion velocity follows a Maxwellian distribution (figure 2.13). The good agreement between the theoretical signal obtained from a Maxwellian IVDF after Zeeman effect (labelled IVDF + Zeeman) and the LIF signal measured in the source of the ECR thruster, where the magnetic field amplitude is 954 G, confirms that the Maxwellian distribution is a reasonable assumption.

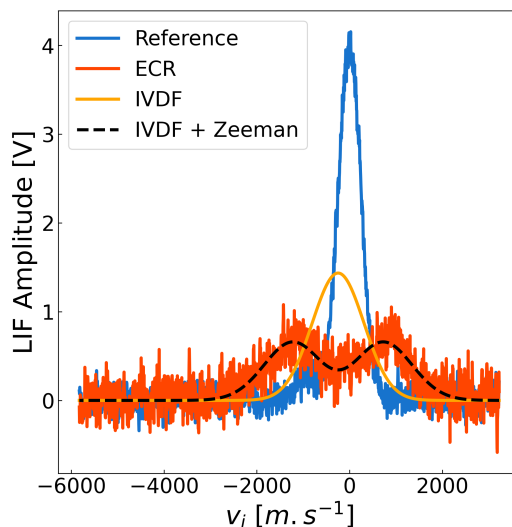


Figure 2.13: LIF profiles with the Zeeman effect correction.

## 2.4 Generation of an unidirectional and mono-energetic ion beam with an ion source

### 2.4.1 Description of the ion source

An ion source (figure 2.14) is used to characterise the directional Faraday cup in chapter 4. This device has been developed at ONERA, and a complete and detailed analysis can be found in R. Gueroult's thesis [65]. It is composed of a wire anode running through a cylindrical cavity of 10 cm in length and 5 cm in diameter (the cathode) filled with either argon or xenon. The mass flow rate of the gas is controlled with a Bronkhorst mass flow meter. The whole system is mounted on the B09 vacuum facility to benefit from its pumping system. The pressure inside the cavity is around  $1e-2$  mbar and the pressure inside the vacuum tank is  $5e-6$  mbar. A Heininger 1200-20POS high voltage power supply imposes a voltage difference between the anode and the cathode, denoted by  $V_d$ , which generates a plasma inside the cavity. Thanks to a second power supply, the whole device is floated at a voltage  $V_f$  with respect to the B09 vacuum tank which is tight to ground. A hole of 8 mm in diameter in the cathode lets an ion beam flow out of the device, this beam is accelerated by a metallic ring tight to ground inside the vacuum chamber. The ion source parameters that are varied are  $I_d$ ,  $V_f$ , the type of gas used and its mass flow rate  $\dot{m}$ . In this work,  $I_d$  is varied between 1.5 mA and 15 mA, this leads to values of  $V_d$  between 400 V and 1200 V. The floating voltage  $V_f$  is varied between -200 V and 200 V, but the power supply is removed from the setup when not needed, i.e. when  $V_f=0$  V. The value of the balast resistor which stabilises the discharge is fixed to  $R_{balast} = 60$  k $\Omega$ .

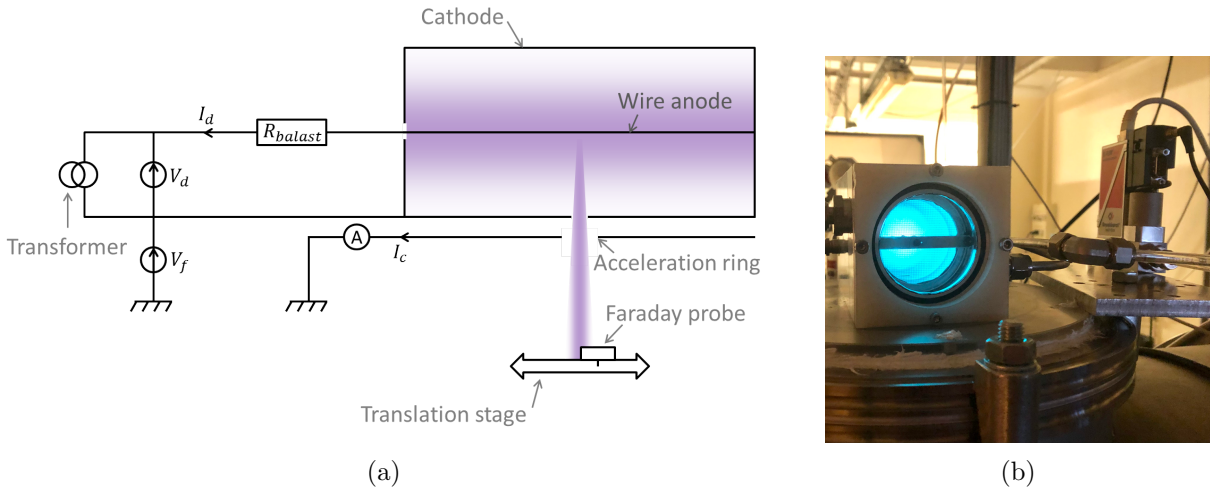


Figure 2.14: (a) Schematic and (b) photograph of the ion source.

The experimental results presented in this section are not intended to replace the extensive study of the source found in [65]. However, it is necessary to characterise the ion beam produced by this device and verify that it suits the needs of this work. In fact, for the experimental validation of the directional Faraday cup acceptance presented in section 4.2, the ion beam needs to be unidirectional with a controlled radius and mono-energetic with a controlled ion energy. Therefore, in the analysis led below, the beam is supposed to be mainly constituted of ions, with a circular section and a current density uniformly distributed.

## 2.4.2 Characterisation of the ion beam

The current  $I_c$  flowing from the accelerating ring to ground is a good estimation of the beam current. It is measured with an ammeter as pictured in the schematic in figure 2.14a. The first experiment consists in measuring the evolution of  $I_c$  with  $I_d$  for several values of argon mass flow rate (figure 2.15). Results show that the beam current increases with the value of the discharge current and is greater at low mass flow rates. Therefore, in order to maximise the beam current, the mass flow rate is fixed to the minimum value for which the discharge is sustained. Thus,  $\dot{m} = 0.016 \text{ mg.s}^{-1}$  in the remaining of the source characterisation. Indeed, for lower mass flow rates, the regime of the discharge changes from the diffuse mode to the contracted mode which is not investigated in this work.

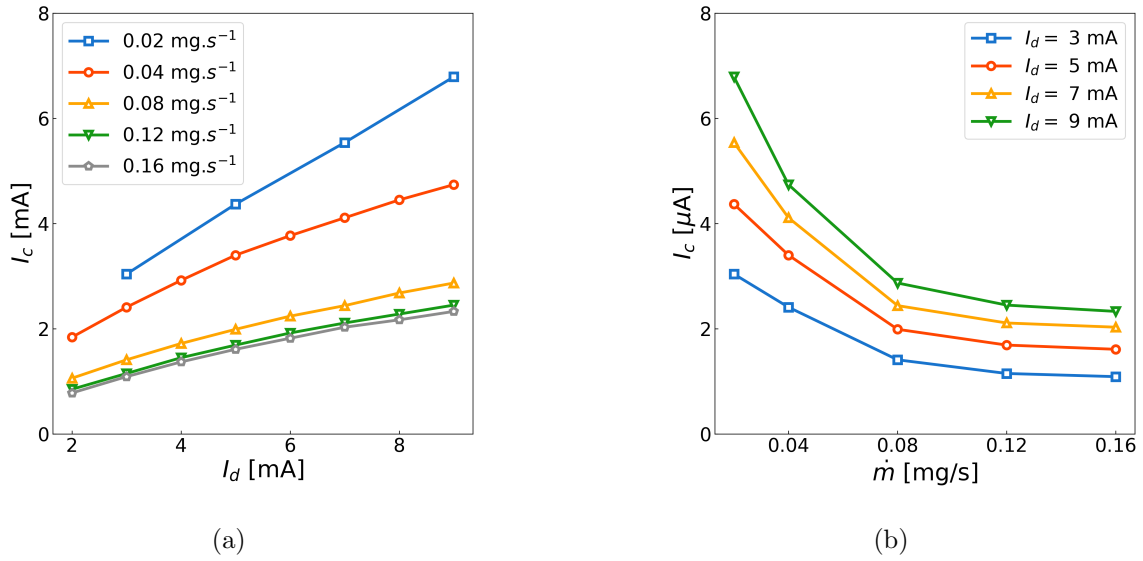


Figure 2.15: (a) Beam current versus discharge current for different values of argon mass flow rate and (b) beam current versus argon mass flow rate for different values of discharge current.

To estimate the radius of the ion beam, the Faraday probe with guard ring (section 2.2.3) is mounted on a translation stage in front of the source exit, as pictured in 2.14a, and its current is measured during its lateral displacement. As the ion beam is supposed to be cylindrical, the current measured is proportional to the intersection area between two discs of radius  $r_{beam}$  and  $r_{probe}$  shifted from one another. An optimisation process on the function that computes this area for a given beam radius allows to find the best fit of the data (figure 2.16a). For example, from the current measured with a probe positioned at  $Z = 7$  cm from the ion source exit, the beam radius associated is  $r_{beam} = 1.542$  cm. This measurement is repeated for different distances from the source exit and the slope of a linear fit of the data gives a beam divergence of 9.87 degrees (figure 2.16b). Though slightly divergent, the ion beam is sufficiently unidirectional for the characterisation of the directional Faraday cup led in section 4.2.

The ion beam radius is estimated for xenon and argon for the whole range of discharge current allowed by the power supply with the Faraday probe being placed at  $Z = 4$  cm from the source exit (figure 2.17). The data is fitted with an exponential function to better highlight the evolution of  $r_{beam}$  with  $I_d$ . A greater dispersion of  $r_{beam}$  is observed for xenon because less current is measured by the Faraday probe for this gas, resulting in a lower signal to noise

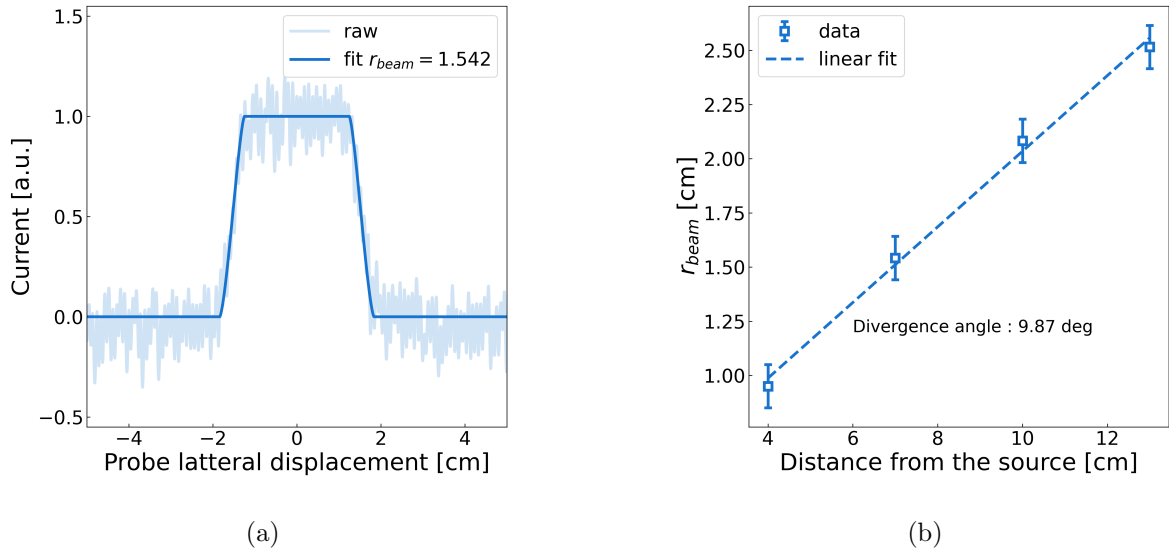


Figure 2.16: (a) Current measured during the displacement of a Faraday probe in front of the ion source at a distance of  $Z = 7$  cm and (b) beam radius versus the distance from the source.

ratio. However, the fit shows that  $r_{beam}$  does not depend on the gas type used, and is comprised between 0.7 cm for low discharge currents and around 1 cm for high discharge currents. This result gives confidence that the divergence of the beam is not affected by the gas type either. Moreover, with regard to the value of  $r_{beam}$ , a greater beam current is prioritised over a small beam radius. Therefore, as it is the maximum value allowed by the power supply with xenon, a value of  $I_d = 14$  mA is fixed in the remaining of the experiments.

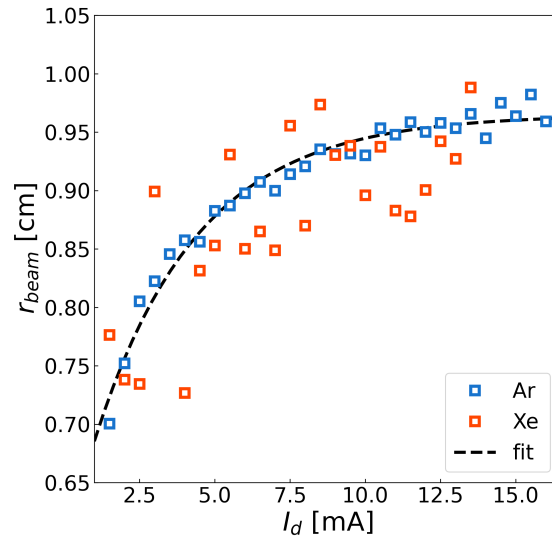


Figure 2.17: Ion source beam radius versus discharge current.

To measure the ion energy of the beam, the collector and the guard ring of a Faraday probe placed in front of the ion source are biased from  $V_{bias} = -250$  V to  $V_{bias} = +600$  V. The current measured versus the bias voltage is called IV-curve (blue solid line in figure 2.18a). The more positively biased the Faraday probe, the more it repels the ions and the smaller the current collected. In fact, for a given bias voltage  $V_{bias}$ , only ions with an energy  $E_i > V_{bias}$  are collected. Therefore, the ion energy distribution function (IEDF) is  $dj_i/dV_{bias}$  (orange solid line in figure 2.18a). In the example, the ion energy peaks at  $E_i = 372$  eV with a half width at half maximum of 12 eV. This is sufficiently narrow to consider that the ion beam is nearly mono-energetic. The ion energy is also measured for several values of source floating voltages  $V_f$  (figure 2.18b). Results show that the ion energy varies linearly with  $V_f$ . Because the accelerating ring is tight to ground, the accelerating potential seen by the ions is close to the voltage of the wire anode, whose value is  $V_{anode} = V_d + V_f - R_{balast} \times I_d$ . The good agreement between the measured ion energy and  $V_{anode}$  shows that this quantity is a good approximation of the mean ion energy. For the sake of clarity, results presented here are obtained with the ion source operated with argon because the signal to noise ratio is greater with this gas. Nevertheless, they remain valid with xenon.

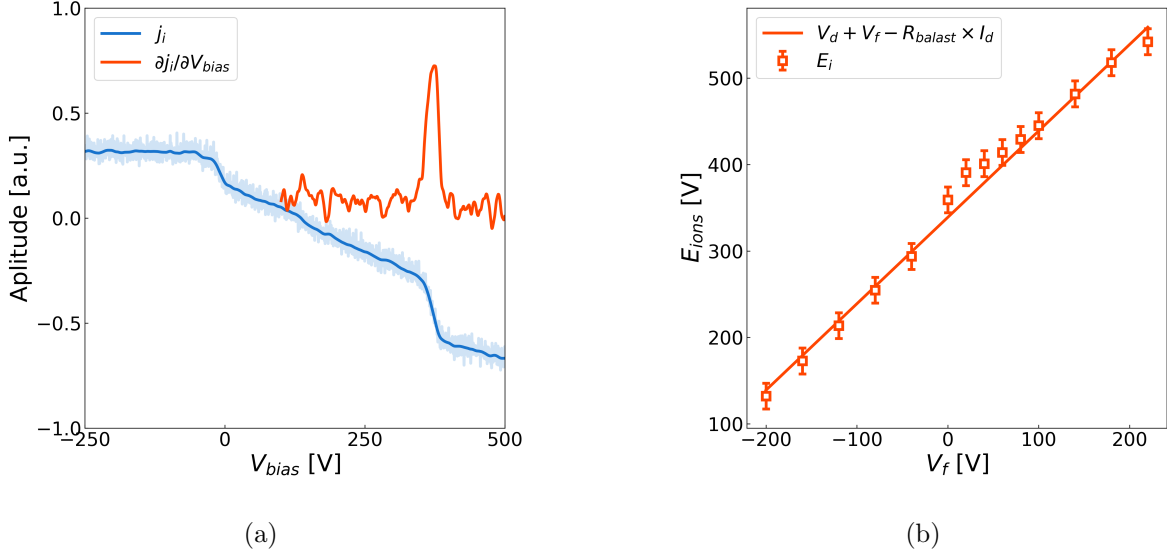


Figure 2.18: (a) IV curve measured with a Faraday probe in front of the ion source and (b) ion energy versus floating potential of the ions source.

To conclude, the characterisation of the ion source presented in this section shows that the ion beam is sufficiently unidirectional and sufficiently mono-energetic for the needs of this work. Moreover, the tuning of the different parameters of this source allows to select the ion energy and maximise the ion current extracted from the source. The type of gas has no influence on the beam radius, but the signal to noise ratio of the current measured with a Faraday probe is significantly greater for argon than for xenon. These results are used in section 4.2

### 3 | Description of the plasma acceleration in the magnetic nozzle of the ECR thruster

**Motivation and objectives:** Measurements of the ion velocity field in the magnetic nozzle of a thruster are necessary to understand the plasma dynamics in this region. In fact, as reviewed in the introduction in chapter 1, several theoretical models and simulations of the expansion of a plasma in a magnetic nozzle are found in the literature but lack of a comparison with experimental data.

Several measurements of the ion velocity in the plume of magnetic nozzle thrusters were performed in previous studies. However, some limitations arose from these experiments. In Ref. [50], the authors performed a two dimensional mapping of the ion velocity measured by Laser Induced Fluorescence (LIF). However, this optical diagnostic allows to measure only one component of the ion velocity field at a time, projected along the direction of the excitation laser, and the authors only measured the longitudinal component of the ion velocity field. Concerning the ECR thruster, in Ref. [53], the ion velocity has been measured along the axis of the thruster, showing the acceleration of the plasma in the magnetic nozzle. Besides, no ion velocity measurements were performed in the source of the thruster.

The first objective of this chapter is to present the measurements of the longitudinal component of the ion velocity field performed in the source of the ECR thruster and the measurements of both the longitudinal and the transversal components of the ion velocity field measured in the plume of the thruster. The comparison of this extensive dataset with a theoretical model of ion expansion in a diverging magnetic field allows to describe the plasma dynamics during its acceleration in the magnetic nozzle. The second objective is to analyse the evolution of the plasma acceleration for different operating conditions of this device, in thruster mass flow rate, microwave power and magnetic topology. These measurements are insightful on the link between the plasma parameters in the source region, where the plasma is created, and its acceleration in the magnetic nozzle.

**Main results:** In a first part, measurements performed with the LIF diagnostic in the plasma of the ECR thruster are presented. First, the longitudinal component of the ion velocity field is measured in the source region for several operating conditions in mass flow rate and microwave power. Results show an acceleration of the ions, which is greater on the edges of the source close to the outer conductor wall. Moreover, the width of the ion velocity distribution function in the source region slightly increases along the acceleration of the ions. Besides, in the region of the source close to the backplate of the thruster, negative velocities are measured, indicating that the ions created upstream the ECR region are not ejected but collected by the backplate. Second, the two components of the ion velocity field, i.e. longitudinal and transversal components, are measured in the plume region of the thruster. Measurements are performed in the axis of the thruster for several operating conditions and in the whole plume region for one condition and two magnetic topologies. The first observation is that the acceleration takes place in the whole domain probed, and has a different profile in the source and the plume regions.

In a second part, a theoretical fluid model of plasma expansion in a diverging magnetic nozzle is presented with the justification of the main assumptions. The plasma expansion is first considered to be isothermal, and an analytical solution is found for the supersonic flow. For all the thruster operating conditions tested, this model performs well at describing the acceleration of the ions in the axis of the thruster. The analytical solution also shows a good agreement with experimental data measured along the magnetic field lines which are off-axis and inside the plume of the magnetic nozzle.

The experimental data are also tested against the analytical solution of a polytropic expansion model. However, the polytropic index that best fits the data is close to the isothermal case, i.e.  $\gamma = 1$ . Nevertheless, an electron cooling could happen in the far field region, where the ion velocity has not been measured due to the lack of the LIF signal.

Overall, the good comparison of these theoretical models with experimental data illustrates that, in the source region, the ion acceleration is driven by the electron temperature and the shape of the magnetic field. It is found that the electron temperature increases with the microwave power and decreases with the mass flow rate, while being poorly dependant on the magnetic nozzle topology.

### 3.1 Measurements of the ion velocity field in the source and the plume of an ECR thruster

The ion velocity field of the plasma in expansion in the magnetic nozzle of the ECR thruster is measured by Laser Induced Fluorescence (LIF) in a two dimensional region downstream of the plasma ejection of the ECR thruster (figure 3.1). The ECR thruster source is axi-symmetrical, and the plasma ejection region can be considered as such. In fact, several measurements presented throughout this manuscript and in previous studies confirm this assumption. Therefore, the knowledge of the plasma behaviour in a two dimensional plane in front of the thruster allows a good description of the plasma dynamics in the whole plume. The detailed experimental setup and methodology used to measure the longitudinal and radial components of the ion velocity is presented in the experimental apparatus in chapter 2.

In the remaining of the chapter, the source region refers as the area inside the source of the ECR thruster. In this region, measurements of the longitudinal component of the ion velocity are performed on a rectangular grid from  $Z = 2$  mm to  $Z = 30$  mm and from  $R = -13$  mm to  $R = 13$  mm (with the notations of figure 3.1). In the source, the magnetic field ranges from  $\approx 100$  G to  $\approx 1000$  G. Because of these strong values of magnetic field, the Zeeman effect must be taken into account in the LIF signals analysis, as presented in section 2.3.2. The plume region refers as the area of coordinates ranging from  $Z = 30$  mm to  $Z = 180$  mm and from  $R = -80$  mm to  $R = 80$  mm. In this region, the two components of the ion velocity in the measurement plane, i.e. the longitudinal and transversal components, are measured. The Zeeman effect is neglected because  $B \leq 100$  G. The ion velocity distribution in this region is fitted with a skewed Gaussian function and the ion velocity is the position of the maximum of the fit, as detailed in section 2.3.2 of the experimental apparatus.

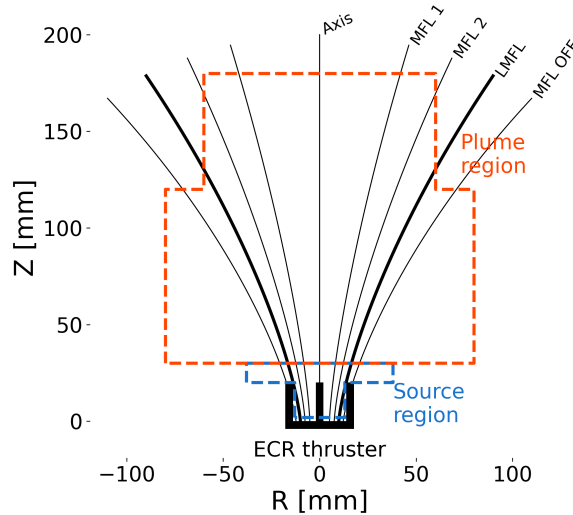


Figure 3.1: Schematic of the source and the plume region.

### 3.1.1 Ion velocity field in the source region

In the source region, the ion velocity distribution function is assumed to follow a Gaussian distribution function. This hypothesis allows a satisfactory fit of the fluorescence signal with the Zeeman effect taken into account (figure 3.2). This distribution reads:

$$G(v) \propto e^{-\frac{(v-u_{iz})^2}{2\sigma_{u_{iz}}^2}} \quad (3.1)$$

where  $v$  is obtained from the excitation laser wavelength and equation 2.5 of the experimental apparatus (chapter 2). In equation 3.1,  $u_{iz}$  is the longitudinal ion velocity, which is the distance between the peak of the distribution function and the reference fluorescence signal. The width of the Gaussian distribution is denoted by  $\sigma_{u_{iz}}$ . It results from this equation a most probable velocity associated to the broadening of the distribution, denoted by  $u_{i\sigma_z}$ , expressed as follows:

$$u_{i\sigma_z} = \sqrt{2}\sigma_{u_{iz}} \quad (3.2)$$

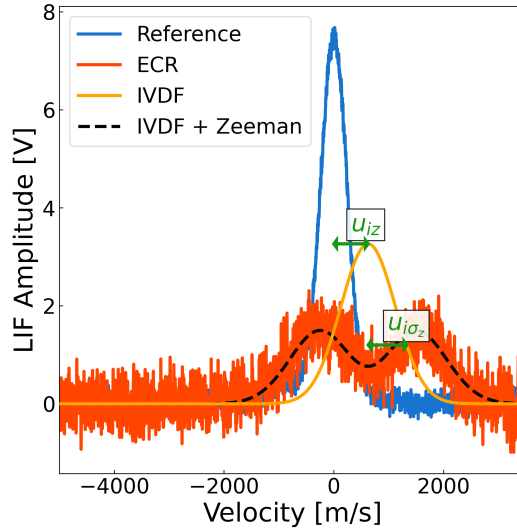


Figure 3.2: Example of the LIF profiles with the Zeeman effect correction. The location in the source is  $R = 7$  mm and  $Z = 10$  mm.

The measurements of the longitudinal component of the ion velocity and the broadening of the ion velocity distribution function in the source region are similar for positive and negative values of  $R$ . Therefore, for the sake of clarity, the data are symmetrised and the results are plotted against  $|R|$  (figure 3.3). In this figure, the black dashed lines serve as visual guides to indicate the position of the inner and the outer conductor of the ECR thruster source respectively. The longitudinal component of the ion velocity shows the acceleration of the ions in the source of the thruster. In fact, at  $Z = 5$  mm, the ion velocity is close to  $0 \text{ m.s}^{-1}$  while velocities over  $4000 \text{ m.s}^{-1}$  are measured at  $Z = 30$  mm. Negative longitudinal velocities are measured at  $Z = 2$  mm. It means that the ions at this position are not ejected from the thruster but hit the backplate of the source. In fact, the ECR region, where the ionisation of the propellant gas takes place is located where the value of the magnetic field is near 875 G. For the magnetic topology  $M_1$ , this condition is verified between  $Z = 4$  mm and  $Z = 6$  mm. Therefore, these result show that upstream the ECR region, the ions have negative velocity and downstream, their velocity is positive.

A plasma sheath is formed all around the walls of the source. The velocity of the ions that enter the sheath is the so called Bohm velocity, denoted by  $u_B$ , which reads [1]:

$$u_B = \sqrt{\frac{eTe}{m_i}} \quad (3.3)$$

With an electron density of  $10^{17} \text{ m}^{-3}$  and an electron temperature of 25 eV (values justified in Ref. [5] and section 3.2.2 respectively), the Bohm velocity is  $u_B \approx 4300 \text{ m.s}^{-1}$  and the Debye length is  $\lambda_D \approx 0.1 \text{ mm}$ . However, at the vicinity of the inner conductor and the backplate, the electron temperature could be greater and the electron density lower, resulting in a greater Debye length. It would explain the ion velocity which is measured at  $Z = 2 \text{ mm}$  and  $R \leq 3 \text{ mm}$ . In fact, at this location, ions have a greater velocity than that at the other location because they may be already accelerated in the sheath.

It is also observed that the acceleration of the ions is more important at the edges of the source, close to the wall of the outer conductor, than close to the wall of the inner conductor. Moreover, as soon as the ions leave the source, i.e. for  $Z > 26 \text{ mm}$ , the longitudinal ion velocity measured at  $R = 0 \text{ mm}$  gets close to that measured at  $R = 20 \text{ mm}$ . This behaviour is not clearly understood, it could be investigated with complex sheath and collision models inside the source.

The longitudinal component of the ion velocity field takes negative values at  $Z = 23 \text{ mm}$  and  $R \geq 25 \text{ mm}$ . These coordinates correspond to locations outside of the source of the ECR thruster. Hence, this observation shows that a part of the ions that are ejected from the source of the thruster go backward, with an unwanted negative contribution to the thrust. A possible explanation of the presence of ions going backward is that some ions might lose a significant part of their kinetic energy in a collision with the wall of the outer conductor, and would be accelerated in the sheath at the surface of the thruster outside the source. However, the ion density is very small at this location, as shown in ref [5], so the part of ions going backward is negligible compared to the part of ions ejected in the magnetic nozzle.

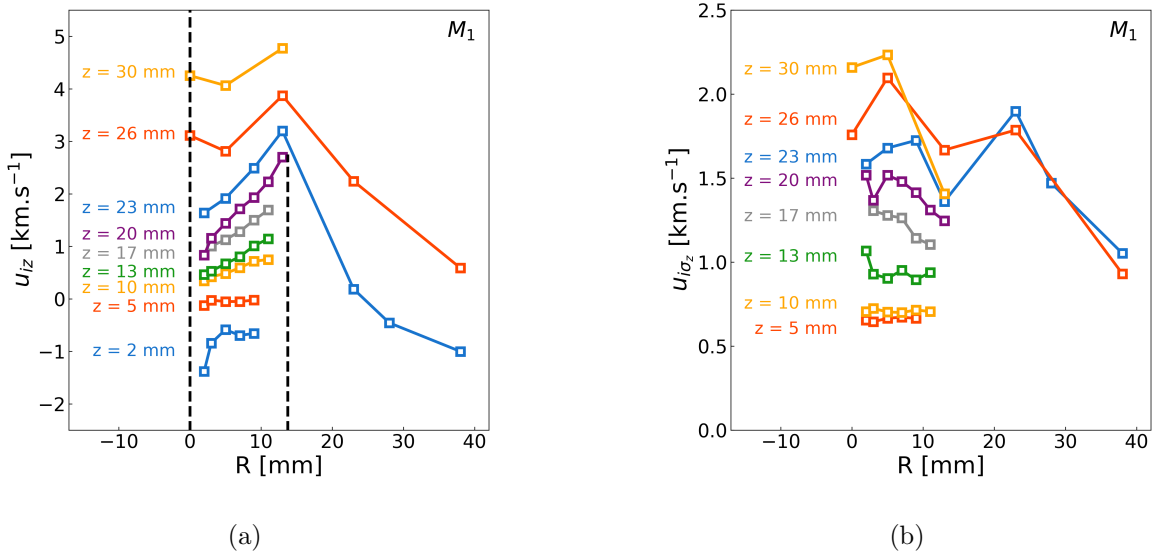


Figure 3.3: (a)  $u_{iz}$  and (b)  $u_{i\sigma_z}$  in the source of the ECR thruster with the magnetic topology  $M_1$ . The dashed black lines represent the physical inner and outer conductor of the ECR thruster source. The thruster is firing at 1 sccm and 32 W.

One way of describing the broadening of the ion velocity distribution  $u_{i\sigma_z}$  is to consider that it is due to the thermal energy of the ion population. In this case, a temperature  $T$  can be associated to  $u_{i\sigma_z}$  thanks to the following relation:

$$u_{i\sigma_z} = \sqrt{\frac{2k_b T}{m_i}} \quad (3.4)$$

For the thruster condition of 1 sccm of mass flow rate and 32 W of microwave power with the magnetic topology  $M_1$ , the velocity  $u_{i\sigma_z}$ , is comprised between  $650 \text{ m.s}^{-1}$  and  $2300 \text{ m.s}^{-1}$  (figure 3.3b). According to equation 3.4, it corresponds to temperatures comprised between 3300 K and 42000 K, which is very high compared to the temperature of the neutrals injected (around 300 K). Therefore, it is unlikely that the broadening of the ion velocity distribution function is due to thermal agitation only.

To understand these values, the longitudinal component of the ion velocity field  $u_{iz}$ , as well as  $u_{i\sigma_z}$ , measured at the constant radial coordinate  $R = 5 \text{ mm}$ , are plotted against  $Z$  for several thruster operating conditions in mass flow rate and power with the magnetic topology  $M_1$  (figures 3.4a and 3.4b respectively). First, it appears that, in the source of the ECR thruster,  $u_{iz}$  is poorly dependent on the thruster operating condition. However, as soon as the ions leave the source at  $Z = 20 \text{ mm}$ , (black dashed line in figures 3.4a and 3.4b), the ions are more accelerated when the thruster power increases and when the thruster mass flow rate decreases. The same evolution of the acceleration of the ions with the operating conditions is observed for the negative velocities measured close to the backplate of the thruster, i.e. at  $Z = 2 \text{ mm}$ .

Concerning the broadening of the ion velocity distribution function, the minimum value is measured at  $Z = 5 \text{ mm}$  for every thruster operating conditions tested (figure 3.4b). In the source of the thruster, the ECR heating region is broadened by the Doppler effect associated to the velocity of the electrons, and ranges between  $Z = 4 \text{ mm}$  and  $Z = 6 \text{ mm}$  (see Ref. [34]). Therefore, the ions are not created exactly at the same location in the source of the thruster and do not all see the same accelerating potential, leading to the broadening of the ion velocity distribution as observed.

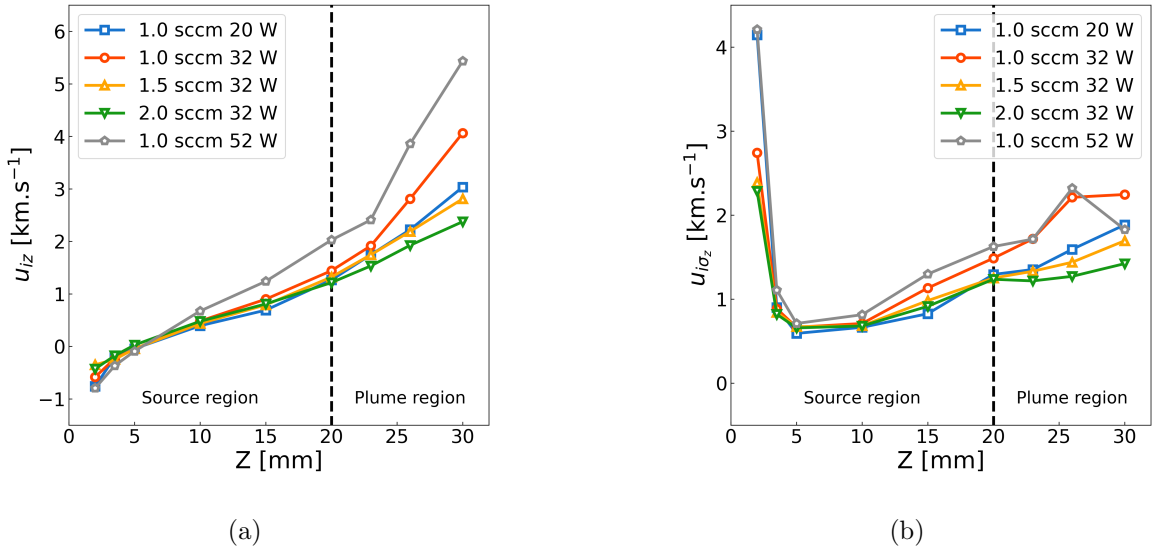


Figure 3.4: (a)  $u_{iz}$  and (b)  $u_{i\sigma_z}$  in the source of the ECR thruster at the radial coordinate  $R = 5 \text{ mm}$  with the magnetic topology  $M_1$ .

The increase of  $u_{i\sigma_z}$  below and above  $z = 5$  mm can be explained by the collisions which happen inside the source. It is not symmetrical around  $Z = 5$  mm because the neutral density is greater close to the backplate, where the gas is injected, than at the exit of the source. Moreover, the ion velocity distribution function is supposed to follow a Maxwellian distribution in the source. This approximation might lose its validity as far as  $Z$  increases. In fact, outside the source of the thruster, the LIF fluorescence signal is fitted by a skewed Gaussian, as discussed later in the chapter.

Finally, it is worth noting that the transversal component of the ion velocity field cannot be measured in the source of the thruster. In fact, the physical presence of the outer conductor prevents the transversal excitation laser of the LIF experimental setup from probing the source region (see section 2.3.1). Hence, the measurement of the transversal component of the ion velocity field is only performed in the plume region, as shown in the next section.

### 3.1.2 Ion velocity field in the plume region

In the plume region, both components of the ion velocity field, i.e. the longitudinal component  $u_{iz}$  and the transversal component  $u_{ir}$ , are measured with respectively the longitudinal and transversal excitation laser of the LIF experimental setup presented in section 2.3.1. For these measurements, the Zeeman effect is not taken into account in the post processing of the data. In fact, because the magnetic field in the plume region is too weak ( $\leq 100$  G), the Zeeman splitting can be neglected with respect to the broadening of the ion velocity distribution function. The ion fluorescence signals are fitted with a skewed Gaussian instead. Similarly to the source region, both the longitudinal and transversal component of the ion velocity field in the plume region are symmetrical around the axis of the thruster due to the axi-symmetry of the ejection. Therefore, in this case again the data is symmetrised and plotted against  $|R|$  for the sake of clarity (figure 3.5).

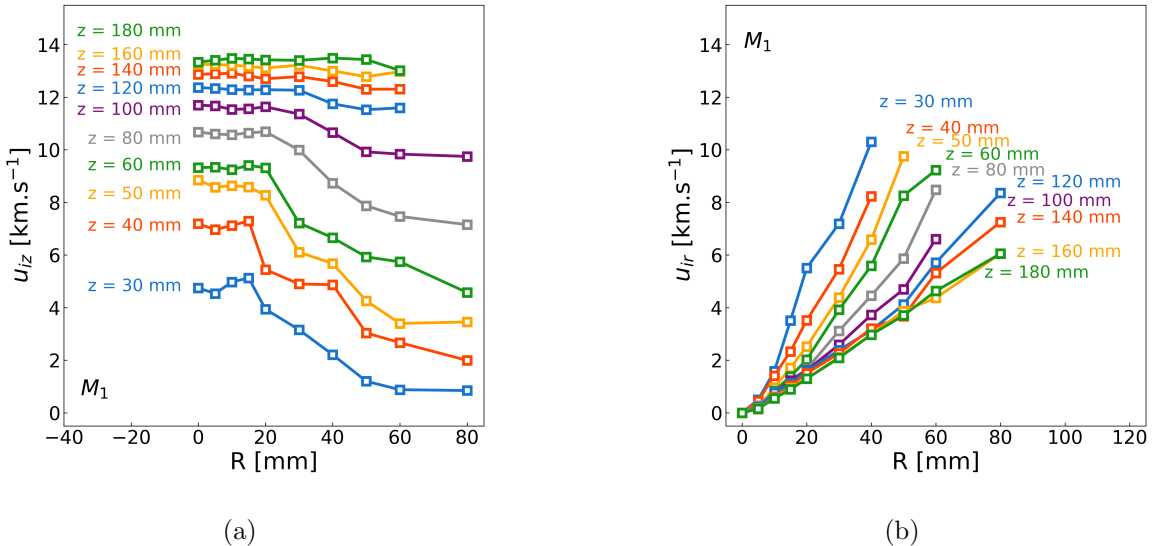


Figure 3.5: (a) Longitudinal and (b) transversal components of the ion velocity in the plume of the ECR thruster with the magnetic topology  $M_1$ .

The thruster is firing at 1 sccm and 32 W.

Results show the acceleration of the ions in the 18 first centimetres of the magnetic nozzle of the ECR thruster. In fact,  $u_{iz}$  increases with the distance  $Z$ . This acceleration is further analysed in the remaining of this chapter. Concerning the transversal component of the ion velocity field  $u_{ir}$ , it increases linearly with the radial direction  $R$ . Moreover, the fact that this component is not zero shows that the ions do not have a trajectory only projected along the axis  $Z$ . Using this data, the local trajectory of the ions is discussed in the next section.

To conclude this section, the acceleration of the ions in the magnetic nozzle of the ECR thruster is represented for the operating condition 1 sccm and 32 W and the magnetic nozzle  $M_1$ , in the axis of the thruster (figure 3.6) and in two dimensions in the whole probed domain (figure 3.7). Due to the presence of the inner conductor in the source of the thruster, the measurements shown in the figure for the source region are the one at the location  $R = 2$ . The measurements presented in figure 3.6 illustrate the fact that the acceleration of the ions is different in the source and the plume of the ECR thruster. In fact, in the source of the thruster, the ion velocity increases linearly with the distance. As soon as the ions leave the source, a change of slope is observed in their acceleration profile. For this thruster operating condition, the acceleration takes place in the whole range of 18 cm probed and the longitudinal component of the ion velocity is  $13400 \text{ m}\cdot\text{s}^{-1}$  at  $Z = 18 \text{ cm}$ . Moreover, 90% of the acceleration takes place outside of the source.

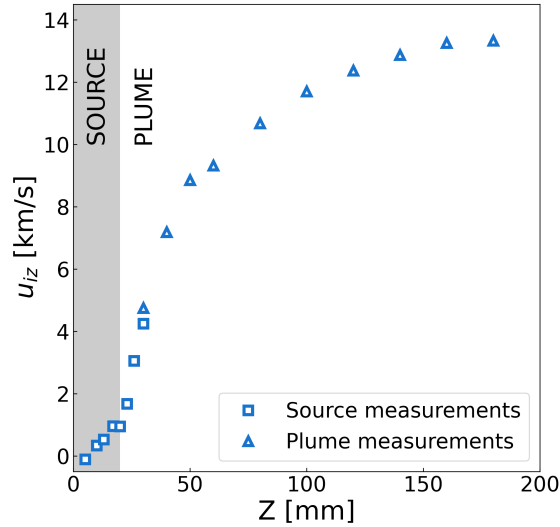


Figure 3.6: Acceleration of the ions in the axis of the magnetic nozzle of the ECR thruster. The thruster is firing at 1 sccm and 32 W with the magnetic topology  $M_1$ .

The results presented in this section show that the acceleration of the ions can be studied distinctively in the source and the plume region. It appears that the gain of velocity is linear in the source region, and seems to be driven by the magnetic nozzle in the plume region. In order to describe this acceleration, a theoretical model of plasma expansion in a diverging magnetic field is presented in the next section. In section 3.3, an analytical solution is found and compared with the experimental data for several thruster operating conditions in mass flow rate and microwave power as well as for two different magnetic nozzle configurations  $M_1$  and  $M_2$ . The results are then discussed in section 3.4.

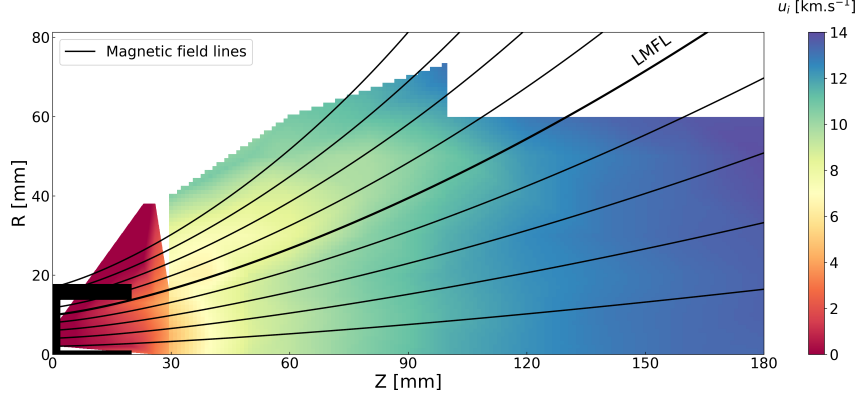


Figure 3.7: 2D map of the ion velocity in the plume of the ECR thruster. The thruster is firing at 1 sccm and 32 W with the magnetic topology  $M_1$ .

## 3.2 Theoretical model of isothermal expansion of a plasma in a diverging magnetic field

In order to describe the expansion of the ions in the magnetic nozzle of the ECR thruster, the experimental results are compared with a theoretical model of plasma expansion along a diverging magnetic field. The equations and hypothesis of this model are inspired from the theoretical models of Refs. [66], [47] and [48], except that, first, the equations are rewritten in a different formalism which allows to find an analytical solution and, second, the expansion of the electrons is supposed to be isothermal. This assumption is a major hypothesis of the model, it is further discussed in section 3.4. The comparison of the analytical solution of the model with the experimental results is done in section 3.3.

### 3.2.1 Description of the model

The model presented in this section describes the acceleration of a plasma in a diverging magnetic field with the fluid formalism presented in the introduction in chapter 1. It relies on several assumptions, which are analysed in the next subsection. First the plasma is supposed to be quasi neutral, meaning that the ion density  $n_i$  and the electron density  $n_e$  are equal to a general quantity, called the plasma density and denoted by  $n$ . This assumption reads :

$$n_i = n_e = n \quad (3.5)$$

#### Conservation of electron momentum

The first equation of the model is the conservation of the electron momentum, it is derived from the consideration of two forces: the Lorentz force  $\vec{F}_L$  and the pressure gradient force  $\vec{F}_P$ . The plasma is supposed to be collisionless, hence the force associated to collisions is neglected in the fluid momentum conservation equation. These forces read :

$$\begin{aligned} \vec{F}_L &= -e \left( \vec{E} + \vec{u} \times \vec{B} \right) \\ \vec{F}_P &= -\frac{\nabla (nk_b T_e)}{n} \end{aligned} \quad (3.6)$$

where  $e$  is the elementary charge,  $\vec{u}$  is the fluid velocity of the electrons and  $\vec{E}$  and  $\vec{B}$  are respectively the electric and magnetic fields encountered by the plasma during its acceleration in the magnetic nozzle.

The fluid momentum equation for the electrons reads :

$$\begin{aligned} m_e \frac{dv}{dt} &= \vec{F}_L + \vec{F}_P \\ &= -e \left( \vec{E} + \vec{u} \times \vec{B} \right) - \frac{\nabla (nk_b T_e)}{n} \end{aligned} \quad (3.7)$$

The model is studied in stationary regime, i.e. the left hand term of equation 3.7 is null. Moreover, in order to solve analytically the equations of the model, the plasma is supposed to follow the magnetic field lines of the magnetic nozzle. Therefore, in the remaining of the section, the equations are projected along the local direction of the magnetic field. In this assumption, the detachment of the plasma from the magnetic nozzle is not considered. This point is discussed in section 3.4.

The projection of equation 3.7 along a magnetic field line gives the electron momentum conservation equation which can be rewritten as follows:

$$\begin{aligned} \nabla \phi - \frac{\nabla (nT_e)}{n} &= 0 \\ \Leftrightarrow \nabla \phi &= \nabla T_e + T_e \frac{\nabla n}{n} \end{aligned} \quad (3.8)$$

where  $T_e$  is the electron temperature expressed in eV and  $\phi$  is the potential from which derives the electric field, as defined by the relation  $\vec{E} = -\nabla \phi$ .

### Conservation of ion energy

In this model, the total ion energy is the sum of the kinetic energy and the potential energy. Indeed, it is supposed that there is no collisional losses for the ion population along their expansion in the magnetic nozzle. Therefore, the conservation of energy for the ions in expansion in the magnetic nozzle reads:

$$\nabla \left( \frac{m_i}{2e} u^2 + \phi \right) = 0 \quad (3.9)$$

where  $m_i$  is the ion mass and  $u$  is the fluid velocity of the ions.

### Conservation of ion flux

The third equation that completes the set of equations of the model is the conservation of the ion flux, which is supposed to be constant along a given magnetic flux tube of section  $\Sigma$ . It appears that the section of a magnetic flux tube varies as  $\Sigma \sim \frac{1}{B}$ , this result being verified later in the section. Therefore, the conservation of the ion flux along a magnetic field tube reads:

$$\nabla \left( \frac{nu}{B} \right) = 0 \quad (3.10)$$

Equations 3.8, 3.9 and 3.10 constitute the set of equations of this model. Nevertheless, a closing relation which links the variation of the electron temperature  $T_e$  with the other variables needs to be determined. In a first time, in order to find an analytical solution of the model, the electron temperature is supposed to be constant along the magnetic field line along which the plasma accelerates. The model is then referred to as isothermal and this condition is written  $\nabla T_e = 0$ . Equation 3.8 becomes:

$$\nabla \phi = T_e \nabla (\ln(n)) \quad (3.11)$$

This isothermal closing relation is further discussed in section 3.4. In fact, other closing relations can also be found in the literature for the description of the plasma expansion in a diverging magnetic nozzle. For example the form  $\nabla (T_e n^{1-\gamma}) = 0$ , where  $\gamma$  is called the polytropic coefficient, is commonly found. An analytical solution of the polytropic model is derived in section 3.4.1.

### 3.2.2 Verification of the assumptions of the model

In this section, the validity of the different equations is verified in the plume region, for several operating conditions in mass flow rate and microwave power and for the two magnetic topologies  $M_1$  and  $M_2$ . Along the axis of the thruster, the transversal component of the ion velocity field is null, hence the ions follow the central magnetic field line and the ion velocity  $u$  is equal to the longitudinal component of the ion velocity  $u_{iz}$  measured by LIF (see section 3.1). The plasma density is estimated in the plume region of the ECR thruster for every conditions tested with curling probe and LIF measurements. The development of the curling probe and the measurements of plasma density are extensively detailed in the work of F. Boni in Ref. [5].

#### Plasma attached to the magnetic field lines

The validity of the analytical solution of the model, which is determined below in section 3.2.3, lies in the fact that the expansion of the plasma is calculated along a magnetic field line. In fact, it is assumed that the plasma velocity field is aligned with the magnetic field. In order to verify this assumption, the local angle between the ion velocity field and the magnetic field, denoted by  $\beta_i$  is introduced. It is calculated in the plume region as follows:

$$\beta_i = \arctan\left(\frac{Br}{Bz}\right) - \arctan\left(\frac{u_{ir}}{u_{iz}}\right) \quad (3.12)$$

According to equation 3.12, the angle  $\beta_i$  is positive when the ion flux is more converging than the magnetic field, and negative otherwise. This angle is represented in the plume region for the ECR thruster condition 1 sccm and 32 W with the magnetic topologies  $M_1$  (figure 3.8) and  $M_2$  (figure 3.9). It appears that for both magnetic topologies, the angle  $\beta_i$  ranges from 0 to 5 degrees in the whole region of the plume comprised inside the limit defined by the last magnetic field line. For recall, the last magnetic field line, labelled LMFL, is the most diverging magnetic field line which does not cross physically the source of the thruster, defining a limit of the magnetic nozzle. This result is also illustrated by the red arrows which represent the ion velocity field. Indeed they are aligned with the magnetic field lines (black solid lines). These observations justify the assumption of the ions following the magnetic field lines inside the magnetic nozzle.

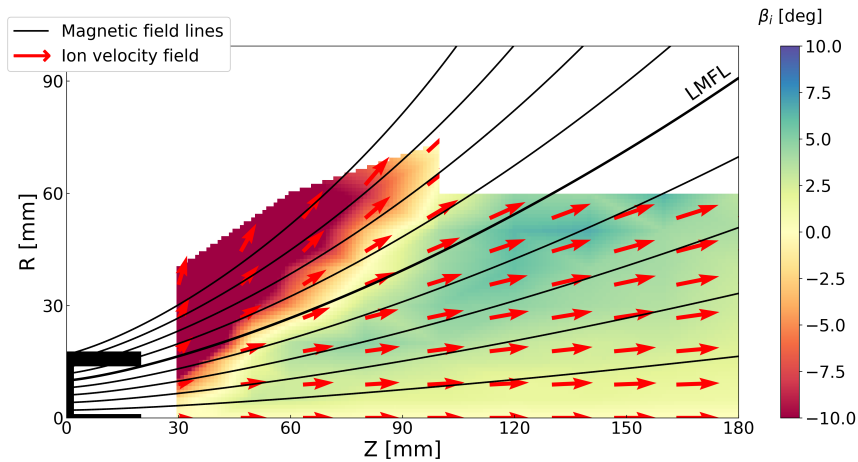


Figure 3.8: Two-dimensional map of the local angle between the ion velocity field and the magnetic field for the  $M_1$  magnetic configuration. The ion velocity field is represented with red arrows.

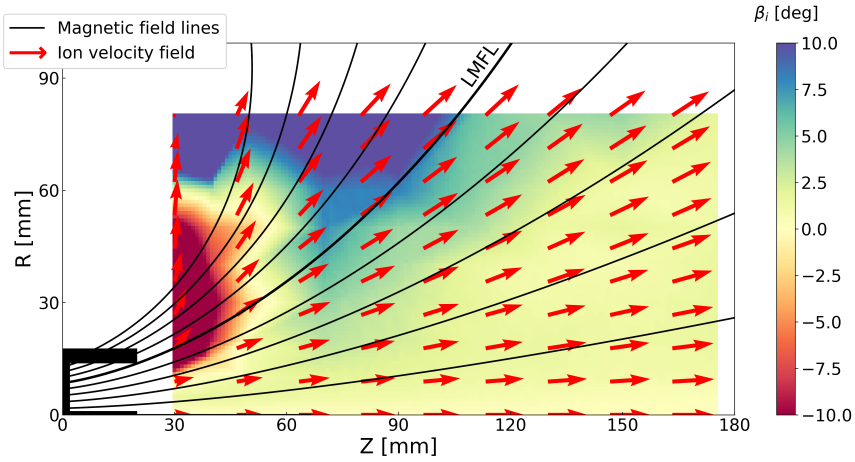


Figure 3.9: Two-dimensional map of the local angle between the ion velocity field and the magnetic field for the  $M_2$  magnetic configuration. The ion velocity field is represented with red arrows.

Note that for both magnetic topologies, there is an area, close to the source and outside the last magnetic field line, for which the ions are more diverging than the magnetic field (red area on figure 3.8 and 3.9). In this region, the ions start to be ejected backward, as discussed above in section 3.1.1. However, the density in this region is very small so the negative contribution of these ions to the thrust is negligible.

### Isothermal closing relation

The isothermal closing relation introduced above is a major assumption which drives the acceleration of the plasma in a diverging magnetic nozzle. According to equation 3.11, the potential  $\phi$  should vary linearly with the logarithm of the plasma density, the slope of this linear fit being the electron temperature  $T_e$ .

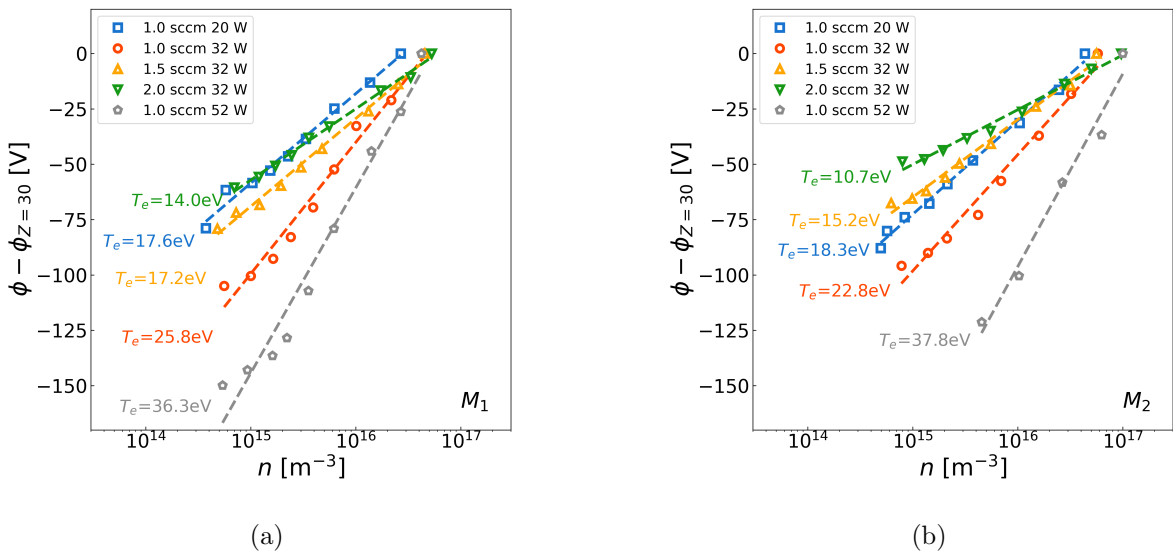


Figure 3.10: Verification of the isothermal approximation for the (a)  $M_1$  and (b)  $M_2$  magnetic configurations.

The potential  $\phi$  is evaluated from the measurements of the ion velocity with equation 3.9. However, this quantity is known to within a constant. Therefore,  $\phi - \phi_{Z=30}$ , where  $\phi_{Z=30}$  is the potential at  $Z = 30$  mm, is plotted against the logarithm of the plasma density  $\log(n)$  for several operating conditions and the two magnetic topologies  $M_1$  and  $M_2$  (figure 3.10). These figures show that there is effectively a linear relation between these two quantities, and a linear fit is represented on the figures with dashed lines to illustrate this relation. In the isothermal approximation, the slope of the fit is the electron temperature  $T_e$  (see equation 3.11).

The value of  $T_e$  is evaluated for several thruster mass flow rates at the constant power of 32 W (figure 3.11a) and for several powers at the constant mass flow rate 1 sccm (figure 3.11b). Results show that for both magnetic topologies  $M_1$  and  $M_2$ ,  $T_e$  decreases when the thruster mass flow rate increases and  $T_e$  increases when the power increases. This behaviour is the same than that observed with the ion energy measured at the far end of the vacuum facility with the ion analyser (results presented in chapter 6). This observation shows the link between the electron temperature and the acceleration of the ions in the magnetic nozzle. Moreover,  $T_e$  appears to be fairly independent of the magnetic topology. This result supports the fact that the production of the plasma and its acceleration in the diverging magnetic nozzle are two distinct processes, as discussed in section 3.1. The fact that the electron temperature is slightly higher for the magnetic topology  $M_1$  could be explained by the position of the ECR heating region in the source of the thruster which is slightly closer to the backplate with this magnetic topology.

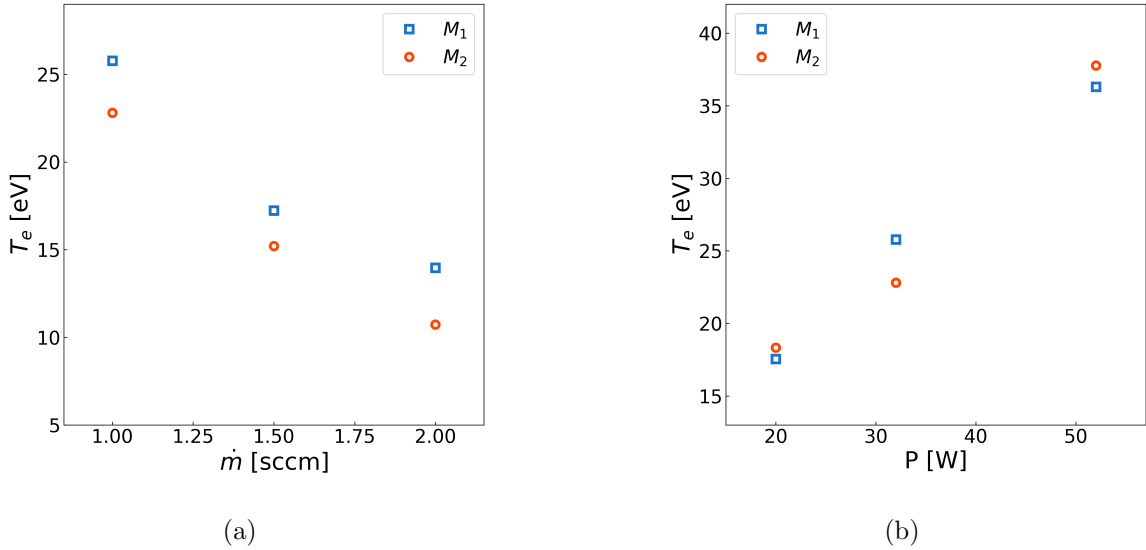


Figure 3.11: Evolution of the electron temperature  $T_e$  for the two magnetic topologies  $M_1$  and  $M_2$  with (a) the thruster mass flow rate at a power of 32 W and (b) the thruster power at a mass flow rate of 1 sccm.

### Conservation of the ion flux

The last assumption that must be verified is the conservation of the ion flux along the magnetic nozzle (equation 3.10). According to this equation, the quantity  $\frac{nu}{B}$  is conserved. Let  $\hat{n}$ ,  $\hat{u}$ ,  $\hat{\phi}$  and  $\hat{B}$  be respectively the plasma density, velocity, potential and the value of magnetic field at a given arbitrary position of a magnetic field line of the magnetic nozzle. In the remaining of this section, this position is  $R = 0$ ,  $Z = 30$ . The quantity  $B/\hat{B}$  is compared with  $nu/\hat{n}\hat{u}$  for the different thruster conditions and the two magnetic topologies  $M_1$  and  $M_2$  (figure 3.12). The value of the magnetic field is simulated with the software Comsol Multiphysics<sup>®</sup>. The excellent agreement between these two quantities shows that, on the one hand, the variation of the magnetic field tube section  $\Sigma$  as  $1/B$  is verified and, on the other hand, the validity of equation 3.10 is justified for all the operating conditions and for both magnetic topologies.

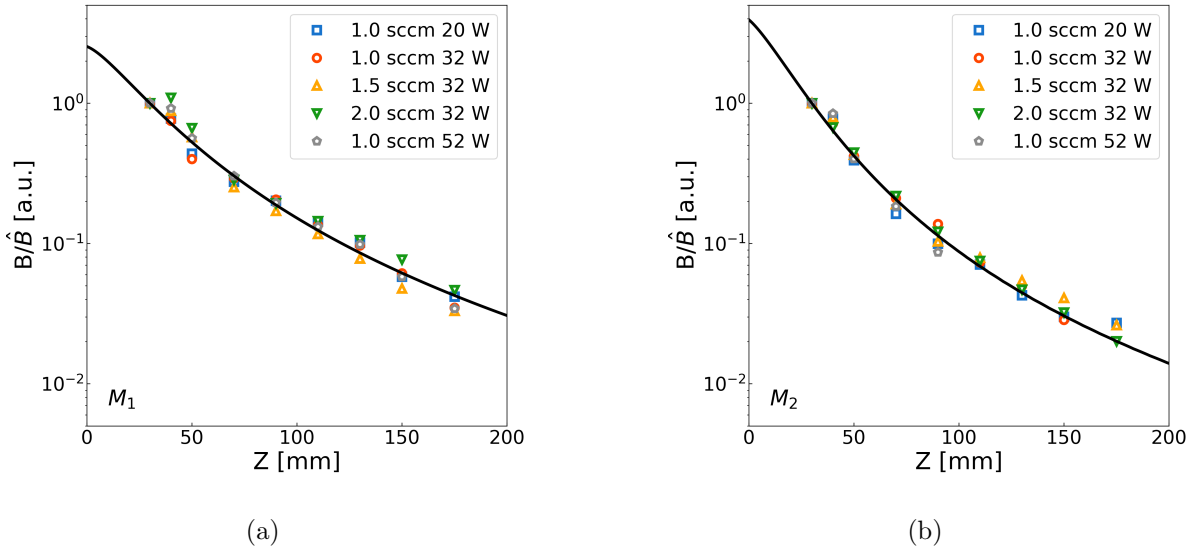


Figure 3.12: Verification of the conservation of the ion flux by comparing  $B/\hat{B}$  (black solid line) and  $nu/\hat{n}\hat{u}$  (scattered symbols) for the magnetic topologies (a)  $M_1$  and (b)  $M_2$ .

The results presented in this section justify the validity of the different assumptions and equations of the model. An analytical solution is derived in the next subsection and compared with experimental measurements in section 3.3.

### 3.2.3 Analytical solution

In order to find an analytical solution of the model presented above, the equations are solved along an arbitrary magnetic field line, with the initial conditions  $\hat{n}$ ,  $\hat{u}$ ,  $\hat{\phi}$  and  $\hat{B}$  being respectively the plasma density, velocity, potential and the value of magnetic field at a given arbitrary position along this magnetic field line.

First, equation 3.11 is rewritten as follows:

$$\frac{n}{\hat{n}} = \exp \left[ \frac{\phi - \hat{\phi}}{T_e} \right] \quad (3.13)$$

Second, with the same formalism, equation 3.9 gives:

$$\begin{aligned}\phi - \hat{\phi} &= \frac{m_i}{2e} (\hat{u}^2 - u^2) \\ &= \frac{m_i \hat{u}^2}{2e} \left(1 - \frac{u^2}{\hat{u}^2}\right)\end{aligned}\quad (3.14)$$

and equation 3.10 reads:

$$\frac{u}{\hat{u}} = \frac{\hat{n}B}{n\hat{B}}\quad (3.15)$$

The combination of equations 3.13, 3.14 and 3.15 gives the following equation:

$$\frac{n}{\hat{n}} = \exp \left[ \frac{m_i \hat{u}^2}{2eT_e} \left(1 - \left(\frac{\hat{n}}{n}\right)^2 \frac{B^2}{\hat{B}^2}\right) \right]\quad (3.16)$$

Three variables,  $x$ ,  $\alpha$  and  $\beta$  are introduced for the sake of clarity in order to solve equation 3.16 and get the evolution of the plasma density along the expansion of the plasma in the magnetic nozzle. They are defined as follows:

$$\begin{aligned}x &= \frac{n}{\hat{n}} \\ \alpha &= \frac{m_i \hat{u}^2}{2eT_e} \\ \beta &= \left(\frac{B}{\hat{B}}\right)^2\end{aligned}\quad (3.17)$$

Thus, equation 3.16 is rewritten with these non dimensionless variables:

$$x - \exp \left[ \alpha \left(1 - \frac{\beta}{x^2}\right) \right] = 0\quad (3.18)$$

The analytical solution of equation 3.18 is:

$$x = \sqrt{\frac{-2\alpha\beta}{W(-2\alpha\beta e^{-2\alpha})}}\quad (3.19)$$

where  $W$  is the Lambert's function, defined by the relation:

$$z = we^w \iff w = W(z)\quad (3.20)$$

where  $z$  and  $w$  are two complex numbers. The Lambert's function is not injective, meaning that it has two branches called  $W_0$  and  $W_{-1}$ .

The solution 3.19 gives the evolution of the density of the plasma along a magnetic field line from one initial condition taken arbitrarily along this magnetic field line. The evolution of the plasma velocity and potential are then retrieved from equations 3.14 and 3.15 respectively. It is worth noting that the interval of definition of the Lambert's  $W$  function is  $]-\frac{1}{e}; +\infty[$ . At the

location of the initial condition, the condition  $\beta = 1$  is verified. Therefore, at this location, the following inequality must be verified:

$$\begin{aligned}
 -2\alpha e^{-2\alpha} &\geq -e^{-1} \\
 \Leftrightarrow -2\alpha &\leq W_{-1}(e^{-1}) = -1 \\
 \Leftrightarrow \alpha &\geq \frac{1}{2}
 \end{aligned} \tag{3.21}$$

From equations 3.17 and 3.21 it comes:

$$\hat{u} \geq \sqrt{\frac{eT_e}{m_i}} = c_s \tag{3.22}$$

where  $c_s$  is the sound velocity of the flow. Therefore, the analytical solution previously derived describes the expansion of the plasma for supersonic flows only.

### 3.3 Comparison of the model with experimental data

#### 3.3.1 Expansion along the axis of the thruster

The analytical solution of the isothermal model of plasma expansion in a magnetic nozzle derived above is computed for several thruster operating conditions and magnetic nozzle topologies in the axis of the thruster. The initial condition is taken at  $Z = 40$  mm in order to be certain to meet the supersonic flow condition required for a well defined solution. The solution is compared with experimental measurements of the ion velocity (figure 3.13). Results show a good agreement between the theory and the experiments, which confirms the capability of the model with an isothermal approximation to describe the plasma expansion in the axis of the ECR thruster. Moreover the good comparison between the model and the experiments is independent from the thruster condition and from the magnetic topology.

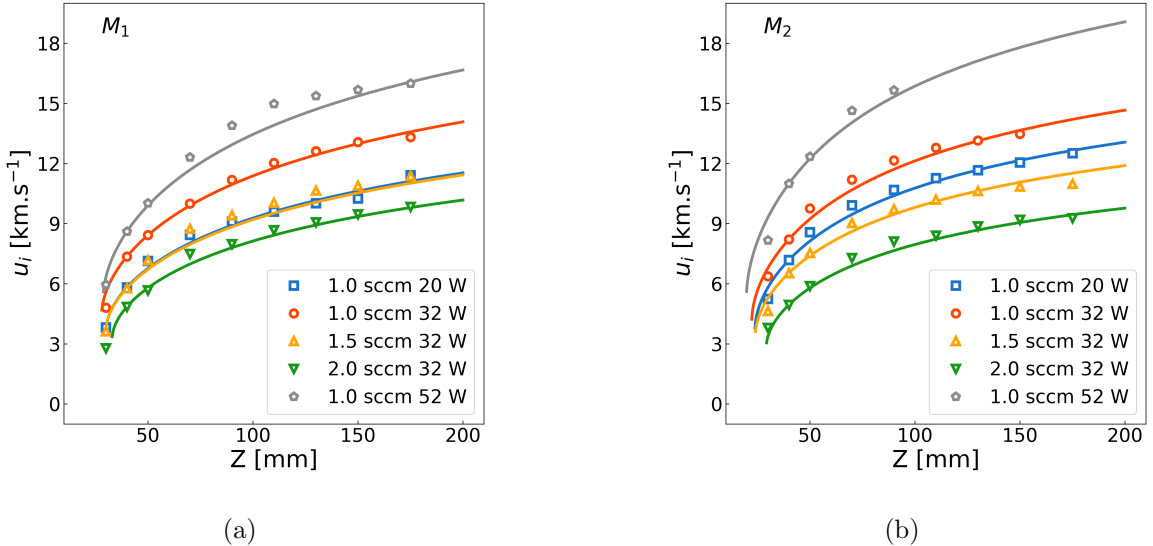


Figure 3.13: Comparison between the measured ion velocity (scattered symbols) and the analytical solution of the isothermal model (solid line) for several thruster operating conditions with the magnetic topologies (a)  $M_1$  and (b)  $M_2$  along the axis of the thruster.

The experimental results presented in this figure show that the evolution of the ion acceleration in the axis of the thruster scales with the evolution of the electron temperature with the different thruster operating conditions (figure 3.11). In fact, ions are more accelerated when the microwave power of the thruster increases and when the mass flow rate decreases. This observation confirms the correlation between electron temperature and ion acceleration previously discussed: the higher the electron temperature (of the isothermal description of expansion) the more accelerated the ions. This point is further discussed in section 3.4.

The location of the subsonic to supersonic transition, denoted by  $z_{c_s}$  is represented for several thruster mass flow rates at the constant power of 32 W (figure 3.14a) and for several powers at the constant mass flow rate 1 sccm (figure 3.14b). First, the results justify the choice of taking the initial condition at  $Z = 40$  mm for each thruster condition since it is above the sonic point. Second, results show that  $z_{c_s}$  is systematically greater with the magnetic topology  $M_1$  than with the magnetic topology  $M_2$ . This is due to the fact that the magnetic field decreases sharper with the magnetic topology  $M_2$ , implying a greater acceleration of the ions in the first centimetres of the plume. Moreover, for both magnetic topologies,  $z_{c_s}$  increases with the mass flow rate and decreases with the thruster power. This evolution is contrary to what is observed for the value of the sound speed (table 3.1) or with the electron temperature (subsection 3.2.2).

Topology	1 sccm 20 W	1 sccm 32 W	1 sccm 52 W	1.5 sccm 32 W	2 sccm 32 W
$M_1$	3.36	4.35	5.17	3.36	3.20
$M_2$	3.67	4.10	5.27	3.34	2.80

Table 3.1: Value of the sonic speed (in  $\text{km.s}^{-1}$ ) for several thruster operating conditions for the two magnetic topologies  $M_1$  and  $M_2$ .

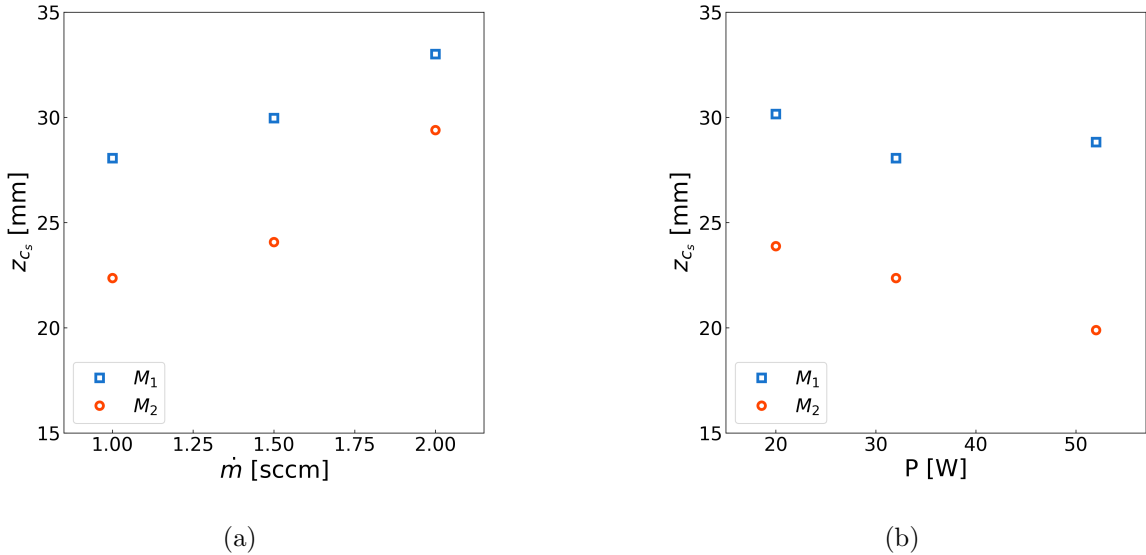


Figure 3.14: Evolution of the subsonic to supersonic transition location for the two magnetic topologies  $M_1$  and  $M_2$  with (a) the thruster mass flow rate at a power of 32 W and (b) the thruster power at a mass flow rate of 1 sccm.

The results presented so far are obtained in the axis of the ECR thruster. However, thanks to the two dimensional mapping of the ion velocity field, it is possible to solve the model along any magnetic field line which is off-axis. This analysis is done in the following section.

### 3.3.2 Expansion in the whole plume of the thruster

The analytical solution of the isothermal model of ion expansion is also computed along the magnetic field lines MFL\_1, MFL\_2 and MFL\_OFF which are off-axis for the magnetic topology  $M_1$  (see figure 3.1 for the definition of these particular magnetic field lines). It appears that for these three magnetic field lines, the potential  $\phi$  seems to evolve linearly with the logarithm of the ion density  $n_i$ . Since there is a lack of spatial resolution of the density measurements, it is however not possible to perform a proper interpolation of the data along the different magnetic field lines to obtain a satisfactory fit of the electron temperature  $T_e$  in the isothermal approximation. Therefore,  $T_e$  is supposed to be constant for the three magnetic field lines considered and equal to that measured in the axis of the thruster in figure 3.10. The comparison of the analytical solution of the model with the experimental data along MFL\_1, MFL\_2 and MFL\_OFF (figure 3.15) shows a very good agreement for the magnetic field lines MFL\_1 and MFL\_2. This result shows that the model can be solved along any magnetic field lines inside the magnetic nozzle of the ECR thruster.

However, a discrepancy is observed between the analytical solution of the model and the ion velocity measured along the magnetic field line MFL\_OFF. This result is not surprising since the hypothesis of the model are not verified in this region of the plume. In fact, the ions are created inside the source of the thruster and the ions located outside of the magnetic nozzle limit necessarily undergone a collision or a drift, which are not considered in the model.

Similar results are obtained for the magnetic topology  $M_2$ .

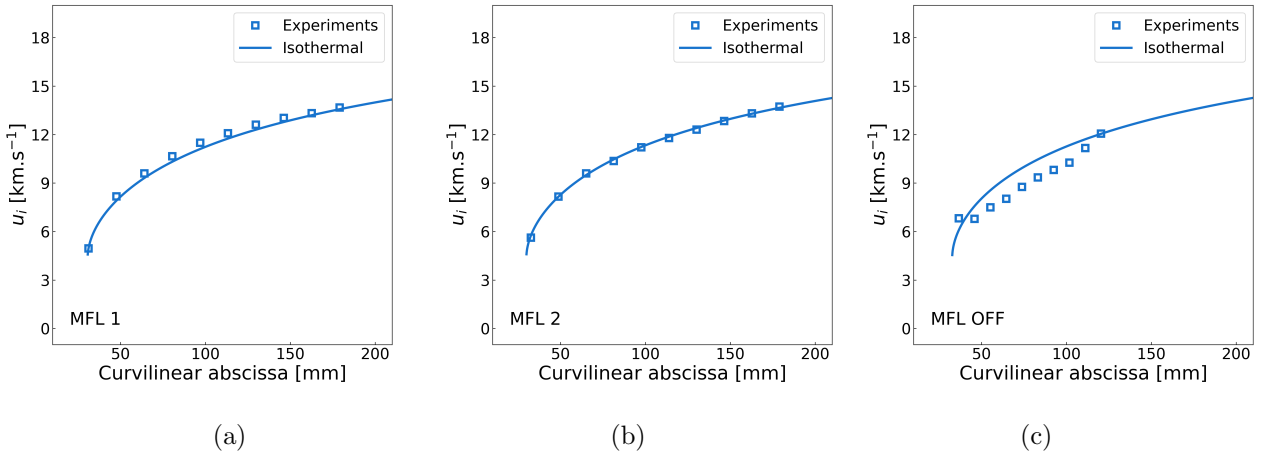


Figure 3.15: Comparison between the measured ion velocity (scattered symbols) and the analytical solution of the isothermal model (solid line) for the different magnetic field lines (a) MFL 1, (b) MFL 2 and (c) MFL OFF of the magnetic topology  $M_1$ .

The results presented in this section show that the model introduced above in section 3.2 does describe the expansion of the ions along every magnetic field line which is inside the magnetic nozzle of the ECR thruster. Moreover, the model is valid for two different magnetic field topologies and several thruster operating conditions in mass flow rate and microwave power. It is also found that a constant electron temperature in the whole magnetic nozzle allows a good description of the ion expansion with the model. However, the model does not describe the behaviour of the ions in the plume region outside the last magnetic field lines. In fact, in this region, the hypothesis of the ions following the magnetic field lines is necessarily broken because the ions are produced inside the source of the thruster.

In the following section, the limits of the model, as well as the polytropic closing relation for the electron temperature are further discussed.

## 3.4 Discussion of the results

### 3.4.1 Polytropic assumption

The main characteristic of the model presented in section 3.2 lies in the isothermal closing relation for the electron temperature. Results show a good agreement between the analytical solution found under this approximation and the experimental measurements. Nevertheless, measurements of electron temperature performed in the axis of the magnetic nozzle of several electric propulsion devices show that the electron temperature decreases along the plasma expansion. For example, Little and Choueiri measured an electron cooling along the expansion of a radio frequency produced plasma in a diverging magnetic nozzle [51].

The closing relation commonly used to describe the variation of the electron temperature along a magnetic nozzle is the polytropic cooling law. It reads:

$$\nabla (T_e n^{1-\gamma}) = 0 \quad (3.23)$$

where  $\gamma$  is called the polytropic index. It is worth noting that the case  $\gamma < 1$  represents an electron heating,  $\gamma = 1$  is the isothermal description studied in the previous sections, and  $\gamma = 5/3$  is called adiabatic expansion, for which there is no heat transfer. In the case where  $\gamma$  is supposed to be strictly greater than 1, equation 3.23 is developed as follows:

$$\begin{aligned} \nabla (T_e n^{1-\gamma}) &= 0 \\ \Leftrightarrow n^{1-\gamma} \nabla T_e + T_e \nabla n (1-\gamma) n^{-\gamma} &= 0 \\ \Leftrightarrow T_e \nabla (\ln(n)) &= \frac{\nabla T_e}{\gamma-1} \end{aligned} \quad (3.24)$$

Equation 3.8 becomes:

$$\nabla \phi = \frac{\gamma}{\gamma-1} \nabla T_e \quad (3.25)$$

If the electron temperature takes the value  $\hat{T}_e$  at an arbitrary position along a magnetic field line, 3.24 can be written:

$$\phi - \hat{\phi} = \frac{\gamma}{\gamma-1} (T_e - \hat{T}_e) \quad (3.26)$$

and from equation 3.14, 3.15, 3.23 and 3.26 it comes:

$$\begin{aligned} \frac{m_i \hat{u}^2}{2e} \left( 1 - \frac{u^2}{\hat{u}^2} \right) &= \frac{\gamma \hat{T}_e}{\gamma-1} \left( \frac{T_e}{\hat{T}_e} - 1 \right) \\ \Leftrightarrow \frac{m_i \hat{u}^2}{2e} \left( 1 - \left( \frac{\hat{n}}{n} \right)^2 \frac{B^2}{\hat{B}^2} \right) &= \frac{\gamma \hat{T}_e}{\gamma-1} \left( \left( \frac{\hat{n}}{n} \right)^{1-\gamma} - 1 \right) \end{aligned} \quad (3.27)$$

For the sake of clarity, equation 3.27 is rewritten with the notations  $x$ ,  $\alpha$  and  $\beta$  defined above (equation 3.17) such that:

$$\alpha \left( 1 - \frac{\beta}{x^2} \right) = \frac{\gamma}{\gamma - 1} (x^{\gamma-1} - 1) \quad (3.28)$$

This equation is solved numerically and the solution is compared with the experimental measurement of ion velocity in the axis of the thruster for the polytropic coefficients  $\gamma = 1.15$  and  $\gamma = 5/3$ . The initial electron temperature  $\hat{T}_e$  is equal to the electron temperature previously determined in the isothermal approximation in section 3.2.2 (figure 3.16)

Results show that the solution of the polytropic model does tend to the solution of the isothermal model in the limit  $\gamma \rightarrow 1$ , as expected according to equation 3.23. Moreover, it appears that the adiabatic expansion, i.e the limit  $\gamma \rightarrow 5/3$  does not describe the ion acceleration in the magnetic nozzle of the thruster measured by LIF. On the other hand, the polytropic expansion with  $\gamma = 1.15$ , chosen according to the value find by Little and Choueiri in Ref. [51], shows a quite good agreement with the data, even though less accurate than the results obtained with an isothermal model. A conclusion on the nature of the electron cooling, would necessitate either measurements of the electron temperature or measurements of the ion velocity at greater distances from the thruster.

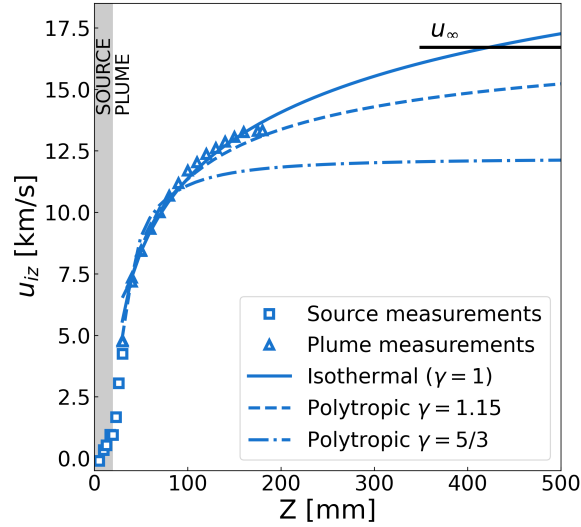


Figure 3.16: Comparison of the acceleration of the ions in the axis of the ECR thruster with an isothermal, polytropic and adiabatic expansion model. The thruster is firing at 1 sccm and 32 W with the magnetic topology  $M_1$ .

The comparison between the isothermal and the polytropic solutions of the model show that an electron cooling results in a lower acceleration of the ions. It illustrates the fact that the dynamic of the ions is driven by the electron expansion and ambipolar electric field resulting from this acceleration in the diverging magnetic nozzle.

The energy of the ions is measured at the far end of the B09 vacuum facility for the thruster firing at 1 sccm and 32 W with an ion analyser (see section 2.2.2) is  $E_\infty \approx 190$  eV. At this location, the ion energy is supposed to be purely kinetic so this energy corresponds to a velocity of  $u_\infty = \sqrt{2eE_\infty/m_i} \approx 16.7$  km.s<sup>-1</sup>. This value is represented in figure 3.16 with a black solid line, and appears to be lower than the ion velocity obtained when the isothermal solution is prolonged in the axis of the thruster. This observation shows a limit of the model of acceleration of the ions in the magnetic nozzle of the ECR thruster. Two phenomena can explain this result. First, it is possible that for distances greater than 20 cm away from the thruster source, the electrons cool down, therefore reducing the acceleration of the ions. This result is not necessarily in contradiction with the fact that an isothermal model well describes the ion acceleration in the first 20 cm. In fact, some models and simulations found in the literature suggest a cooling of the electrons which varies along the plasma expansion. This is the case of a one dimensional model derived by Correyero et al. in Ref. [53] or more recently the Particle in Cells code developed by Vatansever and Levinin in Ref. [67]. A similar behaviour could be suggested by the experimental data measured at greater distances, i.e. at lower plasma density, presented in the figure 3.10 of section 3.2.2, for which a deviation from the linear fit is observed. This point should be further investigated with measurements of the electron temperature or measurements of the ion velocity and density at greater distances from the thruster. Second, one condition of the production of a thrust force by the ECR thruster is the ion detachment from the magnetic nozzle. Such process stops the acceleration of the ions, which could explain the difference between the measured  $u_\infty$  and the ion velocity computed by isothermal model. This point is discussed below.

### 3.4.2 Limits of the assumptions

#### Sub-sonic solution

Equation 3.22 shows that an analytical solution of the model of isothermal expansion of a plasma in the magnetic nozzle can only be derived for supersonic flows. However, in the source of the ECR thruster, the ions have a velocity which is lower than the sound velocity. Therefore, along their expansion in the magnetic nozzle, they necessarily cross the subsonic - supersonic boundary. Moreover, as shown in section 3.1.2, the ion acceleration is very different in the source region and in the plume region. Therefore, in order to have a complete description of the ion acceleration in the magnetic nozzle of the ECR thruster, the model presented in this chapter should be, first, extended for sub-sonic flows, and, second, linked to a model of ion expansion in the source region.

#### Plasma detachment from the magnetic nozzle

One necessary condition to the production of a thrust force by an electric propulsion device which accelerates a plasma in a diverging magnetic nozzle is the separation, or detachment, of the plasma from the magnetic field lines downstream of the ejection region. In fact, without the detachment, the net force would be 0 as a result of the plasma looping back to the thruster. One assumption of the model developed in this chapter is that the plasma follows the magnetic field lines of the magnetic nozzle, as justified in section 3.2.2. Therefore, the results presented in this chapter show that the plasma detachment occurs further than 20 cm away from the thruster exit. However, measurements of the ion velocity and ion density cannot be performed with the LIF diagnostic at these distances due to the lack of fluorescence signal. To remedy this issue, measurements with electrostatic diagnostics can be performed. Hence, a innovative Faraday cup, whose development is detailed in chapter 4, is used to measure the ion trajectory and characterise the detachment of the ions from the magnetic nozzle of the ECR thruster. The results of this study are presented in chapter 5.

## Conclusion

This chapter presents measurements of the longitudinal component of the ion velocity field in the source of an ECR thruster and measurements of the two components (longitudinal and transversal) of the ion velocity field in the plume of the thruster, performed with the Laser Induced Fluorescence diagnostic. These experimental results show that, on the one hand, the acceleration of the ions takes place mostly in the 20 first centimetres in the magnetic nozzle of the ECR thruster and, on the other hand, the radial component of the ion velocity field is not null. In fact the ions follow the magnetic field lines inside the magnetic nozzle. It is also found that the ion acceleration profile is different in the source region, which is bounded by the physical walls of the ECR thruster source, and in the plume region. Therefore, these two regions should be studied independently.

In the source of the thruster, the ions are created near the ECR region, located between  $Z = 4$  mm and  $Z = 6$  mm. Upstream this location, the ions are accelerated toward the backplate. Downstream of the ECR region, the ions accelerate toward the exit of the source. The ions are not all created at the same location in the source, therefore they do not all see the same accelerating potential. It leads to a broadening of the ion velocity distribution function which increases along the expansion in the source.

The longitudinal component of the ion velocity field in the source of the ECR thruster does not depend on the thruster operating condition in mass flow rate and microwave power. However, as soon as the ions leave the source, their acceleration is driven by the magnetic nozzle, with a gain of velocity greater at higher power and lower mass flow rate. 90% of the acceleration of the ions takes place in the plume region.

In order to describe the ion acceleration in the plume region, a fluid model, is developed. An analytical solution is derived with an isothermal condition for the electrons, and shows a very good agreement with the experimental measurements of ion velocity for the different conditions of the ECR thruster in mass flow rate and power and for the two different magnetic topologies tested. The equations of the model are projected along the magnetic field lines, and a good agreement is found between the experimental data and the solution computed along several magnetic field lines off-axis. However, the model fails at describing the ion acceleration along magnetic field lines more diverging than the last magnetic field line.

A solution of the model is also derived under a polytropic closing relation that describes the cooling of the electron along their expansion in the magnetic nozzle. The adiabatic solution (polytropic index  $\gamma = 5/3$ ) does not describe the acceleration of the ions measured. It appears that the solution for  $\gamma=1.15$ , proposed by previous authors, is less accurate than the isothermal solution. Nevertheless, results indicate that an electron cooling could appear at distances greater than 20 cm away from the thruster backplate. At such distance, the ion velocity cannot be measured with the current Laser Induced Fluorescence setup due to a lack of fluorescence signal. The Directional Faraday cup, which is the object of the next chapter, allows to perform measurements of the ion current density in the far field region of the plume of the ECR thruster.

The results presented in this chapter show that the ion acceleration is driven by the dynamics of the electrons in the magnetic nozzle of the ECR thruster. The complete description of the plasma expansion would necessitate measurements of the electron temperature in a whole range of distances to the backplate of the thruster, from several centimetres to a few tens of centimetres, with a Langmuir probe for example. However, such measurement is difficult to perform because, on the one hand, the thruster would be perturbed by this electrostatic

diagnostic and, on the other hand, the plasma density varies of several order of magnitude in this range of distances. It would require great precautions in terms of the dimensions of the Langmuir probe. An optical diagnostic such as Thomson scattering setup presented in Ref. [68] could allow to measure the electron temperature in a perturbative-free way.



## 4 | Development of a Faraday cup for the directional measurement of the ion current density

**Motivation and objectives:** Chapter 3 shows that an isothermal model can describe the expansion of the plasma in the first 20 centimetres of the magnetic nozzle of the ECR thruster. However, the phenomenon of detachment of the plasma from the magnetic nozzle, which is a necessary condition to the production of a thrust force, is not taken into account in the model. Moreover, the Laser Induced Fluorescence diagnostic cannot be used to measure the properties of the plasma too far from the thruster exit because, at distances greater than 20 cm, the fluorescence signal is too weak. Electrostatic diagnostics, such as Faraday probes, are generally used to perform measurements of the plasma properties at large distances from the thruster. However, extracting quantitative data to analyse the plume of electric propulsion devices and characterise the detachment of the plasma from the magnetic nozzle with such diagnostic requires, on the one hand, a good knowledge of the current measured by the probe and, on the other hand, an extensive set of experimental data.

In the case of the ECR thruster, the ion current density has been measured so far with a Faraday probe with guard ring. However, a discrepancy is observed between the thrust measured directly with a thrust balance and the thrust estimated from the ion flux measured with this diagnostic. It suggests that some hypothesis made to estimate the thrust using ion flux measurements might be wrong. To challenge these hypothesis, and in particular the local ion flux direction taken in the computation, a directional Faraday cup is developed. This diagnostic is based on an innovative design which captures the local angular distribution of ion current density in the plume of the thruster at distances greater than 20 cm. With such measurement, a quantitative analysis of the detachment of the plasma from the magnetic nozzle of the ECR thruster can be performed. The objective of this chapter is to introduce this new diagnostic and demonstrate that the measured ion current is fully understood. The utilisation of the directional Faraday cup for the experimental characterisation of the detachment of the plasma from the magnetic nozzle of the ECR thruster is addressed in chapter 5 and its utilisation to investigate the comparison between direct measurement and indirect estimation of the thrust of the ECR thruster is detailed in chapter 6.

**Main results:** The directional Faraday cup is an innovative plasma diagnostic built to measure the local angular distribution of ion flux direction in the plume of electric propulsion devices. After a description of the design of the directional Faraday cup, two functions describing the directionality of the cup are defined: the Acceptance and the Opening of the cup. The analytical development of these two functions is confirmed with simulations in an ideal regime with the software SIMION and validated by current measurements in front of an ion source. These results confirm that the design of the directional Faraday allows to select the ions collected on the plate according to their direction with respect to the axis of the cup. This property is used in chapter 5 to characterise the detachment of the ions from the magnetic nozzle of the ECR thruster.

Section 4.3 deals with how the Acceptance and the Opening functions of the directional Faraday cup are modified when the diagnostic is immersed in the plasma plume of the ECR thruster. In a first part, the study of I-V curves performed with the directional Faraday cup in front of the ECR thruster allows to define the recommended practices for the biasing of the different collectors of the cup. In the case of the study of the plasma generated by the ECR thruster, the collectors of the directional Faraday cup should be biased at  $V_b = -350$  V for thruster powers lower than 35 W and  $V_b = -500$  V for thruster powers greater than 35 W. These are highly negative values compared to the bias voltage necessary to study the plasma of other propulsion devices. In a second part, the influence of the biasing voltage of the ring of the directional Faraday cup on the Acceptance function is evaluated with different simulations. Measurements of the ion current density with the cup in rotation in front of the ECR thruster confirm the simulation outcomes and show that the ring should be grounded to measure a meaningful current and keep the property of directionality of the diagnostic.<sup>1</sup>

These results show that the property of angular selectivity of ion flux measured by the directional Faraday cup is correctly understood in ideal and plasma regime. However, they do not guarantee that the current measured by the diagnostic is effectively the ion current density. This point is addressed in chapter 6.

---

<sup>1</sup>The results presented in this chapter are part of the following article [69]: Romain Pioch, Victor Désangles, Pascal Chabert, *Investigation of the directional Faraday cup and improvement of the comparison between direct and indirect thrust measurements of a magnetic nozzle ECR thruster*. Phys. Plasmas 1 April 2024; 31 (4): 043516. <https://doi.org/10.1063/5.0190318>

## 4.1 Design of the directional Faraday cup

The directional Faraday cup, also labelled FCDi in the figures of the manuscript, is an electrostatic plasma diagnostic designed to capture the local angular distribution of ion current density in the plume of electric propulsion devices. To this end, it is inspired by a traditional Faraday cup, but its innovative design allows to distinguish the ions collected with respect to the angle they make with the axis of the cup. In fact, the directional Faraday cup has the peculiarity to be constituted of two distinct metallic collectors that can be biased independently (figure 4.1). The first collector is called the plate. It is placed at the bottom of the cup. The second collector is a hollow cylinder of length  $\ell = 34$  mm and inner radius  $r_p = 2.95$  mm. With the plate, it constitutes the cup shape. The dimensions of the plate and the cup are chosen so that the cup has a large aspect ratio  $\ell/r_p \geq 10$ . In fact, the main point of the directional Faraday cup is its ability to collect on the plate only the current of the ions which make a small angle with the cup axis. Finally, a metallic ring, also called opening ring, closes the cup. It features a hole of radius  $r_o = 1.5$  mm which allows the ions to enter the cup and hit either the cylinder or the plate. All of the different pieces that constitute the directional Faraday cup are separated by dielectric spacers. Therefore, the cylinder and the plate can be biased independently using two distinct acquisition circuit described in the experimental apparatus in section 2.2.3. A structure made of FR4 is built to mount the directional Faraday cup on a stepper motor (figure 4.1b). Thus, the ion current density is measured in the plume of the ECR thruster while the probe rotates on itself (green arrow in figure 4.1a). In the remaining of the manuscript, this kind of measurement is referred to as an  $\alpha$ -scan.

One main advantage of the directional Faraday cup over a standard Faraday cup is that it can be used in two different modes: the directional mode, for which the plate and collector signals are looked at independently and the cup mode, for which the two signals are summed so that all the current entering the cup is collected. The directional mode is used to retrieve the local angular distribution of ion flux direction from the current drawn on the plate during an  $\alpha$ -scan while the cup mode is used to measure the ion current density with no difference from a standard Faraday cup.

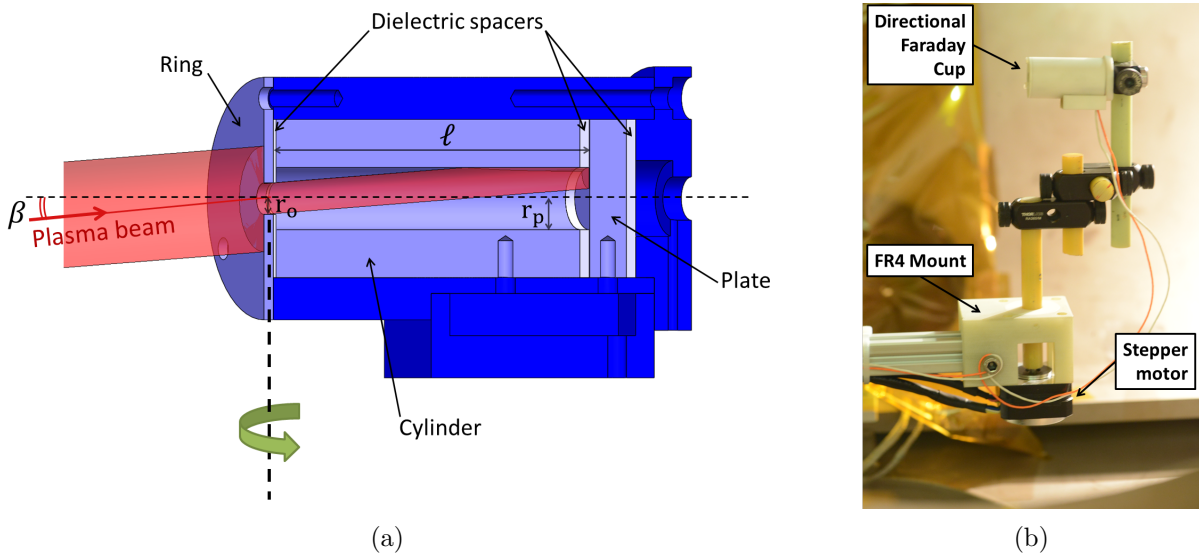


Figure 4.1: (a) Schematic and (b) photograph of the directional Faraday cup.

Several modifications have been made to the initial design of the cup first introduced in Peterschmitt's thesis [33]. They concern the replacement of the dielectric opening ring by a metallic ring, the design of an adaptation mount to place the diagnostic on top of a stepper motor (figure 4.1b) and the amelioration of the acquisition circuit (presented in the experimental apparatus in section 2.2.3). These design improvements allow, on the one hand, a better understanding of the cup in order to define the recommended practices for the biasing of the different parts and, on the other hand, to perform local measurements of the angular distribution of ion current density in the plume of the ECR thruster.

The definition, the computation and the verification of the angular selectivity of the diagnostic is presented in the next section and the behaviour of the cup when immersed in the plasma plume of the ECR thruster is presented in section 4.3.

## 4.2 Angular selectivity of the directional Faraday cup under ballistic ion trajectories

### 4.2.1 Definition and computation of the Acceptance and Opening functions

The Acceptance of the directional Faraday cup, denoted by  $\mathcal{A}$ , is a function used to quantify the directionality of this diagnostic. It is defined as the proportion of plate surface impacted by a rectilinear particle beam entering the cup with a certain angle with respect to the cup axis. The Opening function, denoted by  $\mathcal{O}$ , is the proportion of the cup surface (plate and cylinder) impacted by this beam. These two functions depend on the opening radius  $r_o$ , the plate radius  $r_p$  and the length  $\ell$  of the cup. They are normalised by the area of the entrance hole of the cup, hence  $\mathcal{A} = 1$  and  $\mathcal{O} = 1$  when the particle beam enters the cup with normal incidence.

The analytical expressions of  $\mathcal{A}$  and  $\mathcal{O}$  are obtained as follows. Let  $\beta$  be the angle between the directional Faraday cup axis and an observer's line of sight (figure 4.2). The ring and the plate seen by this observer are then two ellipses separated by a distance  $D = |\ell \sin(\beta)|$  with a semi-major axis  $r_o$  and  $r_p$  and a semi-minor axis  $r_o \cos(\beta)$  and  $r_p \cos(\beta)$  respectively. These two ellipses are denoted by  $\mathcal{E}_o$  and  $\mathcal{E}_p$  for the opening and the plate respectively. In a first approximation, the thickness of the opening ring is neglected and the intersection area of the two ellipses is the approximated Acceptance, denoted by  $\mathcal{A}'$ . The equations of  $\mathcal{E}_o$  and  $\mathcal{E}_p$ ,

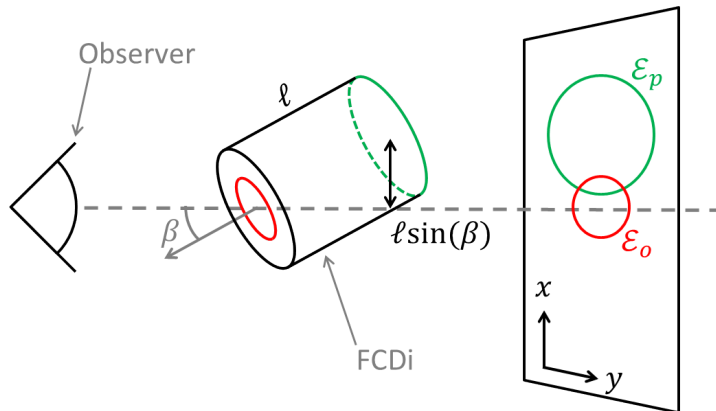


Figure 4.2: Schematic of the ellipses resulting from the rotation of the directional Faraday cup in front of an observer.

projected in the plane normal to the observer's line of sight, are expressed as follows:

$$\mathcal{E}_o(\beta) : \left\{ (x, y) \mid y = \sqrt{r_o^2 - \frac{x^2}{\cos(\beta)^2}} \right\}$$

$$\mathcal{E}_p(\beta) : \left\{ (x, y) \mid y = \sqrt{r_p^2 - \frac{(x - D)^2}{\cos(\beta)^2}} \right\}$$

$\mathcal{A}'$  is the overlapping area of the two ellipses and is therefore:

$$\mathcal{A}'(\beta) = \frac{2}{\pi r_o^2} \int_{-\infty}^{+\infty} \mathcal{C}_\beta(x) dx \quad (4.1)$$

where  $\mathcal{C}_\beta(x)$  is introduced for more readability and is defined as the envelope of the intersection between  $\mathcal{E}_o$  and  $\mathcal{E}_p$ . Three cases are distinguished to solve equation 4.1 (figure 4.3).

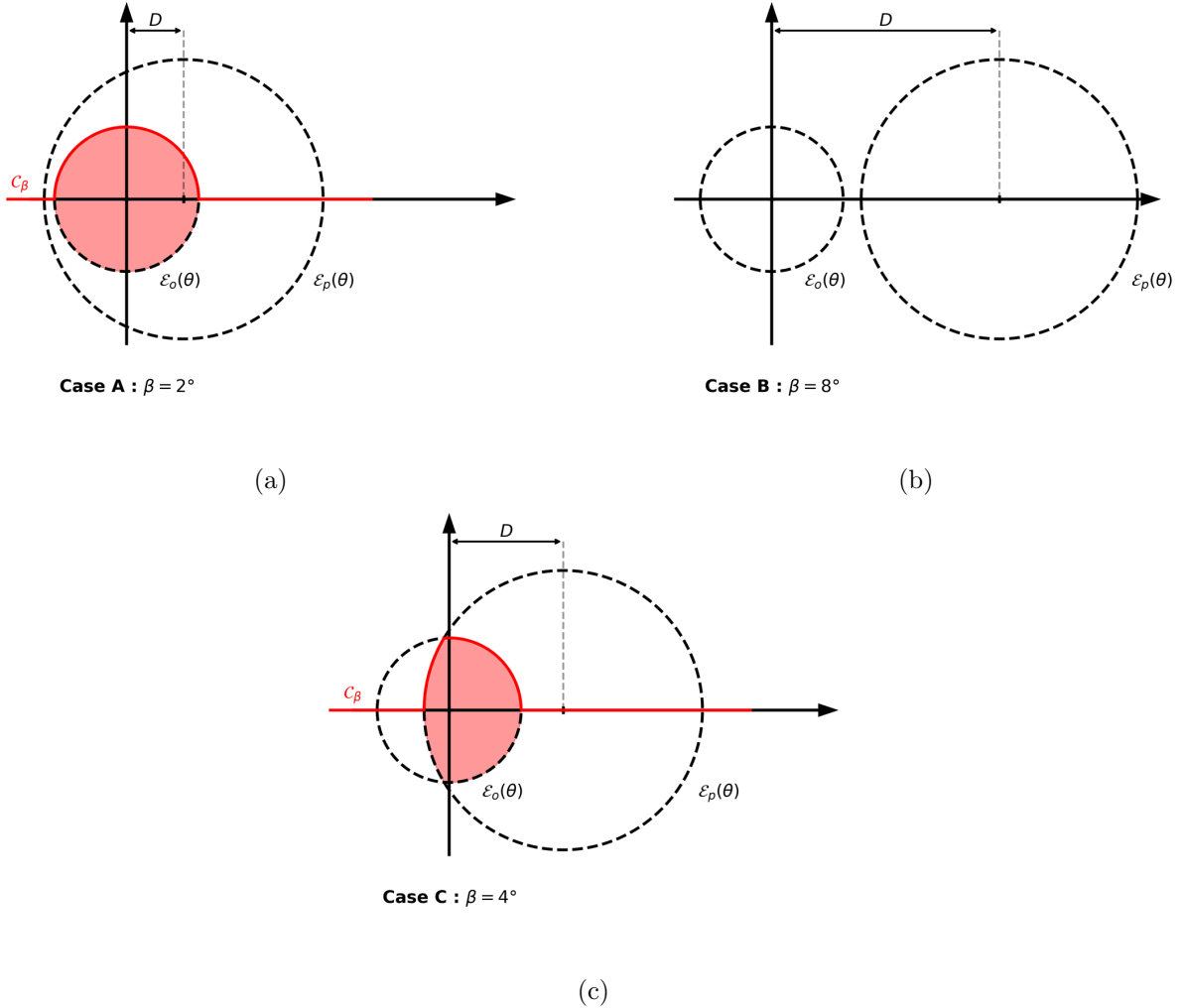


Figure 4.3: Illustration of the recovering area of the ellipses formed by the plate and the opening of the directional Faraday cup for the case where (a) the opening ellipse is inside the plate ellipse, (b) the two ellipses are disjoint and (c) the ellipses partially overlap.

### Case A

In the first case (figure 4.3a), the opening ellipse  $\mathcal{E}_o$  is inside the plate ellipse  $\mathcal{E}_p$ . This case stands for small angles  $\beta$  which satisfy the following relation:

$$\begin{aligned} D - r_p \cos(\beta) + r_o \cos(\beta) &\leq 0 \\ \Leftrightarrow |\beta| &\leq \arctan\left(\frac{r_p - r_o}{\ell}\right) \end{aligned} \quad (4.2)$$

The Acceptance then takes the following value:

$$\mathcal{A}'(\beta) = \frac{\mathcal{A}_{\mathcal{E}_o}}{\pi r_o^2} = \frac{\pi r_o^2 \cos(\beta)}{\pi r_o^2} = \cos(\beta) \quad (4.3)$$

where  $\mathcal{A}_{\mathcal{E}_o}$  is the area of  $\mathcal{E}_o$ .

### Case B

In a second case (figure 4.3b), the two ellipses are disjointed and  $\beta$  satisfies:

$$\begin{aligned} D - r_p \cos(\beta) - r_o \cos(\beta) &\geq 0 \\ \Leftrightarrow |\beta| &\geq \arctan\left(\frac{r_p + r_o}{\ell}\right) \end{aligned} \quad (4.4)$$

In that case  $\mathcal{A}' = 0$ .

### Case C

The third case (figure 4.3c), when the ellipses partially overlap, is the proper resolution of equation 4.1. The Acceptance then reads:

$$\begin{aligned} \mathcal{A}'(\beta) &= \frac{2}{\pi r_o^2} \int_{-\infty}^{+\infty} \mathcal{C}_\beta(x) dx \\ \Leftrightarrow \mathcal{A}'(\beta) &= \frac{2}{\pi r_o^2} \int_a^b \min_x(f_o(x), f_p(x)) dx \end{aligned} \quad (4.5)$$

$$\begin{cases} a = D - r_p \cos(\beta) \\ b = r_o \cos(\beta) \\ f_o(x) = \sqrt{r_o^2 - \frac{x^2}{\cos(\beta)^2}} \\ f_p(x) = \sqrt{r_p^2 - \frac{(x-D)^2}{\cos(\beta)^2}} \end{cases}$$

The formulation of equations 4.3 and 4.5 does not take into account the real geometry of the directional Faraday cup. In fact, the thickness of the opening ring,  $\ell' = 1$  mm has been neglected. In order to compute the true theoretical Acceptance function  $\mathcal{A}$  of the directional Faraday cup, the Opening area  $\mathcal{O}$  of the cup, which is the proportion of ion that enter the cup at a given beam angle, is computed. In the case of a cup with a ring with 0 thickness ( $\ell' = 0$ ),  $\mathcal{O}$  is a cosine function. However, if the thickness of the ring is taken into account, the opening area  $\mathcal{O}$  of the directional Faraday cup is computed with a geometrical problem similar to that solved to find  $\mathcal{A}'$ , which is to find the intersection area between two ellipses of major-axis  $r_o$  and minor-axis  $r_o \cos(\beta)$  separated by a distance  $D = |\ell' \sin(\beta)|$  (figure 4.4). The opening area  $\mathcal{O}$  is then multiplied to  $\mathcal{A}'$  to get the true Acceptance function  $\mathcal{A}$  of the directional Faraday cup.

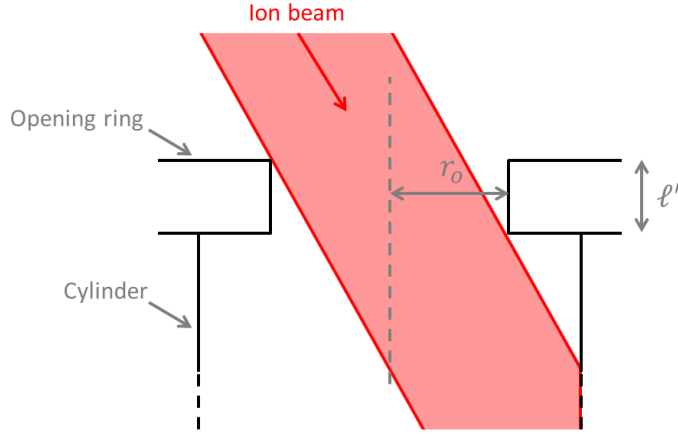


Figure 4.4: Schematic of the opening ring thickness  $\ell'$ .

The analytical expressions of  $\mathcal{A}$  and  $\mathcal{O}$  resulting from this theoretical analysis are computed numerically and represented with a black solid line in figure 4.7. The expression of  $\mathcal{A}$  and  $\mathcal{O}$  are based on a description purely geometric of the directional Faraday cup. In order to validate these theoretical expressions, simulations of the cup and experimental measurements of  $\mathcal{A}$  and  $\mathcal{O}$  are performed, in a first place, in a regime called the ideal regime, which is slightly different from the plasma regime found in the plume of the ECR thruster. The definition of the ideal regime and the detail of the simulations and the experiment performed is found in the next section. Then, in section 4.3, the modification of  $\mathcal{A}$  and  $\mathcal{O}$  in the plasma plume of the ECR thruster is investigated.

#### 4.2.2 Validation of the cup directionality in ideal regime

The Acceptance and Opening functions defined and computed in the previous section are based on a ballistic consideration of the charged particles trajectories which might be different from the behaviour of the ions of a plasma. Hence, in order to validate this description, simulations of the cup and experimental measurements of  $\mathcal{A}$  and  $\mathcal{O}$  are performed in an ideal regime. In this ideal regime, the particles are supposed to follow rectilinear ballistic trajectories, no collision between the particles is considered and a particle that hit a surface is supposed to be absorbed without rebound or emission. First, the software SIMION [70] is used to simulate  $\mathcal{A}$  and  $\mathcal{O}$  and, second, the ion source presented in the experimental apparatus in section 2.4 is used to measure experimentally the Acceptance and Opening functions of the directional Faraday cup in ideal regime. Finally, simulations and the experiments are compared with the theoretical expression of  $\mathcal{A}$  and  $\mathcal{O}$  to confirm that the directional Faraday cup is sufficiently directional to select the ions collected according to the direction they make with respect to the cup axis.

#### Simulations

The software SIMION is used to get a better understanding of the particle behaviour inside and around the directional Faraday cup. This software allows to simulate the trajectories of charged particles in a potential array defined by the user given their initial energy distribution. A mesh of the cup, respecting its physical dimensions, is generated and the potential of the different parts, namely the plate, the cylinder and the ring, are adjusted independently. The simulation domain is surrounded by walls at potential 0 V far from the probe, i.e. at a distance greater than  $10^3 r_0$ . In order to get meaningful simulation results, 1000 particle are simulated, with the

mass of the  $Xe^+$  ions and an initial energy distributed according to a Gaussian distribution centred at 190 eV with a standard deviation of 40 eV. Such distribution is representative of the ion energy distribution measured using an ion energy analyser in the plume of the ECR thruster at 1 sccm of flow rate and 30 W of microwave power, which is a thruster operating condition widely used throughout this manuscript. The initial position of the simulated particles is uniformly distributed on a disc that faces the cup, at a distance at which the potential is nearly 0. The radius of this disc is two times bigger than the opening radius of the directional Faraday cup. The initial direction of the velocity of the particles can be adjusted to make an angle with the probe axis (figure 4.5).

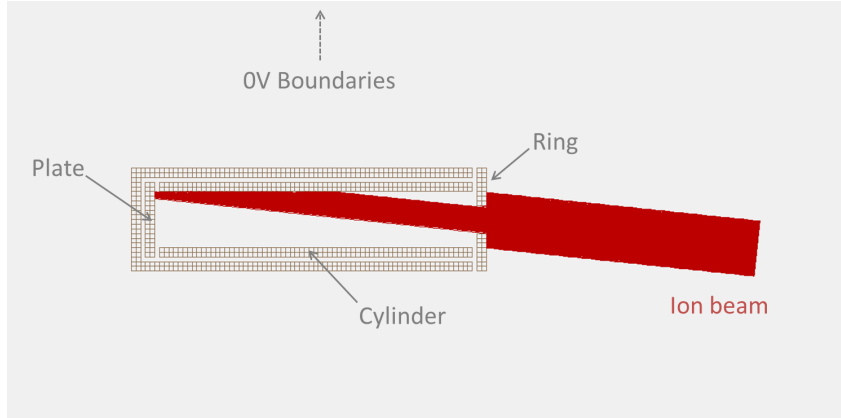


Figure 4.5: Mesh of the directional Faraday cup in the software SIMION.

The ion beam makes an angle of 6 deg with the cup axis.

The trajectories of the particles are simulated in the potential array generated by the software. When a particle hits a surface, it disappears and its position is recorded. Then, the number of particles that hit the plate and the cylinder is counted and divided by the number of particles that should theoretically have entered the probe at normal incidence, which is proportional to the ratio between the area of the opening hole and area of the disc in which the particles are initially distributed. This simulation is repeated for several values of initial particle direction angle to get the simulated Acceptance and Opening functions of the directional Faraday cup.

In a first place, in order to compare these simulated functions to the theoretical description developed in section 4.2.1, no bias is applied to the electrodes and the potential is 0 V in the whole simulation domain. Thus, all of the ions have a rectilinear and ballistic trajectory which is not modified by any electrostatic effect, and this simulation is representative of the ideal regime. The Acceptance and Opening functions simulated in ideal regime are represented with black scattered symbols in figures 4.7a and 4.7b respectively. The comparison of the simulation with the theory is discussed below in the section.

## Experiments

The ion source presented in the experimental apparatus in section 2.4 is used to measure experimentally the Acceptance and Opening functions of the directional Faraday cup in ideal regime and compare it with the theory and the simulations. As verified in the experimental apparatus, the ion beam produced by the source is uni-directional and mono energetic. The operating parameters of the source are  $I_d = 14$  mA,  $V_f = 0$  V, the gas used is xenon with a mass flow rate of  $\dot{m} = 0.016$  mg.s<sup>-1</sup>. With these parameters, the ion energy is around 300 V. The directional Faraday cup is mounted on the stepper motor at a distance of 7 cm in front

of the ion source (figure 4.6). The current of the ion beam produced by the source, collected by the plate and the cylinder of the cup, is measured simultaneously on these two parts during the rotation of the diagnostic. Both the plate and the cylinder of the directional Faraday cup are biased at -100 V. This value is chosen sufficiently low to prevent the electrons from entering the cup, but not too low, so as not to affect the trajectory of the ions by mean of electrostatic field too high compared to the ion energy. Therefore, the conditions of this experiment are as close as possible to the ideal regime, and the signal measured on the plate and the cylinder of the directional Faraday cup can be compared to the theoretical and simulated Acceptance and Opening functions.

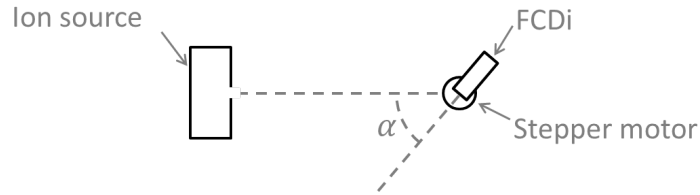


Figure 4.6: Experimental setup to measure the Acceptance and the Opening functions of the directional Faraday cup in ideal regime with the ion source.

The signals measured on the plate and the cylinder of the directional Faraday cup in front of the ion source are represented with grey solid lines in figures 4.7a and 4.7b respectively. The comparisons between experiments, simulations and theory are discussed below.

### Comparison

A very good agreement is observed between the theoretical, simulated and measured functions  $\mathcal{A}(\alpha)$  and  $\mathcal{O}(\alpha)$  (figures 4.7a and 4.7b respectively). On the one hand, the fact that the simulation is comparable to the theory indicates that the mesh of the directional Faraday cup in the software SIMION does allow to simulate the behaviour of the ions entering the cup in ideal regime. Moreover, it confirms that the number of particles simulated is sufficient to get meaningful simulation results. On the other hand, the comparison between the theory and the current measured by the directional Faraday cup in rotation in front of the ion source, in arbitrary units, confirms that the Acceptance and the Opening functions are well defined. Moreover, these results confirm that the Acceptance is a narrow function (figure 4.7a). In fact, the Acceptance is close to 1 in the region  $\alpha \in [-2 : 2]$  deg, and decreases sharply for  $|\alpha| \geq 2$  deg. Finally, the good agreement between the theoretical Opening and the current measured in cup mode confirms that the thickness of the opening ring cannot be neglected. Indeed, the Opening function would have been a cosine function otherwise (see figure 4.7b).

The results presented in this section show that the angular selectivity of the directional Faraday cup is well defined and understood. Moreover, the fact that the Acceptance is a narrow function is due to the sufficient deepness of the cup. This property is used in chapter 5 to assess the local trajectory of the ions in the plume of the ECR thruster and study the detachment of the ions from the magnetic nozzle.

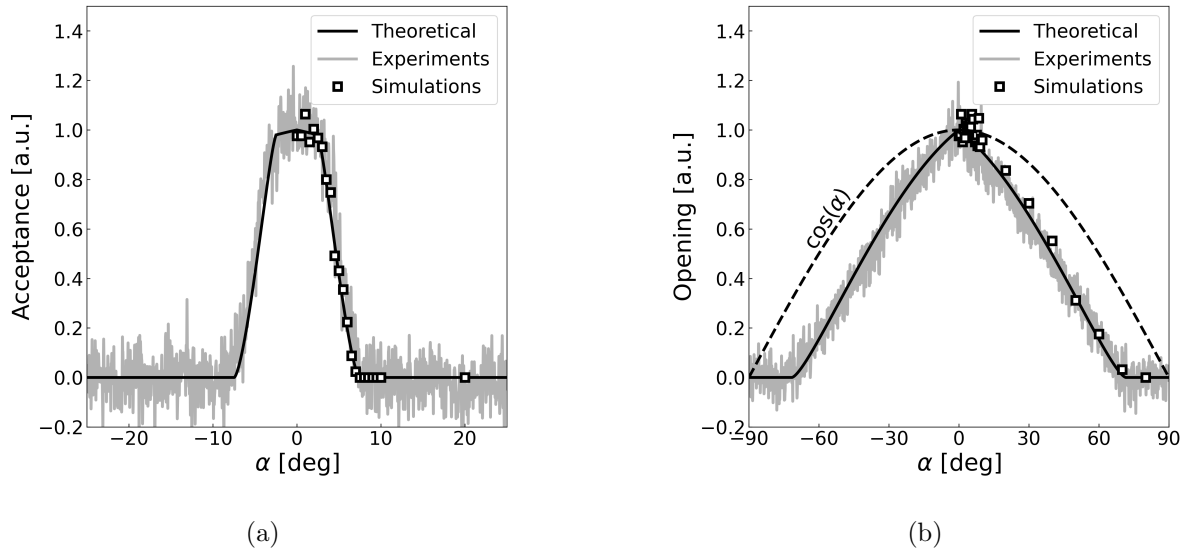


Figure 4.7: Comparison between the theoretical, simulated and measured (a) Acceptance and (b) Opening function in ideal regime.

In the next section, the influence of the plasma plume of the ECR thruster on the Acceptance and Opening of the directional Faraday cup is investigated by simulations with the software SIMION and by measurements of ion current density. Moreover, in the plasma regime, the collectors of the cup must be biased at high negative voltages to measure the ion saturation current, which can alter the trajectories of the ions inside and around the diagnostic. Hence, recommended practices are given to select these biasing voltage in order to be able to measure the angular distribution of ion current density in the plasma plume of the ECR thruster.

### 4.3 Angular distribution of ion current density measured in plasma regime

#### 4.3.1 Recommended practices for the directional Faraday cup collectors biasing

Results presented so far show that the angular selectivity of the directional Faraday cup is well understood in the ideal regime. However, this diagnostic is intended to be used to measure the ion current density in the plume of electric propulsion devices, especially the one of the ECR thruster which is constituted of electrons with an energy of hundreds of eV. In plasma regime, the current measured can be altered in several ways. First, electrons are collected if the probe is not biased at a sufficiently low voltage. In this case, the current measured is reduced and the ion current density is underestimated. To determine which bias voltage to chose in order to measure only the ion current in the plasma produced by the ECR thruster, the directional Faraday cup is placed facing the thruster at a distance of 22 cm from the thruster backplate. The plate and the cylinder bias voltages are swept from -600 V to +100 V and the current is measured in cup mode. For this experiment, the plate and the cylinder have the same bias voltage  $V_b$  and the opening ring is grounded. These two choices are addressed later in the section. The variation of the current collected in cup mode with the bias voltage of the collectors is called I-V curve (figure 4.8). The region at high negative voltage, i.e. at values of  $V_b$  lower than  $\approx -350$  V on the figure, is called the ion saturation region. In this region, the bias voltage is

sufficiently low to repel all of the electrons and the current collected by the cup is called the ion saturation current. The ion saturation current increases when the bias voltage decreases due to the expansion of a plasma sheath that forms in front of the probe. This evolution is fitted by a linear function (red dashed line in figure 4.8). The objective of this section is to define a value of a bias voltage, denoted by  $V_b^{IS}$ , for which the current measured is the ion saturation current with a limited effect of the sheath expansion. In the remaining of the section,  $V_b^{IS}$  is defined in a systematic way as the bias voltage for which the current collected by the cup is 2% lower than the current obtained by the linear fit of the ion current in the saturation region.

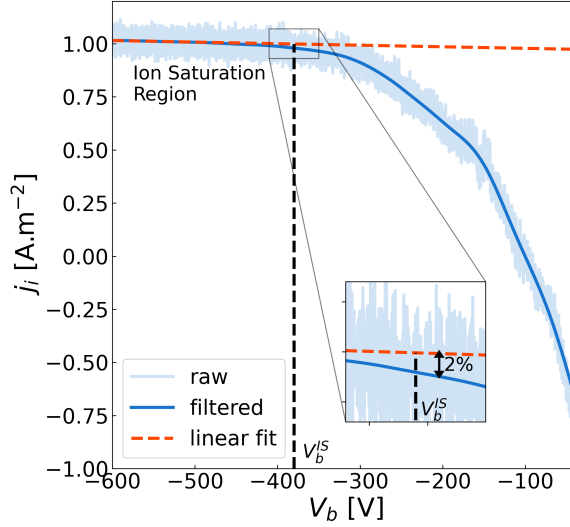


Figure 4.8: I-V curve with the directional Faraday cup in front of the ECR thruster firing at 1 sccm and 30 W.

The ion saturation bias voltage  $V_b^{IS}$  is extracted from the I-V curves measured at several thruster mass flow rates between 0.85 sccm and 2.2 sccm and microwave powers between 20 W and 60 W (figure 4.9a). This range of parameters covers the major part of operating conditions accessible to the ECR thruster. Results show that  $V_b^{IS}$  decreases with both the thruster power and the thruster mass flow rate. The numerical values of  $V_b^{IS}$  measured for the different thruster operating conditions of mass flow rate and power are recalled in the table B.1 of appendix B. They constitute a set of recommended values of bias voltages of the directional Faraday cup for precise measurements of the ion current density. It is worth mentioning that in the case of the plasma produced by the ECR thruster,  $V_b^{IS}$  is low compared to other electric propulsion devices. This is due to the presence of electrons with a great electron temperature  $T_e$  of the order of several tens of eV, as estimated in chapter 3.

In the experiments presented in the remaining of the manuscript, the ion current density is either measured at various mass flow rates with a fixed thruster power of 30 W or at various powers at a fixed mass flow rate of 1 sccm. For the sake of simplicity, and in order to avoid to change the bias voltage of the directional Faraday cup for each different thruster operating condition, the biasing voltage of the collectors of the cup are fixed to  $V_b = -350$  V, except for powers greater than 35 W, for which they are biased at  $V_b = -500$  V. The error associated to the measurement of the ion current density at this value of bias voltage, compared to the current measured when the collectors are biased at  $V_b^{IS}$ , is lower than 4% (figure 4.9b). This

error is acceptable and its low value is due to the nearly flat ion saturation region, attributed to the cup shape of the diagnostic. Thus, with the directional Faraday cup, choosing a bias voltage 50 V greater or lower than  $V_b^{IS}$  is not necessarily a problem to measure an accurate ion current. It is worth mentioning that with a flat probe, such as the Faraday probe with guard ring presented in the experimental apparatus, the sheath size in front of the collector can become greater than the collector size at very low bias voltage, increasing the current measured by the probe. This point is dealt with in chapter 6.

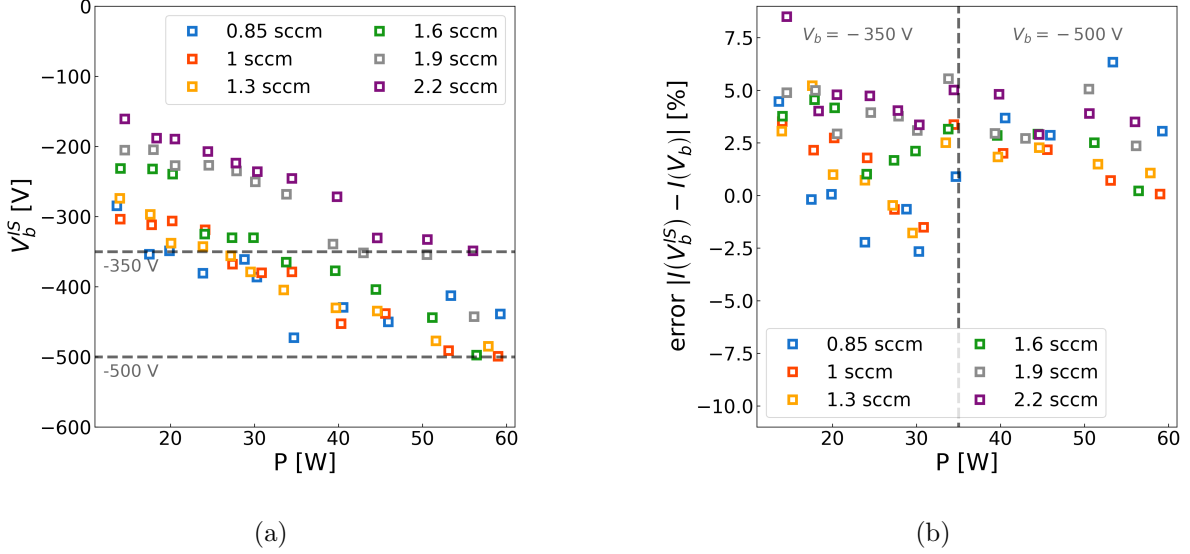


Figure 4.9: (a) Evolution of  $V_b^{IS}$  with the thruster power for several mass flow rates and (b) error on the measurement of the ion current density if the probe collectors are biased at  $V_b = -350$  V if  $P \leq 35$  W or  $V_b = -500$  V if  $P \geq 35$  W compared to a bias voltage of  $V_b^{IS}$ .

The values of  $V_b^{IS}$  presented above are determined from I-V curves measured with the directional Faraday cup placed in the axis of the thruster. The fact that the value of bias voltage  $V_b$  is kept constant when the position of the cup is swept in front of the thruster away from the axis should not induce a modification of the current measured. In fact, it is shown in Ref. [71] that the plasma potential increases off axis. Moreover, in chapter 3, results show that a constant electron temperature  $T_e$  in the whole plume of the thruster is a valid approximation. Hence, an I-V curve performed off axis should be shifted towards the right (positive  $V_b$ ). The fact that the slope of the linear fit of the curve in the ion saturation region is very low induces an error on the measured current which is acceptable. This point is verified in chapter 6, in which angular scans of the ion current density with the directional Faraday cup are presented and discussed.

The value of the bias voltage recommended to measure the ion current density is greater, in absolute value, than the energy of the ions in the plume of the ECR thruster. Hence, a modification of the ion trajectories due to the high gradient of electric field can occur inside and around the cup, modifying the Acceptance and Opening functions defined in the previous section. This effect is investigated in the subsection below, with simulations performed with the software SIMION, and with  $\alpha$ -scans of ion current density performed with the directional Faraday cup in the plume of the ECR thruster.

### 4.3.2 Modification of the Acceptance and Opening functions in plasma regime

The objective of this section is to investigate the influence of the biasing voltage of the different parts of the directional Faraday cup on the signal measured during an  $\alpha$ -scan. To this end, the Acceptance of the probe is simulated with the software SIMION under different configurations of biasing voltage. In order to make a link between a modification of the Acceptance function of the cup and the signal measured by the cup during an  $\alpha$ -scan, and therefore allow for the comparison between simulations and experiments, a one-dimensional model is developed as follows. At a given position in the plume of the ECR thruster, defined by the cylindrical coordinates  $(\rho, \theta)$ , the ion current density is supposed to be distributed following an arbitrary angular distribution, denoted by  $\Psi$  (see figure 4.10 for the notations). This distribution is *a priori* a function of the angle  $\alpha$  and of the azimuthal angle  $\phi$ . However, in a one dimensional approximation, if the components of the ion velocity field projected along the local unit vectors  $\vec{e}_\rho$  and  $\vec{e}_\theta$  are significantly greater than the azimuthal component of the ion velocity field projected along  $\vec{e}_\phi$ , the distribution  $\Psi$  can be supposed to be a function of  $\alpha$  only. In this one dimensional approximation, the current density measured on the plate of the directional Faraday cup when it is rotated of an angle  $\alpha$  in front of the thruster at the position  $(\rho, \theta)$ , denoted by  $j_{i|\rho,\theta}(\alpha)$ , accounts for the whole distribution of ion flux direction and the proportion of the flux collected on the plate of the cup. It is then the convolution between the  $\mathcal{A}$  and  $\Psi$  which reads :

$$\begin{aligned} j_{i|\rho,\theta}(\alpha) &= \int_{-\frac{\pi}{2}}^{\frac{\pi}{2}} \Psi(\beta) \mathcal{A}(\beta - \alpha) d\beta \\ &= [\Psi * \mathcal{A}] (\alpha) \end{aligned} \quad (4.6)$$

This formulation is too simple to get quantitative results because it assumes that the function  $\mathcal{A}$  is not modified by the plasma, which is not necessarily the case, as shown below in the section. Nevertheless, it shows that a wider or greater Acceptance translates into respectively a wider or greater current  $j_{i|\rho,\theta}(\alpha)$  measured on the plate of the directional Faraday cup during an  $\alpha$ -scan. This link is used in the remaining of this section to compare simulations of the Acceptance function and experimental measurements.

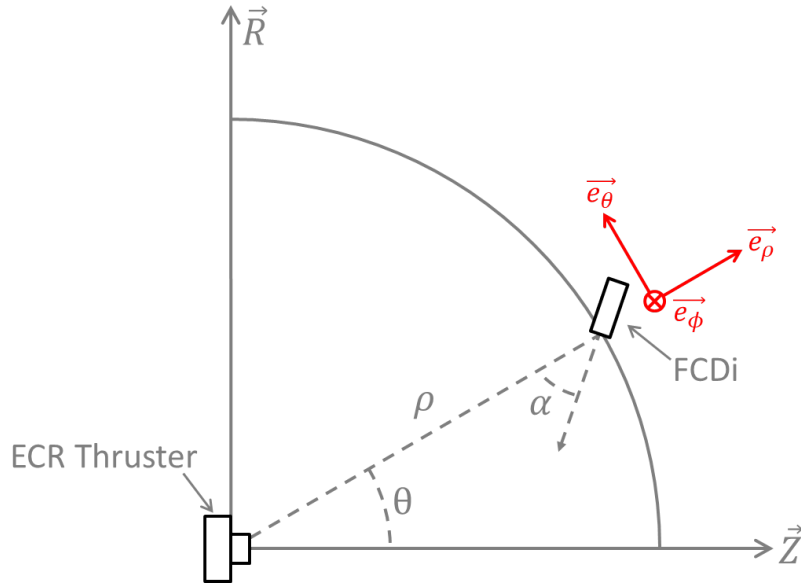


Figure 4.10: Schematic of the directional Faraday cup in front of the ECR thruster.

It is shown in the previous section that the bias voltage of the collectors of the directional Faraday cup must be relatively low to measure the ion saturation current. Hence, it can be the source of electric fields inside and outside the cup which modify the trajectory of the ions, i.e. which modify the Acceptance and Opening functions. Two effects should be considered. On the one hand, if the ion trajectories are bent inside the probe, the Acceptance function is modified but the current collected in cup mode is unaffected. On the other hand, if there is a plasma sheath in front of the cup whose thickness is not negligible compared to the probe dimensions, particle trajectories are likely to be bent in front of the probe with a modification of the Acceptance and Opening functions affecting the current collected in plate and cup mode.

### Modification of the ion trajectories inside the cup

First, to simulate the effect of different bias voltages of the collectors on the Acceptance function, the bias voltage of the plate is set to  $V_b^{plate} = -300$  V and the bias voltage of the cylinder is set to  $V_b^{cyl} = 0$  V (figure 4.11). In this case, an electrostatic lens appears at the bottom of the cup and bends the trajectories of the particles inside the cup. In fact, ions that would be collected by the cylinder in ideal regime are collected by the plate, resulting in a widening of the Acceptance function. Therefore, a good practice to discard this unwanted effect is to always bias the cylinder and the plate at the same voltage.

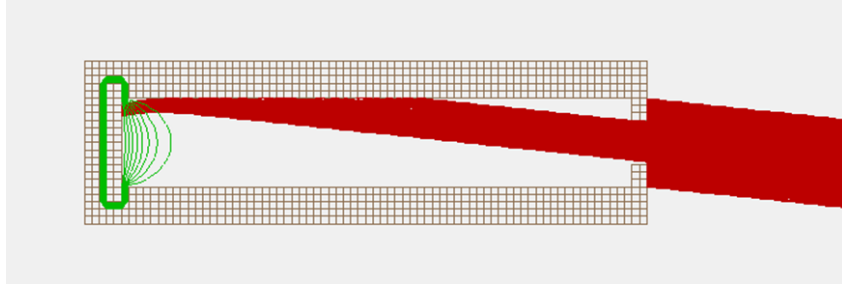


Figure 4.11: Simulation of the directional Faraday cup with a different bias voltages of the collectors. The plate is biased at  $V_b^{plate} = -300$  V, the cylinder is biased at  $V_b^{cyl} = 0$  V and the opening ring is biased at  $V_b^{ring} = 0$  V.

### Modification of the ion trajectories outside the cup

The other effect that might change the Acceptance and Opening functions of the directional Faraday cup is the modification of the ion trajectories outside of the cup before they hit a collector. To illustrate this effect, the directional Faraday cup is simulated with the plate, the cylinder and the ring biased at  $V_b = -300$  V (figure 4.12). No plasma sheath is considered here, and the particles are subject to the electrostatic field induced by the bias voltage of the opening ring. When the bias voltage of the ring is  $V_b = -300$  V, a large electrostatic lens appears and focuses the ion beam upstream the entrance of the cup. In order to study the consequence of this modification of ion trajectory which occurs outside the cup, the Acceptance of the directional Faraday cup is simulated for different values of the bias voltage of the ring  $V_b^{ring}$  comprised between 0 and -300 V (figure 4.13). The procedure used to simulate the Acceptance function is the same to that used previously in section 4.2.2. Results confirm that the more negatively biased the opening ring, the greater the Acceptance function for low incidence angle  $\alpha$ . Moreover, the fact that the Acceptance becomes greater than 1 signifies that there is an excess of ions entering the cup. According the one dimensional model discussed above and equation 4.6, an Acceptance greater than 1 translates into an overestimation of ion current density measured by the cup.

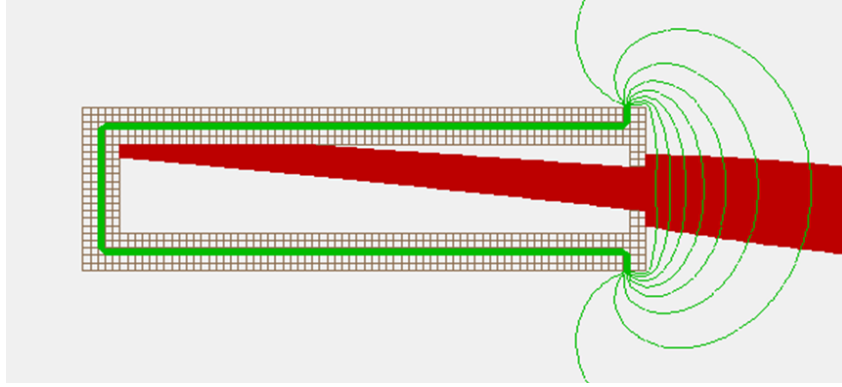


Figure 4.12: Simulation of the directional Faraday cup with the plate, the cylinder and the ring biased at  $V_b = -300$  V. No sheath is simulated.

For all simulation cases, the fact that the bias voltage of the plate and the cylinder is  $V_b^{plate} = V_b^{cyl} = -300$  V induces the presence of a small electrostatic lens inside the cup, just downstream the opening. This lense is too weak to be observed in figure 4.12, it has however the effect of a slight widening of the Acceptance function of the cup. This effect can be observed in figure 4.13 in the comparison between the theoretical Acceptance of the directional Faraday cup and the case  $V_b^{ring} = 0$  V (black and blue solid lines respectively). In fact, for this biasing condition, there is no large electrostatic lens outside the cup. This point is further discussed below when the plasma sheath that forms in front of the opening is taken into account in the simulations.

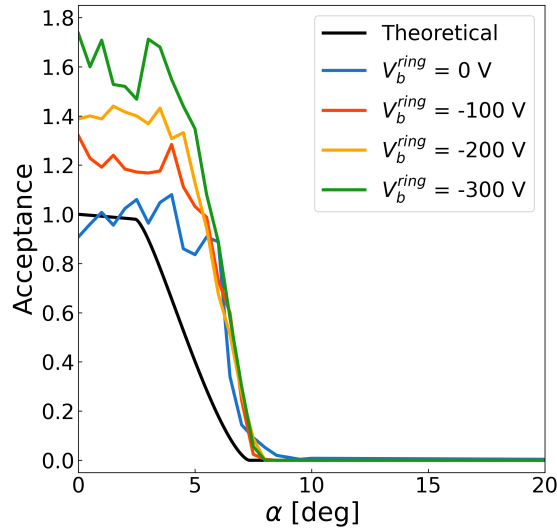


Figure 4.13: Simulation of the Acceptance function for several values of  $V_b^{ring}$  with  $V_b^{plate} = V_b^{cyl} = -300$  V. No sheath is simulated.

The results presented above show that the software SIMION can be used to simulate the modification of the Acceptance function of the directional Faraday cup under different configurations of collectors biasing voltage. However, this software is only intended to simulate the trajectories of charged particles in potential arrays, and a plasma sheath that forms in front of a surface cannot be simulated. In fact, the effect of the large electrostatic lens observed in front of the cup in figure 4.12 will be limited by the presence of a plasma sheath in the experiments. To tackle the software limitation, a grid, fully transparent to the simulated particles, with a potential fixed at 0 V, is set around the probe in order to mimic the effect of a plasma sheath. This simulation trick allows to ensure that the potential fall in front of the cup occurs in a few probe opening radius. The distance between the grid and the probe can be adjusted to simulate different sheath thicknesses.

### Effect of the plasma sheath on the Acceptance and Opening functions

A different behaviour is observed when a transparent grid biased at 0 V surrounds the cup. Two different cases are represented to illustrate the influence of the bias voltage of the ring on the Acceptance function when the sheath is simulated. First, if the ring is biased at  $V_b^{ring} = -300$  V, an electrostatic lens appears at the entrance of the cup and diffracts the ion beam inside the cup (figure 4.14a). This effect has no incidence on the current collected in cup mode because the quantity of ions entering the cup is not affected by this electrostatic lens. However, it has a strong influence on the Acceptance of the diagnostic, i.e. the angular selectivity of the cup. Conversely, if the ring is biased at  $V_b^{ring} = 0$  V, the effect on the Acceptance is limited because the burst of the ion beam inside the cup is reduced. This configuration seems to be the best way to measure a correct ion current in cup mode while keeping the angular selectivity of the diagnostic.

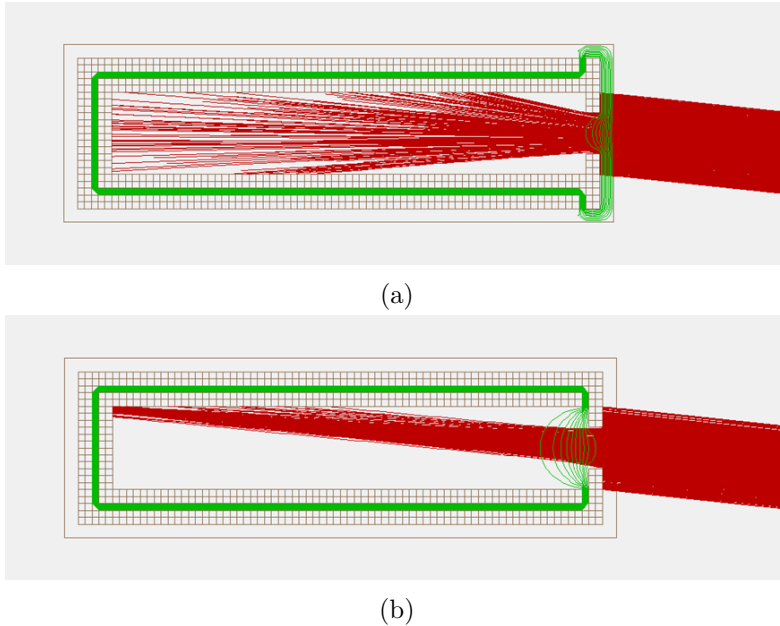


Figure 4.14: Simulation of the directional Faraday cup with the plate and the cylinder biased  $V_b^{plate} = V_b^{cyl} = -300$  V and the ring is biased at (a)  $V_b^{ring} = -300$  V and (b)  $V_b^{ring} = 0$  V.

The two figures above show the importance of selecting the good bias voltage of the ring of the directional Faraday cup in order to keep its property of directionality and not overestimate the ion current. To verify the influence of the bias voltage of the ring, the Acceptance of the directional Faraday cup is simulated for different ring bias voltages with the plate and cylinder biased at  $-300\text{ V}$  (figure 4.15a). The transparent grid biased at  $0\text{ V}$  is placed in front of the probe entrance at a distance equal to the opening radius, i.e.  $1.5\text{ mm}$ . This distance is chosen because the Debye length in the plume of the ECR thruster is of the order of  $1\text{ mm}$ . Results show that, as expected, the more negatively biased the ring, the wider and lower the Acceptance because the burst of the beam inside the probe is more pronounced when the ring bias voltage is more negative.

### Comparison of the simulations with experiments

To verify these simulation outcomes,  $\alpha$ -scans of ion current density are performed in front of the ECR thruster  $30\text{ cm}$  away from the thruster backplate. The operating condition of the ECR thruster is  $1\text{ sccm}$  and  $30\text{ W}$ . The opening ring of the directional Faraday cup is biased at various negative voltages between  $0$  and  $-300\text{ V}$ , as done in the simulations and the bias voltage of the plate and the cylinder is fixed to  $V_b = -350\text{ V}$ . The ion current density is also measured with a Faraday probe with guard ring (introduced in the experimental apparatus in section 2.2.3) at the same location with normal incidence of the ECR thruster ( $\alpha = 0$ ) (figure 4.16). The comparison between the simulations and the  $\alpha$ -scans can only be qualitative because, in the simulations, the position of the transparent grid that simulates the plasma sheath is arbitrarily chosen to one opening radius. Nevertheless, the shape of the simulated Acceptance and the measurements of ion current density are similar. In fact, as observed in the simulations, when the biasing voltage of the opening ring is getting more negative and closer than the plate and cylinder biasing, the current measured on the plate decreases in the centre of the  $\alpha$ -scan ( $\alpha = 0$ ) and widens on the sides ( $\alpha \geq 20$ ). This result is in line with the burst of the ion beam observed on figure 4.14a and with the wider Acceptance function shown in figure 4.15a when  $V_b^{ring} = -300\text{ V}$ .

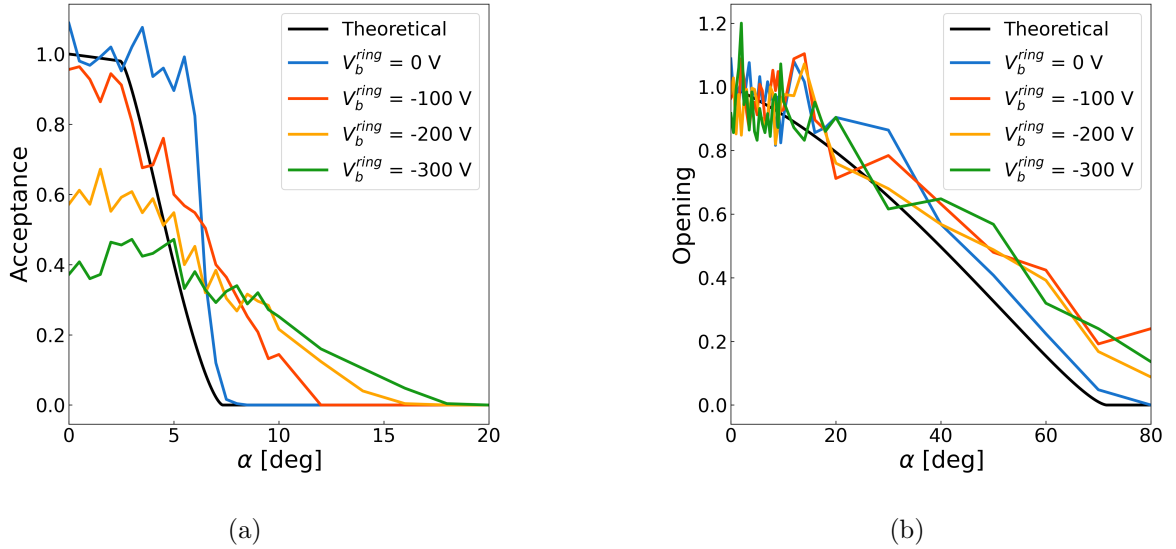


Figure 4.15: Simulation of (a) the Acceptance function and (b) the Opening function for several values of  $V_b^{ring}$  with  $V_b^{plate} = V_b^{cyl} = -300\text{ V}$ .

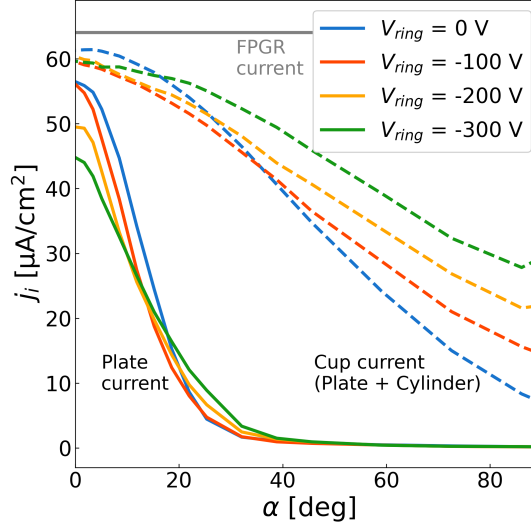


Figure 4.16:  $\alpha$ -scans performed with the directional Faraday cup for several values of  $V_b^{ring}$  with  $V_b^{plate} = V_b^{cyl} = -350V$  in front of the ECR thruster. The grey solid line is the current collected by a Faraday probe with guard ring facing the thruster.

These measurements do not insure that the Acceptance function has remained unperturbed when going from the ideal case to the plasma case but allow to select the operation regime of the directional Faraday cup which limits an eventual perturbation. Besides, the cup current, i.e. sum of the plate and cylinder currents, remains constant at the centre of the scan ( $\alpha = 0$ ) for every ring bias voltages. It confirms the fact that particle deflections induced by the biasing of the opening ring mainly occur inside the probe. On the contrary, the cup current increases at high  $\alpha$  angles (about  $30^\circ$  and above) when the ring biasing voltage decreases. This is believed to be due to an ion deflection towards the probe at high approaching angles. Finally, the current collected by the Faraday probe with guard ring biased at  $-350V$  and placed in front of the thruster exit (grey solid line labelled FPGR in figure 4.16) is larger than the directional Faraday cup current in cup mode at  $\alpha = 0$ . This point is dealt with in chapter 6.

The results presented in this section show that the property of the directional Faraday cup to select the ions collected according to their angle with respect to the cup axis is sufficiently well understood when the diagnostic is immersed in the plasma plume of the ECR thruster. However, it cannot be confirmed that the biasing of the probe inside the plasma does not induce a widening of the Acceptance function. Hence, only qualitative ion angular distribution functions can be assessed. A comparison with other diagnostics, such as the two dimensional LIF or the tomographic LIF presented in Ref. [27], could be used to challenge the accuracy of the ion flux angular distribution function given by the directional Faraday cup.

The property of angular selection of ion flux collection is used in chapter 5 to measure the local direction of the ion trajectories and study the detachment of the ions from the magnetic nozzle of the ECR thruster. Then, in chapter 6, the directional Faraday cup is used in cup mode to estimate the thrust of the ECR thruster.

## Conclusion

The results presented in this chapter confirm that the directional Faraday cup is sufficiently directional to be used to retrieve qualitatively the local angular distribution of ion current density in the plume of the ECR thruster. In a first part, in section 4.2, this property of directionality is defined theoretically and confirmed by simulations and experimental measurements in front of an ion source. In a second part, the effect of the immersion of the directional Faraday cup in the plasma plume of the ECR thruster is investigated. First it is found that the plate and the cylinder should be biased at the same voltage and sufficiently negatively to insure the collection of the ion saturation current, i.e. at -350 V (-500 V at high thruster power). However, the high negative bias voltage of the collectors of the cup may induce a perturbation of the ion trajectories inside and outside the cup, resulting in a modified Acceptance function of the diagnostic. To limit this perturbation, the ring should be kept close to 0 V, it is therefore tight to ground in the remaining of this manuscript.

Besides, the results presented so far do not confirm that the level of current measured by this diagnostic is effectively the correct value of ion current density. In order to verify this point, in chapter 6, the thrust estimated from an angular scan of ion current density is compared with a direct measurement of the thrust performed with a thrust balance.

In order to be able to compare the simulations of the Acceptance function with  $\alpha$ -scans of ion current density, the analysis relies on the assumption of an angular distribution of ion flux direction. A one dimensional model presented in section 4.3.2 neglects the distribution of ion flux direction along the azimuthal direction. The validity of this assumption is justified by the good agreement between the evolution of the Acceptance simulated for different values of ring bias voltage and the  $\alpha$ -scans performed with the same values of bias voltage. Nevertheless, in order to get a complete description of the angular distribution of ion flux in the plume of the ECR thruster, measurements could be performed with optical diagnostics such as the LIF-tomography setup presented in [27] for example.



## 5 | Experimental characterisation of the ion detachment from the magnetic nozzle of the ECR thruster

**Motivation and objectives:** The understanding of the physics at stake in the detachment of the plasma from the magnetic nozzle has an interest for the technological development of the ECR thruster. In fact, the comprehension of the plasma parameters that influence this process would allow the optimisation of the plasma acceleration and the reduction of the divergence of the exhausted matter. Moreover, the study of the plasma detachment would allow to design new magnetic topologies favourable to a directed and efficient ejection of plasma, increasing the performances and the efficiency of the device.

Results presented in chapter 3 show that in a region close to the source of the ECR thruster, the acceleration of the ions can be described by a model in which the plasma follows the magnetic field lines of the magnetic nozzle. However, due to the lack of fluorescence signal at low plasma densities, the Laser Induced Fluorescence diagnostic cannot be used to gather data farther than 20 cm away from the thruster exit to study the detachment of the ions from the magnetic nozzle. To address this problem, the directional Faraday cup has been developed and is presented in chapter 4. This diagnostic allows to measure locally, and farther than 20 cm away from the thruster backplate, the angular distribution of the ion current density. Thus, it allows to capture the local direction of the ion flux. The objective of this chapter is to present how this property of the directional Faraday cup is used to observe and characterise the detachment of the ions from the magnetic nozzle of the ECR thruster. In a first part, the experiment that enables the observation of the ion detachment is presented with the uncertainties associated. In a second part, the operating conditions of the thruster are varied in order to assess their influence on the detachment. Experiments are performed for different microwave powers, mass flow rates, vacuum conditions and magnetic topologies. Finally, a model is developed to discuss the physical mechanisms that lead to the detachment of the ions from the magnetic nozzle of the ECR thruster.

**Main results:** The first section of this chapter shows how the mean local trajectory of the ion flux is retrieved from an angular scan of ion current density performed with the directional Faraday cup in the plume of the ECR thruster. The comparison of this measured trajectory with the local direction of the magnetic field lines shows that the ions are attached at the centre of the plume and detached at the edges of the plume, i.e. for angular locations greater than an angle denoted by  $\theta_{det}$ . In the magnetic coordinate system, the variation of  $\theta_{det}$  with the distance from the thruster is fitted with an exponential function. The prolongation of this fit shows that far from the thruster, at a distance of 0.72 m in the case of the magnetic topology  $M_1$ , the ions are eventually completely detached from the magnetic nozzle.

The comparison of the location of the ion detachment for different operating conditions of the thruster in mass flow rate, microwave power, magnetic nozzle topology and for two vacuum conditions of the vacuum facility shows that the location of the plasma detachment depends very little on these conditions. However, a strong influence of the conditions on the trajectory of the ions that are already detached from the magnetic field lines is observed.

The analysis of the measured ion trajectories and the prolongation of the trajectories of the detached ions show that, once detached, the ions follow a straight line trajectory which is not affected by the magnetic field anymore. This result, added to the fact that the thruster operating condition has an influence on the trajectory of the detached ions can be explained by a theory of diverging detachment, with an angle of detachment that increases with an increase of the mass flow rate of the thruster or an increase of the pressure inside the vacuum facility. In this case, diverging means that the ion trajectories at the location of the detachment are more diverging than the local direction of the magnetic field lines. However, considering the global divergence of the magnetic nozzle and the fact that detached ions have a straight line trajectory, the trajectory of the ions can be observed to be more converging than the magnetic field trajectory, especially at larger distances to the source of the thruster.

Finally, a two ion population model is developed to explain the asymmetry, or skewness, of the ion current density signal measured on the plate of the directional Faraday probe during a rotation of this diagnostic at a given position in the plume of the ECR thruster. Results are in line with a diverging theory of ion detachment. However, they do not allow to conclude on the physical origin of the detachment of the ions in the diverging magnetic nozzle of the ECR thruster.

## 5.1 Measurement of the plasma detachment location

### 5.1.1 Description of the experiment

The property of the directional Faraday cup to capture locally the angular distribution of ion current density described in chapter 4 is used to study the detachment of the ions from the magnetic nozzle of the ECR thruster. The experiment presented in this chapter consists in measuring the local ion direction at several positions in the plume of the thruster and compare it to the local direction of the magnetic field lines to assess if the ion trajectories are driven by the magnetic nozzle or not. In order to provide a complete characterisation of the ion detachment, this experiment is performed for several operating conditions of the thruster: microwave power, mass flow rate, vacuum condition and magnetic topology. It is conducted as follows. The directional Faraday cup is mounted on a stepper motor at the extremity of an arm of 20 cm in length. The other extremity of this arm is fixed to a translation stage which is placed on top of a rotation stage (figure 5.1). Therefore, this configuration allows to perform measurements with the cup at different angular positions  $\theta$  and different distances  $\rho$  from the backplate of the thruster, where the position  $\theta = 0$  corresponds to a measurement made in the axis of the thruster. Measurements are performed for distances  $\rho \in [20, 60]$  cm and, because of the walls of the vacuum facility, the accessible angular positions are restricted depending on  $\rho$ . For  $\rho = 20$  cm, the whole range  $\theta \in [-90, 90]$  degrees is accessible but for  $\rho = 60$  cm, accessible angular positions are restricted to  $\theta \in [-30, 30]$  degrees.

For each  $(\rho, \theta)$  position, the ion current density is measured on the plate and the cylinder of the directional Faraday cup during its rotation around  $\alpha \in [-90, 90]$  degree, where the angle  $\alpha = 0$  corresponds to the position for which the probe faces the thruster. Each measurement

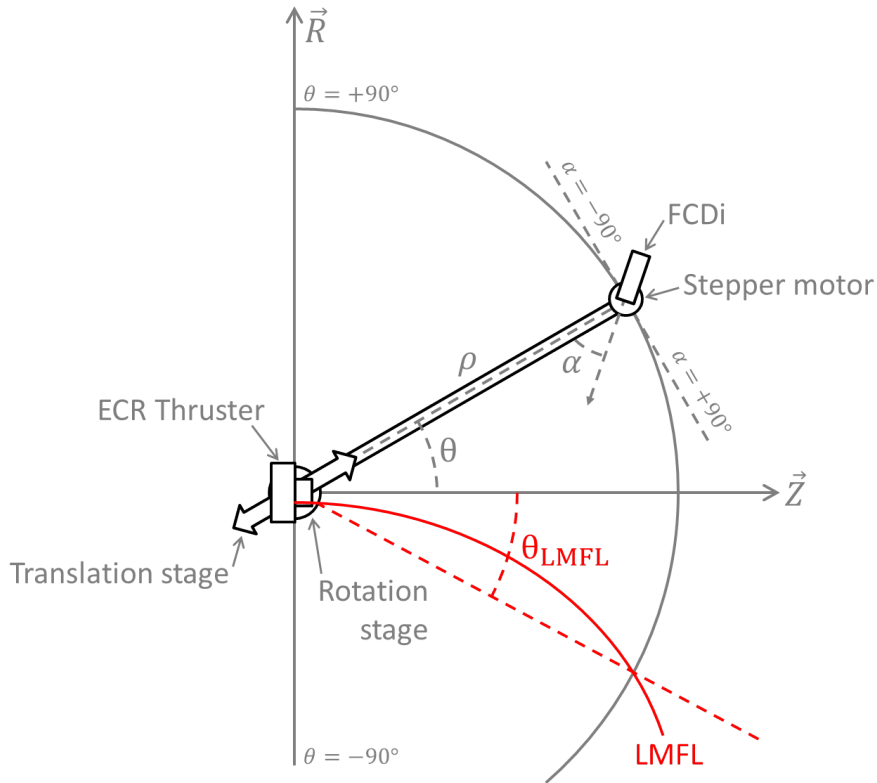


Figure 5.1: Experimental setup used to characterise the ion detachment.

is performed with the probe going clockwise from  $\alpha = -90$  deg to  $\alpha = +90$  deg and returning counterclockwise to  $\alpha = -90$  deg with a stepper motor rotation speed of 28.125 deg/s and an acquisition frequency  $f_s = 939$  Hz. Such measurement is referred to as an  $\alpha$ -scan in the remaining of the manuscript. First, in order to observe the behaviour of the plasma in the magnetic nozzle of the ECR thruster, a collection of  $\alpha$ -scans performed for several accessible angular positions  $\theta$ , called  $(\alpha\theta)$ -map and performed at different distances  $\rho$  is constituted. Then, in order to evaluate the influence of the operating conditions of the thruster on the signals acquired,  $(\alpha\theta)$ -maps are measured for several thruster microwave powers between 22 W and 50 W, several xenon mass flow rates between 0.75 sccm and 1.75 sccm and two different vacuum conditions. Finally, the experiment is performed for two different magnetic topologies. Otherwise mentioned, the thruster is firing at 1 sccm of xenon mass flow rate, 30 W of microwave power with the magnetic topology  $M_1$  and the vacuum condition  $V_1$  defined in chapter 2. The different parts constituting the directional Faraday cup are biased according to the practices recommended in chapter 4.

The method presented above is referred to as continuous  $\alpha$ -scan and is used for distances  $\rho \in [21.5, 41.5]$  cm. However, in order to maximise the acquisition signal, an other method of acquisition, called discrete  $\alpha$ -scan, is used for distances  $\rho \in [40, 60]$  cm. In this case, the acquisition is no longer continuous during the rotation of the probe, the current is acquired during 3 seconds for a discrete collection of  $\alpha$  positions. This method increases the quality of the  $\alpha$ -scans for the post processing of the data with an increase of the signal to noise ratio but it reduces significantly the resolution in  $\alpha$ . Therefore, it is used only for the thruster operating condition 1 sccm, 30 W with the magnetic topology  $M_1$  in order to constitute an extended dataset for this condition.

### 5.1.2 Assessment of the local ion trajectory

The signal acquired on the plate of the directional Faraday cup during a continuous  $\alpha$ -scan shows a narrow peak (figure 5.2). Due to the angular selectivity of this diagnostic (see chapter 4), the position of the centre of the peak corresponds to the local most probable direction of the ion flux. In the remaining of the manuscript, this angle, taken relatively to the radial trajectory, is denoted by  $\alpha_i$ . To begin with, the signal presents a slight asymmetry that can induce a systematic error when evaluating the position of the centre of the peak. Therefore, only the part of the signal above a threshold of half the value of the maximum of the peak (represented in dark blue in figure 5.2) is treated to find  $\alpha_i$ . The asymmetry of the  $\alpha$ -scans is discussed in section 5.3.3. Several quantities are good candidates to evaluate  $\alpha_i$ . First, the position of the maximum of the peak, denoted by  $\alpha_{max}$  is a good first approximation of  $\alpha_i$ , it captures the very peak of the signal. However, due to the noise of the signal, an error can arise. Therefore, the directional Faraday cup signal is smoothed with a low-pass filter (Savitzky–Golay filter : 501 points, order 3) before determining  $\alpha_{max}$ . Second, the median value of the signal, denoted by  $\alpha_{med}$ , is an other way to approximate  $\alpha_i$ . This quantity slightly differs from  $\alpha_{max}$  because it is as much influenced by the top part of the signal than by the lower part, and therefore better takes into account the general shape of the signal. Third, the weighted arithmetic mean of the signal, denoted by  $\alpha_{avg}$  allows to take into account the whole part of the signal above the threshold, pondered by its amplitude. Therefore, it seems to give the best estimate of  $\alpha_i$ . Thus,  $\alpha_i = \alpha_{avg}$  is retained in the remaining of the manuscript, and the error associated, denoted by  $\Delta\alpha_i$ , is taken equal to the standard deviation of  $\alpha_{avg}$ ,  $\alpha_{med}$  and  $\alpha_{max}$ . It reads:

$$\Delta\alpha_i = \sqrt{\frac{1}{3} \left( (\alpha_{avg} - \bar{\alpha})^2 + (\alpha_{med} - \bar{\alpha})^2 + (\alpha_{max} - \bar{\alpha})^2 \right)} \quad (5.1)$$

where  $\bar{\alpha} = \frac{1}{3} (\alpha_{avg} + \alpha_{med} + \alpha_{max})$ .

In the example shown in figure 5.2a, the error is  $\Delta\alpha_i = 0.674$  deg. This uncertainty is only relative to the methodology to evaluate  $\alpha_i$ , it does not take into account a misalignment of the cup or the position stages used in the experimental setup.  $\Delta\alpha_i$  ranges from 0.1 deg to 1.6 deg, and increases with the angular position  $\theta$  and the distance from the thruster  $\rho$ . In fact, the current measured by the directional Faraday cup is lower in these cases, with a lower signal to noise ratio.

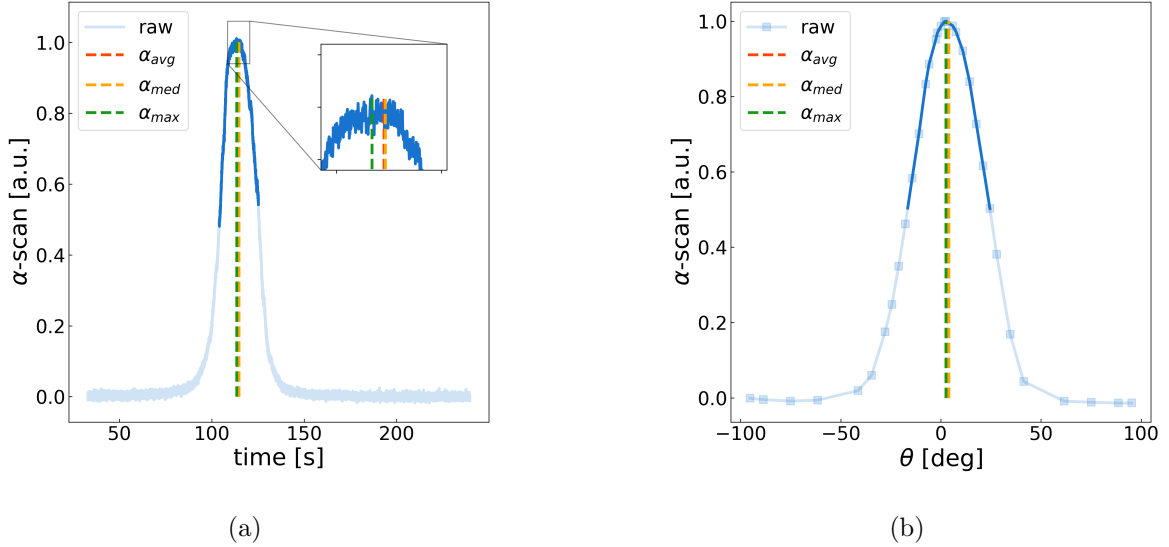


Figure 5.2:  $\alpha$ -scan with (a) the continuous measurements method at the position ( $\theta = 9$  deg,  $\rho = 31.5$  cm) and (b) the discrete measurements method at the position ( $\theta = 2.5$  deg,  $\rho = 44$  cm).

In the case of discrete measurements of ion current density, the  $\alpha$  resolution is not sufficient to determine  $\alpha_i$  the way it is described above and the raw signal is linearly interpolated in this case (figure 5.2b). However, the sparsity of the data could induce a bias in the determination of  $\alpha_i$  with this method, hence the value  $\Delta\alpha_i = 2$  deg is retained in the remaining of the manuscript to take into account this source of uncertainty.

The x-axis of the continuous angular scan of ion current density (figure 5.2a) is the timeline of the scan. This time is multiplied by the stepper motor rotation speed to get the relative angular location of  $\alpha_i$ . The acquisition sequence lasts 10 seconds, and the rotation of the stepper motor starts 2.7 s after the acquisition is launched. The high reproducibility of this sequence and the fact that it is the same for the clockwise and counterclockwise rotation of the stepper motor allows to suppress the unknown offset and retrieve the absolute position of the stepper motor during its rotation.

### 5.1.3 Measurement of the local magnetic field direction

As stated in section 5.1.1, the main point of this chapter is the comparison between the local ion direction  $\alpha_i$  and the local magnetic field line direction, denoted by  $\alpha_B$ .  $\alpha_B$  is a function of the angle  $\theta$  and depends on the distance  $\rho$  from the thruster backplate. It is computed from the longitudinal and transversal components of the magnetic field,  $B_z$  and  $B_r$  respectively. Thus, for a given distance  $\rho$ , the function  $\alpha_B$  reads:

$$\alpha_B(\theta) = \arctan\left(\frac{B_r(\theta)}{B_z(\theta)}\right) - \theta \quad (5.2)$$

The function computed with equation 5.2 from the magnetic nozzle of the ECR thruster simulated with the software Comsol Mutiphysics<sup>®</sup> is denoted by  $\alpha_B^{MN}(\theta)$  in the remaining of the manuscript. In order to verify that it is effectively the local direction of the magnetic field lines, the experiment presented in section 5.1.1 is conducted with a SS495A Hall sensor mounted in place of the directional Faraday cup. This sensor is supplied with a 5 V power supply and outputs a voltage that is proportional to the strength of the magnetic field projected along the normal of its face. Contrary to the cup, the signal acquired by this sensor during an  $\alpha$ -scan can be fitted with a cosine function (figure 5.3), the position of the centre of this fit, denoted by  $\alpha_B^{mes}(\theta)$ , being the local direction of the magnetic field. To constitute a relevant dataset,  $(\alpha\theta)$ -maps of the magnetic field direction are measured at distances  $\rho=21.5$  cm,  $\rho=31.5$  cm and  $\rho=41.5$  cm for the two magnetic topologies  $M_1$  and  $M_2$ . It is worth mentioning that the local direction of the magnetic field line is known to within an offset, denoted by  $\alpha_{OFF}$ , because the absolute direction of the Hall sensor is unknown during its rotation. However, the fact that the acquisition is performed clockwise and counterclockwise allows to suppress this offset. In fact, the magnetic field direction measured during the clockwise rotation of the sensor is  $\alpha_{CW} = \alpha_{OFF} + \alpha_B^{mes}$  and the angle measured during the counterclockwise rotation of the sensor is  $\alpha_{CCW} = \alpha_{OFF} - \alpha_B^{mes}$ , where  $\alpha_B^{mes}$  is the effective direction of the magnetic field measured by the sensor. Hence, this direction is  $\alpha_B^{mes} = (\alpha_{CW} + \alpha_{CCW})/2$ .

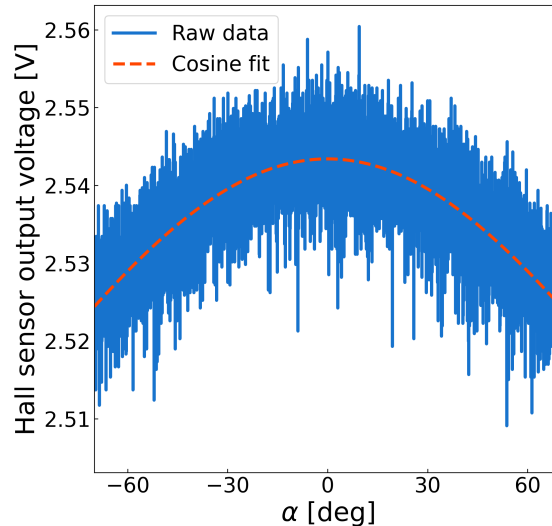


Figure 5.3:  $\alpha$ -scan with the Hall Sensor at the position ( $\theta = 0$  deg,  $\rho = 21.5$  cm). The raw data is fitted with a cosine function.

A discrepancy between  $\alpha_B^{MN}(\theta)$  and  $\alpha_B^{mes}(\theta)$  is observed (figure 5.4). It is greater for negative angular positions  $\theta$ , increases with the distance  $\rho$  and is greater for  $M_2$  than  $M_1$ . A possible explanation of this observation is the influence of the Earth magnetic field on the magnetic nozzle of the ECR thruster which is not taken into account in the computation of  $\alpha_B^{MN}$ . This field is entirely characterised by a magnitude  $B_\oplus = 0.21$  G and a direction  $\theta_\oplus = -64$  deg compared to the B09 vacuum facility. Its expression in the measurement plane defined with the two vectors  $(\vec{e}_r, \vec{e}_z)$  is expressed as follows:

$$\vec{B}_\oplus = B_\oplus \sin(\theta_\oplus) \vec{e}_r + B_\oplus \cos(\theta_\oplus) \vec{e}_z \quad (5.3)$$

The magnetic field resulting from the sum of the this external magnetic field with the magnetic field induced by the magnet of the ECR thruster is called experimental magnetic field in the remaining of the chapter and its local direction is denoted by  $\alpha_B^{exp}$ . It reads:

$$\alpha_B^{exp}(\theta) = \arctan \left( \frac{B_r(\theta) + B_\oplus \sin(\theta_\oplus)}{B_z(\theta) + B_\oplus \cos(\theta_\oplus)} \right) - \theta \quad (5.4)$$

The good agreement between the experimental and measured magnetic field directions (red dotted line and black squares respectively in figure 5.4) and their disagreement with  $\alpha_B^{MN}$  (black solid line in figure 5.4) shows that the Earth magnetic field significantly changes the shape of the magnetic nozzle, especially for larger distances from the thruster backplate. It is also observed that the discrepancy between  $\alpha_B^{MN}$  and  $\alpha_B^{exp}$  is more important for  $M_2$  than for  $M_1$  at equal distances, this is due to the fact that  $M_2$  decreases sharper with the distance to the thruster because of its greater divergence.

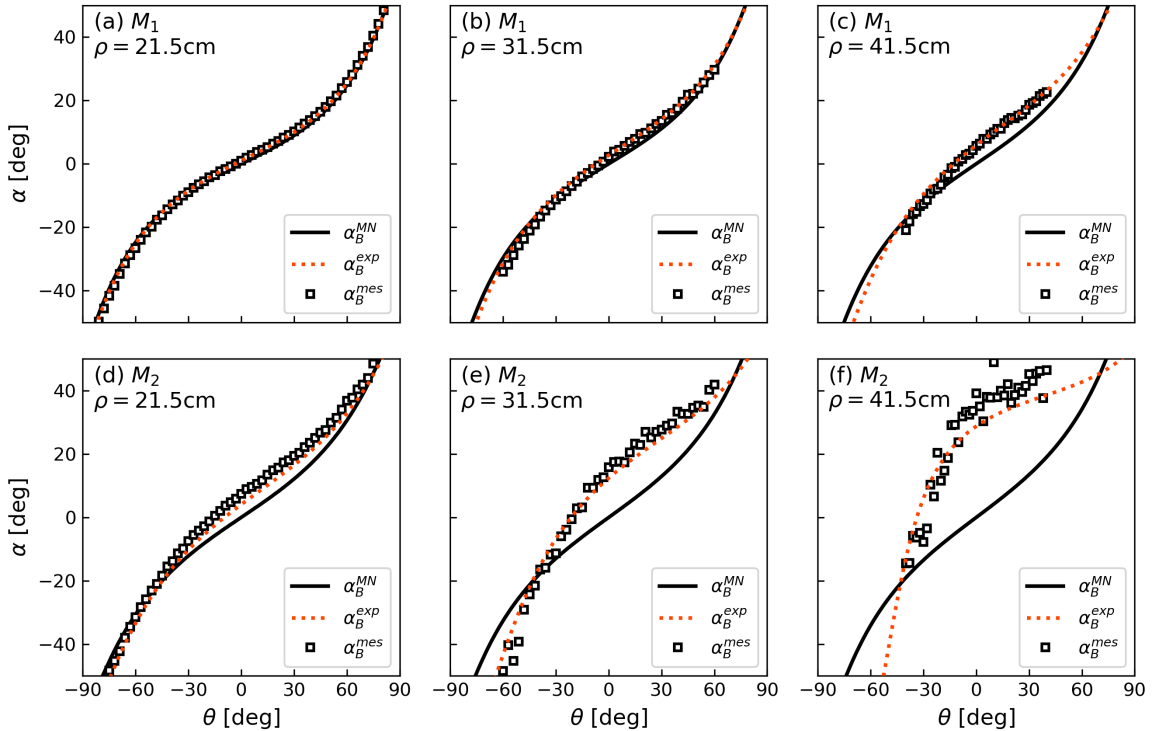


Figure 5.4:  $(\alpha\theta)$ -maps of the local magnetic field direction at distances  $\rho = 21.5$  cm,  $\rho = 31.5$  cm and  $\rho = 41.5$  cm for the magnetic topologies  $M_1$  ((a), (b) and (c)) and  $M_2$  ((d), (e) and (f)).

An other local magnetic field direction is considered in this chapter. It corresponds to a diverging magnetic nozzle equal to the sum of the magnetic nozzle produced by the magnet of the ECR thruster and the average effect of the Earth magnetic field in the azimuthal direction. In fact, if the plasma has a rotational dynamic around the axis of the thruster with a sufficiently high velocity, it would encounter this peculiar magnetic field during one rotation. This major hypothesis of a plasma in rotation in the magnetic nozzle is discussed in section 5.3. The analytical development of this peculiar magnetic field, denoted by  $\langle \vec{B} \rangle = \langle \vec{B} + \vec{B}_\oplus \rangle$  is led below, where the notation  $\langle . \rangle$  is used for the azimuthal averaging, i.e. the average along the  $\phi$  component of the cylindrical coordinate system (figure 5.5).

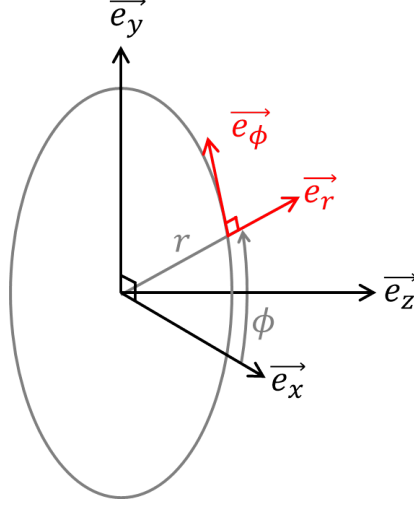


Figure 5.5: Schematic of the cartesian and cylindrical coordinate system.

First, the magnetic field produced by the permanent magnet of the ECR thruster, denoted by  $\vec{B}$ , is expressed in the cylindrical coordinate system  $(\vec{e}_r, \vec{e}_\phi, \vec{e}_z)$  :

$$\vec{B} = (B_r, 0, B_z) \quad (5.5)$$

Then, the Earth magnetic field,  $\vec{B}_\oplus$  is expressed in the cartesian coordinate  $(\vec{e}_x, \vec{e}_y, \vec{e}_z)$  with the generic notation  $\vec{B}_\oplus = B_{\oplus x} \vec{e}_x + B_{\oplus y} \vec{e}_y + B_{\oplus z} \vec{e}_z$ . The transformation  $(x, y, z) \mapsto (r, \phi, z)$  allows to write  $\vec{B}_\oplus$  in the cylindrical coordinate system as follows:

$$\vec{B}_\oplus = \begin{pmatrix} B_{\oplus x} \cos \phi + B_{\oplus y} \sin \phi \\ -B_{\oplus x} \sin \phi + B_{\oplus y} \cos \phi \\ B_{\oplus z} \end{pmatrix} \quad (5.6)$$

The field  $\langle \vec{B} \rangle$  is the average along  $\phi$  of the sum of  $\vec{B}$  and  $\vec{B}_\oplus$ . It is expressed in the cylindrical coordinate system  $(\vec{e}_r, \vec{e}_\phi, \vec{e}_z)$  as follows:

$$\langle \vec{B} \rangle = (\langle B_r \rangle, \langle B_\phi \rangle, \langle B_z \rangle) \quad (5.7)$$

The three components of  $\langle \vec{B} \rangle$  are computed as the integral over the azimuthal direction  $\phi$  of the three components of  $\vec{B} + \vec{B}_\oplus$  respectively. They read:

$$\begin{aligned} \langle B_r \rangle &= \frac{1}{2\pi} \int_0^{2\pi} (B_r + B_{\oplus x} \cos \phi + B_{\oplus y} \sin \phi) d\phi \\ &= B_r + \frac{1}{2\pi} \left( B_{\oplus x} \int_0^{2\pi} \cos \phi d\phi + B_{\oplus y} \int_0^{2\pi} \sin \phi d\phi \right) \\ &= B_r \end{aligned} \quad (5.8)$$

$$\begin{aligned} \langle B_\phi \rangle &= \frac{1}{2\pi} \int_0^{2\pi} (-B_{\oplus x} \sin \phi + B_{\oplus y} \cos \phi) d\phi \\ &= \frac{1}{2\pi} \left( -B_{\oplus x} \int_0^{2\pi} \sin \phi d\phi + B_{\oplus y} \int_0^{2\pi} \cos \phi d\phi \right) \\ &= 0 \end{aligned} \quad (5.9)$$

$$\begin{aligned} \langle B_z \rangle &= \frac{1}{2\pi} \int_0^{2\pi} (B_z + B_{\oplus z}) d\phi \\ &= B_z + B_{\oplus z} \end{aligned} \quad (5.10)$$

The analytical development led above shows that the azimuthal average of a magnetic field external to the magnetic nozzle is reduced to the consideration of only the component that it is in the axis of the magnetic nozzle. Therefore, only the longitudinal component of the Earth magnetic field modifies the resulting magnetic nozzle. The local direction of this resulting field, denoted by  $\alpha_{\langle B \rangle}$  reads :

$$\alpha_{\langle B \rangle}(\theta) = \arctan \left( \frac{B_r(\theta)}{B_z(\theta) + B_{\oplus} \cos(\theta_{\oplus})} \right) - \theta \quad (5.11)$$

The magnetic field lines of the three fields  $\vec{B}$ ,  $\overrightarrow{B + B_\oplus}$  and  $\langle \vec{B} \rangle$ , as well as the distances  $\rho = 21.5$  cm,  $\rho = 31.5$  cm and  $\rho = 41.5$  cm, are represented for both magnetic topologies  $M_1$  and  $M_2$  in the horizontal plane where ion flux measurements are realised (figure 5.6). This comparison illustrates in two dimensions the conclusions previously discussed, namely the fact that the influence of the Earth magnetic field increases with the distance to the thruster source and is more pronounced for the magnetic topology  $M_2$  at a given distance. Moreover, it shows that the field  $\langle \vec{B} \rangle$  is symmetrical around the axis  $Z$  contrary to  $\overrightarrow{B + B_\oplus}$  which takes the direction of  $\vec{B}_\oplus$  far from the thruster. Second,  $\langle \vec{B} \rangle$  is more converging than  $\vec{B}$ , this behaviour being only due to the orientation of the B09 vacuum facility compared to the Earth magnetic field direction. In fact, if the longitudinal component of  $\vec{B}_\oplus$  had been along  $-\vec{e}_z$ , the field  $\langle \vec{B} \rangle$  would have been more diverging than  $\vec{B}$ .

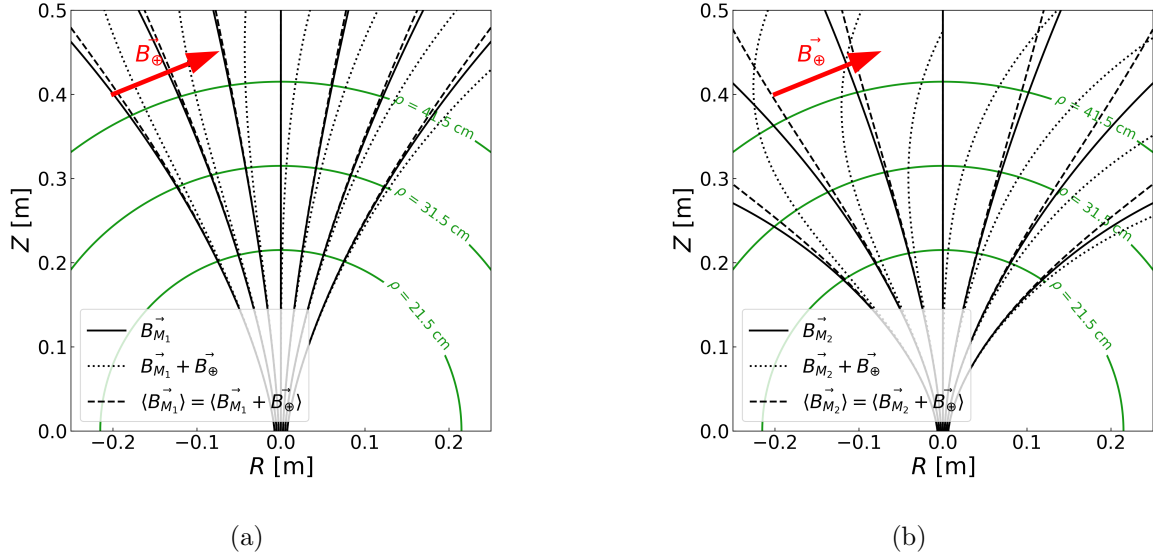


Figure 5.6: Magnetic field lines of the ECR thruster magnetic nozzle with and without the consideration of the Earth magnetic field for (a) the magnetic topology  $M_1$  and (b) for the magnetic topology  $M_2$ .

The results presented in this section show that the influence of the Earth magnetic field cannot be neglected, especially at greater distances from the thruster source and with the magnetic topology  $M_2$ . Therefore, in the remaining of the manuscript, the local direction of the ion flux is compared to the direction of the magnetic field  $\alpha_B^{MN}$ , the direction of the magnetic field corrected with the Earth magnetic field  $\alpha_B^{exp}$  and the direction of the average magnetic field  $\alpha_{\langle B \rangle}$ . The methodology used to assess the location of the ion detachment from the comparison between ion flux and magnetic field lines trajectories is the object of the next subsection.

#### 5.1.4 Methodology for assessing the ion detachment location

In order to assess if the ions are attached (or detached) to the magnetic nozzle of the ECR thruster, the local direction of the ion flux  $\alpha_i$  is compared to the direction of the magnetic field lines for each distance  $\rho$  (figure 5.7). In the remaining of the chapter, on the figures representing  $(\alpha\theta)$ -maps, the grey vertical lines correspond to the angular position  $\theta_{LMFL}$  at which the last magnetic field line crosses the arc of radius  $\rho$ . As a reminder, the last magnetic field line is the most diverging magnetic field line that does not intersect physically the source of the ECR thruster and can be seen as a limit of the magnetic nozzle (see figure 5.1). Therefore,  $|\theta| \leq \theta_{LMFL}$  correspond to angular positions inside the magnetic nozzle. The  $(\alpha\theta)$ -map represented in figure 5.7 shows that the local direction of the ions is  $\alpha_i = 0$  in the axis of the thruster, i.e. for the position  $\theta = 0$ . This observation means that the ions do not follow the magnetic field resulting from the sum of the magnetic nozzle and the Earth magnetic field. In fact, at the distance represented in the figure,  $\alpha_B^{exp}(\theta = 0) = 3.8$  degrees. Therefore  $\alpha_B^{exp}$  is no longer displayed on the next  $(\alpha\theta)$ -map presented in the remaining of the chapter.

At this distance and with the magnetic topology  $M_1$ , the difference between  $\alpha_B^{MN}$  and  $\alpha_{\langle B \rangle}$  is very low, so only  $\alpha_{\langle B \rangle}$  is considered here, this choice being justified further in the chapter. It appears that  $\alpha_i$  is equal to  $\alpha_{\langle B \rangle}$  for values of  $\theta$  around 0. This observation shows that at the centre of the plasma plume, the ions follow the magnetic field lines lines of the magnetic nozzle. Conversely, the ions are said to be detached from the magnetic nozzle when  $\alpha_i \neq \alpha_{\langle B \rangle}$ .

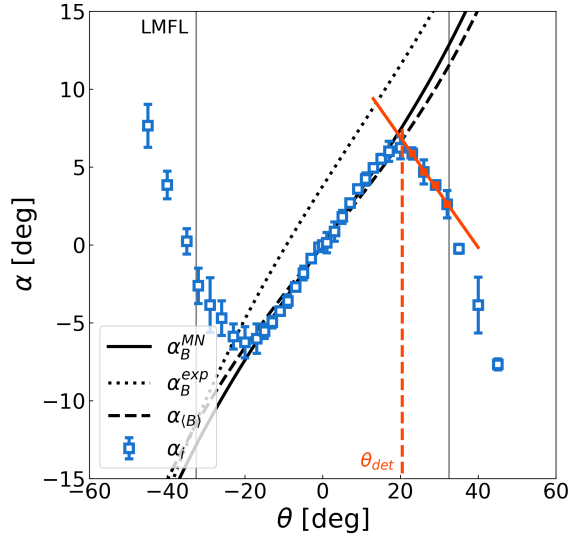


Figure 5.7:  $(\alpha\theta)$ -map of the ion flux direction at the distance  $\rho = 35.5$  cm from the thruster. The magnetic topology is  $M_1$ .

All of the  $(\alpha\theta)$ -maps show that  $\alpha_i$  is equal to  $\alpha_{(B)}$  for value of  $\theta$  around 0 and, above a certain angle  $\theta_{det}$ , this equality is no longer verified. Moreover, the fact that  $\alpha_i$  is smaller than  $\alpha_{(B)}$  for values of  $\theta > \theta_{det}$  (and conversely for  $\theta < -\theta_{det}$ ) indicates that the ion flux direction is more converging than the magnetic nozzle. This point is further discussed in section 5.3. In order to determine in a systematic way the angular position  $\theta_{det}$  at which the plasma no longer follows the magnetic field lines, the  $(\alpha\theta)$ -map are first symmetrised around  $\theta = 0$  to reduce the uncertainty due to the measurements. Then, the data points greater than a first visual estimation of  $\theta_{det}$  which are lower than  $\theta_{LMFL}$ , corresponding to the positions  $\theta \in [23, 32]$  deg in the figure, are fitted by a linear function. The angular location of the detachment  $\theta_{det}$  is defined as the intersection between this fit and  $\alpha_{(B)}$ . However,  $\theta_{det}$  comes with an uncertainty  $\Delta\theta_{det}$  which is due to the symmetrisation of the data, the uncertainty of  $\alpha_i$  and the approximation  $\alpha_B \approx \alpha_{(B)}$ . To take into account these sources of uncertainty, the value  $\Delta\theta_{det} = 1$  deg is retained for distances  $\rho \in [20, 40]$  cm for which  $\alpha$ -scans are acquired continuously and  $\Delta\theta_{det} = 2$  deg is taken for distances  $\rho \in [40, 60]$  cm, for which the  $\alpha$ -scans are discrete.

The methodology presented above shows a systematic way to infer the angular position at which the ion flux is detached from the magnetic nozzle from an  $(\alpha\theta)$ -map. The results are presented in section 5.3.1. In the next section,  $(\alpha\theta)$ -maps are presented for several thruster operating conditions in order to characterise the influence of these conditions on the behaviour of the ion flux and the location of the detachment.

## 5.2 Influence of the thruster operating conditions

The objective of this section is to observe the influence of the microwave power, the xenon mass flow rate, the vacuum condition and the magnetic topology on the ion detachment. To this end, the different conditions tested are 4 different microwave powers between 22 W and 50 W with a mass flow rate of 1 sccm at distances  $\rho = 31.5$  cm and  $\rho = 41.5$  cm, 4 different mass flow rates between 0.75 sccm and 1.75 sccm at the distance  $\rho = 31.5$  cm and two vacuum conditions for the whole range of distance  $\rho \in [21.5, 41.5]$  cm. However, for the sake of clarity, only results at distances  $\rho = 21.5$  cm,  $\rho = 31.5$  cm and  $\rho = 41.5$  cm are displayed. Unlike the results shown in the previous section,  $(\alpha\theta)$ -maps are not symmetrised to allow a proper comparison of the datasets between each other.

### 5.2.1 Variation of the microwave power

First,  $(\alpha\theta)$ -maps are obtained for several ECR thruster microwave powers with a mass flow rate of 1 sccm at distances  $\rho = 31.5$  cm (figure 5.8a) and  $\rho = 41.5$  cm (figure 5.8b). Because of the error associated to  $\alpha_i$ , it is not clear if the detachment location depends on the thruster power or not. However, the fact that for two distances separated by 10 cm, the detachment occurs approximately in the same region of the plasma plume for every thruster powers between 22 W and 50 W shows that, if the power of the thruster has an influence on the ion detachment location, it is very little. However, it has an influence on the ion trajectories once the plasma is detached from the magnetic nozzle. In fact, outside of the magnetic nozzle limit, i.e. for values of  $\theta$  satisfying  $\theta_{LMFL} \leq |\theta|$ , the ions trajectories are more diverging at higher power. This effect is less visible on the detached ions inside the magnetic nozzle, i.e. for angular positions satisfying  $\theta_{det} \leq |\theta| \leq \theta_{LMFL}$ . This point is further discussed in section 5.3. Otherwise mentioned, the magnetic topology is  $M_1$ .

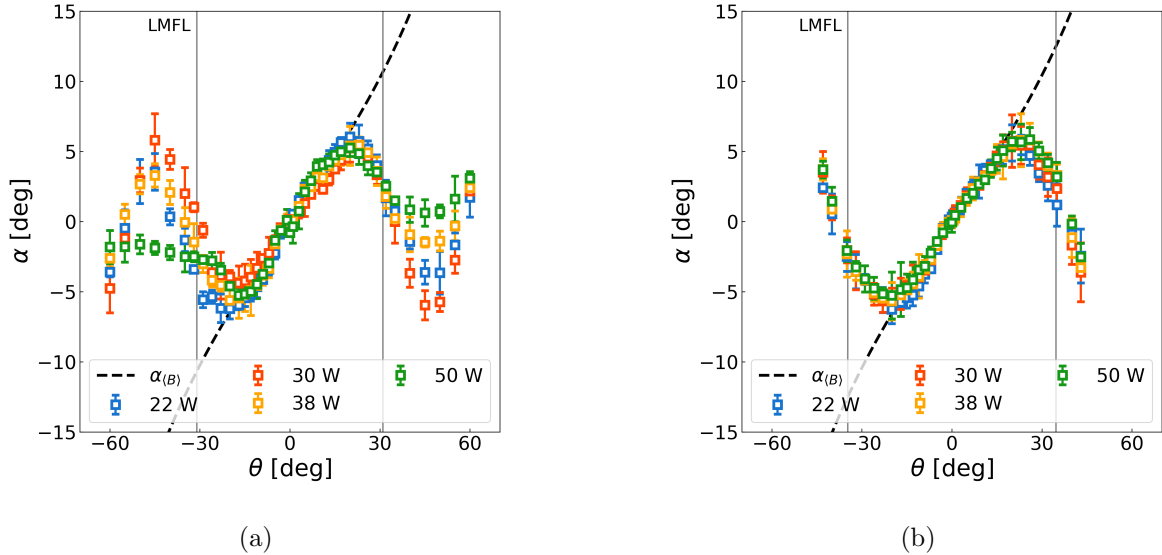


Figure 5.8:  $(\alpha\theta)$ -maps for different thruster powers at (a)  $\rho = 31.5$  cm and (b)  $\rho = 41.5$  cm. The mass flow rate of the thruster is 1 sccm.

## 5.2.2 Variation of the mass flow rate

The analysis of the ion trajectories in the magnetic nozzle of the ECR thruster is also conducted for several thruster mass flow rates at a power of 30 W at the distance  $\rho = 31.5$  cm (figure 5.9). In this case again, it is not clear if the angular location of the ion detachment depends on the thruster condition. However, like the variation of thruster power described in the precedent section, the mass flow rate has an influence on the trajectories of the detached ions. In this case, its effect is visible for all of the detached ions, i.e. for every angular positions satisfying  $|\theta| \geq \theta_{det}$ . Indeed, the lower the mass flow rate, the sharper the decrease of  $\alpha_{mean}$  after the detachment meaning that the trajectories of the detached ions are more converging when the thruster mass flow rate is low. A possible explanation of this observation is that, once detached, the ion trajectories are not affected by the plasma conditions but by the vacuum condition. In fact, the pressure inside the vacuum facility evolves linearly with the mass flow rate of xenon injected (section 2.2.1). The influence of the vacuum pumping speed and the background pressure on the ion detachment is evaluated with the results presented in the following section.

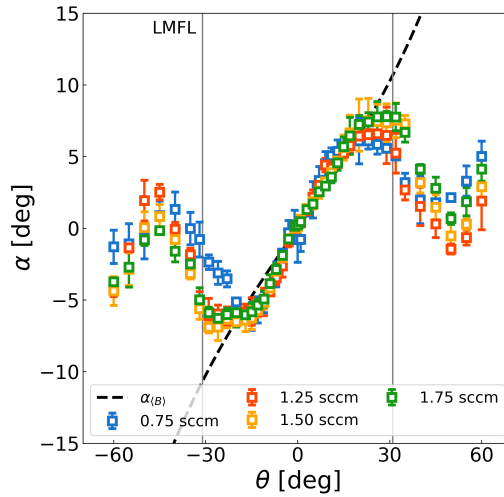


Figure 5.9:  $(\alpha, \theta)$ -maps for different thruster mass flow rate at  $\rho = 31.5$  cm. The power of the thruster is 30 W.

## 5.2.3 Variation of the vacuum conditions

The vacuum condition used in the experiment presented so far is  $V_1$ , meaning that all the pumps are switched on. However, to assess the influence of the vacuum condition on the ion detachment, the experiment is also conducted in a different condition, denoted by  $V_2$ . For this condition, the rough pump and the turbo-pumps are running but the cryo-pump is switched off. The vacuum pumping speeds associated to  $V_1$  and  $V_2$  are calculated in the experimental apparatus in section 2.2.1, they are  $V_{pump}^1 \approx 15300 \text{ L.s}^{-1}$  and  $V_{pump}^2 \approx 2700 \text{ L.s}^{-1}$  respectively and the pressures associated with the thruster firing at 1 sccm and 30 W are  $P_1 \approx 8 \times 10^{-7}$  mbar and  $P_2 \approx 3 \times 10^{-6}$  mbar respectively. For these two vacuum conditions,  $(\alpha, \theta)$ -maps are constituted for the whole range  $\rho \in [21.5, 41.5]$  cm (figure 5.10). The ion trajectories for  $V_1$  and  $V_2$  appear to be very different but  $\alpha_i$  is equal to  $\alpha_{\langle B \rangle}$  in the centre of the plume in both cases. However, for the condition  $V_2$ , the trajectory of the ions is more diverging than the magnetic field lines once they are detached. In fact,  $\alpha_i \geq \alpha_{\langle B \rangle}$  for a range of positive values  $\theta$ . This behaviour is observed only for distances  $\rho \leq 37.5$  cm.

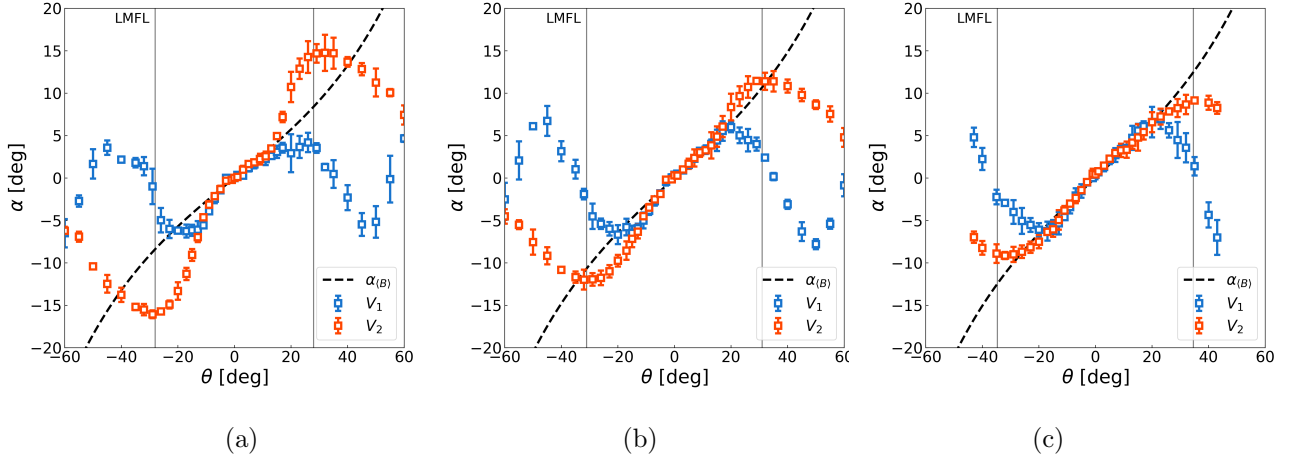


Figure 5.10:  $(\alpha\theta)$ -maps for different vacuum conditions at (a)  $\rho = 21.5$  cm, (b)  $\rho = 31.5$  cm and (c)  $\rho = 41.5$  cm. The thruster is firing at 1 sccm and 30 W.

Due to the shape of the  $(\alpha\theta)$ -map for the vacuum condition  $V_2$ , the methodology introduced in section 5.1.4 to determine  $\theta_{det}$  yields inconsistent results for this condition. Nevertheless, the comparison of the  $(\alpha\theta)$ -maps for the two vacuum conditions suggests that the angular location at which  $\alpha_i$  becomes different from  $\alpha_{\langle B \rangle}$ , i.e. the angular location of the ion detachment, is sensibly the same for both vacuum conditions. However, the vacuum condition has a significant influence on the trajectories of the ions that are already detached from the magnetic field lines. Indeed, for the vacuum condition  $V_2$ , i.e. for a lower pumping speed, the trajectories of the detached ions are more diverging. This observation is in line with the results observed in the section above in the comparison of  $(\alpha\theta)$ -maps for several thruster mass flow rates.

#### 5.2.4 Variation of the magnetic topology

The experiment is also performed with the magnetic topology  $M_2$  (figure 5.11). Three distances are presented, respectively  $\rho = 21.5$  cm,  $\rho = 31.5$  cm and  $\rho = 41.5$  cm. It illustrates that at these distances and with the magnetic topology  $M_2$ , the approximation  $\alpha_B^{MN} \approx \alpha_{\langle B \rangle}$  is no longer verified. Therefore both function,  $\alpha_B^{MN}$  and  $\alpha_{\langle B \rangle}$ , are represented with solid and dashed lines respectively. It appears that at the centre of the plasma plume, the ion direction is the same as that of the magnetic field  $\langle \vec{B} \rangle$ . This observation justifies the pertinence of the comparison of  $\alpha_i$  with  $\alpha_{\langle B \rangle}$  instead of  $\alpha_B^{MN}$  in the  $(\alpha\theta)$ -maps shown above.

This observation also justifies the pertinence of the computation of the magnetic field  $\langle B \rangle$ . In fact, this field is the sum of the magnetic field induced by the permanent magnet of the thruster added to the azimuthal average of the contribution of the Earth magnetic field. The fact that, at the centre of the plume,  $\alpha_i = \alpha_{\langle B \rangle}$  but  $\alpha_i \neq \alpha_B^{MN}$  is very insightful on the plasma dynamics in the magnetic nozzle of the ECR thruster. This point is further discussed in section 5.3.4.

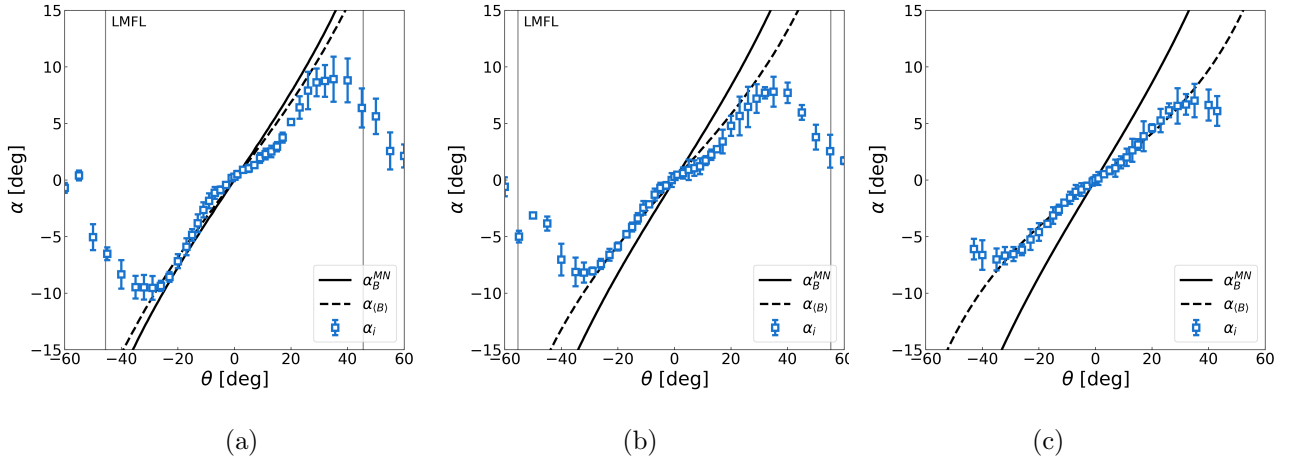


Figure 5.11:  $(\alpha\theta)$ -maps with the magnetic topology  $M_2$  at (a)  $\rho = 21.5$  cm, (b)  $\rho = 31.5$  cm and (c)  $\rho = 41.5$  cm. The thruster is firing at 1 scm and 30 W.

The results presented in this section allow for a characterisation of the ion detachment from the magnetic nozzle of the ECR thruster. First, results show that the variation of the thruster mass flow rate and the thruster power do not have a strong influence on the location of the plasma detachment. However, an influence is observed on the trajectory of the ions that are already detached from the magnetic field lines. Second, the variation of the vacuum condition inside the vacuum facility has also a minor effect on the ion detachment location but significantly influences the trajectory of the ions that are already detached from the magnetic nozzle. In fact, the trajectories of the detached ions are more diverging than the magnetic nozzle when the pumping speed is low (vacuum condition  $V_2$ ). Finally, the comparison of the ion direction and the magnetic field direction at several distances of the thruster for the magnetic topology  $M_2$  stresses the influence of the Earth magnetic field on the shape of the magnetic nozzle. In fact, it is shown in section 5.1.4 that the ion direction does not follow the magnetic field resulting from the sum of the magnetic nozzle and the Earth magnetic field. However, results presented in this section show that the ions follow the magnetic field resulting from the sum of the magnetic nozzle and the azimuthal average of the influence of the Earth magnetic field.

The main point of the next section is to further discuss these observations and give elements of understanding of the ion dynamics in the diverging magnetic nozzle of the ECR thruster.

### 5.3 Discussion of the results

In this section, the experimental observations presented so far are discussed in order to draw conclusions on the dynamics of the ions and their interaction with the magnetic nozzle of the ECR thruster. First, the methodology presented in section 5.1.4 to evaluate the ion detachment location is applied at several distances from the thruster backplate to observe where the detachment of the ions takes place in the plume of the thruster. Second, the influence of the magnetic nozzle on the trajectory of the ions already detached is analysed. This analysis allows to characterise the influence of the thruster operating conditions on the behaviour of the ions at the location of their detachment. Third, a two-population model is developed to give elements of comprehension of the asymmetry of the  $\alpha$ -scans observed in section 5.1.2. Finally, the fact that the ions are attached to the magnetic field produced by the magnet of the thruster and the azimuthal average of the Earth magnetic field is discussed.

### 5.3.1 Location of ion detachment

In order to analyse globally the location of the ion detachment in the whole plume of the ECR thruster,  $\theta_{det}$  is measured for distances  $\rho \in [21.5, 60]$  cm and represented in the  $(\rho, \theta)$  plane (figure 5.12a). On the figure, the angular position of the magnetic field line is represented with a black solid line if the magnetic field considered is  $\vec{B}$  and with a dashed line if the magnetic field considered is  $\langle \vec{B} \rangle$ . Results show that the data can be fitted by a linear function. This fit is referred to as fit 1 in the remaining of the section. It appears that  $\theta_{det}$  decreases when  $\rho$  increases. It means that at greater distances from the thruster backplate, a greater part of the plume is detached from the magnetic nozzle. This observation suggests that at a given distance from the thruster source, all of the ions are eventually detached. On the other hand, the angular location of the ion detachment  $\theta_{det}$  can also be represented in the magnetic coordinate system  $(B/B_0, \psi/\psi_p)$  introduced in section 2.1.2 (figure 5.12b). This frame is magnetic field dependant, and since  $\theta_{det}$  is evaluated from the comparison of  $\alpha_i$  and  $\alpha_{\langle B \rangle}$ , the magnetic field  $\langle \vec{B} \rangle$  is considered here. Furthermore, results presented in section 5.1.3 show that the difference between  $\vec{B}$  and  $\langle \vec{B} \rangle$  is negligible for the magnetic topology  $M_1$ . In this frame, the data can be fitted by an exponential function. In fact, with a logarithmic scale for the y-axis, the value of  $B/B_0$  at the location of the detachment decreases linearly when  $\psi/\psi_p$  decreases. This fit is referred to as fit 2 in the remaining of the section.

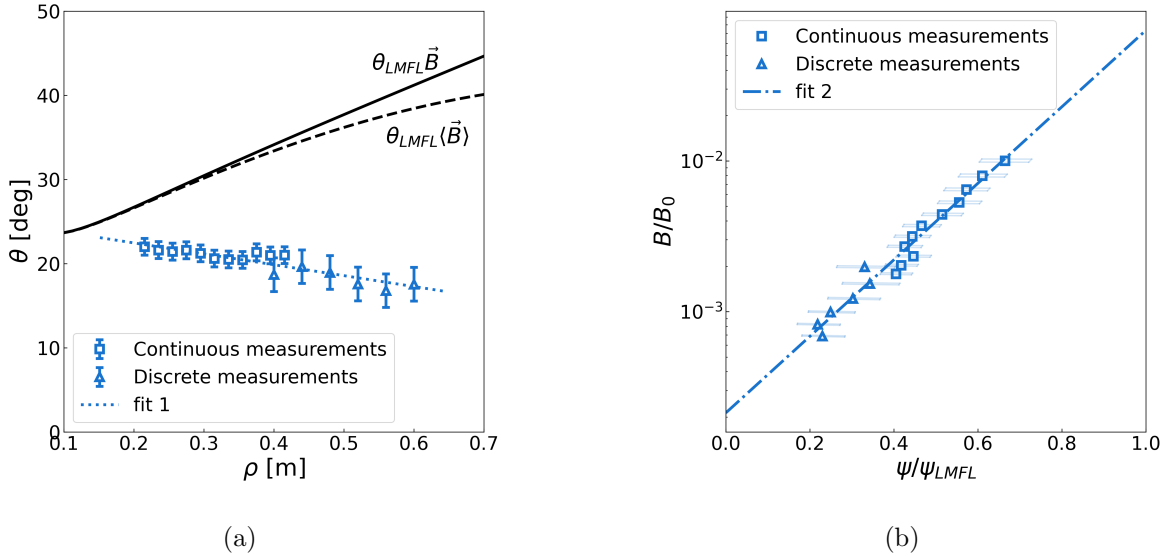


Figure 5.12: Detachment angular location  $\theta_{det}$  in (a) the  $(\rho, \theta)$  frame and (b) the magnetic frame  $(B/B_0, \psi/\psi_p)$ .

The angular location of the ion detachment is also reported in the cartesian frame  $(R, Z)$  (figure 5.13). On the figure, the last magnetic field line is represented with a black solid line for the magnetic field  $\vec{B}$  and with a dashed line for the magnetic field  $\langle \vec{B} \rangle$ . The fit 1 and 2 are also reported on this figure. With such representation, it is not possible to conclude if the best fit for the data is fit 1 or fit 2. In fact, this conclusion would necessitate to observe the location of the ion detachment at distances greater than  $\rho = 60$  cm. However, results show that in the region for which  $\theta_{det}$  is evaluated, the ions are more and more detached from the magnetic field lines when the distance  $\rho$  increases. Also, fit 2 predicts that all of the ions should be detached at a distance equal to 88 cm whereas in the case of fit 1, the ion detachment surface crosses the line  $\theta = 0$  at a distance greater than 2 m.

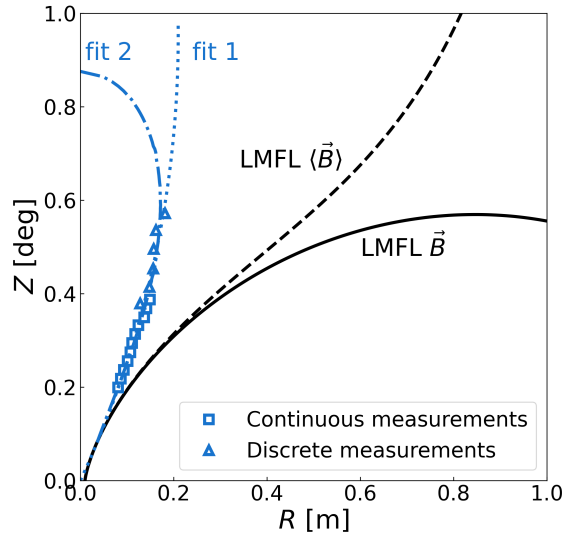


Figure 5.13: Detachment angular location  $\theta_{det}$  in the  $(R, Z)$  frame.

### 5.3.2 Trajectories of the detached ions

If a particle is located at a distance  $\rho_1$  and an angular position  $\theta_1$ , with a trajectory which has a direction of angle  $\alpha_1$ , it is possible to find the angular position  $\theta_2$  and the direction of its trajectory  $\alpha_2$  it would have at the distance  $\rho_2$  if it follows a straight line trajectory (figure 5.14). The details of the calculations are presented in appendix C.

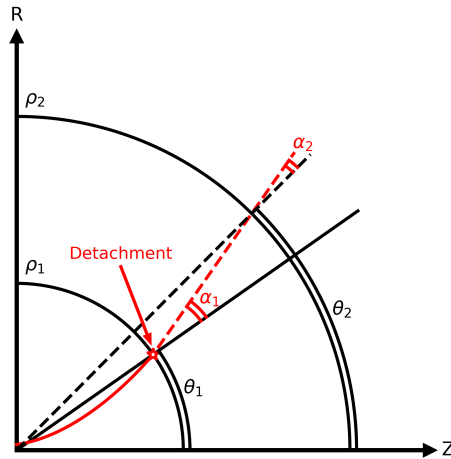


Figure 5.14: Schematic of a particle following a straight line trajectory after being detached from the magnetic nozzle.

### Straight line trajectory of the detached ions

For every angular position of the  $(\alpha\theta)$ -map at the distance  $\rho = 21.5$  cm for which the ions are detached from the magnetic nozzle of the thruster, the corresponding position and direction at the distance  $\rho = 41.5$  is computed under the assumption that the detached ions follow a straight line trajectory. This projection is reported on the  $(\alpha\theta)$ -map obtained at the distance  $\rho = 41.5$  cm (figure 5.15). The good agreement between the ion flux direction measured at  $\rho = 41.5$  cm (coloured scattered squares) and the projection of the ion flux direction inferred from an  $(\alpha\theta)$ -map at lower distance (black scattered squares) for the two vacuum conditions  $V_1$  and  $V_2$  supports the hypothesis that, once detached, the ions have a straight line trajectory, i.e. not affected by the magnetic field anymore.

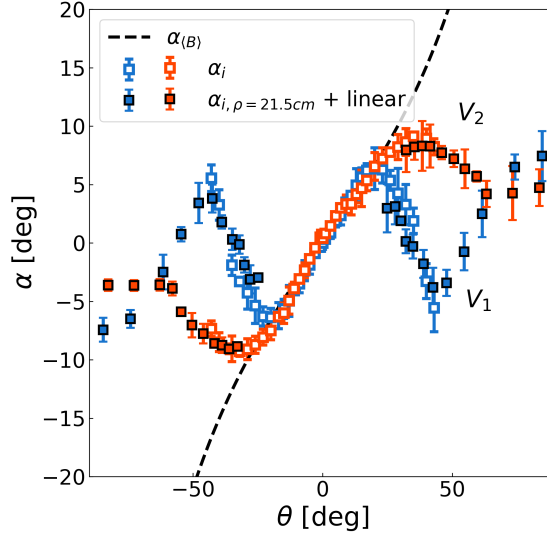


Figure 5.15:  $(\alpha\theta)$ -map at  $\rho = 41.5$  cm (label  $\alpha_i$ ) with the direction of the ions already detached at  $\rho = 21.5$  cm if they follow a straight line trajectory (label  $\alpha_{i, \rho=21.5cm} + \text{linear}$ ). The thruster is firing at 1 sccm and 30 W.

### Direction of the detached ion trajectories

It is shown above that the ions, once detached from the magnetic nozzle, follow a straight line trajectory. The measured trajectory of the detached ions is therefore the projection of the direction they have at the location of the detachment. For every location of detachment  $\theta_{det}$  (see section 5.3.1), the trajectory tangent to the magnetic field  $\langle \vec{B} \rangle$  at the location of the detachment is computed, and the direction is projected at the distance  $\rho = 41.5$  cm. This projection is then reported on the  $(\alpha\theta)$ -map obtained at the distance  $\rho = 41.5$  cm (figure 5.16). The fact that the measured trajectories of the detached ions does not match and is slightly higher (for positive  $\theta$ ) than the straight line trajectory tangent to the magnetic field at the location of the detachment (green solid line) suggests that, at the location of the detachment, ions have a trajectory slightly more divergent than the magnetic field direction.

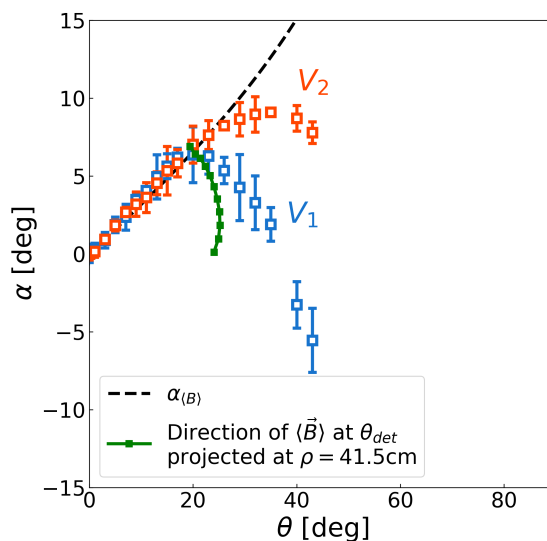


Figure 5.16:  $(\alpha\theta)$ -map at  $\rho = 41.5$  cm (black scattered symbols) with the direction of ions detached closer than  $\rho = 41.5$  cm if they would have a straight line trajectory tangent to the magnetic field at the location of the detachment. The thruster is firing at 1 sccm and 30 W.

The results presented above show that, on the one hand, the ions follow a straight line trajectory when they are detached from the magnetic nozzle and, on the other hand, they have a direction more diverging than the magnetic field lines direction at the location of the detachment. Moreover, it is shown in section 5.2 that the operating conditions of the thruster in mass flow rate and in power, as well as the vacuum condition, has an influence on the direction of the detached ions. Therefore, it can be concluded that the operating condition influence the direction of the ion flux at the location of the detachment. This direction is more diverging than the magnetic field direction for the conditions tested, and the vacuum condition has the greater influence on the divergence angle at the location of the detachment.

It is worth mentioning that the fact that the ions detach with a direction more diverging than the magnetic field direction is not contradictory with the ion flux direction measured far from the thruster exit that are more converging than the magnetic field lines directions. In fact, this observation is due to the global divergence of the magnetic field that eventually becomes more diverging than the straight line trajectories of the detached ions.

### 5.3.3 Analysis of the asymmetry of the ion flux distribution

#### Skewness of the $\alpha$ -scans

The objective of this section is to assess and analyse the asymmetry (or skewness) that is observed in the  $\alpha$ -scans measured for different thruster conditions. In order to quantify this asymmetry, the Fisher's coefficient is evaluated. This coefficient generally measures the skewness of a random variable but it is relevant to compute it in the case of an  $\alpha$ -scan since it is an angular distribution of ion trajectory. The Fisher coefficient of skewness of a random variable  $X$  reads:

$$Skew(X) = \frac{\mathbf{E}[(X - \mu)^3]}{\left(\mathbf{E}[(X - \mu)^2]\right)^{3/2}} \quad (5.12)$$

where  $\mu$  is the centre and  $\mathbf{E}$  is the first moment of the distribution function. If the skewness takes a positive (resp. negative) value, it means that the asymmetry is higher on the right (resp. left) part of the distribution. For example, the  $\alpha$ -scan represented in figure 5.18 illustrates a distribution with a positive skewness.

The skewness of the  $\alpha$ -scans is computed and represented along the angular position  $\theta$  for different thruster power at  $\rho = 31.5$  cm and  $\rho = 41.5$  cm (figures 5.17d and 5.17e respectively), for different thruster mass flow rates at  $\rho = 31.5$  cm (figure 5.17f) and for the two vacuum conditions  $V_1$  and  $V_2$  at  $\rho = 21.5$  cm,  $\rho = 31.5$  cm and  $\rho = 41.5$  cm (figures 5.17a, 5.17b and 5.17c respectively). For each figure, the shadow represents the difference between the skewness computed for the  $\alpha$ -scans performed clockwise and counterclockwise at the given position  $\theta$  and the solid line represents the mean of these two values. This shadow can be viewed as an interval of uncertainty of the skewness.

The first observation made on the signals represented is that the skewness is symmetrical around  $\theta = 0$ . This observation justifies the use of this mathematical coefficient as a relevant metric to study the behaviour of the ions in the magnetic nozzle. In fact, it appears that the evolution of the skewness with  $\theta$  has the same shape than the  $(\alpha\theta)$ -maps previously presented, showing the existence of a correlation between the skewness and the ion dynamics. Moreover, it seems that the maximum of skewness coincides with the location of the detachment  $\theta_{det}$ , this observation being better described later in the section. Second, the skewness does not depend on the mass flow rate while it takes different amplitude for the two different vacuum conditions, especially at the lowest distance  $\rho = 21.5$  cm (figure 5.17a). On the other hand, the increase of the thruster power has a fairly visible impact on the skewness. In fact, the greater the power the more skewed the  $\alpha$ -scans. These observations are detailed later in the section. The last point worth mentioning is that for positive (resp. negative) values of  $\theta$ , the skewness is positive (resp. negative). This observation means that the  $\alpha$  distribution of ion angular direction is always skewed toward the "more diverging" directions. All things considered, though the Fisher's coefficient of skewness shows the correlation between ion trajectories and skewness of the  $\alpha$ -scans, it is not sufficient to understand physically the mechanism at stake in the behaviour of the ions in the magnetic nozzle of the ECR thruster.

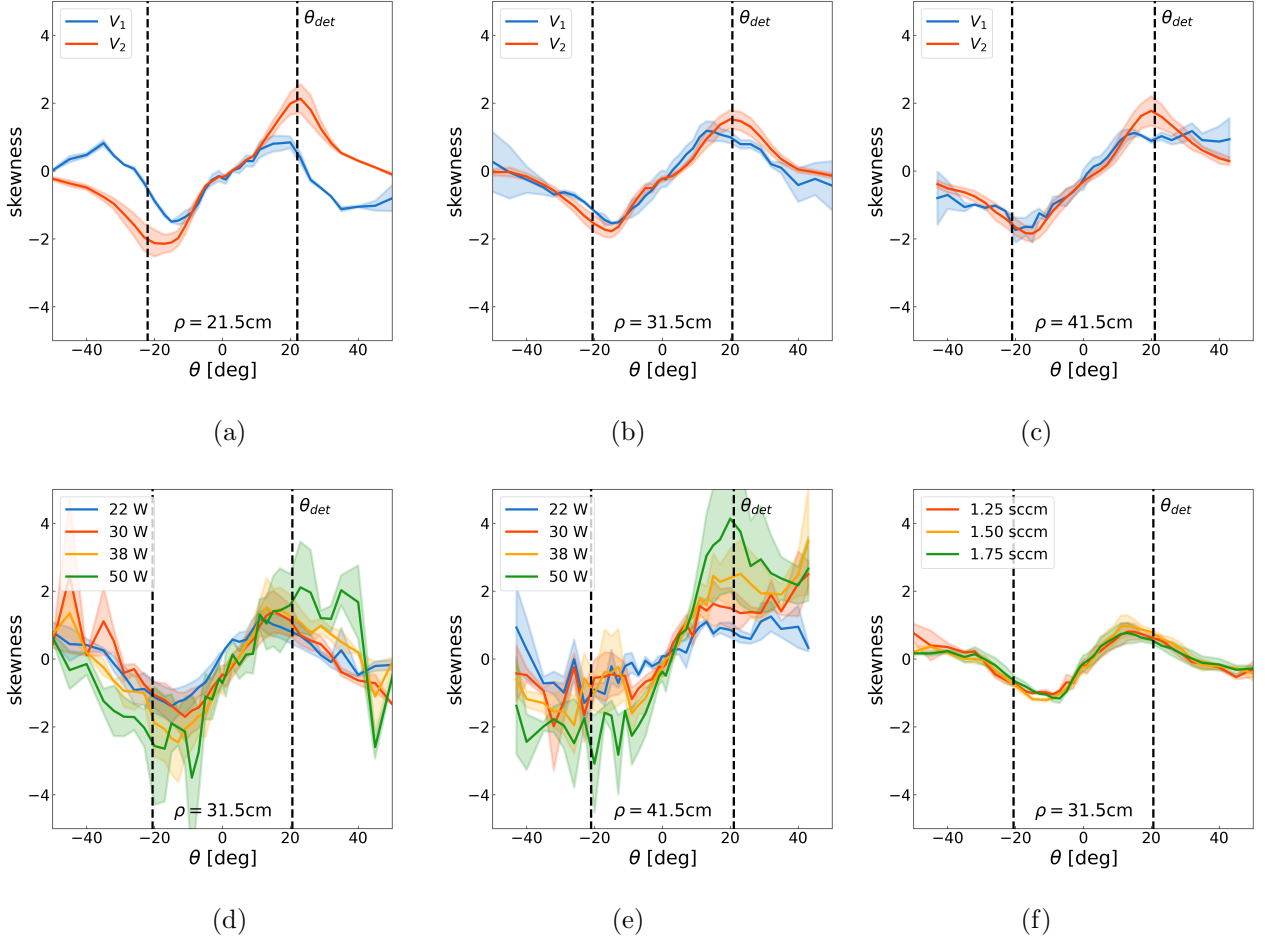


Figure 5.17: Skewness of the  $\alpha$ -scans for different vacuum conditions at (a)  $\rho = 21.5$  cm, (b)  $\rho = 31.5$  cm and (c)  $\rho = 41.5$  cm with the thruster is firing at 1 sccm and 30 W and skewness of the  $\alpha$ -scans for different thruster power at (d)  $\rho = 31.5$  cm and (e)  $\rho = 41.5$  cm and (f) for different thruster mass flow rate at  $\rho = 31.5$  cm.

## Two ion population model

In order to model and further analyse the asymmetry of the  $\alpha$ -scans, two ion populations with two distinct angular distribution of current density are considered. In the remaining of the chapter, they are called the main population, which is responsible for the bell shape of the  $\alpha$ -scan, and the secondary population, which explains the asymmetry (figure 5.18). In order to simplify the framework of this analysis, this model is restricted to basic functions. Hence, the angular distributions of ion current density of the main and the secondary population are supposed to follow Gaussian-like distributions. Therefore, the  $\alpha$ -scans are fitted by the following function:

$$f(\beta) = a_1 e^{-\frac{(\beta-\mu_1)^2}{\sigma_1^2}} + a_2 e^{-\frac{(\beta-\mu_2)^2}{\sigma_2^2}} \quad (5.13)$$

where  $a_1$ ,  $\mu_1$  and  $\sigma_1$  represent the height, the centre and the width respectively of the main distribution and  $a_2$ ,  $\mu_2$  and  $\sigma_2$  represent the height, the centre and the width respectively of the secondary distribution and  $\beta = \alpha - \alpha_i$ . To reduce the number of fitting parameters, normalised  $\alpha$ -scans are considered. Thus, the maximum of the fit is close to 1 and it is easier to analyse

the evolution of the fitting parameters with the various thruster conditions. Moreover, several constraints are added to the model in order to help the optimisation algorithm to best fit the signals. They read:

$$\begin{aligned}
 0.5 &\leq a_1 \leq 1.2 \\
 \mu_1 &= 0 \\
 0 &\leq a_2 \leq 0.5 \\
 \sigma_1 &\geq 0 \\
 \sigma_2 &\geq 0
 \end{aligned}
 \tag{5.14}$$

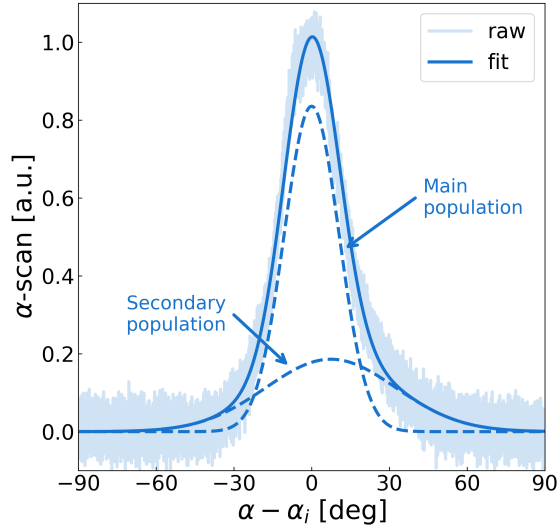


Figure 5.18:  $\alpha$ -scan at the position (a) ( $\theta = 26$  deg,  $\rho = 31.5$  cm) fitted by a the sum of two Gaussian functions. The thruster is firing at 1 sccm and 30 W.

First, the evolution of the fitting parameters  $a_1$ ,  $a_2$ ,  $\sigma_1$ ,  $\sigma_2$  and  $\mu_2$  with the angular position  $\theta$  is compared between the two vacuum conditions  $V_1$  and  $V_2$  at distances  $\rho = 21.5$  cm,  $\rho = 31.5$  cm and  $\rho = 41.5$  cm (figure 5.19). For each figure, like the skewness, the shadow represents the difference between the fitting parameters computed for the  $\alpha$ -scans performed clockwise and counterclockwise at the given  $\theta$  position and the solid line represents the mean of these two values. Moreover, for each distance, the detachment location  $\theta_{det}$ , defined in section 5.1.4, is plotted with a black dashed line. It appears that some of the signals presented on figure 5.19 are not continuous. It is the case when the optimisation algorithm is not able to fit correctly an  $\alpha$ -scan. Nevertheless, results show that the constraints on the fitting parameters are not too restrictive. In fact, all of the parameters found are within the range given by equation 5.14. This observation gives confidence in the pertinence of this analysis to study the ion dynamics in a magnetic nozzle.

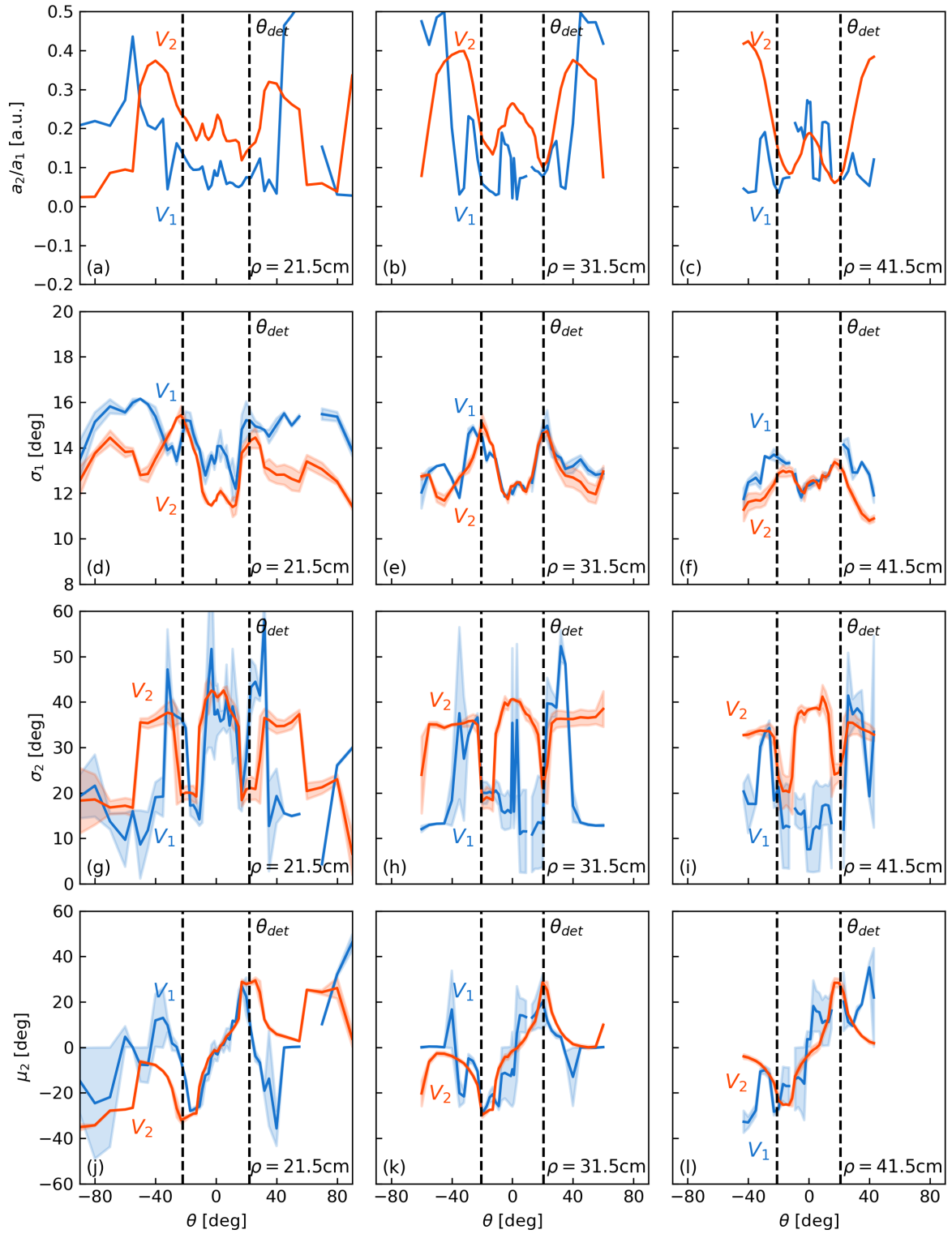


Figure 5.19: Evolution of the fitting parameters  $a_2/a_1$ ,  $\sigma_1$  and  $\sigma_2$  and  $\mu_2$  with  $\theta$  at distances  $\rho = 21.5$  cm (resp. (a), (d), (g), (j)),  $\rho = 31.5$  cm (resp. (b), (e), (h), (k)) and  $\rho = 41.5$  cm (resp. (c), (f), (i), (l)) for two vacuum conditions  $V_1$  and  $V_2$ . The black dashed lines correspond to the detachment location  $\theta_{det}$ .

It is first observed that the parameters are very little influenced by the vacuum condition. Indeed, even though the uncertainty on the value of these parameters is difficult to estimate, the difference between the fitting parameters for the two vacuum conditions is not significant contrary to what is observed in the  $\alpha$ -scans for these two vacuum conditions (section 5.2.3). Nevertheless, the difference observed in the skewness at the distance  $\rho = 21.5$  cm (figure 5.17a) is associated to a smaller ratio  $a_2/a_1$  (figure 5.19a) and a smaller parameter  $\mu_2$  (figure 5.19j) at the vacuum condition  $V_1$ . In fact a smaller height of the secondary population which is closer to the main population yields a smaller value of skewness. Second, a general pattern can be observed for each parameters and for both vacuum conditions. In fact, a significant change in the value of each parameter appears close to the location of the detachment of the ion from the magnetic nozzle. The fact that this change is observed at the same location for the two vacuum conditions supports the hypothesis stated in section 5.2.3 according to which the detachment location does not depend on the vacuum condition.

This analysis is also conducted for different thruster operating conditions. The evolution of the fitting parameters  $\sigma_1$  and  $\mu_2$  with  $\theta$  are compared for the different microwave power at the distance  $\rho = 31.5$  cm (figures 5.20a and 5.20d) and at the distance  $\rho = 41.5$  cm (figures 5.20b and 5.20e) and for different xenon mass flow rates at distance  $\rho = 31.5$  cm (figures 5.20c and 5.20f). The evolution of the ratio  $a_2/a_1$  and the parameter  $\sigma_2$  is not shown because the analysis of the parameters  $\sigma_1$  and  $\mu_2$  is sufficient to compare the influence of the thruster operating conditions on the fitting parameters.

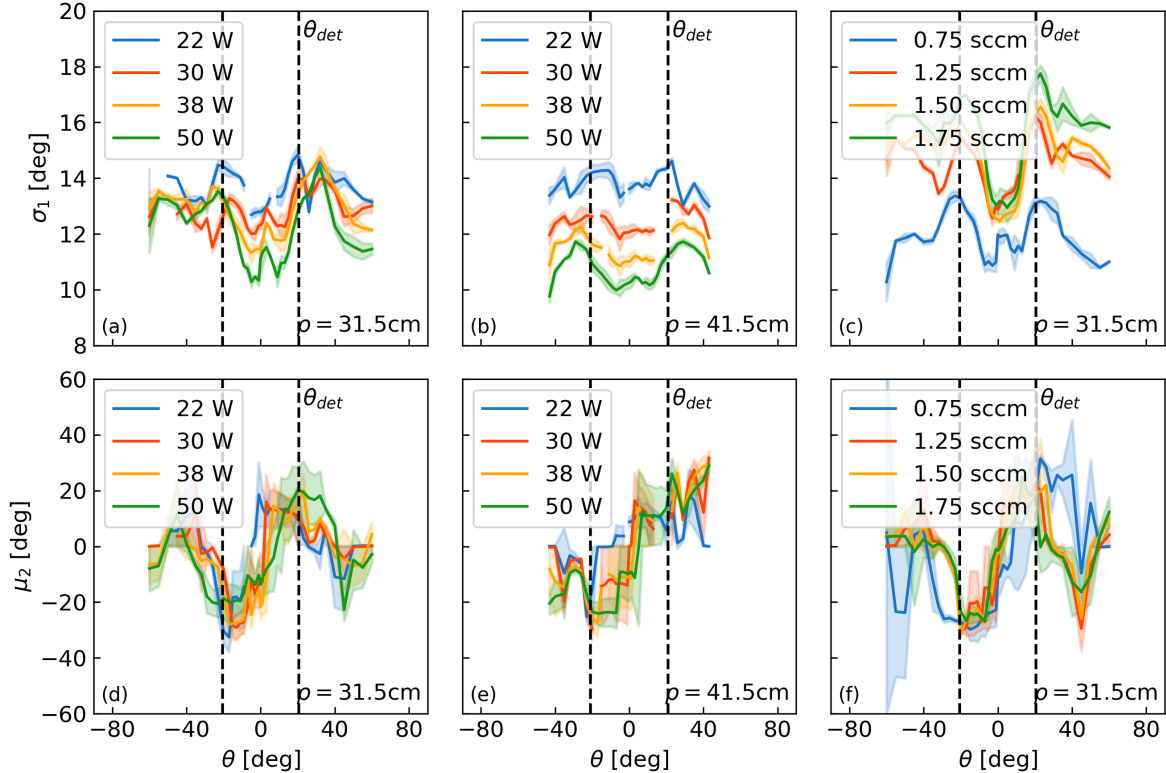


Figure 5.20: Evolution of the fitting parameters  $\sigma_1$  and  $\mu_2$  with  $\theta$  for different thruster microwave power at distance  $\rho = 31.5$  cm (resp. (a) and (d)) and  $\rho = 41.5$  cm (resp. (b) and (e)) and for different thruster Xenon mass flow rate at distance  $\rho = 31.5$  cm (resp. (c) and (f)). The black dashed lines correspond to the detachment location  $\theta_{det}$ .

The fact that, for each thruster operating condition, a significant change is observed for the fitting parameters  $\sigma_1$  and  $\mu_2$  at the angular position  $\theta_{det}$  supports in this case again the hypothesis of detachment location independent from the thruster operating condition. Nevertheless, the thruster operating condition has a significant influence on the value of  $\sigma_1$  while all of the other fitting parameters remain sensibly the same regardless of the microwave power or the mass flow rate. In fact,  $\sigma_1$  is higher for low microwave powers and high mass flow rates. This result is in line with a greater skewness observed for high microwave power. Indeed, if the parameters  $\sigma_1$  which represents the width of the main population is small, it means that the  $\alpha$ -scan is more likely to be skewed by the secondary population.

The results presented in this section show that the asymmetry of the  $\alpha$ -scans is directly linked to the location of the ion detachment. It supports the observation of a detachment location independent from the thruster mass flow rate, the thruster power and the vacuum condition. The two-population model is developed to have a finer understanding of the asymmetry of the  $\alpha$ -scans. The analysis of the evolution of the fitting parameters for several distances and thruster operating conditions reveals that a higher parameter  $\sigma_1$ , which represents the width of the main population, is associated to more converging trajectories of the detached ions. In fact,  $\sigma_1$  decreases with an increase of the thruster power and is greater for the vacuum condition  $V_1$  than for the vacuum condition  $V_2$ .

### 5.3.4 Plasma mitigation of the magnetic nozzle deformation by the Earth magnetic field

Results presented in sections 5.1.3, 5.1.4 and 5.2.4 show that the Earth magnetic field cannot be neglected far from the thruster source because it is of the order of the magnetic field produced by the permanent magnet of the thruster in this region. However, it appears that for all of the conditions tested, the ion trajectories measured do not follow the magnetic field resulting from the sum of the magnetic field produced by the magnet of the thruster and the Earth magnetic field. In fact, the influence of the Earth magnetic field is azimuthally averaged, this result being best illustrated by figure 5.11 discussed in section 5.2.4.

A physical explanation of this observation could be a global dynamic of rotation of the plasma. In fact, with such dynamic, the influence of the Earth magnetic field would be averaged. For the value of longitudinal ion velocity of the order of  $15 \text{ km.s}^{-1}$  measured by Laser induced fluorescence in chapter 3 at a distance of 20 cm away from the backplate of the thruster, the global frequency of rotation of an ion should be of the order of 15 GHz for it to cover a distance of the order of 1 mm during one rotation, which is the scale of variation of the magnetic field strength. This rotation frequency corresponds to azimuthal velocities of the order of  $10^7 \text{ m.s}^{-1}$ , which is not viable for the ions. For the electrons, if they have a global rotation speed sufficient compared to their longitudinal velocity, the ambipolar electric field resulting from their acceleration averages azimuthally the influence of the Earth magnetic field. The acceleration of the ions would then be governed by an electron dynamics driven nozzle in this case.

A different explanation of the observations relies on the modification of the local magnetic field by the highly energetic plasma flow. This effect can be estimated by computing the  $\beta$  parameter of the plasma. This figure of merit represents the ratio between the kinetic pressure  $P_{kin}$  of the plasma and the magnetic pressure  $P_{mag}$ . It reads:

$$\beta = \frac{P_{kin}}{P_{mag}} = \frac{\frac{1}{2}m_i n_i u_i^2}{B^2/2\mu_0} \quad (5.15)$$

where  $\mu_0$  is the vacuum magnetic permeability and the kinetic pressure term is the density of kinetic energy of the ions. If  $\beta < 1$ , the magnetic pressure is dominant and the plasma flows in the fixed magnetic field lines. However, if  $\beta > 1$ , the kinetic pressure is dominant and the plasma transports the magnetic field lines [1].

The  $\beta$  parameter is computed in the axis of the thruster for the magnetic topologies  $M_1$  and  $M_2$  with and without taking into account the Earth magnetic field from the output of the isothermal model presented in chapter 3 (figure 5.21). On this figure, data points labelled “Experiments LIF” correspond to measurements performed with Laser Induced Fluorescence already presented in chapter 3. Results show that the  $\beta$  parameter becomes of the order of 1 at a distance  $Z = 85$  cm in the case of the magnetic topology  $M_1$  and  $Z = 33$  cm in the case of the magnetic topology  $M_2$ . However, the consideration of the Earth magnetic field (dashed lines in figure 5.21) increases the magnetic pressure, resulting in a lower  $\beta$  parameter. Nevertheless, the fact that  $\beta$  is of the order of unity in the region in which the measurements were performed with the magnetic topology  $M_2$  indicates that the kinetic energy of the ions could transport the magnetic field lines of the magnetic nozzle. This possible scenario should be investigated with regards to the MHD theory of plasma detachment presented in the introduction in chapter 1.

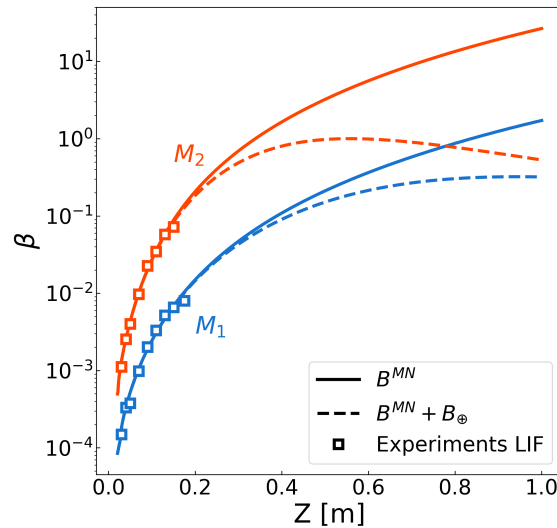


Figure 5.21:  $\beta$  parameter of the plasma along the axis of the ECR thruster the magnetic topologies  $M_1$  and  $M_2$ . The thruster is firing at 1 sccm and 30 W.

## Conclusion

The use of the directional Faraday cup in directional mode in the plasma plume of the ECR thruster yields valuable information on the dynamics of the ions in the magnetic nozzle and their detachment from the magnetic field lines. In a first part, the comparison of the  $(\alpha\theta)$ -maps gathered for several thruster conditions shows that the ions follow the magnetic field lines at the centre of the plume and are detached at the edges of the plume. Moreover, results show that the location of the ion detachment does not depend on the thruster condition. It does not depend on the vacuum condition of the vacuum facility either. However, it is observed that the

thruster operating condition and the vacuum condition have an impact on the trajectory of the ions that are already detached from the magnetic field lines.

In a second part, it is found that the propagation of the trajectories of the ions detached at  $\rho = 21.5$  cm according to a straight line trajectory matches the direction of the trajectory of the detached ions measured at  $\rho = 41.5$  cm. This result confirms that the ions detached from the magnetic nozzle of the thruster follow a straight line trajectory. It has been verified for the two vacuum conditions  $V_1$  and  $V_2$ . Hence, the thruster operating condition has an influence on the trajectory of the ions at the location of the detachment. For all the conditions tested, the trajectories of the ions at the location of their detachment is more diverging than the local direction of the magnetic field. In fact, this divergence increases when the vacuum speed decreases, i.e. at higher mass flow rate or with the vacuum condition  $V_2$ . Therefore, the collisions of the ions with the neutrals, whose population increases at higher mass flow rate, could play a role in the phenomenon of detachment. It is worth mentioning that this result is not contradictory with the ion trajectories more converging than the local direction of the magnetic field lines observed in the  $(\alpha\theta)$ -map. In fact, This behaviour is due to the magnetic field shape that, eventually, becomes more diverging than the ion trajectories.

Then, the asymmetry of the  $\alpha$ -scans is analysed, the signals are fitted by a two population distribution function model. The evolution of the skewness of the  $\alpha$ -scans and the fitting parameters of the model with the angular position supports that the angular location of ion detachment does not depend on the thruster condition. Moreover, it appears that the alpha scan are always skewed toward the more diverging directions. This observation is in line with a diverging theory of ion detachment. This model however does not allow to distinguish if the two ion populations model could refer to the ions ionised once and twice, the fast ions and the slow ions resulting from a charge exchange collision or an other pair of two ion populations present in the plume of the ECR thruster.

It is last found that the influence of the Earth magnetic field on the magnetic nozzle produced by the magnet of the thruster must be averaged azimuthally to explain the measured ion trajectories. A possible explanation of this result is to consider a global rotational dynamic of the plasma. However, the rotation frequency of the ions should be at least of a few GHz for the influence of the Earth magnetic field to be averaged azimuthally, which is not plausible. The electron dynamics could however explain the behaviour of the ions. The other explanation lies on the  $\beta$  parameter of the plasma which compares the plasma kinetic pressure to the magnetic pressure. This parameter is of the order of unity in the region in which the measurements were performed with the magnetic topology  $M_2$ , indicating that the kinetic energy of the ions could transport the magnetic field lines of the magnetic nozzle. This explanation should be investigated with regards to the MHD theory of plasma detachment presented in the introduction in chapter 1 and in Refs. [59,62].



## 6 | Accuracy of the indirect thrust measurement of an ECR thruster

**Motivation and objectives:** The thrust is one of the main figures of merit of an electric propulsion device. In fact, from its value, most of the performance indicators can be assessed, such as the thrust to power ratio (TTPR), the thrust efficiency or the specific impulse (ISP). The thrust can be measured with a thrust balance, and this measurement is then referred to as direct measurement. It can also be estimated from the measurement of the plasma properties in the plasma ejection region by means of optical or electrostatic diagnostics and with an integration of the ejected particles momentum over a closed surface around the thruster. In this case, the method to retrieve the thrust is called indirect thrust measurement. A direct measurement of the thrust of an electric propulsion device is difficult to perform because to build a thrust balance necessitates years of development, and this diagnostic cannot easily be transferred from one facility to another. Hence there is a need for the community to be able to perform a trustworthy indirect estimation of the thrust. Moreover, the measure of the plasma properties necessary to retrieve the thrust can be very insightful on the behaviour of the thruster because they allow to estimate other figures of merit such as the divergence efficiency and the mass efficiency. In the case of Hall Effect Thrusters (HET), Gridded Ion Thrusters (GIT) or Field Emission Electric Propulsion devices (FEEP), the indirect estimation of the thrust is comparable to the direct measurement of the thrust [33,72]. However, Vialis showed in Ref. [3] that a discrepancy is observed in the case of the ECR thruster. The objective of this chapter is, first, to verify the precision of the measurement of the ion current density with a Faraday probe in the plume of the ECR thruster and, second, to understand the role of the different assumptions made on the indirect estimation of the thrust that could lead to such discrepancy.

To this end, the thrust of an ECR thruster is estimated by direct and indirect measurements. Results are compared and the assumptions made in the indirect estimation of the thrust are analysed. The ion current density measured with the directional Faraday cup presented in chapter 4 is validated, and the influence of the local ion trajectories in the expression of the indirect thrust estimation is evaluated, as well as other assumptions such as the presence of multiply charged ions or slow ions resulting from a charge exchange collision in the plume of the thruster.

**Main results:** The methodology used to estimate the thrust of an ECR thruster from the ion current density measured by means of electrostatic probes is detailed in section 6.1 with the assumptions associated to this estimation. The comparison is made between the thrust measured with a thrust stand and estimated from the ion current density measured with a Faraday probe with guard ring and with the directional Faraday cup. It shows that, first, the Faraday probe with guard ring overestimates the ion current density which results in an error of 20% to 30% on the thrust. Second, the directional Faraday cup allows to reduce this error to between 8% to 9%, which is acceptable since the uncertainty of the direct thrust measurements is 5%. However, for high thruster mass flow rates, the indirect method of evaluation of the thrust yields largely underestimated results no matter which probe is used.

In section 6.2, elements are given to analyse the overestimation of the thrust by the Faraday probe with guard ring. Indeed, a large plasma sheath is formed in front of this diagnostic due to its high negative bias voltage. The sheath bends the trajectories of the ions, artificially increasing the ion collection area. Electrostatic simulations of the probe with the software SIMION support the experimental results.

In section 6.3, the approximations used in the first section to estimate the thrust of the ECR thruster are analysed one by one in order to increase the accuracy of the indirect measurement of the thrust with the directional Faraday cup. It is first found that the local ion trajectories play a very little role in this overestimation. In fact, if they are taken into account, the error is reduced by only 1.5%. Second, the study of the contribution of doubly charged ions to the thrust reveals that, if they are not considered, it can lead to an overestimation of the thrust of 6% and therefore explain the general tendency observed. Finally, the presence of slow ions and fast neutrals resulting from charge exchange collisions is studied. Results show that the contribution of the fast neutrals to the thrust, which are not collected by any electrostatic diagnostic, may induce an underestimation of the thrust by up to 25% depending on the thruster mass flow rate, and can therefore explain the behaviour observed at high mass flow rates.

Overall, the results presented in this chapter show that the discrepancy that used to be observed in the comparison between the direct and the indirect measurements of the thrust of an ECR thruster comes, on one side, from the Faraday probe with guard ring which overestimates the ion current density, and, on the other side, from some of the assumptions made in the indirect measurement of the thrust which are too restrictive. In fact, the presence of doubly charged ions and species resulting from charge exchange collisions cannot be neglected in the indirect estimation of the thrust of the ECR thruster.<sup>1</sup>

---

<sup>1</sup>The results presented in this chapter are part of the following article [69]: Romain Pioch, Victor Désangles, Pascal Chabert, *Investigation of the directional Faraday cup and improvement of the comparison between direct and indirect thrust measurements of a magnetic nozzle ECR thruster*. Phys. Plasmas 1 April 2024; 31 (4): 043516. <https://doi.org/10.1063/5.0190318>

## 6.1 Comparison between direct and indirect thrust measurements

### 6.1.1 Methodology of the indirect thrust measurement

The thrust force generated by the ECR thruster is due to the acceleration and the ejection of the plasma at high velocity in the diverging magnetic nozzle. It can thus be retrieved from the measurement of the local properties of this plasma. The method to estimate the thrust in this case is called indirect method, by comparison with the direct measurement of the thrust with a thrust stand (see section 2.2.4).

Several assumptions can be made to limit the number of plasma parameters necessary to estimate the thrust of the ECR thruster. First, because the thrust is mainly due to the acceleration and the ejection of the xenon ions, it can be estimated from the ion properties only. In fact, the contribution of the electrons to the thrust is neglected regarding their weak mass compared to that of the ions. Second, the contribution of the neutrals to the thrust is also neglected because they are not accelerated in the magnetic nozzle and have therefore a small velocity compared to the ions. In that respect, the first approximation of the elementary thrust  $\delta T_z$  is the pressure force produced by the ion flux on a small surface  $\delta S$  located downstream the thruster ejection [31]. It reads:

$$\delta T_z = m_i n_i v_i^2 \cos(\theta) \delta S \quad (6.1)$$

where  $m_i$ ,  $n_i$  and  $v_i$  are the ion mass, density and velocity respectively and the notations  $\rho$ ,  $\theta$  and  $\alpha$  used in this section are the same than that defined in chapter 5. The thrust  $T$  of the ECR thruster is obtained by integrating  $\delta T_z$  over half a sphere of radius  $\rho$ , denoted by  $\mathcal{S}_\rho$ . It is assumed here that all of the plasma is ejected in the direction of the thruster, meaning that no ion or electron is ejected backwards. Moreover, the ejection region is supposed to be axi-symmetrical regarding the cylindrical geometry of the plasma source. Several measurements already presented in this manuscript such as the ion velocity in chapter 3 or the ion trajectory in chapter 5 confirm that the plume of the ECR thruster is effectively symmetrical around  $\theta$ . Hence,  $T$  is retrieved from only one angular scan of the ion current density along the angular position  $\theta$  and one measurement of ion velocity as follows:

$$\begin{aligned} T &= \int_{\mathcal{S}_\rho} \delta T_z \\ &= \int_{\phi=0}^{\phi=\pi} \int_{\theta=-\frac{\pi}{2}}^{\theta=\frac{\pi}{2}} \delta T_z \rho^2 \cos(\theta) |\sin(\theta)| d\phi d\theta \\ &= \pi \rho^2 \int_{-\frac{\pi}{2}}^{\frac{\pi}{2}} m_i n_i v_i^2 \cos(\theta) |\sin(\theta)| d\theta \\ &= \pi \rho^2 \frac{m_i v_i}{e} \int_{-\frac{\pi}{2}}^{\frac{\pi}{2}} j_i(\theta) \cos(\theta) |\sin(\theta)| d\theta \end{aligned} \quad (6.2)$$

In this formulation,  $j_i = en_i v_i$  is the ion current density. Two assumptions allows to take the ion velocity  $v_i$  out of the integral in equation 6.2. First, it has been verified from retarding field energy analyser measurements in Ref. [32] that  $v_i$  does not depend on the angle  $\theta$ . This assumption is also verified with Laser Induced Fluorescence measurements in chapter 3.

Second, in this section, the ion velocity is the most probable ion velocity extracted from ion energy analyser measurements. Because the ion energy analyser is placed at the far end of the vacuum chamber, 1.7 m away from the thruster, the ion energy  $E_i$  is supposed to be purely kinetic at this location and the ion velocity is computed as follows:

$$E_i = \frac{m_i v_i^2}{2e} \quad (6.3)$$

$$\Rightarrow v_i = \sqrt{\frac{2eE_i}{m_i}}$$

To get the mean energy of the ions, the signal measured with an ion energy analyser is fitted with a Gaussian function and  $E_i$  is the centre of this fit (figure 6.1). In the example shown in the figure, the ion energy is  $E_i = 202.6$  eV and, visually, the uncertainty associated is 5%. This value corresponds to an uncertainty of 2.5% for the ion velocity and the thrust, according to equation 6.3. In addition to these assumptions, in this first approach to estimate the thrust, all of the ions are supposed to be ionised once. If present in the plume of the ECR thruster, the multiply charged ions are neglected. Furthermore, the population at low energy observed in the energy scan shown below is also neglected in this section. It corresponds to slow ions, consequence of a charge exchange collision for example. Their contribution to the thrust is neglected and all of the ions are supposed to have the same velocity. These two major assumptions are discussed in the sections 6.3.3 and 6.3.4.

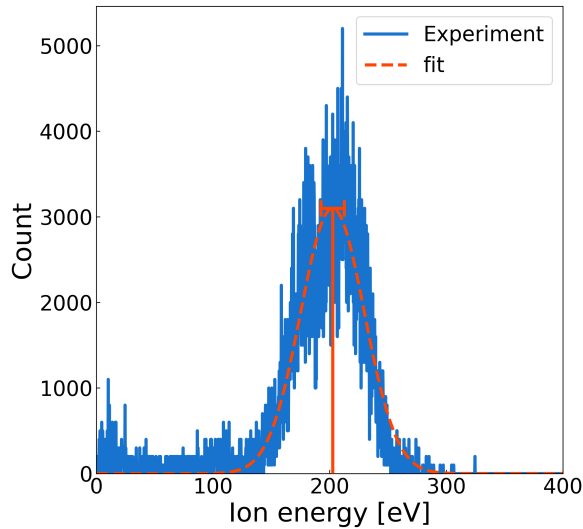


Figure 6.1: Ion energy scan performed with the ion energy analyser fitted with a Gaussian function. The ECR thruster is firing at 1 sccm and 30 W.

The ion current density  $j_i$  in equation 6.2 is measured with either the Faraday probe with guard ring presented in the experimental apparatus in section 2.2.3 or with the directional Faraday cup presented in chapter 4. To carry out the measurements presented in the remaining of this section, the experimental setup used is similar to the one used to characterise the detachment of the plasma from the magnetic nozzle of the ECR thruster presented in the previous chapter (section 5.1, figure 5.1) except that the translation stage is removed from the setup and the distance between the probe and the backplate of the ECR thruster is fixed at  $\rho = 29$  cm. In

the case of measurements of ion current density performed with the Faraday probe with guard ring, the probe faces the thruster and the ion current density is measured at several angular positions  $\theta$ . For each angular position  $\theta$ , the current is measured during 3 s with an acquisition frequency  $f_s = 939$  Hz and averaged to increase the signal to noise ratio. In the case of the directional Faraday cup, the cup is placed on the stepper motor and the ion current density is measured at several local directions  $\alpha$  for each angular positions  $\theta$  in front of the thruster (as done in the discrete methodology presented in section 5.1.1). For each local direction  $\alpha$  of the cup, the current is measured during 2 s with the same acquisition frequency  $f_s$  and averaged. The cylinder and the plate of the directional Faraday cup are biased as recommended in section 4.3.1 and the signal is acquired simultaneously on those two collectors. Otherwise mentioned, to estimate the thrust with equation 6.2, the ion current density is measured when the cup faces the thruster, i.e. at  $\alpha = 0$ , and in cup mode (sum of the plate and cylinder current). Thus, in the first comparison between direct and indirect measurements of the thrust, the local trajectory of the ions is not taken into account and all of the ions are supposed to be ejected from the thruster with a radial trajectory. This assumption is discussed in section 6.3.1.

The angular scans of ion current density measured with the Faraday probe with guard ring and with the directional Faraday cup at  $\rho = 29$  cm with the thruster firing at 1 sccm and 20 W are compared between each other (figure 6.2). The two signals are acquired during two different measurement campaigns. The slight variations of the vacuum condition and the fact that the thruster is manipulated between two measurement campaigns have a strong effect on the thruster performances, hence the difference between the two signals measured. However, this figure shows that, for these conditions and at this distance, the ion current density of the ECR thruster is comprised between  $0 \text{ A}\cdot\text{m}^{-2}$  and  $\approx 0.6 \text{ A}\cdot\text{m}^{-2}$ .

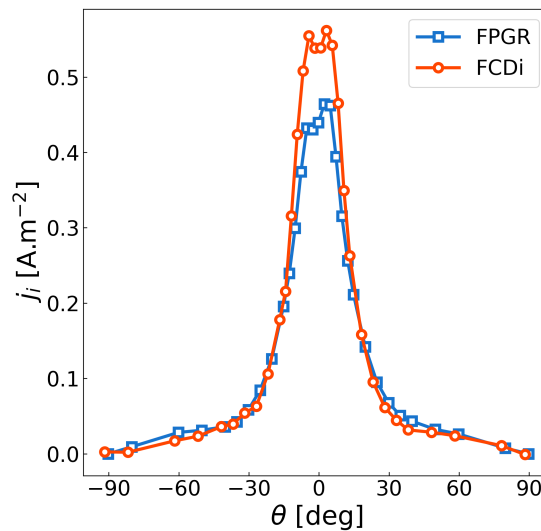


Figure 6.2: Angular scan of ion current density measured with the Faraday probe with guard ring (FPGR) and with the directional Faraday cup (FCDi) at  $\rho = 29$  cm. The ECR thruster is firing at 1 sccm and 20 W.

<b>Hypothesis</b>	<b>Justification</b>
The contribution of the electrons to the thrust is neglected	The ratio between the mass of the ions and the electrons is $m_i/m_e = 2.4 \times 10^5$
The ion ejection is axi-symmetrical	Figure 6.2, LIF measurements presented in chapter 3 and Faraday cup measurements presented in chapter 5
The ion velocity is independent from the angular position $\theta$	Verified in Ref. [32] and with LIF measurements in chapter 3
The Faraday probe allows a correct measurement of the true ion current density	Verification in section 6.2
The ions follow radial trajectories	Discussed in section 6.3
The secondary electron emission by ion impact is neglected	
The ions ionised more than one time are neglected	
Charge exchange collisions are neglected	

Table 6.1: Different hypothesis made in the indirect estimation of the thrust of the ECR thruster with the justification associated.

The different assumptions made to get an indirect estimate of the thrust of the ECR thruster are recalled above in table 6.1 with the justifications associated. The indirect estimations made so far in the literature are based on these assumptions. They led to estimations different from the direct measurements of the thrust. The objective of the following part is to observe and analyse this discrepancy. Then, in sections 6.2 and 6.3, these assumptions are analysed one by one in order to present a way to get a correct indirect estimate of the thrust of the ECR thruster from the measurement of the ion current density with a Faraday probe.

### 6.1.2 Results of the comparison for two types of Faraday probes

The thrust of the ECR thruster is estimated with equation 6.2 from the ion current density measured with the Faraday probe with guard ring, labelled FPGR in the figures, and with the directional Faraday cup introduced in chapter 4, labelled FCDi in the figures. The results are compared with the thrust measured with the thrust balance described in the experimental apparatus (section 2.2.4). For each thruster operating condition, the thrust is measured three times consecutively with the balance and the results are averaged to reduce the uncertainty of this diagnostic, which is 5% as discussed in section 2.2.4. Also, in order to better compare the direct and indirect thrust measurements between each other, the thrust is measured with the balance before each measurement of ion current density with a Faraday probe. Because the measurements of ion current density with the two different Faraday probes were performed

during two different measurement campaigns, the relevant figure used to compare the results is the error between the direct measurement and the indirect estimation of the thrust. In fact, by doing so, the variation of external parameters such as the level of vacuum inside the vacuum facility or the manipulation of the ECR thruster between two experimental campaigns that may create measurements repeatability issues are dismissed. Since the thrust stand is a calibrated diagnostic, the thrust measured with this device is supposed to be exact and serves as a reference.

In order to cover a significant range of thruster operating conditions, the measurements are performed for several xenon mass flow rates between 0.6 sccm and 2.4 sccm at 30 W of microwave power and for several powers between 20 W and 48 W at 1 sccm of mass flow rate (figure 6.3). The mean of the relatives errors made by the indirect method of estimation of the thrust compared to the direct measurement, in absolute value, of the different data points is represented with dashed lines on the figures and recalled in table 6.2 to evaluate the quality of the indirect thrust estimation. Results show that for every condition, the mean absolute value of the error between direct and indirect estimation of the thrust is reduced from a value between 20% and 30% to a value between 8% and 9 % when the ion current density is measured with the directional Faraday cup instead of the Faraday probe with guard ring (table 6.2). Moreover, the thrust estimated with the directional Faraday cup seems to better capture the evolution of the thrust with the operating conditions. In fact, for a microwave power of 30 W, the thrust estimated with the Faraday probe with guard ring is largely overestimated at low mass flow rates and underestimated at high mass flow rate (figure 6.3a). For a constant mass flow rate 1 sccm, the dispersion of the error of the thrust estimated with the Faraday probe with guard ring is more pronounced compared to the directional Faraday cup (figure 6.3b).

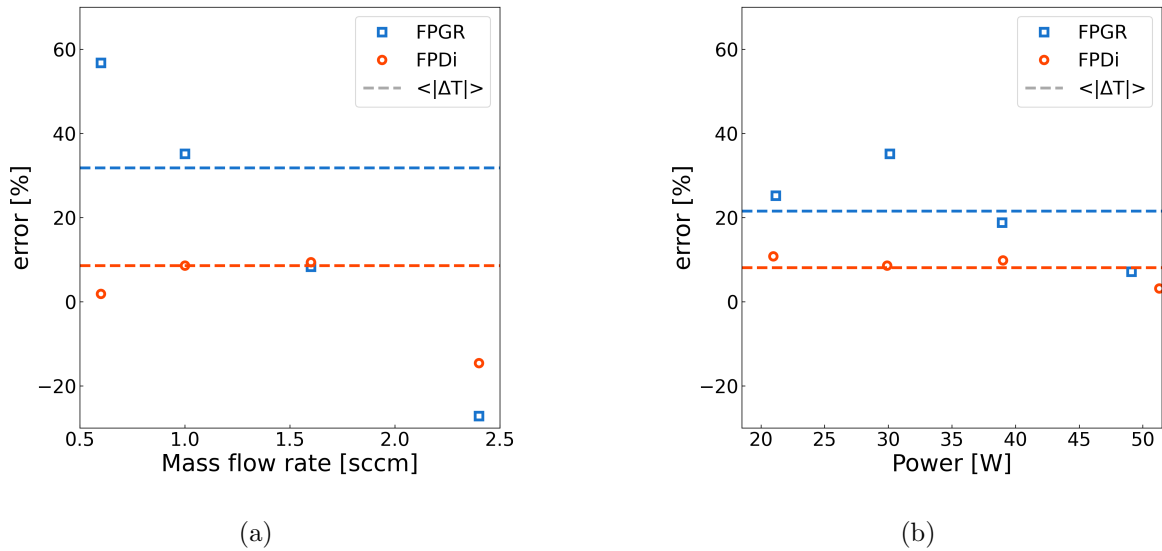


Figure 6.3: Comparison between the direct measurement of the thrust and its indirect estimation from the ion current density measured with either the Faraday probe with guard ring (FPGR) and the directional Faraday cup (FPDi) for (a) several thruster mass flow rates at 30 W of microwave power and (b) several thruster powers at 1 sccm of xenon mass flow rate.

	<b>FPGR</b>	<b>FCDi</b>
Constant power	31.84	8.65
Constant mass flow rate	21.70	8.10

Table 6.2: Averaged absolute values of the relatives errors (in %) made on the indirect thrust estimated from the ion current density measured with the Faraday probe with guard ring (FPGR) and the directional Faraday cup (FCDi).

Overall, the results presented in this section show that the directional Faraday cup allows a better estimation of the thrust than the Faraday probe with guard ring. The origin of a greater error with this latter diagnostic is analysed in the following section. Moreover, the uncertainty of the direct measurement of the thrust is 5% and, given the multiple assumptions made above and recalled in table 6.1, an error of 8% for an indirect estimation of the thrust is satisfactory as a first approximation. Nevertheless, this comparison shows that the indirect methodology generally overestimates the thrust of the ECR thruster. In fact, it is the case for every thruster operating condition, except the data point measured at high mass flow rate (2.4 sccm) for which an underestimation is observed whether the Faraday probe with guard ring or the directional Faraday cup is used. In order to address this systematic error and increase the accuracy of the estimation of the thrust from ion current density measurements, the assumptions made to estimate the thrust are analysed in section 6.3.

## 6.2 Analysis of the origin of the error when using a Faraday probe with guard ring

### 6.2.1 Comparison of the ion flux measurements performed with a Faraday probe with guard ring and a directional Faraday cup

The comparison between direct and indirect thrust measurements with the Faraday probe with guard ring presented above indicates that this diagnostic may not be suited to measure the true ion current density in the plume of the ECR thruster. In fact, the comparison of the integrand of equation 6.2 with the ion current density  $j_i$  measured with the Faraday probe with guard ring and with the directional Faraday cup shows the different shapes of the signal measured with these two probes (figure 6.4). The results presented in this figure are normalised to 1 to better illustrate that the overestimation of the current by the Faraday probe with guard ring has a greater contribution to the thrust at large absolute values of  $\theta$ . The ion current density reads  $j_i = en_i v_i$  and it has been shown that  $v_i$  does not depend on  $\theta$ . Therefore, given the shape of the angular scan of ion current density (figure 6.2), the ion density is lower in the region at large absolute value of  $\theta$  compared to the centre of the plume, i.e. for values of  $\theta$  around 0.

In order to confirm that the overestimation of ion current density measured by the Faraday probe with guard ring increases when the ion density decreases, angular scans of ion current density are performed at several distances  $\rho$  from the thruster backplate with both probes (notation and experimental setup introduced in figure 5.1). The thruster mass efficiency  $\eta_m$  is computed at each distance to compare the current measured by the Faraday probe with guard ring and by the directional Faraday cup (figure 6.5). This performance indicator is chosen because it is comprised between 0 and 100% and does not depend on the distance from the

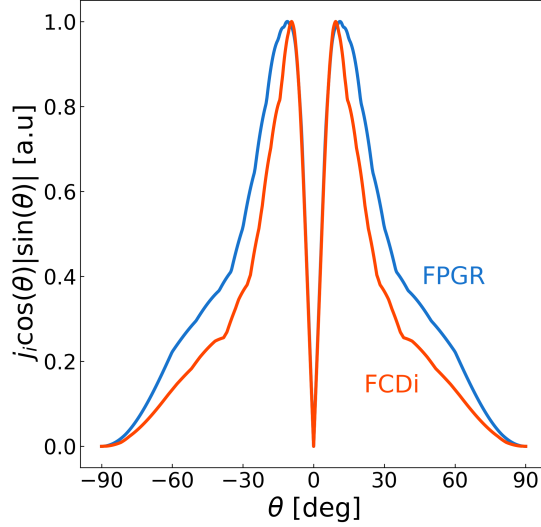


Figure 6.4: Comparison between the integrand of equation 6.2 with the ion current density  $j_i$  measured with the Faraday probe with guard ring (FPGR) and the directional Faraday cup (FCDi). The ECR thruster is firing at 1 sccm and 20 W.

thruster. In fact, it is constant at least for distances greater than 10 cm because no ionisation occurs at such distances. It is defined as the ratio between the ion mass flow rate ejected from the thruster, denoted by  $\dot{m}_{Xe^+}$ , and the gas mass flow rate fed to the thruster, denoted by  $\dot{m}$ . With the same hypothesis made in the previous section, it reads:

$$\begin{aligned}
 \eta_m &= \frac{\dot{m}_{Xe^+}}{\dot{m}} \\
 &= \frac{m_i I_b}{\dot{m} e} \\
 &= \frac{m_i}{\dot{m} e} \pi \rho^2 \int_{-\frac{\pi}{2}}^{\frac{\pi}{2}} j_i(\theta) |\sin(\theta)| d\theta
 \end{aligned} \tag{6.4}$$

where  $I_b$  is the total ion beam current. Results show that the thruster mass efficiency is greater when computed from the ion current density measured with the Faraday probe with guard ring instead of the directional Faraday cup. Moreover, it increases with the distance to the thruster. This observation is in line with an overestimation of the ion current density measured with this diagnostic when the ion density decreases. On the other hand, whatever the distance at which the ion current density is measured with the directional Faraday cup, the thruster mass efficiency computed with equation 6.4 is constant and is around 40%. This result shows that if there is any overestimation of the current measured by the directional Faraday cup, it does not depend on a plasma parameter that varies with the distance at which the measurement is performed. The computation of the other types of efficiency as well as a value of the integrated current for several thruster conditions are found in appendix D.

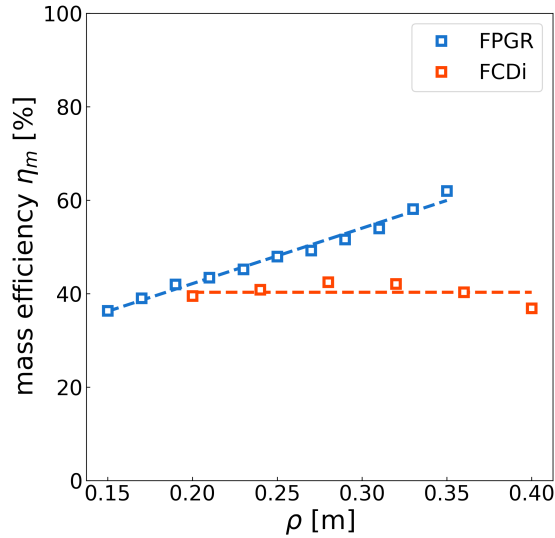


Figure 6.5: Evolution of the mass efficiency  $\eta_m$  with the distance from the thruster backplate  $\rho$ . The thruster is firing at 1 sccm and 30 W.

The results presented in this section show that the overestimation of the thrust of the ECR thruster when the ion current density is measured by the Faraday probe with guard ring comes from an overestimation of ion current density measured by this diagnostic which happens when the ion density decreases. This effect is not observed when the ion current density is measured with the directional Faraday cup though. The difference of behaviour observed between these two diagnostics could lie in the different shapes of the diagnostics, leading to different shapes of plasma sheath that forms in front of the collectors. In order to investigate this point, the effect of a large plasma sheath in front of a flat collector is analysed in the following subsections by means of electrostatic simulations of the Faraday probe with guard ring with the software SIMION and with an estimation of the plasma sheath thickness.

### 6.2.2 Electrostatic simulation of a Faraday probe with guard ring with the software SIMION

The Faraday probe with guard ring has been designed by S.Peterschmitt in Ref. [33] according to the recommended practices of Ref. [4] which advise to select a guard ring diameter  $\varnothing_{FPGR}$  greater than 50 times the Debye length  $\lambda_D$  of the plasma. Therefore, the diameter of the guard ring is  $\varnothing_{FPGR} = 50$  mm because the Debye length of the plasma a few tenths of centimetres away from the ECR thruster backplate was estimated to be of the order of the millimetre. Moreover,  $\varnothing_{FPGR}$  has been chosen to be not too large in order to limit the perturbation of the plasma that a large metallic surface biased at large negative voltage would induce. The criterion  $\varnothing_{FPGR}/\lambda_D > 50$  is referred to as Brown's criterion in the remaining of this section. If it is satisfied, the sheath that forms in front of the probe should be flat in front of the collector and the ion collection area should therefore be flat and equal to the collector area. In fact, conversely, a plasma sheath too thick can be round in front of the collector of a probe, inducing an artificial and unwanted increase of the ion collection area. An ion collection area greater than the area of the probe collector leads to an overestimation of the ion current density (illustration in figure 6.6).

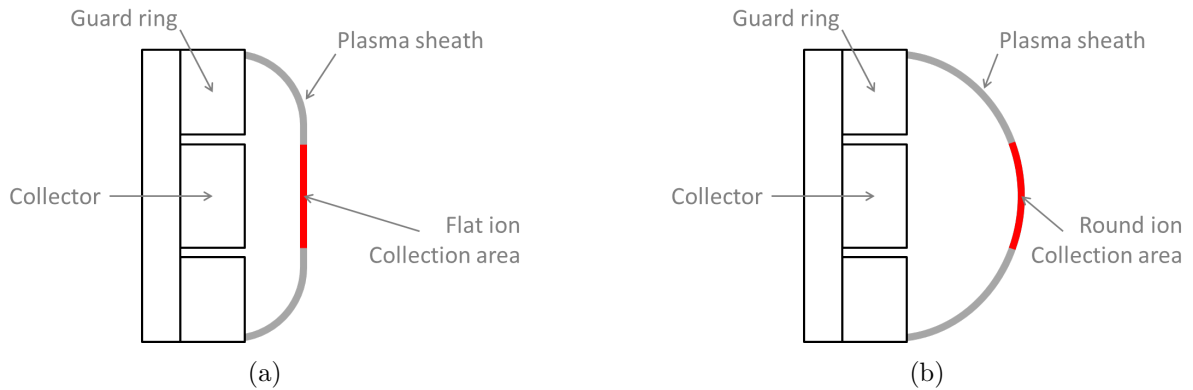


Figure 6.6: Illustration of the ion collection area in front of a Faraday probe with guard ring for (a) a flat sheath and (b) a non-flat sheath.

To model the effect of a sheath that is too thick in front of the probe collector, the Faraday probe with guard ring is simulated with the software SIMION presented in section 4.2.2. The parameters used are identical to that used to simulate the Acceptance function of the directional Faraday probe. The collector and the guard ring are biased at a voltage of  $-300\text{ V}$  and a transparent grid at a potential  $0\text{ V}$  is placed in front of the mesh of the probe to simulate a virtual sheath thickness as done in chapter 4. The distance between the probe and the grid is adjusted to simulate different guard ring diameter to sheath thickness ratios (figure 6.7).

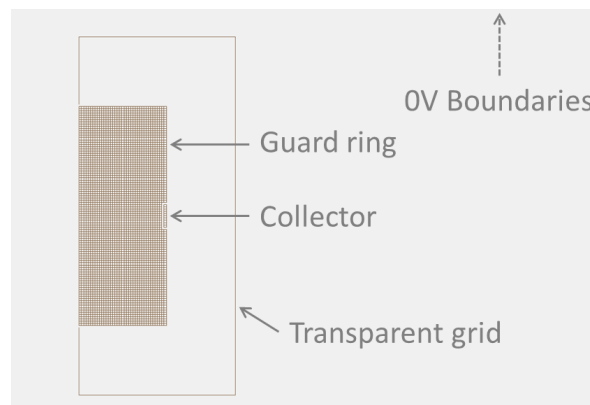


Figure 6.7: Mesh of the Faraday probe with guard ring in the software SIMION.

The Acceptance of the Faraday probe with guard ring is simulated for several  $\varnothing_{FPGR}$  to  $s_{sheath}$  ratio, where  $s_{sheath}$  is the position of the transparent grid biased at  $0\text{ V}$  placed all around the probe. The simulation in ideal regime, i.e. with no bias applied either to the collector or to the guard ring of the Faraday probe, is also carried out and the results are compared to the theoretical Acceptance of the Faraday probe, which is a cosine in the range  $-\pi/2 \leq \beta \leq \pi/2$  and 0 elsewhere (figure 6.8). Results show that the ratio  $\varnothing_{FPGR}/s_{sheath}$  should be at least 6 to neglect the effect of the sheath thickness on the Acceptance function of the Faraday probe with guard ring. However, this value is only indicative because the simulation is electrostatic and the software SIMION cannot simulate the true behaviour of a plasma sheath. A quantitative analysis of the error induced by the presence of a sheath in front of the Faraday probe with guard ring would require more precise simulations that could be achieved with a particle in cell

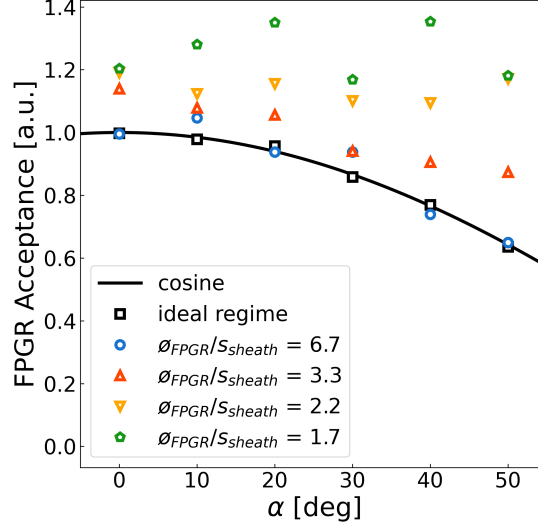


Figure 6.8: Theoretical Acceptance function (black solid line) of the Faraday probe with guard ring and Acceptance simulated with SIMION at several  $\emptyset_{FPGR}/s_{sheath}$  ratios.

(PIC) code for example.

The increase of the Acceptance function due to the expansion of the plasma sheath is the combination of two effects. First, for values of  $\alpha$  around 0, it is due to a electrostatic lens that forms in front of the collector of the probe which focuses the ion beam and induces an over-collection of ions. Second, at large values of  $\alpha$ , the overestimation of current comes from a bending of the ion trajectories, which hit the collector instead of the guard ring. Overall, both effects are due to a too large sheath thickness in front of the Faraday probe. The thickness of the sheath that forms in front of the Faraday probe with guard ring when it is immersed in the plasma plume of the ECR thruster is evaluated, and the validity of Brown's criterion is assessed in the next section.

### 6.2.3 Estimation of the sheath thickness and its relation to the probe design

One explanation of the overestimation of ion current density measured by the Faraday probe with guard ring observed in the previous section is that the Brown's criterion is no longer verified when the ion density is low, i.e. at low Debye length. The Debye length reads:

$$\lambda_D = \sqrt{\frac{\epsilon_0 e T_e}{e^2 n_e}} \quad (6.5)$$

where  $T_e$  is the electron temperature expressed in eV, and  $\epsilon_0$  is the vacuum permittivity. In the approximation of a neutral plasma, already discussed in the manuscript, the electron and ion densities are equal, i.e.  $n_e = n_i$ . Also, with the ion current density written as  $j_i = e n_i v_i$ , it comes:

$$\lambda_D \approx \sqrt{\frac{\epsilon_0 T_e v_i}{j_i}} \quad (6.6)$$

Brown's criterion is represented along an angular scan of ion current density measured with the Faraday probe with guard ring at  $\rho = 29$  cm with a thruster firing at 1 sccm and 20 W for

two values of electron temperature,  $T_e = 10$  eV and  $T_e = 100$  eV (figure 6.10). These values are chosen as lower and upper bounds of the electron temperature encountered in the plume of the ECR thruster. This figure shows that Brown's criterion  $\varnothing_{FPGR}/50\lambda_D > 1$  is not satisfied whatever the value of the electron temperature. Moreover, it shows that the greater the value of  $\theta$ , the less verified the criterion. It is in line with the overestimation of ion current observed in this region.

Given the high negative voltage used to bias the collector and the guard ring of this probe in the case of the ECR thruster ( $V_b = -350$  V), the size of the sheath might be governed by the Child-Langmuir sheath law. The sheath thickness governed by this law is denoted by  $s_{CL}$ . According to the simulation results presented in the previous section, the criterion  $\varnothing_{FPGR}/s_{CL} \gg 1$  should then be satisfied to ensure a flat sheath in front of the collector of the Faraday probe with guard ring and therefore measure the true ion current density with this diagnostic. The thickness of the sheath that forms in front of a wall at potential  $V_0$  governed by the Child-Langmuir law is [9]:

$$s_{CL} = \frac{2}{3} \sqrt{\frac{\epsilon_0}{j_i}} \left( \frac{2e}{m_i} \right)^{1/4} V_0^{3/4} \quad (6.7)$$

In the plume of the ECR thruster, at the location of the measurements performed with the Faraday probe with guard ring, the ion current density is comprised between  $0$  A.m<sup>-2</sup> and  $0.6$  A.m<sup>-2</sup> (figure 6.2). With this value of ion current density, the Child-Langmuir sheath thickness is comprised between  $5$  mm and  $20$  cm and increases when the ion current density decreases (figure 6.9). This value can then be comparable to the diameter of the guard ring of the probe which is  $\varnothing_{FPGR} = 50$  mm.

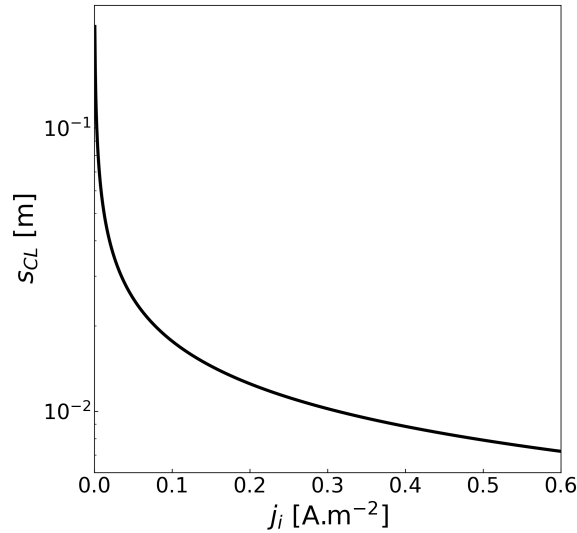


Figure 6.9: Child-Langmuir sheath thickness for a wall at potential  $V_0 = -350$  V.

The Debye length and the Child-Langmuir sheath thickness are compared with the diameter of the Faraday probe with guard ring along the  $\theta$ -scan of the thruster operating condition 1 sccm of mass flow rate and 20 W of power (figure 6.10). The value of this second criterion is  $\varnothing_{FPGR}/s_{CL} \approx 6$  at the centre of the plume and  $\varnothing_{FPGR}/s_{CL} \approx 0.8$  on the edges. Therefore, the guard ring diameter is not significantly larger than the Child-Langmuir sheath thickness when the bias voltage of the probe is low. Finally, results show that the dependence on  $1/\sqrt{j_i}$  of both the Debye length and the Child Langmuir sheath thickness implies that the sheath that forms in front of the Faraday probe with guard ring probably increases sufficiently to induce an effective ion collection area greater than the geometrical area of the collector. It implies an overestimation of the ion current density measured by this probe where the ion density is low, i.e. far from the centre of the plume, for high values of  $\theta$ . This is in line with the results presented in figure 6.4 and 6.5 and discussed above.

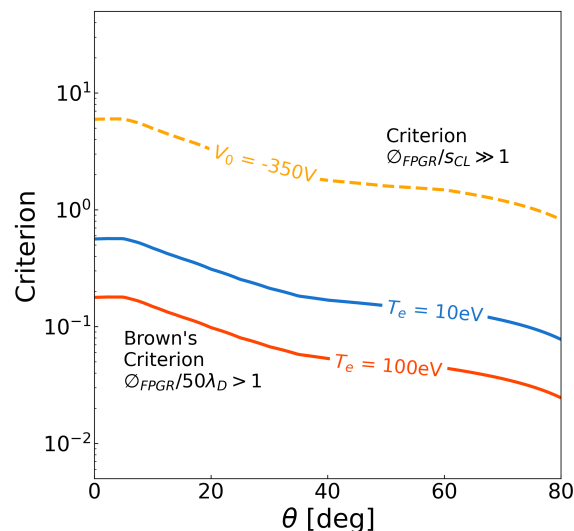


Figure 6.10: FPGR guard ring diameter to fifty Debye length ratio (Brown's criterion [4]) and Child-Langmuir sheath thickness to FPGR guard ring diameter ratio for several electron temperatures and probe bias voltages.

The results presented in this section show the cause of the overestimation of ion current density measured by the Faraday probe with guard ring. They bring an explanation to the general overestimation of thrust indirectly estimated with this diagnostic observed in figure 6.3. The fact that the directional Faraday cup has a metallic opening ring tight to ground at the entrance of the cup limits the expansion of a sheath governed by the Child-Langmuir law, and permits to collect a meaningful value of current, even at low plasma densities. However, even with this diagnostic, a discrepancy is still observed when the thrust estimated from the measurement of ion current density is compared with the direct measurement of the thrust. To address this problem, the different approximation used to estimate the thrust are discussed in the next section.

## 6.3 Accuracy of the hypothesis made in the indirect estimation of the thrust

In this section, all of the hypothesis made to estimate the thrust from the measurement of ion current density performed with the directional Faraday cup, which are recalled in table 6.1, are analysed one by one. In fact, from the results of the section above, it is possible to conclude that the ion current density measured with this diagnostic is meaningful but a discrepancy remains when the indirect estimation of the thrust is compared with the direct measurement of the thrust with a thrust stand. In fact, a general overestimation is observed for all of the thruster conditions except at high thruster mass flow rate where the estimation is lower than the direct measurement of the thrust.

### 6.3.1 Local ion trajectories

In equation 6.2, all of the ions are supposed to be ejected from the thruster with a radial trajectory. However, results presented in chapter 5 show that, in the centre of the plume, the ions follow the magnetic field lines at distances comprised between  $\rho = 20$  cm and  $\rho = 60$  cm away from the thruster backplate. In fact, the ions have a local trajectory  $\alpha_i$  which is different from 0 and comprised between -10 degrees and +10 degrees. Even though the ion current density is measured with the current collected in cup mode (sum of the plate and cylinder), the fact that two separate acquisitions circuits are used allow to determine the most probable local ion trajectory. The details of the determination of  $\alpha_i$  from an angular scan of the ion current density performed with the directional Faraday cup are found in chapter 5. Three angular scans of ion current measured on the plate of the directional Faraday cup are compared to illustrate this point (figure 6.11). In this figure, the thruster is firing at 1 sccm and 20 W.

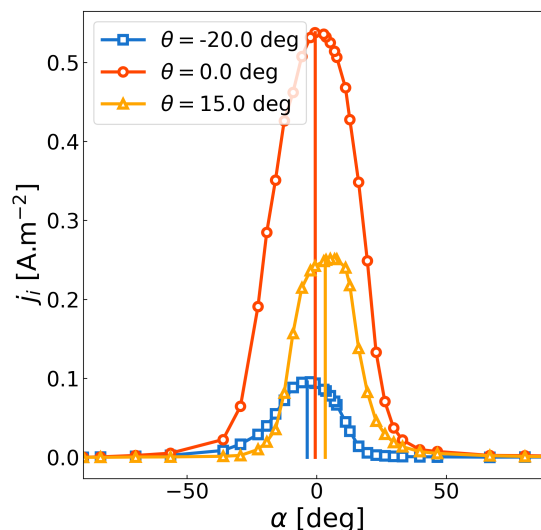


Figure 6.11: Examples of three angular scans of ion current measured on the plate of the directional Faraday cup at the angular positions  $\theta = -20$  deg,  $\theta = 0$  deg and  $\theta = 10$  deg. The ECR thruster is firing at 1 sccm and 20 W.

To take into account the local trajectory of the ion flux in the indirect estimation of the thrust, the integral term of equation 6.2 is modified. First, similarly to the thrust estimated in equation 6.2, in the estimation of the thrust, denoted by  $T_A$ , the ion current density is measured with the directional Faraday cup facing the thruster, i.e. for  $\alpha = 0$ , and the ion trajectories are projected along the radial direction. It reads:

$$T_A = \pi \rho^2 \frac{m_i v_i}{e} \int_{-\frac{\pi}{2}}^{\frac{\pi}{2}} j_i(\theta, 0) \cos(\theta) |\sin(\theta)| d\theta \quad (6.8)$$

The second variation of equation 6.2, denoted by  $T_B$ , takes into account the true trajectory of the ions in the  $j_i$  term and in the projection term. In fact, in this case, the ion current density is measured when the directional Faraday cup faces the most probable direction of the ion flux, i.e. when it is rotated of an angle  $\alpha = \alpha_i$ , and the ion current is projected along the true direction of the ion flux. It reads:

$$T_B = \pi \rho^2 \frac{m_i v_i}{e} \int_{-\frac{\pi}{2}}^{\frac{\pi}{2}} j_i(\theta, \alpha_i(\theta)) \cos(\theta + \alpha_i(\theta)) |\sin(\theta)| d\theta \quad (6.9)$$

The comparison between these two ways of computing the thrust from the ion current density measured with the directional Faraday cup with a direct measurement of the thrust (figure 6.12 and table 6.3) shows that taking into account the ion trajectory in the expression of the indirect estimation of the thrust does not contribute significantly to reduce the error made on this estimation. In fact, taking into account the local most probable direction of the ion flux to project the ion speed improves very marginally (about 1 %) the accuracy of the indirect thrust measurements. To better compare the results, the means of the absolute value of the error at constant thruster power and constant thruster mass flow rate are recalled in table 6.3.

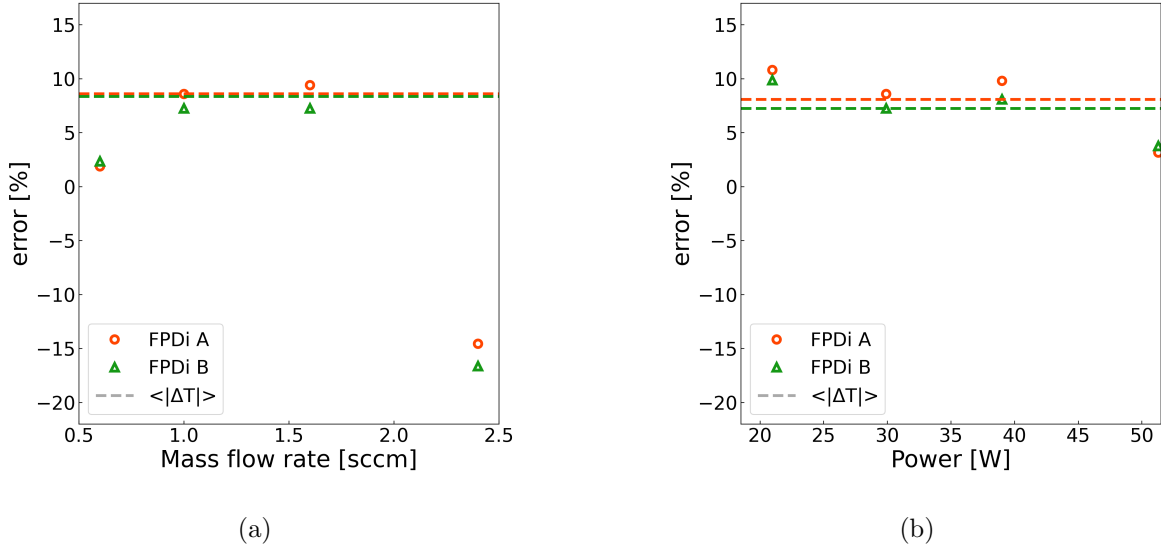


Figure 6.12: Comparison between the direct measurement of the thrust and its indirect estimation from the ion current density measured with the directional Faraday cup according to equations 6.8 and 6.9 for (a) several thruster mass flow rates at 30 W of microwave power and (b) several thruster powers at 1 sccm of xenon mass flow rate.

	FCDi A	FCDi B
Constant power	8.65	8.35
Constant mass flow rate	8.10	7.24

Table 6.3: Averaged absolute values of the relatives errors (in %) made on the thrust for the different indirect thrust estimation methods of equations 6.8 and 6.9.

In equation 6.9, the fact that the ion current is measured when the directional Faraday cup faces the ion flux (in  $\alpha = \alpha_i$ ) necessarily increases the estimation of the thrust, by definition of the position  $\alpha_i$ . However, the fact that  $\alpha_i$  is always positive (resp. negative) for positives (resp. negative) values of  $\theta$ , as presented in chapter 5, implies a reduction of the estimation of the thrust. In fact, the cosine of  $\theta + \alpha_i$  is lower than the cosine of  $\theta$ . However, the combination of these two effects does not explain the general overestimation of the thrust by indirect method. The other assumptions should therefore also be analysed.

### 6.3.2 Secondary electron emission

The secondary electron emission by ion impact on the Faraday probe collector is often cited as a term to take into account in electrostatic probes measurements. In fact, if the electrons emitted are not recollected by the Faraday probe, the current measured is artificially increased, which is likely with a Faraday probe with guard ring regarding its planar geometry. The correcting factor to take into account the secondary electron emission is [4]:

$$K_{SEE} = \frac{1}{1 + \sum_{k=I,II,\dots} \frac{\Omega_k \gamma_k}{Z_k}} \quad (6.10)$$

where  $\Omega_k$  is the fraction of ions ionised  $k$  times, of charge state  $Z_k$  and secondary electron emission yield coefficient  $\gamma_k$ . The secondary electron emission yield coefficients for  $Xe^+$  and  $Xe^{2+}$  ions on molybdenum are around  $\gamma_I = 0.02$  and  $\gamma_{II} = 0.2$  respectively for energies below 1 keV [73]. In the case of the Faraday probe with guard ring, it induces an error of 2% to 5%, depending on the proportion of doubly ionised ions. However, in the case of the directional Faraday cup, the cylinder is made of graphite, with a yield coefficient of a few  $10^{-3}$ , which is significantly lower than the molybdenum [74]. With the cup design, secondary emitted electrons are more likely to be recollected, which lowers the influence on the signal measured in cup mode. Hence, the role of the secondary electron emission in the overestimation of the thrust of the ECR thruster when the current is measured with the directional Faraday cup is discarded.

### 6.3.3 Multiply charged ions

In section 6.1.1, the plasma is considered to be constituted of singly charged ions only and the contribution of multiply charged species to the thrust is neglected. However, this hypothesis might be too strong. In fact, the ion mass scan obtained with the ion analyser with a thruster firing at 1 sccm and 30 W shows that the population of ions ionised twice cannot be neglected (figure 6.13). In fact, in this signal, a peaks corresponding to the population ionised  $N$  times is observed at the atomic mass unit  $m_i/N$ . Therefore, the absence of signal below  $m_i/2$  confirms that the ions ionised more than two times can effectively not be considered in this analysis.

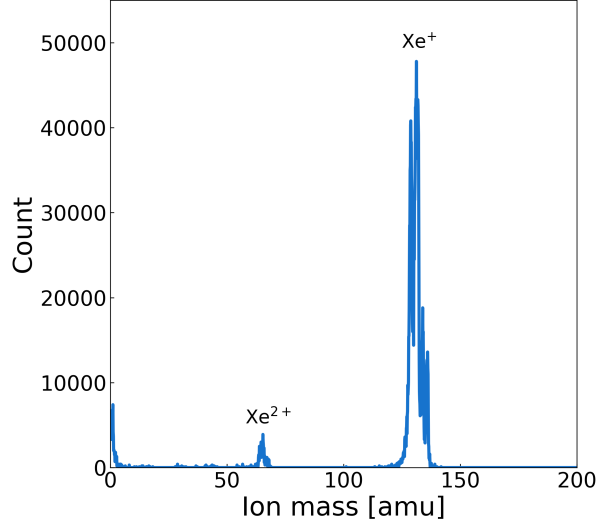


Figure 6.13: Ion mass scan measured with the ion analyser at 1 sccm and 30 W.

Let consider that the plasma is constituted of singly ionised ions of density  $n_I$ , velocity  $v_I$  and energy  $E_I$  and doubly charged ions of density  $n_{II}$ , velocity  $v_{II}$  and energy  $E_{II}$ . The parameter  $\eta$  is introduced as the ratio between the densities of the two populations such that  $n_{II} = \eta n_I$ . The ion energies of these two populations are considered to be equals because the ionisation occurs in the source of the ECR thruster and particles undergo an acceleration in the magnetic nozzle which does not depend on their charge:

$$\begin{aligned} E_I = E_{II} &\Rightarrow \frac{m_i}{2e} v_I^2 = \frac{m_i}{4e} v_{II}^2 \\ &\Rightarrow v_{II} = \sqrt{2} v_I \end{aligned} \quad (6.11)$$

On the one hand, the thrust  $T^{mes}$  estimated from Faraday cup measurements of ion current density is:

$$\begin{aligned} T^{mes} &= \pi \rho^2 \frac{m_i v_I}{e} \int_{-\frac{\pi}{2}}^{\frac{\pi}{2}} (e n_I v_I + 2 e n_{II} v_{II}) \cos(\theta) |\sin(\theta)| d\theta \\ &= (1 + 2\sqrt{2}\eta) T_I \end{aligned} \quad (6.12)$$

where  $T_I$  is the contribution of the singly charged ions to the thrust. On the other hand, the total thrust  $T^{tot}$ , measured with the thrust stand, is the sum of the contribution of the singly and doubly charged ions:

$$\begin{aligned} T^{tot} &= T_I + T_{II} \\ &= (1 + 2\eta) T_I \end{aligned} \quad (6.13)$$

Therefore, the error  $\epsilon_{multi}$  made on the indirect estimation of the thrust because of the contribution of doubly charged ions is:

$$\begin{aligned} \epsilon_{multi} &= \frac{T^{mes} - T^{tot}}{T^{tot}} \\ &= \frac{2(\sqrt{2} - 1)\eta}{1 + 2\eta} \end{aligned} \quad (6.14)$$

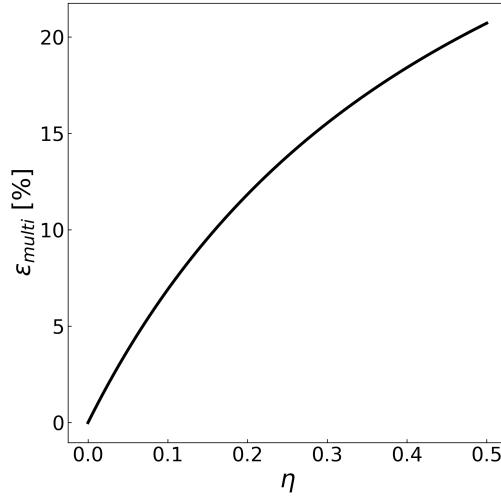


Figure 6.14: Evolution of  $\epsilon_{multi}$  with  $\eta$ .

The parameter  $\eta$  is extracted from the ion mass scans performed with the ion analyser (figure 6.13). It is comprised between 0 and 0.1 in the range of thruster operating conditions tested and leads to an error  $\epsilon_{multi}$  comprised between 0% and 6% (figure 6.14). Therefore, it could explain the general overestimation of the thrust obtained by indirect methodology observed in figure 6.3. However, it does not explain the large underestimation of the thrust for a mass flow rate greater than  $\dot{m} = 2$  sccm. This point is dealt with in the following subsection.

### 6.3.4 Charge exchange collisions

Results presented in section 6.1.2 show that the thrust estimated at high mass flow rate, i.e. at 2.4 sccm, is lower than the thrust measured with the thrust balance, whether it is estimated with the ion current density measured with the directional Faraday cup or the Faraday probe with guard ring. This is in contradiction with the general overestimation of the thrust with the indirect method observed in the other cases. This observation can be explained by the rise of the vacuum chamber pressure (see section 2.2.1) and the diminution of the ion energy when the thruster mass flow rate increases (figure 6.15). In fact, these two factors increase the neutral density encountered by the ion flux and the charge exchange cross-section respectively [75]. The mean free path of the  $Xe^+$  ions is then reduced and the ions are more likely to encounter a charge exchange collision during their acceleration in the magnetic nozzle of the thruster. Therefore, at high mass flow rate, the plume of the thruster may contain a significant amount of neutrals at high velocity that contribute to the thrust without being measured by any ion collection probe.

To assess the contribution of charge exchange collisions to the indirect estimation of the thrust, let us consider a population of ions that have encountered a charge exchange collision during their acceleration in the magnetic nozzle of the ECR thruster. It results from these collisions a population of slow ions with a density  $n_{i,s}$  and an energy  $E_{i,s}$  and a population of fast neutrals with a density  $n_{n,f}$  in addition to the main (and fast) population of ions of density

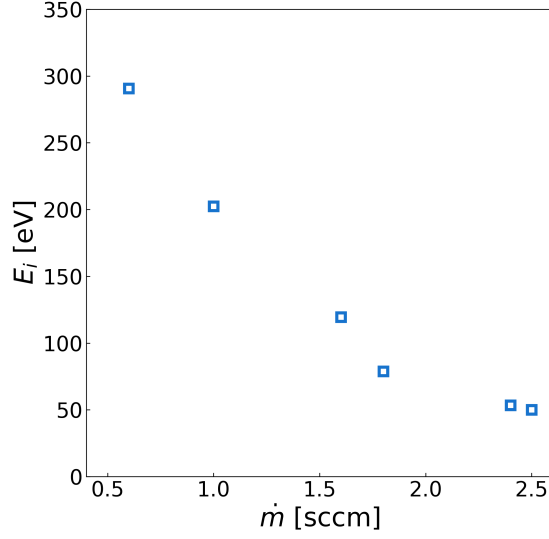


Figure 6.15: Evolution of the ion energy with the mass flow rate of the ECR thruster.

$n_{i,f}$  and energy  $E_{i,f}$ . Two parameters,  $\tau$  and  $\kappa$ , are then defined as follows:

$$\begin{aligned} n_{i,s} &= \tau n_{i,f} \\ E_{i,s} &= \kappa E_{i,f} \\ v_{i,s} &= \sqrt{\kappa} E_{i,f} \end{aligned} \quad (6.15)$$

First, the fact that every charge exchange collision results in one fast neutral per slow ion gives:

$$n_{n,f} = n_{i,s} \quad (6.16)$$

Moreover, the energy of a fast neutral depends on the energy of the ion before its collision with a slow neutral. The energy gained by the slow ion population in the magnetic nozzle after the charge exchange collision is  $E_{i,s}$ . Therefore, the energy of the fast neutrals is  $E_{i,f} - E_{i,s}$ . It reads:

$$\begin{cases} n_{n,f} = n_{i,s} = \tau n_{i,f} \\ E_{n,f} = E_{i,f} - E_{i,s} = (1 - \kappa) E_{i,f} \end{cases} \quad (6.17)$$

On the one hand, the thrust estimated with equation 6.2 takes into account the contribution of the slow ions resulting from a charge exchange collision only in the ion current density term. The ion velocity term captures only the energy of the fast ions. Hence, the indirect measurement of the thrust  $T^{mes}$  is:

$$\begin{aligned} T^{mes} &= \pi \rho^2 \frac{m_i v_{i,f}}{e} \int_{-\frac{\pi}{2}}^{\frac{\pi}{2}} e (n_{i,s} v_{i,s} + n_{i,f} v_{i,f}) \cos(\theta) |\sin(\theta)| d\theta \\ &= (1 + \tau \sqrt{\kappa}) T_{i,f} \end{aligned} \quad (6.18)$$

where  $T_{i,f}$  is the contribution of the fast ions to the thrust. On the other hand, the total thrust  $T^{tot}$ , measured with the thrust stand, is the sum of the contributions of the fast ions, slow ions

and fast neutrals to the thrust, respectively  $T_{i,f}$ ,  $T_{i,s}$  and  $T_{n,f}$ , such that:

$$\begin{aligned}
 T^{tot} &= T_{i,f} + T_{i,s} + T_{n,f} \\
 &= (1 + \tau\kappa + \tau(1 - \kappa)) T_{i,f} \\
 &= (1 + \tau) T_{i,f}
 \end{aligned} \tag{6.19}$$

Therefore the error  $\epsilon_{cex}$  made on the indirect estimation of the thrust because of the contribution of the charge exchange collisions is:

$$\begin{aligned}
 \epsilon_{cex} &= \frac{T^{mes} - T^{tot}}{T^{tot}} \\
 &= \frac{\tau(\sqrt{\kappa} - 1)}{1 + \tau}
 \end{aligned} \tag{6.20}$$

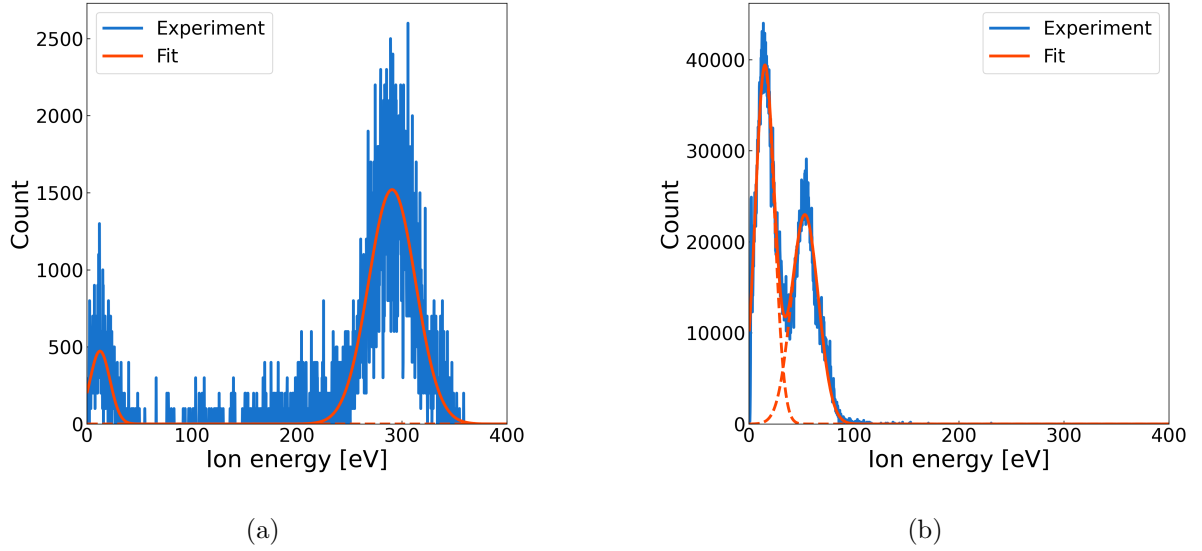


Figure 6.16: Ion energy distribution function measured with the ion energy analyser at (a) 0.6 sccm and (b) 2.5 sccm.

The ion energy scan performed with the ion energy analyser shows two peaks that are fitted with a Gaussian function to ease the analysis (figure 6.16). The peak at high energy corresponds to the energy distribution of the fast population while the peak at low energy corresponds to the slow ion population. From this signal, the factors  $\tau$  and  $\kappa$  are measured as the ratio between the integral of the two peaks and the ratio between the average energy of the two peaks respectively. The two signals presented on these figures correspond to the mass flow rates 0.6 sccm (figure 6.16a) and 2.5 sccm (figure 6.16b) and illustrate the influence of this condition on the ratio between the fast and slow ions. In fact, at low mass flow rates, the dominant population is the fast ions population while at high mass flow rates, the slow ions population is significantly higher than the fast ions population. This is mainly due to the increase of the pressure in the vacuum chamber at higher mass flow rates, therefore reducing the mean free path associated to the charge exchange collisions.

The parameters  $\kappa$  and  $\tau$  are estimated for the different thruster mass flow rates at 30 W of microwave power (figure 6.17a). On the one hand,  $\tau \geq 1$  for values  $\dot{m} \geq 2$ , meaning that the slow ion population becomes dominant at high mass flow rate. On the other hand,  $\kappa$  is comprised between 0.05 and 0.4 but no clear tendency is observed. The error  $\epsilon_{ceex}$  is computed with the values of  $\kappa$  and  $\tau$  for the range of thruster mass flow rates considered (figure 6.17b). First, the contribution of the slow ions to the thrust is :

$$T_{i,s} = \tau \kappa T_{i,f} \quad (6.21)$$

Therefore, because  $\tau \geq 0$  and  $\kappa \geq 0$  (by definition) and using equation 6.18, it comes:

$$T^{mes} \geq T_{i,f} + T_{i,s} \quad (6.22)$$

Equation 6.22 shows that the presence of slow ions in the plume of the ECR thruster measured by the Faraday probes induces an overestimation of the thrust compared to the effective thrust resulting from slow and fast ions only. However, figure 6.17b shows that  $\epsilon_{ceex} \leq 0$ , i.e.  $T^{mes} \leq T^{tot} = T_{i,f} + T_{i,s} + T_{n,f}$ . This result shows that the contribution of the fast neutrals to the thrust, which is taken into account when the thrust is measured by the thrust balance but not when it is estimated by any ion collection probe induces an underestimation that is significantly greater than the overestimation induced by the presence of slow ions. Thus, for mass flow rates lower than 1.6 sccm, the error  $\epsilon_{ceex}$  is comprised between -2% and -9%. However, for mass flow rates greater than 2 sccm, it drops down to -25%. Hence, the presence of neutrals at high velocity due to charge exchange collisions could explain the large underestimation of the thrust calculated by indirect method of more than 20% and the tendency observed in figure 6.3. This discrepancy between indirect and direct thrust measurement is observed with either the Faraday probe with guard ring and the directional Faraday cup and may then be due to the test conditions and not to the probe performances.

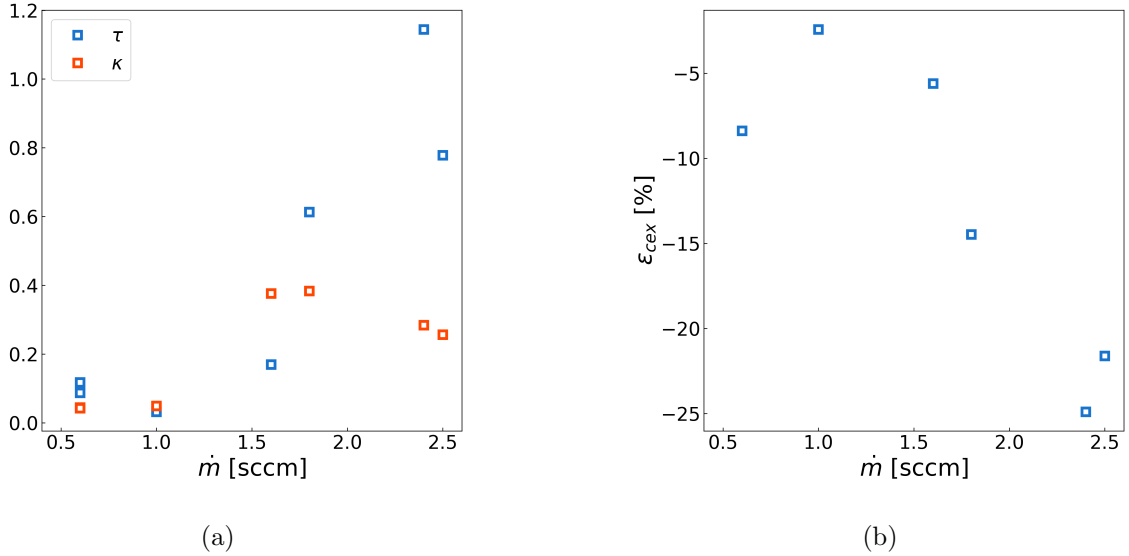


Figure 6.17: Evolution of (a)  $\kappa$  and  $\tau$  and (b)  $\epsilon_{ceex}$  with the thruster mass flow rate.

## Conclusion

Results presented in this chapter show that the estimation of the thrust of an ECR thruster from ion flux measurements is possible. First, the use of the directional Faraday cup instead of the Faraday probe with guard ring allows the measurement of the accurate ion current density. In fact, in the plume of the ECR thruster, the collectors of electrostatic probes must be biased at high negative voltage. It induces a large plasma sheath that leads to an overestimation of the current density measured in the case of a flat Faraday probe with guard ring, especially at low ion density. The metallic ring tight to ground that closes the directional Faraday cup limits significantly this effect. Second, the assumptions made to estimate the thrust in a first place are too restrictive. Results show that the thrust induced by the ions ionised twice is significant and these species cannot be neglected. Also, the presence of slow ions and fast neutrals resulting from a charge exchange collision must also be considered. In fact, the population of fast neutrals becomes significant at mass flow rates higher than 2 sccm and, if their contribution is not taken into account, it can lead to a large underestimation of the thrust. Finally, results show that taking into account the local trajectory of the ions in the thrust has only a minor effect on the estimation, reducing the error by only 1%.

A recommended practice to estimate the thrust of the ECR thruster without using a thrust balance would then be to use the directional Faraday cup in cup mode, and for each thruster condition, perform a mass and an energy scan of the ions to determine the proportion of doubly charged ions and the proportion of ions that encountered a charge exchange collision. The contribution of doubly charged ions and charge exchange collisions can thus be taken into account in the estimation of the thrust. Moreover, according to the results presented in section 6.3.1, a angular scan of ion current density with the directional Faraday cup facing the thruster, i.e. fixed at the position  $\alpha = 0$  for all  $\theta$ , is sufficient to get a satisfactory estimate of the thrust and limit the complexity of the measurements.

To integrate the ion current density measured with an electrostatic diagnostic is not the only way to estimate the thrust of an electric propulsion device without measuring it with a thrust balance. In fact, a new type of force probe is being developed at ONERA in the electric propulsion laboratory [76]. This probe is intended to measure directly the momentum of the different particles that hit its surface and will offers several advantages for the estimation of the thrust. First, it is independent from the degree of ionisation of the charged specie, and, second, it also measures the flux of neutrals which is not probed with electrostatic diagnostics. Finally, the estimation of the thrust with this sensor will not rely on measurements performed with the ion analyser measurement anymore, which will reduce the uncertainties.



# Conclusion

The main objective of this work, as stated in the introduction, was the production of experimental data necessary to confront theoretical models and simulations which describe the dynamics of a plasma in expansion in a diverging magnetic nozzle. To this end, several diagnostics were used to perform measurements of the plasma parameters in the plume of a low power Electron Cyclotron Resonance (ECR) thruster.

First, the existing Laser Induced Fluorescence (LIF) setup was improved thanks to the installation of a perpendicular injection laser in addition to the injection laser parallel to the thruster axis. This modification allowed the measurement of the transversal component of the ion velocity field in the plume region of the thruster. First, measurements of the longitudinal component of the ion velocity field in the source, with a millimetric spatial resolution, were performed for several thruster operating conditions in mass flow rate and power. Results showed that the longitudinal ion velocity increases in the source from the ECR region to the exit plane. This acceleration does not depend much on the thruster operating conditions. Negative values of ion velocity were measured close to the backplate of the thruster, signifying that upstream the ECR region, the ions are directed toward the backplate. The analysis of the broadening of the ion velocity distribution function in the source showed that the ions are not created exactly at the same location in the source. This result was confirmed by an asymmetric ion velocity distribution function measured in the plume region of the thruster. In the plume region, the longitudinal component of the ion velocity field was measured for several thruster operating conditions and two magnetic nozzle configurations in the axis of the thruster. Results showed that the acceleration profile of the ions is different in the plume than that in the source. Moreover, in the plume, the acceleration of the ions depends on the thruster operating condition, with a greater acceleration for higher powers and lower mass flow rates. In addition to these measurements made in the axis of the thruster, and to extend the dataset, the two components of the ion velocity field were measured in a two dimensional plane of  $8 \times 18$  cm in the plume region, for the thruster operating conditions of 1 sccm in mass flow rate and 32 W of power and for two different magnetic topologies.

An isothermal model, fluid for both ions and electrons, of plasma expansion in a diverging magnetic field was derived, and an analytical solution was computed under the assumption of a plasma attached to the magnetic field lines. A good agreement was found between the model and the experimental data, both along the central magnetic field line and along magnetic field lines off-axis. The electron temperature, estimated from the measurements of the ion velocity and density, increases with the thruster power and decreases with the thruster mass flow rate, illustrating the fact that the ion acceleration is driven by the electron dynamics. The analytical solution for a polytropic expansion was also computed, and results showed that the polytropic index is close to  $\gamma = 1$ . It confirmed that the isothermal model is a fairly valid approximation to describe the ion acceleration in a diverging magnetic nozzle.

Two limits arose from this study presented in chapter 3. First, the model did not describe the detachment of the ions from the magnetic field lines, and, second, due to the lack of LIF signal, the plasma parameters were not measured at distances greater than 20 cm away from the thruster source.

A directional Faraday cup was developed to deal with these two limitations, and was introduced in chapter 4. This electrostatic diagnostic has an innovative design with a cup separated in two parts, the plate and the cylinder, which allows to measure locally the angular distribution of ion current density. The Acceptance and the Opening functions of the cup, which quantify the ability of the diagnostic to select the ion flux collected according to its direction with respect to the axis of the cup, were defined, computed and validated thanks to ballistic simulations and experimental measurements in front of an ion source. Then, simulations of the diagnostic and measurements of the ion current density in the plume of the ECR thruster allowed to define recommended values of biasing voltage of the cup in order to be able to effectively assess the angular distribution of ion current density in the plume of the ECR thruster.

In chapter 5, the directional Faraday cup was used to measure the local ion flux trajectories in the plume of the ECR thruster, for distances ranging from 20 cm to 60 cm from the thruster source, for several thruster operating conditions in mass flow rate, power and vacuum conditions in the vacuum facility, as well as for two magnetic topologies. The comparison of the local ion flux trajectory with the local direction of the magnetic field showed that the ions are attached to the magnetic field lines in the centre part of the magnetic nozzle while they are separated on the lateral part. The good angular resolution of these measurement allowed for a precise determination of the location of the ion detachment. Results showed that the location of the ion detachment does not depend on the thruster operating condition. This observation was confirmed by the analysis of asymmetry of the local angular distribution of ion current density. However, the mass flow rate, the power and the vacuum condition have an influence on the trajectories of the ions that are already detached from the magnetic field lines. Changing the vacuum condition most significantly influences the trajectories of the detached ions, which are more diverging at greater background pressure. The analysis of the trajectories of the ions detached from the magnetic field lines showed that, once detached, ions follow a straight-line trajectory. Therefore, the operating condition influences the direction of this trajectory. For all the condition tested, the trajectory of the ions at the location of the detachment is more diverging than the local direction of the magnetic field.

One last observation of the experimental characterisation of the ion detachment is the influence of the Earth magnetic field on the ion trajectories. In fact, it is shown that, at the distances at which the directional Faraday cup measurements were performed, this constant external magnetic field cannot be neglected. However, the trajectory of the ions seems driven by the sum of the magnetic field produced by the magnet and the azimuthal average of the Earth magnetic field. This observation could be explained by a global rotational dynamic of the plasma. Due to the great inertia of the ions, it suggests that the dynamics of the ions is driven by the ambipolar electric field produced by the dynamics of the electrons which rotate at high frequency in the magnetic nozzle. An other explanation could be the modification of the magnetic field by the plasma dynamics. This point needs to be further investigated.

In chapter 6, the thrust of the ECR thruster was estimated from measurements of the ion current density performed with the directional Faraday cup and with a flat Faraday probe with guard ring. These estimations were compared to direct measurements of the thrust performed with a thrust stand. Results showed that the Faraday probe with guard ring yields an overestimation of the ion current density and therefore an overestimation of the thrust. It is due to the fact that the plume of the ECR thruster is composed of electrons with a high energy, so the electrostatic diagnostics must be biased at high negative voltages to measure the ion saturation current. It results the presence of a thick plasma sheath in front of the probe which bends the ion trajectories. The design of the Faraday cup limits significantly this effect, and using this diagnostic to estimate the thrust reduces the error from 30% to 10%.

The approximation made in the estimation of the thrust from measurements of the ion current density in the plume of the ECR thruster were challenged to reduce the error of estimation. It was found that taking into account the local trajectory of the ions has a minor effect on the estimation. However, the contribution to the thrust of the ions ionised twice cannot be neglected. Moreover, The presence of slow ions and fast neutrals resulting from a charge exchange collision in the source of the thruster must also be taken into account, especially at high mass flow rates greater than 2 sccm.

### **Perspectives for future work**

The findings presented in this manuscript lead to several perspectives for future studies, which could be conducted in a view of better understanding the physics of magnetic nozzles and optimising the ECR thruster.

Concerning the experimental part, a proper measurement of the electron temperature should be performed along the expansion of the plasma in the plume of the ECR thruster, close to the source, i.e. at several centimetres, and at greater distances of several tens of centimetres. Associated to measurements of the ion or electron density, they would allow to deeply investigate the electron cooling, if any. These measurements could be performed with the Thomson scattering diagnostic, or with a Langmuir probe. In both cases, a good care should be taken in the choice of the experimental setup and the post processing of the data since the density varies of several orders of magnitude in this range of distances. Moreover, it could also be very insightful to consider the anisotropy of the electron temperature, which has not been taken into account in this study. Such measurements would complete the dataset presented in chapter 3. For an off-axis analysis, if the measurements are not performed along a magnetic field line different from the axis of the thruster, the spatial resolution should be sufficient for a proper interpolation of the data. Such measurements would allow to make the link between electron and ion dynamics in an experimental way and compare it with the model described in chapter 3.

In order to go further in the analysis of the ion detachment from the magnetic nozzle of the ECR thruster led in chapter 5, measurements of the ion trajectories could be compared to measurements of plasma potential, performed with an emissive probe for example. Such parameter could be very insightful on the link between the properties of the electron dynamics and the detachment of the ions. The direction of the ambipolar electric field perpendicular to the magnetic field at the detachment location could explain the outward detachment observed in chapter 5. Moreover, a measurement of the three components of the magnetic field in the plume region in presence and in absence of plasma could be a straightforward way of testing the MHD detachment scenario. Finally, an other phenomenon which should be investigated is the plasma fluctuations in the source and the plume of the ECR thruster. In fact, several studies suggest that they could take part in the plasma detachment [61, 77].

The results presented in this work also give indications on the way to lead an optimisation of the performances of the ECR thruster. It is clear from the study of the plasma acceleration in chapter 3 that the source and the plume of the thruster can be considered as two distinct regions to analyse separately. Hence, an optimisation of the properties of the source (geometry, material, thruster operating conditions, ...) can be performed with a constant magnetic topology. Since the electron dynamics drive the ion acceleration, and therefore the performances, the electron temperature inside the source of the thruster seems to be a good parameter to look at during the optimisation process. It can be measured in a non-intrusive way with an embedded curling probe for example. The magnetic topology should be optimised only in a second phase, once the optimisation of the source properties yields optimised initial conditions. The optimisation of the magnetic topology should be tackled with a deep understanding of the plasma detachment. In particular, the study of the detachment should focus on the link between acceleration and detachment of the ions and the link between the thruster operating condition and the trajectory of the detached ions.

Finally, the different results presented in this manuscript should be further confronted to theoretical models and numerical simulations. In particular, a 3D3V Particle in Cell code is being developed at ONERA and could yield valuable information on the physical processes at stake in both the acceleration and the detachment of the plasma from the magnetic nozzle. The findings of the last part of chapter 6 concerning the charge exchange collisions and the presence of ions ionised twice in the plume of the ECR thruster could be used as input values in the different models and simulations.

Overall, the results presented in this study constitute an extensive set of experimental data useful for the comprehension of the ion dynamics in the magnetic nozzle of the ECR thruster, from their creation in the source of the device to their detachment from the magnetic field lines. The data concerning the ion detachment remains to be compared to theoretical models and numerical simulations for a in-depth study of the processes at stake in this phenomenon.

# A | Intensities of the Zeeman transitions

Transverse observation

Transition	$I_\pi$	$I_\sigma(M \rightarrow M - 1)$	$I_\sigma(M \rightarrow M + 1)$
$\gamma J \rightarrow \gamma' J$	$M^2$	$\frac{1}{4}(J + M)(J + 1 - M)$	$\frac{1}{4}(J - M)(J + 1 + M)$
$\gamma J \rightarrow \gamma'(J - 1)$	$J^2 - M^2$	$\frac{1}{4}(J + M)(J - 1 + M)$	$\frac{1}{4}(J - M)(J - 1 - M)$
$\gamma J \rightarrow \gamma'(J + 1)$	$(J + 1)^2 - M^2$	$\frac{1}{4}(J + 1 - M)(J - M + 2)$	$\frac{1}{4}(J + 1 + M)(J + M + 2)$

Longitudinal observation

Transition	$I_\pi$	$I_\sigma(M \rightarrow M - 1)$	$I_\sigma(M \rightarrow M + 1)$
$\gamma J \rightarrow \gamma' J$	0	$\frac{1}{2}(J + M)(J + 1 - M)$	$\frac{1}{2}(J - M)(J + 1 + M)$
$\gamma J \rightarrow \gamma'(J - 1)$	0	$\frac{1}{2}(J + M)(J - 1 + M)$	$\frac{1}{2}(J - M)(J - 1 - M)$
$\gamma J \rightarrow \gamma'(J + 1)$	0	$\frac{1}{2}(J + 1 - M)(J - M + 2)$	$\frac{1}{4}(J + 1 + M)(J + M + 2)$

Table A.1: Intensities of the Zeeman transitions with respect to the quantum numbers J and M of the initial and final states (reproduced from [7]).



## B | Numerical values of ion saturation bias voltage of the directional Faraday cup

The table below represents the value of voltage necessary to bias the collectors (plate and cylinder) of the directional Faraday cup to enter the ion saturation region (see section 4.3.1 for more details).

	0.8 sccm	1 sccm	1.3 sccm	1.6 sccm	1.9 sccm	2.2 sccm
14.1 W	-284.4	-303.7	-274.0	-231.2	-205.5	-160.6
17.8 W	-353.6	-311.5	-296.8	-232.0	-204.6	-187.9
20.2 W	-348.8	-306.0	-337.8	-239.5	-227.0	-189.3
24.1 W	-380.7	-318.7	-342.4	-324.9	-226.9	-207.2
27.7 W	-360.9	-367.6	-355.9	-330.0	-234.7	-223.6
30.2 W	-386.0	-380.1	-378.7	-330.0	-250.2	-235.8
34.1 W	-472.7	-378.7	-404.7	-364.9	-268.0	-245.6
39.9 W	-429.5	-452.7	-430.1	-377.1	-339.1	-271.7
44.7 W	-450.0	-438.0	-434.4	-403.8	-351.7	-330.2
51.7 W	-412.7	-491.0	-477.0	-444.0	-354.1	-332.7
57.4 W	-438.8	-499.0	-484.7	-497.3	-442.6	-348.6

Table B.1: Numerical values of  $V_b^{IS}$  (in V) measured for the different thruster operating conditions of mass flow rate and power.



## C | Direction of a particle following a linear trajectory

Let a particle be located at the distances  $\rho_1$  and the angular position  $\theta_1$  with a direction of angle  $\alpha_1$  (figure C.1). This particle is supposed to follow a linear trajectory. The equation of this trajectory in the cartesian  $(R, Z)$  plane is:

$$z = \rho_1 \cos(\theta_1) + \tan\left(\frac{\pi}{2} - (\theta_1 + \alpha_1)\right) (r - \rho_1 \sin(\theta_1)) \quad (\text{C.1})$$

At the distance  $\rho_2$ , the angular position of the particle is denoted by  $\theta_2$  and its direction is  $\alpha_2$ .  $\theta_2$  is the unique solution of the following equation :

$$\rho_2 \cos(\theta_2) = \rho_1 \cos(\theta_1) + \tan\left(\frac{\pi}{2} - (\theta_1 + \alpha_1)\right) (\rho_2 \sin(\theta_2) - \rho_1 \sin(\theta_1)) \quad (\text{C.2})$$

$\alpha_2$  is then:

$$\alpha_2 = \frac{\pi}{2} - \theta_2 - \arctan\left(\frac{\rho_1 \cos(\theta_1) - \rho_2 \cos(\theta_2)}{\rho_1 \sin(\theta_1) - \rho_2 \sin(\theta_2)}\right) \quad (\text{C.3})$$

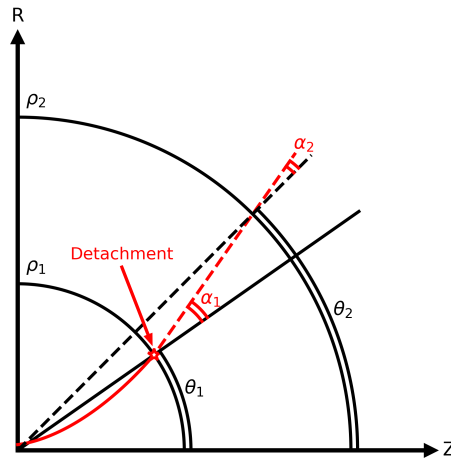


Figure C.1: Schematic of a particle following a linear trajectory after being detached from the magnetic nozzle.



## D | Efficiency of the ECR thruster

The different types of efficiencies of an electric propulsion device, defined in chapter 1, are computed for several values of thruster mass flow rate and thruster power with the magnetic topology  $M_1$  (figure D.1). To compute these efficiencies, the ion current density is measured at  $\rho = 31.5$  cm with the directional Faraday cup in cup mode. The data set is the same than that used in chapter 5.

Results show that the divergence efficiency  $\eta_d$  does not depend on the thruster operating conditions. Moreover, the total efficiency of the device used throughout this manuscript ranges from 2% to 5%. These values are very far from the 40% to 50% obtained with the optimised version of the device presented in ref [38].

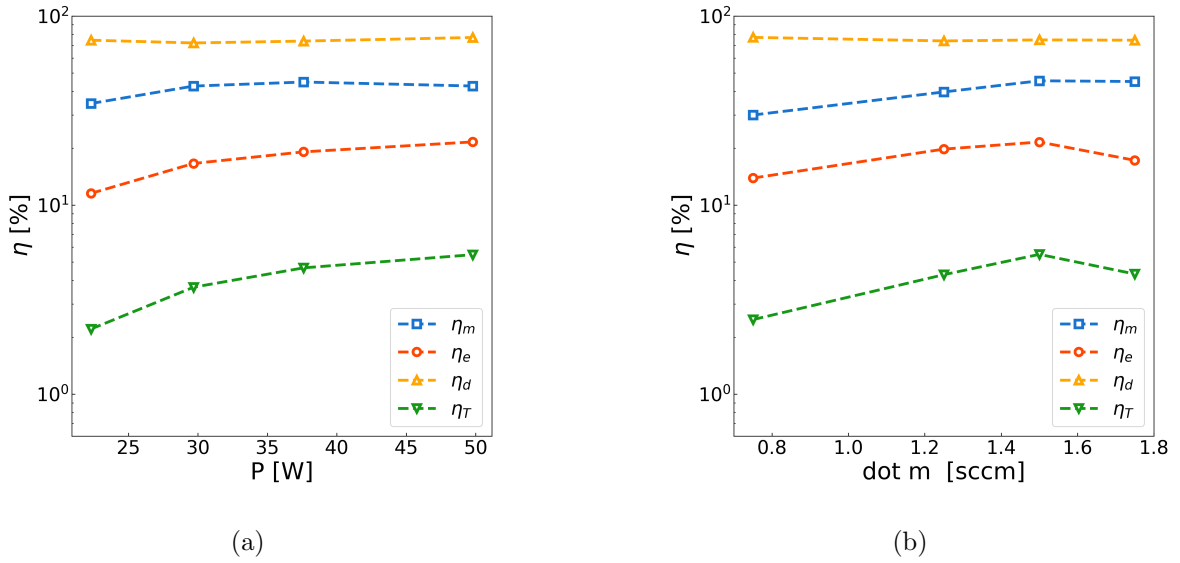


Figure D.1: Efficiencies of the ECR thruster used in this manuscript at (a) constant mass flow rate 1 sccm and (b) constant power of 30 W.



# Bibliography

- [1] Chabert P. *PHY569B : Plasmas in Space Science and Technology*. Ecole Polytechnique, 2021.
- [2] Aroh Barjatya. *Langmuir Probe Measurements in the Ionosphere*. PhD dissertation, Utah State University, 2007.
- [3] T. Vialis, J. Jarrige, A. Aanesland, and D. Packan. Direct thrust measurement of an electron cyclotron resonance plasma thruster. *Journal of Propulsion and Power*, 34(5):1323–1333, 2018.
- [4] Daniel L. Brown, Mitchell L. R. Walker, James Szabo, Wensheng Huang, and John E. Foster. Recommended practice for use of faraday probes in electric propulsion testing. *Journal of Propulsion and Power*, 33(3):582–613, 2017.
- [5] F. Boni. *Development of a microwave plasma diagnostic applied to electric propulsion systems*. PhD dissertation, Université Paris Saclay, 2022.
- [6] E. B. Saloman. Energy Levels and Observed Spectral Lines of Xenon, Xe I through Xe LIV. *Journal of Physical and Chemical Reference Data*, 33(3):765–921, 08 2004.
- [7] R. W. P. McWhirter. *Plasma Diagnostic Techniques*. Academic Press, New York, 1965.
- [8] F. F. Chen. *Plasma Physics and Controlled Fusion*. Plenum Press New York, Second edition, 1984.
- [9] Michael A. Lieberman and Allan J. Lichtenberg. *Principles of plasma discharges and material processing*. WILEY, Second edition, 2005.
- [10] Dan M. Goebel and Ira Katz. *Fundamentals of Electric Propulsion: Ion and Hall Thrusters*. JPL Space Science and Technology Series, 2008.
- [11] Igor D. Kaganovich, Andrei Smolyakov, Yevgeny Raitses, Eduardo Ahedo, Ioannis G. Mikellides, Benjamin Jorns, Francesco Taccogna, Renaud Gueroult, Sedina Tsikata, Anne Bourdon, Jean-Pierre Boeuf, Michael Keidar, Andrew Tasman Powis, Mario Merino, Mark Cappelli, Kentaro Hara, Johan A. Carlsson, Nathaniel J. Fisch, Pascal Chabert, Irina Schweigert, Trevor Lafleur, Konstantin Matyash, Alexander V. Khrabrov, Rod W. Boswell, and Amnon Fruchtman. Physics of ExB discharges relevant to plasma propulsion and similar technologies. *Physics of Plasmas*, 27(12):120601, 12 2020.
- [12] Robert B. Lobbia and Brian E. Beal. Recommended practice for use of langmuir probes in electric propulsion testing. *Journal of Propulsion and Power*, 33(3):566–581, 2017.

- [13] James E. Polk, Anthony Pancotti, Thomas Haag, Scott King, Mitchell Walker, Joseph Blakely, and John Ziemer. Recommended practice for thrust measurement in electric propulsion testing. *Journal of Propulsion and Power*, 33(3):539–555, 2017.
- [14] Kurt A. Polzin, Carrie S. Hill, Peter J. Turchi, Rodney L. Burton, Sarah Messer, Ralph H. Lovberg, and Ashley K. Hallock. Recommended practice for use of inductive magnetic field probes in electric propulsion testing. *Journal of Propulsion and Power*, 33(3):659–667, 2017.
- [15] Casey C. Farnell, Cody C. Farnell, Shawn C. Farnell, and John D. Williams. Recommended practice for use of electrostatic analyzers in electric propulsion testing. *Journal of Propulsion and Power*, 33(3):638–658, 2017.
- [16] J. P. Sheehan, Yevgeny Raitses, Noah Hershkowitz, and Michael McDonald. Recommended practice for use of emissive probes in electric propulsion testing. *Journal of Propulsion and Power*, 33(3):614–637, 2017.
- [17] John W. Dankanich, Mitchell Walker, Michael W. Swiatek, and John T. Yim. Recommended practice for pressure measurement and calculation of effective pumping speed in electric propulsion testing. *Journal of Propulsion and Power*, 33(3):668–680, 2017.
- [18] H. M. Mott-Smith and Irving Langmuir. The theory of collectors in gaseous discharges. *Physical Review*, 28:727–763, Oct 1926.
- [19] J. D. Swift and M. J. R. Schwar. *Electrical Probes for Plasma Diagnostics*. Elsevier, New York, 1970.
- [20] I. H. Hutchinson. *Principles of Plasma Diagnostics*. Cambridge Univ. Press, Second edition, 2002.
- [21] Evgeny V. Shun’ko. *Langmuir Probe in Theory and Practice*. Universal-Publishers, 2009.
- [22] Francis F Chen. Langmuir probes in rf plasma: surprising validity of oml theory. *Plasma Sources Science and Technology*, 18(3):035012, may 2009.
- [23] M. J. Druyvesteyn and F. M. Penning. The mechanism of electrical discharges in gases of low pressure. *Review of Modern Physics*, 12:87–174, Apr 1940.
- [24] I D Sudit and F F Chen. Rf compensated probes for high-density discharges. *Plasma Sources Science and Technology*, 3(2):162, may 1994.
- [25] V. Hugonnaud. *Plasma probe measurements for electric propulsion device ion beam: optimization and standardization*. PhD dissertation, Technische Universität Wien, 2022.
- [26] Federico Boni, Julien Jarrige, Victor Désangles, and Tiberiu Minea. The curling probe: A numerical and experimental study. Application to the electron density measurements in an ECR plasma thruster. *Review of Scientific Instruments*, 92(3):033507, 03 2021.
- [27] P. Q. Elias, J. Jarrige, E. Cucchetti, F. Cannat, and D. Packan. 3D ion velocity distribution function measurement in an electric thruster using laser induced fluorescence tomography. *Review of Scientific Instruments*, 88(9):093511, 09 2017.
- [28] David B. Miller, Per Gloersen, Edward F. Gibbons, and D J. BenDaniel. Cyclotron resonance propulsion system. *Electric Propulsion Conference*, 1962.

- [29] J. C. Sercel. *An experimental and theoretical study of the ECR thruster*. PhD dissertation, California Institute of Technology, 1993.
- [30] S. Larigaldie. Plasma thruster and method for generating a plasma propulsion thrust. brevet n°1162545, 2015.
- [31] F. Cannat. *Caractérisation et modélisation d'un propulseur plasma à résonance cyclotronique des électrons*. PhD dissertation, Ecole polytechnique, 2015.
- [32] T. Vialis. *Développement d'un propulseur plasma à résonance cyclotron électronique pour les satellites*. PhD dissertation, Sorbonne Université, 2018.
- [33] S. Peterschmitt. *Development of a stable and efficient electron cyclotron resonance thruster with magnetic nozzle*. PhD dissertation, Institut Polytechnique de Paris, 2020.
- [34] J. Porto. *Kinetic Simulation of a Magnetized Plasma in an Electron Cyclotron Resonance Plasma Thruster with Magnetic Nozzle*. PhD dissertation, Observatoire de Paris, 2021.
- [35] Sara Correyero Piazza. *Physics of plasma plumes accelerated by magnetic nozzles: an experimental and theoretical research*. PhD dissertation, Universidad Carlos III de Madrid, 2020.
- [36] Álvaro Sánchez Villar. *Modeling the plasma discharge in an electron-cyclotron-resonance thruster*. PhD dissertation, Universidad Carlos III de Madrid, 2021.
- [37] Benjamin Wachs. *Optimization and Characterization of Facility Effects for a Low-Power Electron Cyclotron Resonance Magnetic Nozzle Thruster*. PhD dissertation, University of Michigan, 2022.
- [38] Victor Désangles, Denis Packan, Julien Jarrige, Simon Peterschmitt, Patrick Dietz, Steffen Scharmann, Kristof Holste, and Peter J. Klar. ECRA thruster advances: 30W and 200W prototypes latest performances. *Journal of Electric Propulsion*, 2(1), 2023.
- [39] V. Hugonnaud, S. Mazouffre, and D. Krejci. Faraday cup sizing for electric propulsion ion beam study: Case of a field-emission-electric propulsion thruster. *Review of Scientific Instruments*, 92(8):084502, 08 2021.
- [40] V. Hugonnaud and S. Mazouffre. Optimization of a faraday cup collimator for electric propulsion device beam study: Case of a hall thruster. *Applied Sciences*, 11(5), 2021.
- [41] Benjamin Wachs and Benjamin Jorns. Background pressure effects on ion dynamics in a low-power magnetic nozzle thruster. *Plasma Sources Science and Technology*, 29(4):045002, mar 2020.
- [42] S. Baldinucci, S. Bergmann, J. Hondagneu, B. Wachs, and B. Jorns. Impact of Facility Electrical Boundary Conditions on the Performance of an Electron Cyclotron Resonance Magnetic Nozzle Thruster. *37th International Electric Propulsion Conference, Boston USA*, 2022.
- [43] F. Boni, V. Désangles, P. Q. Elias, and D. Packan. Investigation of facility effects on the performance of an electron cyclotron resonance magnetic nozzle thruster. *38th International Electric Propulsion Conference, Toulouse France*, 2024.
- [44] F. R. Chang Diaz. An overview of the VASIMR engine: High power space propulsion with RF plasma generation and heating. *AIP Conference Proceedings*, 595(1):3–15, 10 2001.

- [45] K. Takahashi. Helicon-type radiofrequency plasma thrusters and magnetic plasma nozzles. *Reviews of Modern Plasma Physics*, 3, 2019.
- [46] G. Krulle, M. Auweter-Kurtz, and A. Sasoh. Technology and application aspects of applied field magnetoplasmadynamic propulsion. *Journal of Propulsion and Power*, 14(5):754–763, 1998.
- [47] Justin M. Little and Edgar Y. Choueiri. Thrust and efficiency model for electron-driven magnetic nozzles. *Physics of Plasmas*, 20(10):103501, 10 2013.
- [48] A. I. Smolyakov, A. Sabo, P. Yushmanov, and S. Putvinskii. On quasineutral plasma flow in the magnetic nozzle. *Physics of Plasmas*, 28(6):060701, 06 2021.
- [49] Mario Merino and Eduardo Ahedo. Influence of electron and ion thermodynamics on the magnetic nozzle plasma expansion. *IEEE Transactions on Plasma Science*, 43(1):244–251, 2015.
- [50] T. A. Collard and B. A. Jorns. Magnetic nozzle efficiency in a low power inductive plasma source. *Plasma Sources Science and Technology*, 28(10):105019, oct 2019.
- [51] J. M. Little and E. Y. Choueiri. Electron cooling in a magnetically expanding plasma. *Phys. Rev. Lett.*, 117:225003, Nov 2016.
- [52] T Laffleur, F Cannat, J Jarrige, P Q Elias, and D Packan. Electron dynamics and ion acceleration in expanding-plasma thrusters. *Plasma Sources Science and Technology*, 24(6):065013, nov 2015.
- [53] S Correyero, J Jarrige, D Packan, and E Ahedo. Plasma beam characterization along the magnetic nozzle of an ecr thruster. *Plasma Sources Science and Technology*, 28(9):095004, sep 2019.
- [54] Alfio E. Vinci, Quentin Delavière–Delion, and Stéphane Mazouffre. Electron thermodynamics along magnetic nozzle lines in a helicon plasma. *Journal of Electric Propulsion*, 1, 04 2022.
- [55] Jr. Moses, Ronald W., Richard A. Gerwin, and Kurt F. Schoenberg. Resistive plasma detachment in nozzle based coaxial thrusters. *AIP Conference Proceedings*, 246(1):1293–1303, 01 1992.
- [56] E. B. Hooper. Plasma detachment from a magnetic nozzle. *Journal of Propulsion and Power*, 9(5):757–763, 05 1993.
- [57] Justin Little and Edgar Choueiri. Plasma detachment and momentum transfer in magnetic nozzles. *47th AIAA/ASME/SAE/ASEE Joint Propulsion Conference & Exhibit*, 2011.
- [58] Eduardo Ahedo and Mario Merino. Two-dimensional plasma expansion in a magnetic nozzle: Separation due to electron inertia. *Physics of Plasmas*, 19(8):083501, 08 2012.
- [59] B. N. Breizman, M. R. Tushentsov, and A. V. Arefiev. Magnetic nozzle and plasma detachment model for a steady-state flow. *Physics of Plasmas*, 15(5):057103, 04 2008.
- [60] Eduardo Ahedo and Mario Merino. On plasma detachment in propulsive magnetic nozzles. *Physics of Plasmas*, 18(5):053504, 05 2011.

- [61] Christopher S. Olsen, Maxwell G. Ballenger, Mark D. Carter, Franklin R. Chang Díaz, Matthew Giambusso, Timothy W. Glover, Andrew V. Ilin, Jared P. Squire, Benjamin W. Longmier, Edgar A. Bering, and Paul A. Cloutier. Investigation of plasma detachment from a magnetic nozzle in the plume of the vx-200 magnetoplasma thruster. *IEEE Transactions on Plasma Science*, 43(1):252–268, 2015.
- [62] Christopher A. Deline, Roger D. Bengtson, Boris N. Breizman, Mikhail R. Tushentsov, Jonathan E. Jones, D. Greg Chavers, Chris C. Dobson, and Branwen M. Schuettpelez. Plume detachment from a magnetic nozzle. *Physics of Plasmas*, 16(3):033502, 03 2009.
- [63] Justin M. Little and Edgar Y. Choueiri. Electron demagnetization in a magnetically expanding plasma. *Physical Review Letter*, 123:145001, Oct 2019.
- [64] N. Dorval, J. Bonnet, J. P. Marque, E. Rosencher, S. Chable, F. Rogier, and P. Lasgorceix. Determination of the ionization and acceleration zones in a stationary plasma thruster by optical spectroscopy study: Experiments and model. *Journal of Applied Physics*, 91(8):4811–4817, 04 2002.
- [65] R. Gueroult. *Etude d’une source d’ions obtenue par extraction et accélération d’ions à partir d’une source plasma filaire*. PhD dissertation, Ecole polytechnique, 2011.
- [66] E. Ahedo and M. Merino. Two-dimensional supersonic plasma acceleration in a magnetic nozzle. *Physics of Plasmas*, 17(7):073501, 07 2010.
- [67] D Vatansever and D Levin. Development of a Fully Kinetic 3-D Code for Magnetized Plumes. *38th International Electric Propulsion Conference, Toulouse, France, 2024*.
- [68] Benjamin Vincent, Sedina Tsikata, Stéphane Mazouffre, Tiberiu Minea, and Jérôme Fils. A compact new incoherent thomson scattering diagnostic for low-temperature plasma studies. *Plasma Sources Science and Technology*, 27(5):055002, may 2018.
- [69] R. Pioch, V. Désangles, and P. Chabert. Investigation of the directional Faraday cup and improvement of the comparison between direct and indirect thrust measurements of a magnetic nozzle ECR thruster. *Physics of Plasmas*, 31(4):043516, 04 2024.
- [70] David A Dahl. Simion for the personal computer in reflection. *International Journal of Mass Spectrometry*, 200:3–25, 2000.
- [71] Álvaro Sánchez-Villar, Federico Boni, Victor Désangles, Julien Jarrige, Denis Packan, Eduardo Ahedo, and Mario Merino. Comparison of a hybrid model and experimental measurements for a dielectric-coated coaxial ecr thruster. *Plasma Sources Science and Technology*, 32(1):014002, jan 2023.
- [72] Nina Sarah Mühlich, Joachim Gerger, Bernhard Seifert, and Friedrich Aumayr. Simultaneously measured direct and indirect thrust of a feep thruster using novel thrust balance and beam diagnostics. *Acta Astronautica*, 197:107–114, 2022.
- [73] Homer D. Hagstrum. Auger ejection of electrons from molybdenum by noble gas ions. *Phys. Rev.*, 104:672–683, Nov 1956.
- [74] John Williams, Mark Johnson, and Desiree Williams. Differential sputtering behavior of pyrolytic graphite and carbon-carbon composite under xenon bombardment. *40th AIAA/ASME/SAE/ASEE Joint Propulsion Conference and Exhibit*, 07 2004.

- [75] J. Scott Miller, Steve H. Pullins, Dale J. Levandier, Yu-hui Chiu, and Rainer A. Dressler. Xenon charge exchange cross sections for electrostatic thruster models. *Journal of Applied Physics*, 91(3):984–991, 02 2002.
- [76] Severin Astruc. *Conception et validation d'un micro-capteur pour la mesure de poussée de propulseurs électriques de satellites*. PhD dissertation, Université Paris Saclay, 2023.
- [77] Shadrach Hepner, Benjamin Wachs, and Benjamin Jorns. Wave-driven non-classical electron transport in a low temperature magnetically expanding plasma. *Applied Physics Letters*, 116(26):263502, 07 2020.

**Titre :** Dynamiques ioniques dans la tuyère magnétique d'un propulseur à Résonance Cyclotronique des Electrons.

**Mots clés :** Physique des Plasmas, Tuyères magnétiques, ingénierie spatiale

**Résumé :** Au cours des dernières décennies, les moyens de propulsion des satellites ont évolué et la propulsion électrique s'est imposée face à la propulsion chimique classiquement utilisée. Les propulseurs électriques produisent, accélèrent et éjectent un gaz ionisé, appelé plasma, pour générer une force de poussée. Le propulseur ECRA est un concept de propulseur électrique développé à l'ONERA qui bénéficie d'un design simple et innovant. Le plasma est accéléré dans un champ magnétique divergent appelé tuyère magnétique. L'objectif de cette thèse est de comprendre les phénomènes régissant l'accélération et l'éjection du plasma dans la tuyère magnétique du propulseur ECRA. Dans un premier temps, l'amélioration du diagnostic de Fluorescence Induite par Laser (LIF) a permis la mesure des deux composantes du champ de vitesse des ions dans la source du propulseur et dans les 20 premiers centimètres de la tuyère magnétique du propulseur. La solution analytique d'un modèle fluide et isotherme décrivant l'expansion d'un plasma dans une tuyère magnétique a été dérivée et comparée aux données expérimentales, et un bon accord a été trouvé entre les mesures et la théorie. Dans un second temps, pour pallier au manque de signal de LIF dans la plume du propulseur à des distances supérieures à 20cm, un diagnostic électrostatique a été développé : la coupe de Faraday directionnelle. Grâce à un design innovant, ce diagnostic permet une sélection angulaire du flux d'ion collecté. Cette propriété directionnelle a été validée grâce à des mesures de flux en face d'une source à ions calibrée puis des mesures de flux d'ions dans la plume du propulseur ECRA. De plus, l'utilisation de ce diagnostic pour estimer la poussée du propulseur donne une erreur de 5% par rapport à la mesure directe de poussée effectuée grâce à une balance. Ce résultat est à comparer à une erreur de plus de 20% obtenue quand une sonde de Faraday plate est utilisée, ce qui valide le niveau de courant mesuré par la coupe

de Faraday directionnelle. Ce diagnostic de coupe de Faraday directionnelle a été monté sur un moteur pas à pas, permettant une rotation de la sonde autour d'un axe coupant son orifice d'entrée. Grâce à ce montage, la distribution angulaire de densité de courant des ions a pu être mesurée localement dans la plume du propulseur ECRA. Cette propriété a permis d'évaluer la direction locale du flux d'ions dans une zone s'étendant de 20 à 60 cm de la source du propulseur pour différents débits de gaz, puissances du propulseur, conditions de vide dans l'enceinte de test et topologies de tuyère magnétiques. La comparaison de la direction du flux d'ions avec la direction des lignes de champs magnétique dans la tuyère a permis de mettre en évidence plusieurs résultats. Premièrement, les ions ont une trajectoire colinéaire aux lignes de champ magnétique dans la partie centrale de la plume. Deuxièmement, les ions sont détachés des lignes de champs de la tuyère dans la partie latérale de la plume. La position de ce détachement ne dépend ni des conditions d'opérations du propulseur, ni du niveau de vide dans l'enceinte. En revanche, ces conditions ont une influence sur la trajectoire des ions détachés des lignes de champ magnétique. En effet, il est montré que les ions détachés suivent des trajectoires rectilignes. Par conséquent, les conditions d'opération du propulseur ont une influence sur l'angle que font les ions avec les lignes de champ magnétique à la position du détachement. Pour toutes les conditions testées, ce détachement est plus divergent que le champ magnétique. Enfin, il apparaît que la tuyère magnétique gouvernant la dynamique des ions résulte de la somme du champ magnétique produit par l'aimant permanent du propulseur et de la moyenne azimutale de l'influence du champ magnétique terrestre. Ce résultat inattendu pourrait être expliqué par une dynamique de rotation globale du plasma dans la tuyère magnétique du propulseur ECR.

**Title :** Ion dynamics in the magnetic nozzle of an Electron Cyclotron Resonance thruster

**Keywords :** Plasma physics, Magnetic nozzles, Space engineering

**Abstract :** Over the last decades, the spacecrafts propulsion systems have evolved, and the electric propulsion has been favoured over the traditionally used chemical propulsion. An electric propulsion device produces, accelerates and ejects an ionised gas, called plasma, to generate a thrust force. The ECRA thruster is an electric propulsion concept developed at ONERA which benefits from a simple and innovative design. The plasma is accelerated in a diverging magnetic field, called magnetic nozzle, which simplifies the architecture of the thruster. The objective of this work is to understand the physical phenomena governing the acceleration and the ejection of the plasma in the magnetic nozzle of an ECRA thruster. First, the improvement of the Laser Induced Fluorescence (LIF) diagnostic has allowed for the measurement of the two components of the ion velocity field in the thruster source and within the first 20 centimetres of the magnetic nozzle of the thruster. The analytical solution of a fluid and isothermal model describing the expansion of a plasma in a magnetic nozzle was derived and compared to the experimental data, and a good agreement was found between the measurements and the theory. Secondly, to overcome the lack of LIF signal at distances greater than 20cm in the plume of the ECRA thruster, an electrostatic diagnostic was developed: the directional Faraday cup. Thanks to an innovative design, this diagnostic allows for the angular selection of the collected ion flux. This directional property was validated through ion flux measurements in front of a calibrated ion source and then through ion flux measurements in the plume of the ECRA thruster. Moreover, using this diagnostic to estimate the thrust of the ECR thruster results in an error of 5% compared to the direct thrust measurement performed using a

balance. This result is to be compared with an error of more than 20% obtained when a flat Faraday probe is used, which validates the level of current measured by the directional Faraday cup. This cup has been mounted on a stepper motor to measure the angular distribution of ion current density locally in the plume of the ECRA thruster. It has allowed for the measurement of the local direction of ion flux in an area extending from 20 to 60 cm from the thruster source for different gas flow rates, thruster powers, vacuum conditions in the test chamber, and magnetic nozzle topologies. The comparison of the ion flux direction with the direction of the magnetic field lines of the nozzle has highlighted several results. First, the ions have a trajectory collinear to the magnetic field lines in the centre of the plume. Second, they are detached from the magnetic field lines in the lateral part of the plume. The detachment position does not depend on the operating conditions of the thruster or the vacuum level in the vacuum facility. However, these conditions influence the trajectory of the ions already detached. In fact, it has been shown that the detached ions follow straight-line trajectories. Consequently, the thruster operating conditions influence the angle that the ions make with the magnetic field lines at the detachment location. For all tested conditions, this detachment is more divergent than the magnetic field. Finally, it appears that the magnetic nozzle governing the ion dynamics results from the sum of the magnetic field produced by the thruster permanent magnet and the azimuthal average of the influence of the Earth magnetic field. This unexpected result could be explained by a global rotation dynamic of the plasma in the magnetic nozzle of the ECRA thruster.